Imperial College London

Micro-optics for Opto-genetic Neuro-stimulation with Micro-LED Arrays

Lionel Chaudet

Photonics Group

Department of Physics

Imperial College London

Supervised by Pr. Mark Neil

2014

Thesis submitted in partial fulfilment of the requirements for the degree of Doctor of Philosophy (Ph.D.)

Imperial College of Science, Technology and Medicine

Abstract

The breakthrough discovery of a nanoscale optically gated ion channel protein, Channelrhodopsin 2 (ChR2), in combination with a genetically expressed optically activated ion pump, Halorhodopsin, allowed the direct stimulation and inhibition of individual action potentials with light alone. This thesis describes the development of optics and micro-optics which when used with micro-led array sources, collects and projects light efficiently and uniformly onto such opto-genetically modified specimens. When used with enhanced light gated ion channels and pumps these systems allow us to further our understanding of both brain and visual systems.

Micro-LED arrays (MLA) permit spatio-temporal control of neuron stimulation on sub-millisecond timescales. However, micro-led arrays are disadvantaged by the broad-angular spread of their light emission and their low spatial fill factor. We present the design of macro and micro-optics systems for use with a micro-LED arrays consisting of a matrix of 25µm diameter micro-LEDs with 150 or 80µm centre-to-centre spacing. On one system, the micro-LED array is imaged onto off-the-shelf micro-optics using macro-optics and in the other system; micro-LED array and custom micro-optics are optimised and integrated together. The two systems are designed to improve the fill-factor from 2% to more than 78% by capturing a larger fraction of the LED emission and directing it correctly to the sample plane. This approach allows low fill factor arrays to be used effectively, which in turn has benefits in terms of thermal management and electrical drive from CMOS backplane electronics. These systems were implemented as an independent set that could be connected to a variety of different microscopes available for patch-clamp and multi-electrode measurements. In addition, the feasibility of an eye prosthesis was tested using virtual reality optics and a fake eye to stimulate ganglion cells and a system including an integrated fundus camera was constructed for in-vivo stimulation of the genetically modified retina of a mouse.

Acknowledgement

This thesis has only been possible with the support of many people whom I individually thank here. I would like to thank my supervisor, Professor Mark Neil, for his patience, encouragement and time given in preparation of this thesis. I wish to thank the people I worked with directly on this project, Dr Patrick Degeenar, Dr Rolando Berlinguer-Palmini, Dr Kamyar Mehran, John Barret and Na Dong from Newcastle Universty, Pleun Maaskant from Tyndall, Dr Christian Bamann from MPI, Dasha Nelidova and Daniel Hillier from FMI, and Dr Peter Lanigan and Angelos Loukidis from Scientifica, for their ideas and will to reach a common goal by using their skills and keeping an open mind to others' ideas. I am also grateful to everyone who helped develop my ideas, discussed, commented on and read my work. I thank my research group at Imperial College London. Special thanks are due to all my fellow colleagues for giving me their valuable time and resources: Lionel Fafchamps, James Clegg, Douglass Kelly, Sean Warren, Hugh Sparks, Sunil Kumar, Hugo Sinclair, Vincent Maioli. This work could also not have been completed without the competences of the mechanical and optical workshop, Simon Johnson, Martin Kehoe and Melvyn Patmore. Thanks also to my family and Isabel for their love, and particularly Isabel for patiently reading and correcting my thesis. Anyone I may have missed in the acknowledgement is also thanked.

Author declaration

All the work presented in this thesis is my own with the following exceptions:

- The micro-LED arrays described in chapters 2 to 7 were developed and fabricated by Tyndall in Ireland.
- The development of the micro-LED array CMOS backplane, electronic associated with it and software to drive the micro-LED array was undertaken in the Department of Electrical Engineering, Newcastle University (Chapter 5 and 8).
- One set of opto-mechanics was designed in conjunction with Scientifica (Chapter 6).
- The biological experiments were carried out in conjunction with the Max-Plank Institut (MPI) for Biophysics, Frankfurt (Germany), Department of Electrical Engineering, Newcastle University (United Kingdom) and at Friedrich Miller Institute (FMI), Basel (Switzerland).

To my wife and to my brother

Table of Contents

List of figures

List of tables

List of abbreviations

Al_2O_3	Sapphire (Aluminium Oxyde)
AMD	Age-related macula degeneration
ATP	Adenosine triphosphate
Ca^{2+}	Calcium
ChR2	Channelrhodopsin 2
DH	Digital holography
DMD	Digital micromirror device
DR	Diabetic retinopathy
GaN	Gallium Nitride
GDP/GTP	Guanosine diphosphate/ Guanosine triphosphate
GFP	Green fluorescent protein
GPC	Generalized phase contrast
GPCR	G-protein coupled receptor
InGaN	Indium Gallium Nitride
IP	Ion pump
K^+	Potassium
LED	Light emissive diode
LGIC	Light gated ion channel
MEA	Multi-electrode array
ML	Meniscus lens
MLA	Micro-LED array
MO	Micro-optics
MTF	Modulation transfer function
NA	Numerical aperture
Na^+	Sodium
NpHR	Halorhodopsin
NSC	Non-sequential
OPN4	Melanopsin
PET	Polyethylene terephthalate
PO	Projection optics
QD	Quantum dots
RGC	Retinal ganglion cell
RNIB	Royal national institute of blind people
RO	Relay optics
RP	Retinitis pigmentosa
SLM	Spatial light modulator
TF	Temporal focusing
VR	Virtual reality optics

Chapter 1: Introduction

According to the Royal National Institute for the blind (RNIB), 2 million people are suffering from visual impairment in the UK [1]. The most common causes of impairment are retinal degeneration, glaucoma and diabetic retinopathy (DR). Retinitis pigmentosa (RP) is hereditary [2] and therefore its proportion remains fixed. However, due to the increasing ageing of the population and expanding waistlines, the prevalence of age-related macula degeneration (AMD) and DR are both increasing.

While cataracts can be corrected with surgery and refractive errors with glasses, the degeneration of the photoreceptors cannot be reversed. Treatments exist, which slow down receptor degeneration, for example anti-VEGF drugs [3] and photodynamic therapies [4], however they cannot restore vision. Sufferers of AMD, RP and DR lose their photoreceptors but their optical apparatus remains, which means that an image is still formed on the retina and that a high enough quantity of retinal ganglion cells (RGC), which are usually used to process and transmit the image to the visual cortex, are still viable.

This raises the possibility of stimulating the healthy cells by either replacing the photoreceptors with electrodes, which are in turn stimulating the RGCs or the remaining retinal circuitry layers using electrical signals, or by making the ganglion cells light sensitive such that they work as the image forming detectors.

Different approaches to inserting arrays of electrodes into the retina exist such as epi-retinal, sub-retinal, sub-choroidal and sub-scleral methods [5]. All are powered by either electrical cable, wireless telemetry or optical infra-red illumination. In 2012, the first electronic retina was implanted into the eye of a blind patient and successfully restored some useful vision. However, neuroelectronic interfaces suffer many drawbacks. These devices are very invasive and have poor spatial resolution. Electrical stimuli can excite neurons but not inhibit them. It is not possible to target individual cells or receptive fields. Scalability to large arrays of electrodes is difficult because of the curvature of the retina. Finally, power dissipation in the retina could become a problem for large arrays of stimulators.

Using light to stimulate the RGCs directly would solve many of these problems. Since the 70s, several methods have shown it was possible to stimulate nerve cells with light, but without great efficiency [6], [7] or with possible undesirable effects when UV light was used [8], [9]. In the 2000s, the existence of a third photoreceptor was demonstrated. Some of the RGCs (below 1%), containing a protein called Melanopsin, are sensitive to light and used for the non-image forming processes, such as regulation of the circadian system that synchronises the human body clock [10] and pupil diameter. However, these RGCs react slowly to changes in light level and are physically wired into different parts of the brain than the visual cortex where image information from rods and cones ends up.

In 2003, the breakthrough discovery of a nanoscale optically gated ion channel protein, Channelrhodopsin 2 (ChR2)[11], and its combination with a genetically expressed ion pump, Halorhodopsin, that could be genetically expressed allowed the direct stimulation and inhibition of individual action potentials in neurons with light alone. Optogenetics, encompassing fields as diverse as optics, genetics and virology, really began at that time. This work reports developments of ultra-bright electronically controlled optical array sources with enhanced light gated ion channels and pumps for use in systems to further our understanding of both brain and visual function. As such it also presents a potential route to realising visual prostheses where the programmable array sources are used to stimulate RGCs that have been rendered light sensitive by genetic modification. This work is undertaken as part of the European project, *OptoNeuro*.

Gallium-Nitride micro-LED arrays (MLAs) are a promising technology for delivering the light to the cells of interest. Emitting blue light (470nm) matching the excitation spectrum of ChR2, they permit spatio-temporal control of neuron stimulation on sub-millisecond timescales. However, they are disadvantaged by their spatially broad light emission distribution and low fill factor. The work described in this thesis is based around the design and implementation of an optical set-up to improve the transfer of light from the MLA to biological samples, using micro-lens arrays. Much of the work is based on MLA consisting of a 16x16 matrix of 25µm diameter micro-LEDs with 150µm centre-to-centre spacing, however, design consideration is also made for a 90x90 matrix with 80µm centre-to-centre spacing that was constructed at the end of the Optoneuro project. To achieve the desired goals, two approaches have been taken. The first is to project light from the micro-LED array onto a separate micro-lens array. The second approach is to design and manufacture bespoke micro-lens arrays that can be integrated directly onto the micro-LED array. The effects of the improvement of the illumination are demonstrated on the stimulation of retinal ganglion cells in experiments looking towards the development of an optical retinal prosthesis.

Thesis outline

Chapter 2: Optogenetics: In this chapter, the field in which my project resides is defined. Its toolbox is described, comprising four main components: control, targeting, illumination and measurement. In this project, I am working on the illumination using MLA and MO.

Chapter 3: Technology and Principle: This chapter explains the principle of the project and how micro-optics can help improve the quality and efficiency of the illumination of an MLA when combined with a microscope. Then the technologies used, their evolution and the reasons behind their selection are described.

Chapter 4: Projection optics with off-the-shelf micro-optics: Basic design principle: In this chapter, the reasons and steps behind the development of a proof of principle optical projection system with off-the-shelf MO are described. The different methods to assess the quality of an optical system modelled with an optical design software, Zemax, are shown and then the choice of a basic optical design principle is justified. This will be applied in the relay optical systems presented in chapters 5 and 6.

Chapter 5: Design and implementation of the basic design: "PO 1": In this chapter the development of the first projection optics system "PO 1" using Zemax modelling is described. A physical system is constructed and is tested on microscope platforms. This model is compared to an already existing solution using off-the-shelf components.

Chapter 6: Advance design and implementation: "PO 2": The design of "PO 1" is improved using a more advanced optical design. This design, called "PO 2", is then tested and implemented in opto-mechanical platforms developed in-house and in partnership with Scientifica to allow an easy optical alignment and connection to our partners' different microscope platforms. The advantages of the projection optics and microlenses are demonstrated over bare MLA systems.

Chapter 7: Custom micro-optics development and integration onto micro-LED arrays: An ideal device would consist of an MLA with micro-lenses directly integrated in a single compact device. In this chapter, custom MO and MLA are optimised together using a realistic model of the MLA developed in non-sequential modelling in Zemax. Fabrication of custom micro-lenses is also considered here in a form that can be directly integrated on top of both 16x16 and 90x90 CMOS+MLA devices.

Chapter 8: Biological experiments: The previous set-ups have been specifically constructed to solve the particular situations required by the end application. The micro-lens/micro-LED solutions are shown with a conventional biological microscope system, virtual reality optics for experiments with ex-vivo retina and MEA recording, and a fundus camera for in-vivo experiments with mice.

Chapter 9: Conclusions: An overview of the results obtained in the different chapters is presented and conclusions are drawn from them. Finally, I discuss the possible evolutions and application opportunities following this project.

Chapter 2: Optogenetics

2.1 Introduction

Optogenetics is the combination of genetics, virology and optical methods. It allows scientists to instantaneously activate and silence specific groups of neurons in cells of living tissue with a precision that cannot be achieved by other methods [11]. This chapter describes neuron cells and the way they function, and the importance of optogenetics for their study. The technologies associated to the field and its possible applications are then outlined. Optogenetics groups several technologies. The first and main one is the development of targetable control tools that respond to light and deliver effector function. The others are enabling technologies. They allow the control tools to target the cells of interest, to stimulate them by delivering light into the tissue under investigation and to obtain readouts and perform analysis.

2.2 Neurons

Our sense of the outside world goes through an interaction between peripheral transducers and the brain. The brain is where learning, memory and self-awareness are conferred. The basic structural unit of our nervous system is the neuron, which processes and transmits information though electrical and chemical signals from one part of the body to another. 10^{12} neurons with hundreds of different neuronal types are present in the human brain.

An electrical signal is used to carry messages. It is called a nerve impulse. To create it, a neuron is excited by light, sound, pressure or in most case by chemicals released by other neurons. Neurons are part of neural networks that connect neurons to each other. There are different types of neurons. The sensory neurons are transmitting information from the outside and inside of the body to the central nervous system. The motor neurons pass information from the central nervous system to the rest of the body, such as the muscles. And there are interneurons that associate them.

Neurons are formed of a soma, an axon and dendrites. The soma is the cell body and contains the nucleus. It is the control centre of the neuron. The axon is a cellular extension that grows out of the cell body. It can reach over a metre in humans (see Figure 2-1) and is very thin (1-2µm). At its extremity is the axon terminal and terminal branches, which are the output of the neuron. Dendrites are another set of branches, growing from the soma, a few hundreds micrometres long and sometimes covered by spines, which are small membranous protrusions. They are the primary input to the neuron. Communication takes place at specialized sites known as synapses, which are generally the junction between terminal branches on one neuron and dendrites on the next neuron in the network.

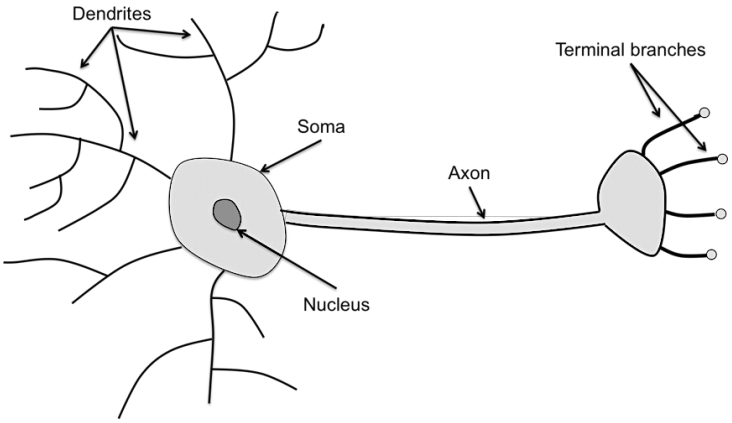

Figure 2-1: Neuron (nerve cell) schematic

There are specific proteins in the plasma membrane that covers the neurons, These proteins are called ion channels or voltage-gated channels, which, when receiving a stimulus (chemical, mechanical…), can arrange themselves to form a passageway from one side to the other side of the membrane that allows ions to pass. This is a quick event that lasts ms after the stimulus. Each ion channel lets only a specific ion through [12]. In the neurons, three ions are important for signalling: Na^+, K^+ and Ca^{2+}. At rest, there is a higher quantity of Na^+ and Ca^{2+} ions on the outside of the cell than on the inside and more K^+ ions inside the cell than outside. Ion pumps maintain the imbalance of these ions by actively moving ions against the concentration gradients.

The imbalance of ion concentrations across the membrane also results in a potential difference between the inside and outside of the cell, which in a human is -70mV. In this state the cell is said to be polarized (see Figure 2-2). When the neuron is stimulated through the synapses on the dendrites, Na^+ channels open letting Na^+ ions go into the cell, changing its concentration inside the cell. This causes a change of the potential inside the cell. If the potential increases above a certain threshold (-55mV), more Na^+ ion channels open, gated by the voltage change, resulting in a massive influx of Na^+ and a resulting spike in voltage called an action potential. The potential can reach +30mV and in this state the cell is said to be the depolarized. Then the Na^+ channels close and K^+ channels open, voltage gated too but more slowly, to let K^+ through the membrane and out of the cell. This causes the neuron to repolarize. The potential goes down to $-90mV$, which is lower than at the resting state. This state is called hyperpolarization. It prevents neurons from receiving another stimulus during this time and prevents any stimulus travelling backwards along the axon, limiting the signalling to one direction. Once the K^+ channels close, Na^+ and K^+ phosphate driven pumps bring the membrane back to its resting state (-70mV) by moving Na^+ back outside and K^+ back inside the cell. The energy required is gained by the hydrolysis of adenosine triphosphate (ATP). It is used to drive a conformational change in the pump, by forming a phosphorylated intermediate[13].

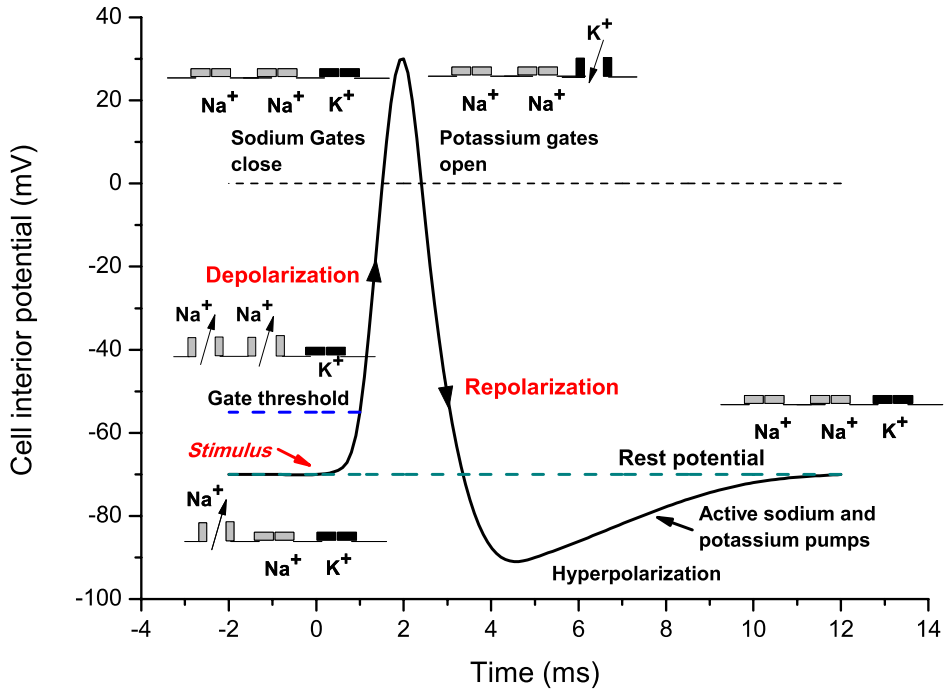

Figure 2-2: Description of the important steps of an action potential happening at the membrane of a neuron

The action potential is an electrical signal. It is sent through the axon to the axon terminal, causing its depolarization and then at the axon terminal activating Ca^{2+} ion channels, letting Ca^{2+} ions into the cell. This triggers a sequence of events leading to the fusion of vesicles with the plasma membrane. Vesicles are specialized subunits within a cell with their own membrane. They contain a high concentration of neurotransmitters, which then diffuse across the synaptic cleft. The synaptic cleft is a structure that allows a neuron to pass a signal to another cell. The neurotransmitters then bind to receptors, which can lead to action potentials in the second neuron [14].

The idea of optogenetics is to use this principle of ion transfer across the membrane of the cell by the addition of a light sensitive ion-channel protein to the membrane, whereby the neuron is rendered sensitive to light instead of electrochemical signals. This enables the stimulation of action potentials with light signals. Similarly, by adding light activated ion-pump proteins, action potentials can be inhibited.

2.3 The visual sensory system

In this project, the main interest is in restoring viewing capabilities in people suffering from age-related macula degeneration and other eye related sickness. It is therefore important to describe the structure of the visual sensory system: the eye, and how it is connected to the brain.

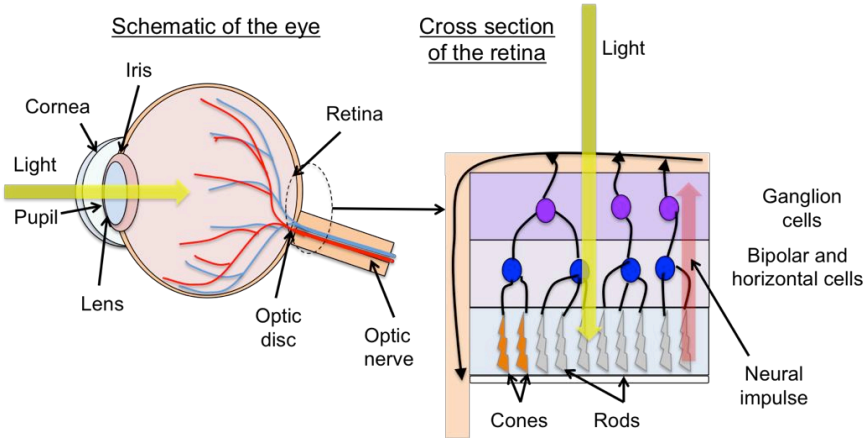

Figure 2-3: Schematic of the eye and of a cross section of the retina

In Figure 2-3, the image on the left shows a schematic of the eye. It is formed of an imaging part composed of the cornea, pupil, iris and lens. Imaging is done onto the posterior segment of the eye, where the retina and the optic disc are. The lens can adapt itself to focus from 25mm onward in the human [15].

The retina is where the photoreceptors are. The image forming photoreceptors are the cones and the rods. The cones are responsible for colour vision and eye colour sensitivity. They work best in bright light as opposed to rods that work in dim light. Rods are mostly responsible for peripheral vision. In Figure 2-3, the cross section of the retina shows that the eye photodetectors are on the back of the retina. The light is therefore going first through the layers of nerve cells. However, the light will first trigger photochemical reactions in the photoreceptors that activate the nerve cells above. These layers are bipolar and horizontal cells. They act to transmit signals, integrate and regulate the input of single and multiple photoreceptor cells to the ganglion cells, which are a type of neuron located near the surface of the retina. The ganglion cells have axons that are converging to form the optic nerve. This nerve transmits information to the visual cortex of the brain [16].

In Figure 2-4, the retina of a rat model is shown before and after its degeneration. A fluorescent marker coupled with light-activated gated protein (ChR2) is used to see if ChR2 is expressed in the cells.

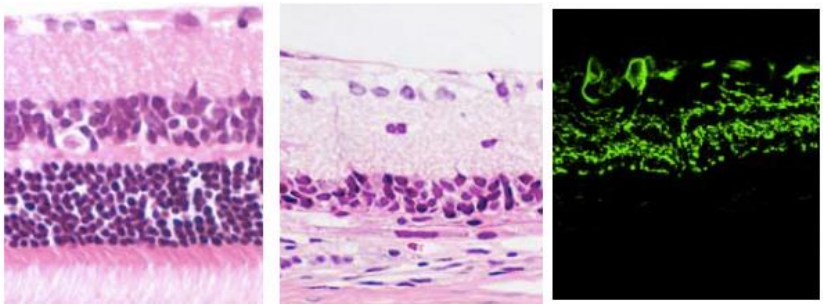

Figure 2-4: Degeneration of the retina in a rat model of retinitis pigmentosa[17]
Left: the intact retina. Middle: degeneration extends throughout the retina. Right: ChR2 (and GFP) are expressed in a subset of retinal ganglion cells. Image: Adapted from Tomita et al., 2009

2.4 Control tools

Optogenetics was conceived 40 years ago with the discovery of the bacteriorhodopsin, which was acting as an ion pump (IP) that can be rapidly activated by visible light and moves H^+ ions across the plasma membrane. In 1977 another IP was discovered, *naturomonas pharaonis* opsin (NpHR), also called halorhodopsin [18], [19]. Scientists looked at multicomponent strategies involving cascades of different genes or combinations of custom-synthesized chemicals and genes. However, an added foreign membrane protein was likely to be toxic to mammalian neurons and the photocurrents were likely to be too low and weak to be useful.

The light gated ion channel (LGIC) channelrhodopsin was discovered in 2002 by Hegemann, Nagel and their colleagues and made the prospect of performing optogenetics a reality. In 2005 and 2007, this was first applied to neurons and the first optical neural interface was tested on freely moving mammals. It was the true beginning of optogenetics [20].

Nowadays, the most known control tools are: LGICs, IPs and G-Protein Coupled Receptors (GPCRs – light activated signalling cascades). There is also another method in development with great prospect, which make cells photosensitive without using genetics or chemical manipulation in conjunction with quantum dots (QDs).

2.4.1 Light gated ion channels (LGIC)

Channelrhodopsin (ChR) is a light-gated ion channel derived from a micro-alga, *chlamydomonas reinhardtii*. In the algae, this visual protein guides the plant towards and away from a light source, therefore optimizing the light conditions for photosynthetic growth. The chemical cofactor needed to absorb photons in rhodopsin is a derivative of vitamin A called retinal, which is a covalently bonded chromophore. It is present in nearly all-neuronal cells of mammals and therefore eliminates the need to administer an exogenous molecule. The light absorption causes an isomerization of the retinal, which in turn triggers the ChR activation and gating of the channel by opening a pore in the membrane through which ions can travel. The channel then spontaneously closes again within milliseconds. By shining light on neurons transfected with ChR, the membrane is depolarized, which causes the change in the membrane potential of the excited cell sufficient to trigger the voltage gated ion channels, and activates transient electrical signals (spiking) (see Figure 2-5), that form the basis of neuronal communication.

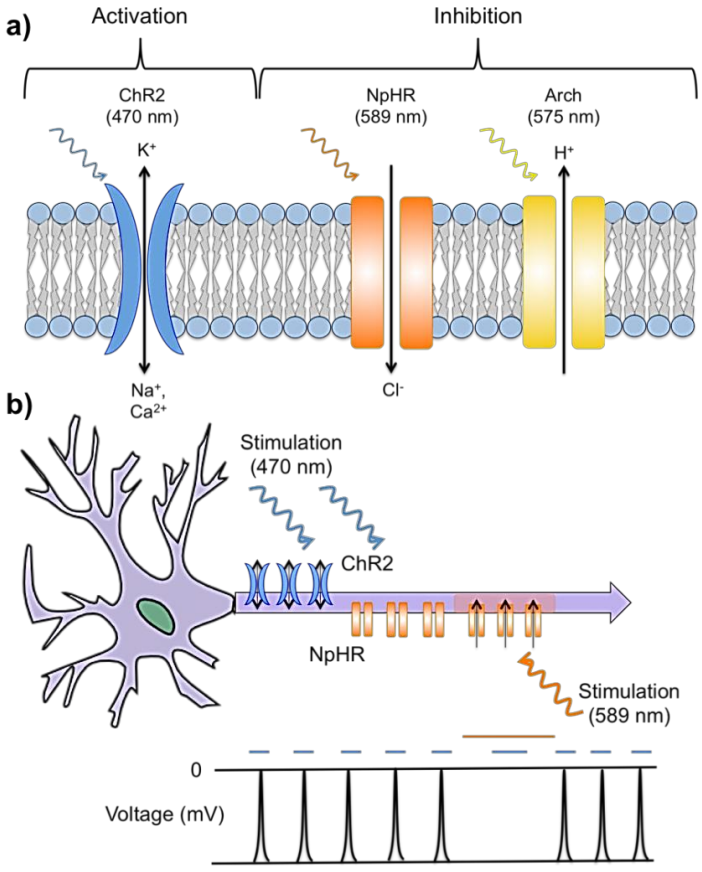

Figure 2-5: Optogenetic tools for modulating membrane potentials

Optogenetic tools for modulating membrane potentials. Activation of membrane potentials: (a) a photon on the membrane of a neuron expressing ChR2 opens a channel, which allows the movement of ions through it. (b) This depolarizes the membrane and then causes a change in the membrane potentials and the spikes. Inhibition of the membrane potentials: (a) A photon hits a light driven ion pump, which then pumps an ion inside (NpHR) or outside (Arch) the cell through the membrane. (b) Part of the cell is thus hyperpolarized and inhibits the membrane potential. No spike is seen then.

The main types of Channelrhodopsin:

- ChR1 and ChR2 from *chlamydomonas reinhardtii*
- VChR1 and VChR2 from *voluox carteri*

ChR2 is the most widely used because it can generate stronger photo-current and it transports sodium and other cations[21]. Researchers from different groups are now engineering new ChR hybrids to allow them to modify its spectral and kinetic properties [21], [22] as well as improve its expression and membrane targeting in the host cell. Originally, ChR2 could not be stimulated more than 30 times a second and could not keep pace with many brain processes. Therefore, fast versions of ChR2 capable of driving more than 200 action potentials per second and slow versions, that can induce prolonged stable excitable states in neurons, were generated (ChETA family and ChIEF) [20], [23]. ChR2 has a peak of absorption around 470 nm[24].

2.4.2 Ion Pumps (IP)

Halorhodopsin (NpHR) is a light driven ion pump with a peak of absorption at 589nm; specific for chloride ions its activation inhibits neuronal signalling (see Figure 2-5). It is found in Halobacteria like Halobacterium Salinarum or Natronobacterium Pharaonis. It shares sequence similarity to ChR and contains the isomerizable vitamin A Retinal. Its absorption peak goes from the yellow to the red [24],[12]. When light is shone on a cell transfected with Halorhodopsin, the neurons are hyperpolarized and therefore inhibit spiking. Combined with ChR2, it is used as an on-off switch for membrane potential and signalling. Similar results can be achieved with light-driven proton pumps, such as archaerhodopsin-3 (Arch), Mac, bacteriorhodopsin (eBR) and rhodopsin-3 (GtR3).

2.4.3 G-protein- coupled receptor (GPCR)

GPCRs are cell surface receptors in eukaryotes that respond to a large variety of external signalling. Their role can be to receive messages and then inform the cell about the absence or presence of life-sustaining light or nutrients in their environment, or to convey information sent by other cells.

GPCRs have all similar architectures. A GPCR is a single polypeptide folded into a globular shape and embedded in a cell's plasma membrane. It is composed of 7 segments that span the entire width of the membrane, inside and outside of the cell. It is called a 7-transmembrane receptor. The extracellular loops form part of the pockets at which the external signalling molecules bind to the GPCR. In humans, there are more than 1000 different GPCRs that are specific to particular signals.

When an external signal or molecule binds to a GPCR, it causes a conformal change of the GPCR, which will trigger the interaction between GPCR and G-proteins in the plasma membrane. These specialized proteins are composed of three subunits (α, β and γ) and have the ability to bind nucleotides guanosine diphosphate (GDP) and guanosine triphosphate (GTP).

In more detail the signalling process can be described in the following way:

In the non-activated state a GDP will bind to a G_α subunit, which will then bind to a nearby GPCR. A signalling molecule joins the GPCR, causing it to change shape and to function as a guanine nucleotide exchange factor (GEF) that stimulate the release of GDP to allow binding of GTP on the G_α subunit, then activating the G-protein. The G-protein dissociates into two parts, the GTP-bound G_α subunit and the β-γ dimer (see Figure 2-6). They remain attached to the plasma membrane and are diffused laterally to interact with other membrane proteins, such as enzymes or ion channels. The interaction with enzymes will then produce so-called second messengers and create a cascade effect and the interaction with ion channels will produce an electrical signal (see ion-gated channels in 2.2). The G-protein remains active until the GTP is hydrolysed back to GDP that re-associates itself with an inactive GPCR nearby [27].

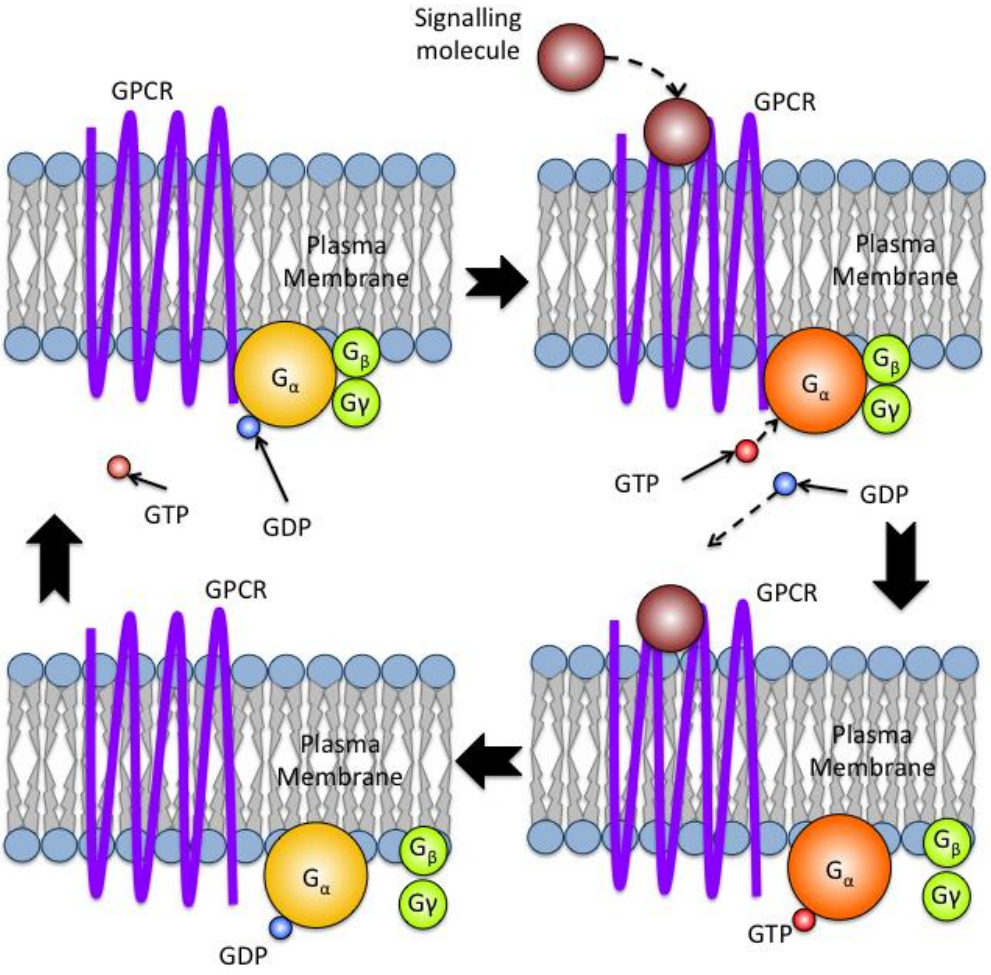

Figure 2-6: Activation cycle of a G-protein by a G-protein-coupled receptor receiving a signaling molecule [27]

This effect is called signalling cascade because it affects multiple molecules within the cell, leading to secretion of substances from the cell, opening of ions channels and transcription. One famous enzyme is the adenylyl cyclase, which, when activated, generates a second messenger called cAMP that modulates cellular signalling.

In optogenetics, light-activated versions of the GPCRs were developed recently. These GPCRs would normally be stimulated by the neurotransmitter adrenaline or noradrenaline, and initiate and regulate a wide variety of cellular responses. This approach can complement the light-gated ion channel approach in the control of neuronal functions and signalling pathways[28]–[30]. For humans, it has the advantage to cover nearly all the visible spectrum with variants absorbing in the blue (414 nm), the green (~514 nm), and the red (~560 nm).

Melanopsin (OPN4), another GPCR, is a photo-pigment found in the RGCs of the retina and regulates the circadian rhythm. These cells are intrinsically photosensitive even if they still receive inputs from the cones and rods. Its peak of absorption is at ~480 nm [31], [32].

Opto-XRs is a family of genetically optical tools that has common structure–function relationships among G-protein-coupled receptors (GPCRs). It was developed to optically recruit and control, with high spatiotemporal precision, receptor-initiated biochemical signalling pathways [20], [28], [33].

2.4.4 New control tool: Quantum dots

A new method was developed recently to make cells photosensitive without using genetic or chemical manipulation, which alters cells, in conjunction with Quantum Dots QDs [34] [35]. A remote switching of the cellular activity was demonstrated by optical Quantum Dot excitation when QDs are integrated with the cells. It has the same advantages as the light-gated proteins and ion pumps but without the need for genetic manipulation of the cell. The events of cell signalling can be controlled remotely. It is non-invasive, and it is flexible enough to probe different locations. However, this technic is toxic for living tissue and therefore in the long term will kill the cell.

QDs are semi-conductors with 3D-confinement. This results in discrete energy levels and a spectrally sharp emission when excited, and a high quantum efficiency resulting in high sensitivity and absorption. In addition, they are suitable for in vivo applications because of their size (~3-4 nm), which is similar to the size of typical proteins. Their surface chemistry could potentially be modified for selective attachment to biological particles. They could then be used to control cellular activity and cell signalling through light excitation of ion channels, which would lead to a membrane depolarization or hyperpolarization.

When QDs are optically excited near the cell membrane, it generates an electrical dipole moment, which in turn produces a change to the local electric field. This perturbs the membrane potential locally by changing the voltage immediately outside the cell. The cell stimulation will occur only if the perturbation is strong enough to modulate a substantial complement of ions channels, causing the cell membrane to sufficiently depolarize or hyperpolarize to produce action potentials or inhibit them. The strength of the electric field is proportional to the QDs proximity to the cell's membrane, the QDs rate generation of Electron-Hole pair (EHp) and depends on the identity of the ion channel near it.

The efficiency of this method was demonstrated using the patch-clamp method, which will be described later in this chapter, to measure the action potential. Hyperpolarization and depolarization of a cell was demonstrated, however the drawback of this technique is that the QDs are toxic to living tissue. In order for this method to be a valuable alternative non-toxic QDs would need to be developed.

2.4.5 Improved control tools: Fusion of light activated proteins

The discovery of the light-gated ion channel channelrhodopsin 2 (ChR2) and ion pumps like halorhodopsin (NpHR) started a new era in neuroscience, yielding an increase number of discoveries in optogenetics [11]. ChR2 allows the triggering of action potential with milliseconds precision, whereas NpHR hyperpolarizes cells and keeps the neurons from firing action potentials. Those actuators are linked into the cells and are, consequently, expressed differently, which leads to variable excitation or inhibition of individual cells. This causes transgenic cells to react differently and more or less efficiently to light activation and deactivation, thus defeating the purpose of optical activity control.

Our partner on this European project, Prof. Bamberg and his colleagues found a solution to that problem. They created a fusion protein, linking the light gated ion protein to the ion pump [36], [37]. A fluorescent protein and a trans-membrane helix taken from a gastric proton pump were used to couple them. It forces equal numbers of the tandem partners into the membrane, ensuring identical excitation-to-inhibition ratios in every transgenic cells. Also, they noticed that the tandem construct was better expressed together than its individual components. It accelerates the orange off-switching time by up to 4 fold and accelerates the closing of the channel in ChR2 due to the presence of a specific linker. In addition, they were able to produce a light activated ion-gate with increased activation spectrum by linking ChR2 with the green light-activated V.Carteri Channelrhodopsin-1 (hVChR1). Tandem constructs of optogenetic actuators can extend the spectral sensitivity of the fusion protein (see Figure 2-7(a)), resulting in a 'white' light sensor, which might yield the key for the restoration of vision. Combining actuators with opposite currents results in wavelength-dependant, bi-direction photocurrents that allow the induction or suppression of action potential in neurons (see Figure 2-7(b)).

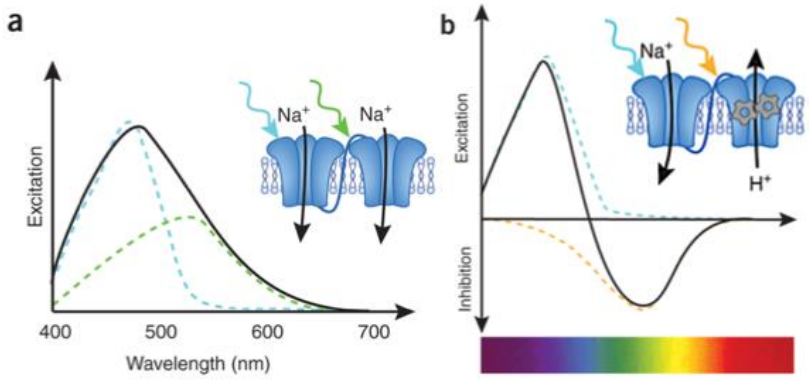

Figure 2-7: Photocurrent amplitude depends on the wavelength of light[38]**.**
(a) Expression of synergistic optogenetic actuators in tandem (ChR2-VChR1) results in extended spectral sensitivity. A flexible linker spans the plasma membrane to connect the C- and N- terminal ends of the two membrane proteins. (b) Tandem constructs of antagonist actuators ideally allow for bidirectional control of membrane potential.

In optogenetics, the three first control tools outlined above have been extensively studied and have well-known characteristics. Essential for their use is the efficiency with which they convert photons into amount of charge transported. The LGIC, ChR2, needs 1 photon to open 1 ion-channel that will allow approximately 50 ions to flow through per ms. This is more than the IP will pump (1 ion per photon) but less than GPCR (~50,000 ions per ms)[39]. However, until recently, GPCRs were far from being as efficient to transform light into current as ChR2. As explained above, in terms of spectrum, GPCRs are more flexible as they were developed to cover the entire visible spectrum, while LGIC work only in the green and blue wavelengths and IP in the red, which limits their use.

However, methods to improve the use of the latter two are well developed. These combine IP and LGIC or several LGICs together in the same protein to force them to express identically, improving activation and inhibition of action potentials. Additionally, new exciting methods, like QDs, have been developed without the need for any genetic modification, contrary to the other methods. However, their efficiency to generate current and the way they influences the environment around them is not yet well known.

2.5 Targeting the cells of interest

Delivering the light activated proteins to host cells is important to be able to generate membrane potential changes in specific neurons. Lizzie Buchen, in the article “Illuminating the brain”, described it as part of the “Six steps to optogenetics”[11]. The first step is to create a genetic construct, such as ChR2 or another opsin, and combine it with genetic elements, which control its expression, such as specific promoter sequences. The second is to insert it in a virus and the third is to inject it into the animal brain, where the opsin will be expressed in targeted neurons. The other steps are dealing with the delivery of the light and reading the outcome.

Transfection is used to introduce a non-viral "transformation" of the host cell membrane by introducing a new gene directly, while viral transduction introduces foreign genes into another cell using viral vectors. Those latter methods need specific promoters to restrict the expression of the opsin to the host cell. For example, promoters to target dopaminergic neurons, which are important in the study of the Parkinson's Disease[40]. However, sometimes no specific promoters are used and instead a complete neuron population can be targeted to study the function of its topological connections[25].

Animal lines can also be created to express an enzyme, called Cre-recombinase, in a subset of neurons to achieve the required specificity. A DNA construct targeting a specific gene is injected to produce a specific protein such as a microbial opsin (or light-optically gated protein). One of the advantages of this method is its specificity. It notably helps distinguishing the roles played by specific neural types in the physiological and pathological functioning of the nervous system[41]. However, the number of mouse lines is limited and not always suitable for particular experiments.

2.6 Light delivery

Optogenetics relies on light delivery, which is used to probe and manipulate cells in specific locations. The ways in which this can be done can be broadly categorised into two different techniques, wide-field or patterned illumination. Micro-LED arrays, employed in this project, provide patterned illumination and a number of advantages compared with the other methods outlined below.

2.6.1 Wide-field illumination

Wide-field illumination refers to a wide-area light source. It can be an external light source like an LED or a LASER Diode, or be implanted directly into the brain, with an optical fibre or a flexible probe with μ-ILEDs [42] to target a general region of interest. These tools have been used with ChR2 photo-stimulation to understand how patterns of action potentials in genetically targeted neurons contribute to behaviour [43], [44]. A recent improvement is a new optical waveguide technique based on hydrogels that could be used to provide distributed light delivery for in-vivo [45]. Most recently, a number of techniques have been developed based around the concept of an optrode. This is a device that can deliver light, for example down a fibre or optical waveguide, and also measure electrical activity at the same time. A device was recently developed integrating a light source and several sensors (light, thermal, electrical). Additionally it has the advantage of being flexible, to be used more easily in-vivo, and the possibility to be controlled wirelessly [46].

The limiting factor of this technique is that there is no way to know the quantity and the repartition of activated neurons.

2.6.2 Patterned illumination

In contrast light-patterning approaches target a smaller group of neurons in a host and not necessarily even the whole cell. There are two different methods to realize patterned illumination: laser beam scanning and image projection methods. In the Optoneuro project, micro-LED arrays are developed to provide a more compact and potentially a more efficient and reliable way to reach that goal, via an image projection method. All the different techniques with their advantages and disadvantages are described below.

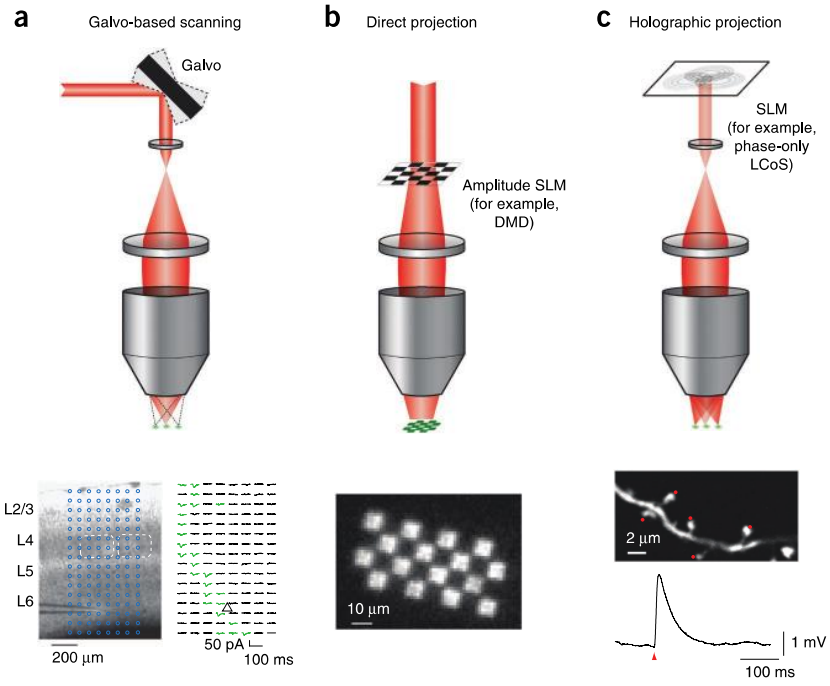

Figure 2-8: Patterned illumination strategies [47].

(a) Serial excitation: Top, pointing a single beam with galvanometer mirrors is directing a focused beam of light onto different locations within a sample. Bottom, this approach is useful for mapping studies in which independent activation of small, localized subsets of labeled neurons or axons is desired. (b) Images projection: Top, multi-beams are directed toward an amplitude spatial light modulator, such as a digital micro-mirror device (DMD), which reshapes the beams, into more complex patterns of activation across large areas of tissue (bottom). (c) Parallel excitation: Top, an SLM creates holographic patterns enabling multi-site activation when combined with two-photon excitation.

Laser-beam scanning

Lasers are used for one- and two-photon photo-stimulation to provide the necessary spatial resolution to excite individual cells. However, the area of neuronal membranes stimulated by a focused laser beam may be very small, < ~1 μm^2, and therefore might not be enough to drive action potentials[48]. The simple solution of increasing the expression level of the transducer, however, is not recommended as it is already expressed more than the other membrane proteins and can cause a cytopathic effects. Therefore, other solutions were studied.

- Serial Excitation: The Serial Excitation is provided by scanning a laser focus across the cell's membrane sufficiently fast to outrun the channel activation. Figure 2-8 (a)) shows a serial excitation done with galvanometric mirrors. A couple of acousto-optic deflectors can also be used to obtain the same result [49]. The average power delivered to the brain is not high, however this method requires high peak intensities of light[48] and could cause nonlinear photo-damage. This method was used for mapping functional neuronal circuitry[50][49] and fore-limb and hind-limb motor cortex in mammalian brains[51]. Serial excitation has several constraints. Only cells with slower deactivation generate photocurrent and therefore it suffers from low temporal resolution. When stimulating several cells, the speed of the scanner limits the rate at which cells can be excited.
- Parallel Excitation: This method allows the stimulation of single cells rapidly and multiple cells simultaneously. The beam can also be reshaped to fit a cell with sufficient 3-dimensional precision, axon or dendrite, etc. Peak intensities are not high and the average power is higher, which could cause a global heating of the cell. The opacity of the sample studied is an important factor. A translucent preparation will heat less than an opaque preparation[48]. Several methods were developed. One uses temporal focusing (TF) and digital holography (DH) with a spatial light modulator (SLM) as shown in Figure 2-8(c), and is able to generate large 2-dimensional patterns with a depth resolution below 6μm[52]. Another combines TF with generalized phase contrast (GPC) to confine the two-photon stimulation patterns in 3 dimensions with higher spatial resolution[52].

Image projection

Image projection methods can be separated into two branches. The first one is based on projection displays (Liquid crystal display (LCD), Digital Light processing (DLP)) and the second one on emissive displays (Micro-LED arrays).

There are two types of image generating device used in projection displays, the DLP and the LCD. Figure 2-8(b) shows a schematic showing how it is done. A DLP is a way of projecting and displaying information using a digital micro-mirror device (DMD), developed by Texas instruments. A light source is projected through colour filters onto the DMD, each mirror corresponding to a pixel, which either reflects the light onto a screen in the on state or to a beam block in the off state. This technology fast and can be used in optogenetics to generate light patterns controlled spatially and temporally in restrained[53] and unrestrained animals[54]. The light source used is either an LED, a metal-halide lamp[55], or a LASER. It is directed toward the DMD[56], that generates the patterns. The light is then collected and fed into the lateral port of an inverted microscope and then focused by an objective onto the sample. The spatial resolution of such systems is set by the pixel density of the DMD and the optics used (~5 µm at 10x magnification), with the temporal resolution being limited by the electrical latency of the DMD system.

Another way to achieve patterned illumination is to employ a modified off-the-shelf LCD projector. This set-up has the advantage that it provides spatial, temporal and chromatic control[57], [58]. It was used to stimulate specific cells expressing ChR2 to record the behaviour of freely moving C.elegans. The light emitted by a mercury lamp is separated into three distinct light paths and filtered by selective filters, before being filtered again by three-color LCDs (475 nm, 568/50 nm and 675 nm) enabling simultaneous multicolour illumination. The light is then emitted into an inverted microscope. Temporal resolution is limited by the image processing time (40 ms) and the refresh rate of the LCD projector (17 ms). Spatial resolution lower than 10 µm could be obtained at medium magnification. This multi-modal set-up allows multicolour stimulation and inhibition while monitoring subsequent behavioural outputs in real time at 25Hz. DMD systems are already available commercially and therefore are a more viable solution that LCD projectors.

Compared to beam scanning two-photon microscopy, DMD systems have a fast refresh rate and therefore a high temporal resolution [52], [59]. However, it requires fine adjustments of the optical alignment, when modifying the emission wavelength.

Light emissive displays are composed of an array of light sources that emit light with spatio-temporal control without the use of an intermediary, such as an LCD or DLP. Micro-LED arrays are one such technology. It has a lot of advantages compared to the others. Two-dimensional patterns can be generated much more efficiently with micrometre and sub-millisecond resolutions and with sufficient irradiance to stimulate ChR2-evoked spiking in neurons[60], as no mirrors or filters (LCD) are used between the light source and the cells. It is a compact solution, which can be simple to operate. However, the fill factor is low (<16%). This technology is the technique of choice for this project and is discussed in more detail in Chapter 3:.

2.7 Reading the outcome

When a neuron or/and a group of neurons is stimulated, changes in membrane potential are generated. Therefore measuring the electrical response to an artificial stimulus of an electrode, allows the investigation of how circuits of cells work together and their role in the brain. The consequence could also be behavioural, which is another way to look at the response to stimuli. Before the discovery of ChR2, electrodes were used to stimulate the brain and the precision of targeting was low with neighbouring cells being stimulated as well as the cells of interest. Photo-stimulating neurons allows a precise targeting without the interference that comes with electrodes.

To measure changes in membrane potential, two direct techniques are used, the patch-clamp technique, which is generally applied to one cell at a time and a multi-electrical array, which involves a population of cells at the same time. Behavioural testing is done by observing the animal response to specific stimuli. While biosensors, like fluorescence markers with compatible excitation profile such as voltage-sensitive fluorescent proteins and calcium indicators, for the main ones, can also be used to measure different cellular readouts.

2.7.1 Patch-clamp

The patch-clamp technique allows the recording either of the activity of ion channels present in a patch of membrane, the “cell-attached” mode, or of the average response of all the ion channels in the entire cell membrane, the “Whole-cell” mode[30], [61]. In the “cell-attached” mode, a micropipette, containing the electrode, is placed next to the neuron membrane. A gentle suction is applied through the micropipette to draw a piece of the membrane into the electrode tip. This forms a high resistance seal with the cell membrane, allowing the low currents through the sealed patch to be measured. In whole-cell mode, more suction is applied and the attached patch perforated, attaching the electrode electrically to the whole interior of the cell (see Figure 2-9). Thus the current flow into the whole cell can be measured.

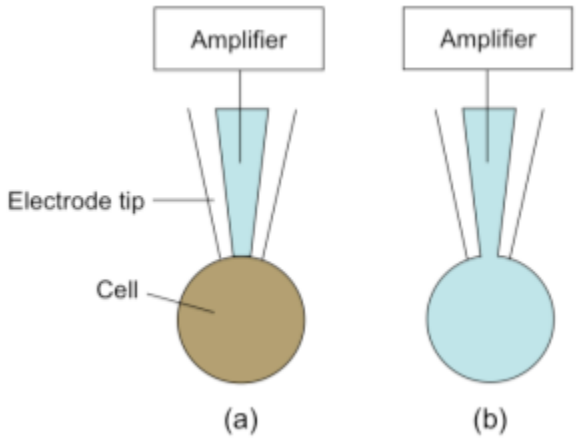

Figure 2-9: Patch-clamping recording configurations schematics [30]**:**
(a) Cell-attached and (b) Whole- attached configurations

2.7.2 Multi-electrodes array

Multi-electrode Array (MEA) technology became widely used recently. It allows multi-site recording and even has stimulation capabilities[62]. It was developed to study electrophysiological processes at the network of neurons level and is commonly used to study the dynamic of interactions within neuron networks[63]. Scientifica, one of the partners in the project, is an expert in Electrophysiology and produces MEAs [64].

These techniques evolved as well to include light sources to excite neurons directly for in-vivo applications. Tae-il Kim, Jordan G. McCall et al[42] developed a flexible and cellular-scale injectable optoelectronic device, which combines stimulation with GaN μ-ILEDs, sensing (light, thermal, electrical) and wireless actuation. Ki Yong Kwon et al. [65] built a transparent micro-electrocorticogram (ECoG) array with 200 μm diameter electrodes for electrical recording and embedded LED for optical neural stimulation. Light sources and electrodes are made more compact, flexible and transparent to be less invasive and therefore make less damage to the brain in in-vivo applications.

2.7.3 Behavioural testing

Behaviour testing can be employed to assess the effect of modulating cellular activity in whole animals. For instance a magnetic field sensor was used to measure the whisker movements of a rat after stimulating its ChR2 expressing neurons in the motor cortex [43]. The advance in technology similarly to flexible light sources and sensors [46], transparent multi-electrode arrays and wireless activation allows for more compact devices improving behavioural testing by decreasing their invasiveness on and in the animal.

2.7.4 Voltage-sensitive fluorescent proteins (VSFPs)

These proteins are able to record changes in voltage across membranes, allowing the visualization of action potentials [66]. They are derived from fluorescent protein (FP) reporters that are fused to protein detectors that convert physiological signals into FP fluorescence. They are genetically encoded to attach to specific cell populations.

In one of the most known ones, VSFP2, two fluorescence proteins are used. When a cell becomes depolarized, the protein detector or voltage sensor brings the two fluorophores closer together, causing a change in the ratio of fluorescence emitted from the two components because of a Förster resonance energy transfer (FRET) from one component to the other. It can be used to measure and observe changes in cells in culture, acute brain slices and living animal [67], [68]. Different VSFPs variants were developed to fit different applications. VSFP2 allows efficient targeting of the plasma membrane and high responsiveness to membrane potential signalling in excitable cells, but has relatively slow fluorescence response kinetics. VSFP3 was therefore developed to match fast neuronal signalling, but it is less sensitive than the previous variants [69].

This technique lags behind other methods such as calcium imaging due to significant challenges associated with biophysical constraints of the measurements themselves. Action potentials happen fast (submilliseconds) causing a quick change in the potential of the cell membrane, localised on a small area (only a few nm wide) and the electric field decreases exponentially with distance from the membrane. Therefore the VSFPs need to be physically inside the membrane or directly in contact with it. Also, the plasma membrane is thin and therefore the amount of chromophores in a volume that report an electric field is physically limited. It necessitates therefore very sensitive detection methods. Most of the membrane around the cell is internal membrane. Only a small part is composed of plasma membrane where action potentials happen. VSFPs that bind indiscriminately to membranes will then bind mostly to internal membranes, which have not direct sensitivity to membrane potentials.

2.7.5 Calcium imaging

Calcium ions generate versatile intracellular signals that control key functions in all types of cells. As explained in Section 2.2, the differences in ion concentration between the inside and the outside of the cell is generally associated with an action potential and with one of the key ions being calcium, its concentration can be used to detect neural activity [70], [71]. Techniques to image calcium have been around for a long time.

Two types of calcium ion indicators exist, chemical fluorescent calcium indicators (such as Fura-2 and Indo-1) and protein-based genetically encoded calcium indicator (GECI). The last one provided the breakthrough that allowed for quicker kinetics and more precise targeting that improved responses. Steven Su and all manage to visualize signal transduction in live primary cilia using GECI that was targeting the primary cilia. Synthetic Ca^{2+} indicator dyes allowed to monitor several cells but were often resulting in signal saturation of the entire cytosol[72]. The cameleon protein was the first GECI. This sensor protein undergoes a conformation change upon calcium binding to the calmodulin element of this GECI and radiates at an altered wavelength [73]. D3cpVenus is another variant. It fluoresces in response to an increase of Ca^{2+} and has been used successfully in vitro and in vivo to detect single action potential spiking [67]. Other probes, such as G-Camp, are showing changes in fluorescence in response to a change in Ca^{2+}.

Calcium imaging and VSFPs are complementary as sufficient sensitivity for action-potential spiking is provided by the calcium imaging, and subthreshold activity is reported by VSFPs. Often in a network of neurons the response of any given neuron might be dependant on the sequence of subthreshold stimuli communicated to it from neighbouring neurons. Measuring subthreshold activity is thus potentially more important in understanding the behaviour of a network that simply measuring its action potentials [74].

2.7.6 Summary

In the scope of this project we will concentrate on the patch clamp and MEA techniques, as they are the most widely used and easiest to implement. ChR2 fluorescence markers, such as GFP, will be used to see how ganglion cells will respond to MLA stimulation.

2.8 Conclusions

Optogenetics opens several doors to the understanding of the way neurons interconnect and function. This has been possible due to breakthroughs such as the expression of ChR2 ion-gated proteins and their photo-stimulation in neurons in various parts of the brain such as the hippocampus, the motor cortex, the cerebellum, and various other regions. These techniques work with animals that can be either restrained or free to move, where it is easier to understand how their behaviour is influenced. Optogenetics has applications in the optical control of whisker movement[43], in locomotion[41], the probing of Parkinsonian neuronal circuits[75] and the restoration of visual function in retinal degradation[76]. It was tested on several types of animals, from the drosophila, worms and flies to the mammals (rats, mice, primates, etc.). This project is directed at the final goal of developing a non-invasive retinal prosthesis, using a micro-LED array to stimulate ON bipolar cells that will induce light-evoked spiking activity in ganglion cells in order to restore partial visual function.

Chapter 3: Technology and principle

In the previous chapter, the field this project is associated with is described. In this chapter, the principle behind this project and the technologies used, micro-LED arrays (MLA) and micro-optics (MO), are explained.

3.1 Principle of the project Optoneuro

The Optoneuro project is a collaboration between 6 different groups in UK (Newcastle University, Imperial College, Scientifica ltd), Ireland (Tyndall Institute), Germany (Max Planck Institute (MPI) in Frankfurt) and Switzerland (the Friederich Miescher Institut (FMI) in Basel). We use the specialist knowledge of each of the groups to combine Gallium-Nitride MLAs, Projection Optics and Microscope Platforms to stimulate and study biological samples transfected with a nanoscale optically gated ion-channel protein, ChR2, as a route to developing sight prostheses. MLA permit spatio-temporal control of neuron stimulation on sub-millisecond timescales. Newcastle University, the FMI and MPI are the specialists in the biological aspects of the project, with Newcastle also producing the electronics and software. Tyndall makes MLA's and Scientifica prepares microscope platforms. At Imperial we are in charge of the development of the projection optics.

The basic principle of our project is based on improving the basic system depicted in Figure 3-1.

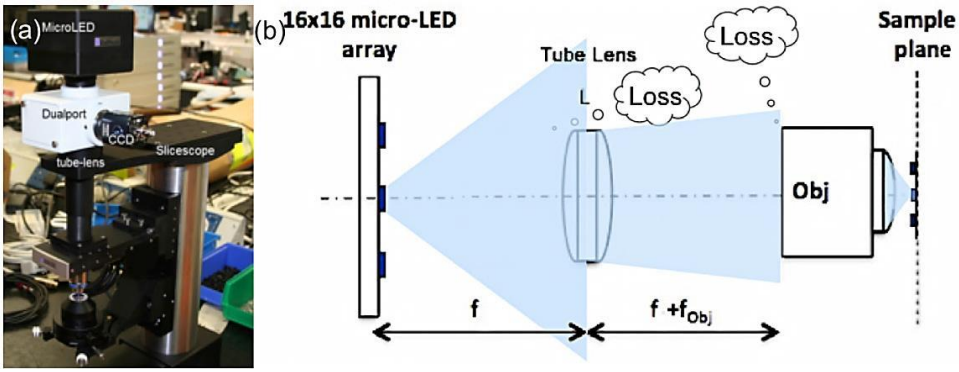

Figure 3-1: Illumination with no projection optics
(a) Scientifica slicecope [64], (b) Schematic

Here an MLA is used to project light through a microscope platform that then focuses an image of the MLA onto a biological sample in order to stimulate neurons. However, previous MLA illuminations suffered from low collection efficiency (<2%) and fill-factor on the sample [60]. This is due to two factors: first the fill-factor of the emitting area of the MLA is low compared to its total area. Secondly, because a LED is an extended source with a widely divergent output, most of the

light is lost within the microscope system. A microscope combines a tube lens and a microscope objective as shown in Figure 3-1(b). The tube lens generally has a focal distance between 160 and 200mm depending on the brand used (Nikon, Leica, Olympus, Zeiss…) and therefore has a low numerical aperture (NA) compare to the MLA (~0.07 vs 0.5 or 1) (see A.1). Light is also lost at the entrance of the microscope objective. This system also exemplifies the case where the MLA is projected into the eye, where the entrance pupil of the eye and its associated optics (lens etc.) effectively replaces the microscope objective. For optogenetics applications it is of importance that both the collection efficiency and the fill factor on the sample are maximised. The high collection efficiency allows for the MLA to be run at lower current and therefore have a longer lifetime and the high fill-factor is necessary for a more uniform illumination of target neurons.

Figure 3-2 shows the alternative arrangement proposed and investigated in this thesis. Here the fill-factor is increased by using micro-lenses, with identical size and pitch, which are filled completely by the light from the MLA and in turn imaged by the microscope onto the sample plane. If the MLA is placed close to the focal distance of the micro-optics, the resulting light output is nearly collimated and therefore has a low numerical aperture (NA), determined by the size of the emitter and the focal length of the micro-lens. The light is therefore collected more efficiently by the tube lens, forming an image of the micro-led on the objective pupil and an image of the micro-lens in the objective image plane. Thus the micro-optics increases the collection efficiency and this is manifested by an improved fill factor. The MLA may overfill the micro-lens because of a higher numerical aperture (NA) compare to the NA of the micro-lens. The light not collected by the micro-lens is partly filling the neighbouring micro-lenses, and therefore is not collimated and travels outside the system or refracts through it causing unwanted artefacts on the sample. Lens tube and aperture stop can be used to filter them.

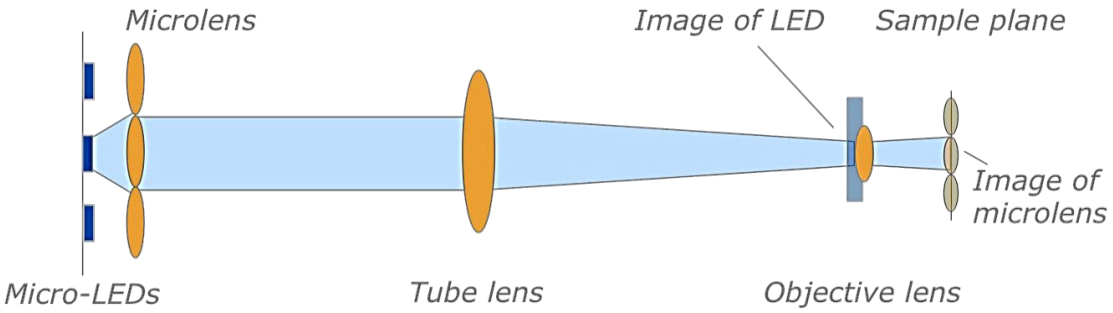

Figure 3-2: Illumination principle with micro-optics

In this project, several systems using micro-optics and MLA were developed and implemented into electrophysiological microscope platforms and in in-vivo experiments, by projecting light directly into a mouse eye or a phantom human eye looking towards the possible construction of a retinal prosthesis.

3.2 Micro-LED arrays (MLA)

Light Emitting Diodes (LEDs) and their applications have evolved from their invention in the 1960s to the present day[77]. In the 90s, the first blue and green LEDs were developed by Nichia Chemical Industries using GaN [78], widening the range of wavelengths that could be emitted to include the whole visible spectrum and even stretching into the UV. This is the technology that forms the basis of the micro-LEDs arrays used in our project, and the blue wavelengths are particularly suited for Optogenetics. Around 2000, the first micro-emitter arrays or micro-LED arrays (MLA) were developed, opening the doors to new applications in neuroscience, micro-displays, microscopy and many other areas [79]. MLA's form an essential part of our project and the micro-optics development is directly dependent on them. Therefore in this section, the different technologies and possible applications will be briefly described, with a focus on the use of MLA within optogenetics and our project, OptoNeuro, as well as their advantages and disadvantages.

3.2.1 Light Emitting Diodes (LED) Technology

Principle of operation

An LED is a semiconductor p-n junction, which can emit radiation by electro-luminescence in the UV, visible or IR regions of the electromagnetic spectrum. When a forward bias is applied, electron carriers in the conduction band of the n-doped side of the junction and holes in the valence band of the p-doped side must recombine at the junction. When the semiconductor has a direct band-gap the energy released when an electron combines with a hole can be emitted in the form of a photon in a process called radiative recombination (see Figure 3-3).

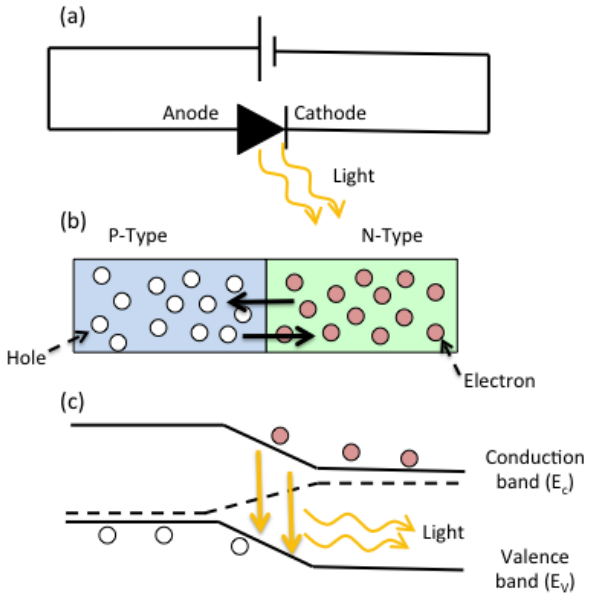

Figure 3-3: Inner working of a LED showing circuit ((a) and (b)) and band diagram (c) when under bias

The wavelength of emitted light is directly related to the difference in energy between the conduction band and the valence band of the material used and hence engineering different materials with different band-gap energies allows the production of LEDs that emit light at a range of different wavelengths (see Equation 3.1).

$$E_g = E_c - E_V = h\nu = \frac{hc}{\lambda} \qquad 3.1$$

The theoretical turn-on voltage[80] to emit light is called the threshold voltage, which is defined as,

$$V_{th} \approx \frac{E_g}{e} \qquad 3.2$$

Where V_{th} is the threshold voltage, E_g the band-gap energy and e the elementary charge.

LEDs have many advantages: they are cheap to produce; cheap to run due to their high quantum efficiency and emit little heat. They are also reliable with a long lifetime compared to incandescent light bulbs (>10000 hours against ~1000h). Common uses of LEDs are signalling, imaging, displays and lighting. Lighting applications in particular have been a particular driver for LED development in recent years and it is largely thanks to this development that the performance of blue GaN LEDs used in this project has become so good.

Materials

III-V materials are mostly used in the LED industry because they are the most opto-electronically efficient semi-conductors. The compounds used interact strongly with light, because they tend to have direct band-gaps and therefore they exhibit high absorption coefficients and radiate light efficiently.

Semiconductor devices are built from single crystals to decrease the amount of crystal defects such as dislocations that could provide non-radiative recombination sites. By combining materials with different band-gap energies into one device, hetero-junctions and quantum wells can be built that are important for carrier confinement. To do this, different materials can be grown on top of each other, provided that their lattices match as closely as possible. Up to four different atomic species are generally used to produce a compound semiconductor, called a quaternary compound. A wide choice of elements from group III and group V can be associated in different concentrations to vary the energy band-gap and therefore the wavelength of a device, as well as the lattice constant. Al, Ga and In from group III can be combined with N or P, As and Sb from group V (see Figure 3-4).

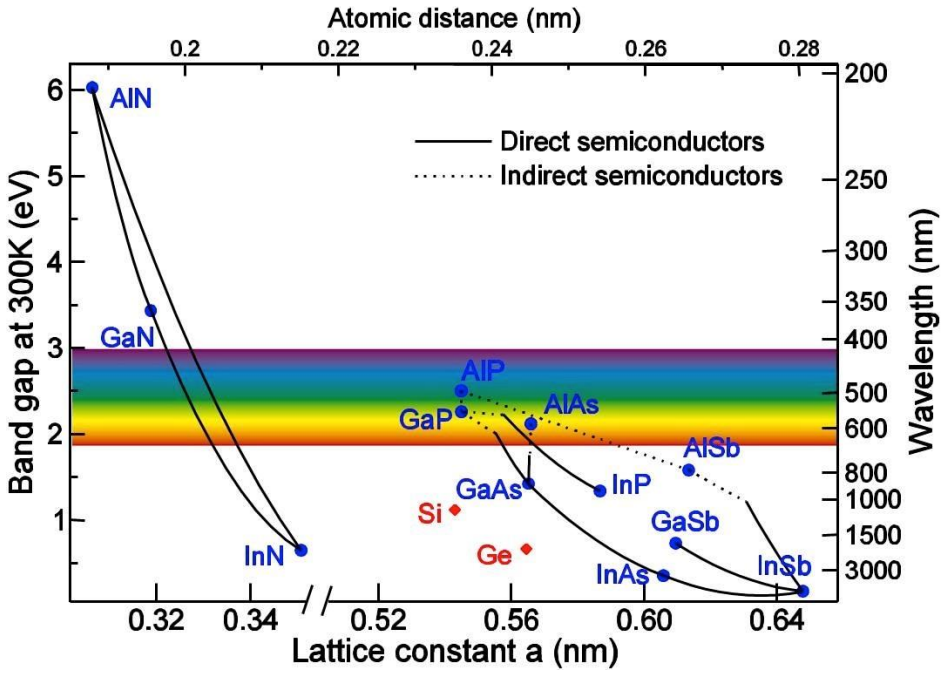

Figure 3-4: Band gap and lattice constant of some compound semiconductors [81]**.**
Solid lines indicate direct band-gap semiconductors, and dashed lines indirect band-gap.

The first III-V semi-conductor LED was made of GaAsP and emitting in the IR[82]. Since then GaAlAs, InGaAsP and AlInGaP based LEDs were developed emitting at wavelengths going from the green to the far IR. However, UV to blue colours could not be generated with these materials. Nitride materials were a solution, but it took time to be developed, as there were no existing P/N materials for these systems and the crystal quality was poor. In the 90s, Nakamura[83] and Amano [84] were able to create the first InGaN/GaN double heterostructure and p-doped GaN material and successfully demonstrated its light emitting properties, despite its relatively poor crystalline structure. It was the start of nitride based opto-electronics. Nitride semi-conductors are generally quaternary compounds AlInGaN, which have a band-gap between 0.7 and 6.2 eV [85]. This corresponds to emission wavelengths from the deep UV to the IR (from 197 nm up to 1700 nm). Nitride materials have advantages over the other materials. First of all, there are the only direct band-gap materials covering all visible wavelengths as well as UV and IR. Secondly, they are more reliable as they are resistant to chemical etching and have higher melting temperatures, which has consequences on how the intensity varies with the temperature [86]. Thirdly, the wavelength shift with temperature is smaller. Furthermore, Nakamura [87] discovered that high defect densities in Nitride materials could be used to improve radiative emission [78], whereas they would produce the inverse effect in GaAs based LEDs [88].

These developments allowed the improvement of several technologies as now emission over the whole visible spectrum as well as UV and IR were possible. In display technology, LED-backlights replaced the cold cathode fluorescent (CCFL) backlighting used in LCDs with advantages, such as lower energy consumption and compactness. In lighting, LEDs have longer lifetimes than Halogen or Tungsten light bulbs (>10000 hours vs ~1000hours). Storage capacities were increased to more than 15Gb on blue-ray disks using 405nm laser diodes compared to DVDs (4.7Gb) using red semi-conductors and CDs (0.67Gb), using IR semi-conductors. Additionally, there is potential for more applications in biophotonics, such as fluorescence imaging.

The emission wavelength of Nitride based LEDs is tuned by varying the quantity of In and Al in the AlInGaN alloy of a multi-quantum well (MQW) [78] active region confined between the n-type and p-type barriers. On one end of the spectrum, in the visible, n- and p- GaN are used as barrier layers and in the UV, n- and p- AlGaN with no In in the compound. In Optoneuro, InGaN semiconductors, with no Al, are used to emit between 470 and 515nm. At 470nm, the layers of InGaN are composed of 25% InN and 75% GaN and could be written as: $In_{0.25}Ga_{0.75}N$.

One of the advantages of LEDs is that while they generate very little heat, the excess heat that they do produce can be dissipated well due to the high thermal conductivity of the semiconductor material. GaN, for example, has a thermal conductivity of 1.3 W/(cm ·K) at 300 K and a melting point above 2500°C [78]. Therefore it is possible to operate LEDs at high current densities. For instance the micro-LEDs supplied by Tyndall can operate at current densities up to 3.5 $kA.cm^{-2}$.

These characteristics and recent technological advances in micro- and nano-fabrication allowed the development of micro-size optoelectronic and photonic devices with different properties and functions compared to their larger area counterparts [79] for applications such as microscopy, micro-displays, photo-lithography, etc. The Optoneuro project focuses on developing micro-structured light emitting diodes with various emitter geometries, sizes, emission wavelengths and electronic drive architectures.

Manufacturing method

Most nitride LEDs start with a set of Nitride layers containing the diode structure in planar form grown on a sapphire (Al_2O_3) or GaN substrate. First the n-doped material is grown, then the active region, including its MQW structures where the emission takes place, and finally a thin p-doped layer (see Figure 3-5(a)). The band-gap structure and the wavelength depend on the composition of the n- and p- doped semiconductor alloys and the quantum well thicknesses. The substrate is a few 100µm thick, the n-doped material is a few µm, the active layer 10s of nm, and the p-type material of the order of hundreds of nm. The total thickness of the device is less than a millimetre. Although there may not be a direct lattice match between the substrate and the diode layers, special growth techniques are used to reduce the dislocation density over a few microns of thickness in the thicker n-doped layer. From wafers of material grown in this way individual diodes and electrical connections are patterned using standard micro-lithography techniques.

An important feature of these LEDs is that the GaN or Al_2O_3 substrate is transparent. So there are two LED packaging options, the top-emission structure and the Flip-chip structure, which was recently developed for high power nitride LEDs [39], [89]. Top emitting devices emit light through the p-layer and any thin current spreading metallic layer. In contrast, Flip-chip devices emit light from the bottom, through the n-doped and substrate regions, (see Figure 3-5(b)). This technique allows an improvement of the current spreading through the device and of the light extraction efficiency and thermal dissipation, which means that higher current densities can be used. This technology does not require wire bonding, in contrast to the top emitting devices, and in particular allows micro-led arrays to be integrated directly with silicon drive circuits. With the increased number of elements in an array, the interconnection between them becomes more

difficult and therefore one of the biggest challenges is to increase the bonding reliability to obtain an homogeneous emission through the array[90]. This design also allows better electrical drive characteristics, which means a faster response [35] and improves its performance in many biological imaging applications[91].

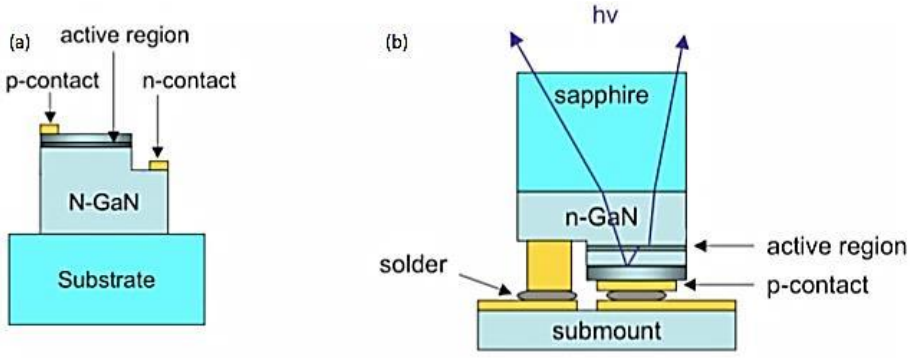

Figure 3-5: LED structures[30]
(a) Top-emitting and (b) Flip-chip

Efficiency and light output distribution

While the internal quantum efficiency of an LED is high, the ability to extract generated photons from the device is severely limited by internal reflection as the materials typically have a high refractive index of the order of 2.4. In order to improve the efficiency, several approaches have been investigated, such as surface texturing[92], photonic crystal patterning[93], and the structure of the chip itself.

Lambert describes the emission profile from a flat emitter emitting uniformly in every direction as directly proportional to the cosine of the angle θ between the observer's line of sight and the normal to the surface. It is called either cosine emission law or Lambert's emission law. The radiance I_θ is defined below:

$$I_\theta = I_0 * cos\theta \qquad 3.3$$

The emitting layers of an LED are flat and emitting uniformly in every direction. They are isotropic. The back of conventional LEDs is flat (see Figure 3-7(a)) and reflects light emitted backwards by the emitters and light reflected on the exit surface due to internal reflections without redirecting them forward. The front surface of the LED lets light through, that is emitted at internal angles up to $\theta_i = \sin^{-1}(n_{air}/n_{GaN}) \approx 24.6°$, where θ_i is determined by the ratio of the refractive indices of air and GaN ($n_{GaN} \approx 2.4$). Higher angle beams are reflected and lost. The energy conversion law defines the intensity refracted outside a LED as:

$$I_i . d\theta_i = I_r d\theta_r \quad 3.4$$

Where I_i, the intensity emitted inside the GaN, θ_i, the incident angle at the interface GaN/air, I_r, the intensity refracted and θ_r, the refracted angle.

Using the Snell-Descartes's law ($n_{GaN} . \sin\theta_i = n_{air} . \sin\theta_r$), the distribution of the light outside a flat emitter without taking into account the Fresnel losses is defined as:

$$I_r = \frac{\cos\theta_r}{\sqrt{{n_{GaN}}^2 - \sin{\theta_r}^2}} . I_i \quad 3.5$$

Figure 3-6 shows the polar plots when using the Lambert's law and Snell/Descartes's law. The two distributions are very close together and justify why the distribution of light emitted from this kind of emitter is often compared to a Lambertian distribution.

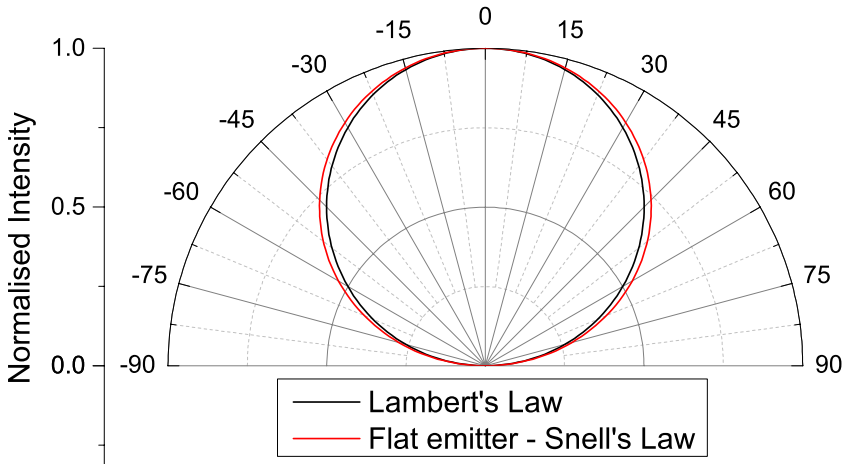

Figure 3-6: Polar plot using Lambert's law and the Snell's/Descartes Law for a flat emitter

This distribution can be modified by either adding optics or modifying the device structure. Tyndall National Institute, our partner in this project, modified the shape of the back of the LED to recycle the light emitted backwards and at wide angle that are totally reflected, and redirect them forward at lower angles, allowing them to pass through the GaN/air interface. This increases the quantity of light emitted at lower angles, decreases the distribution to ±30°, and thus improves the LED efficiency (see Figure 3-7)[94].

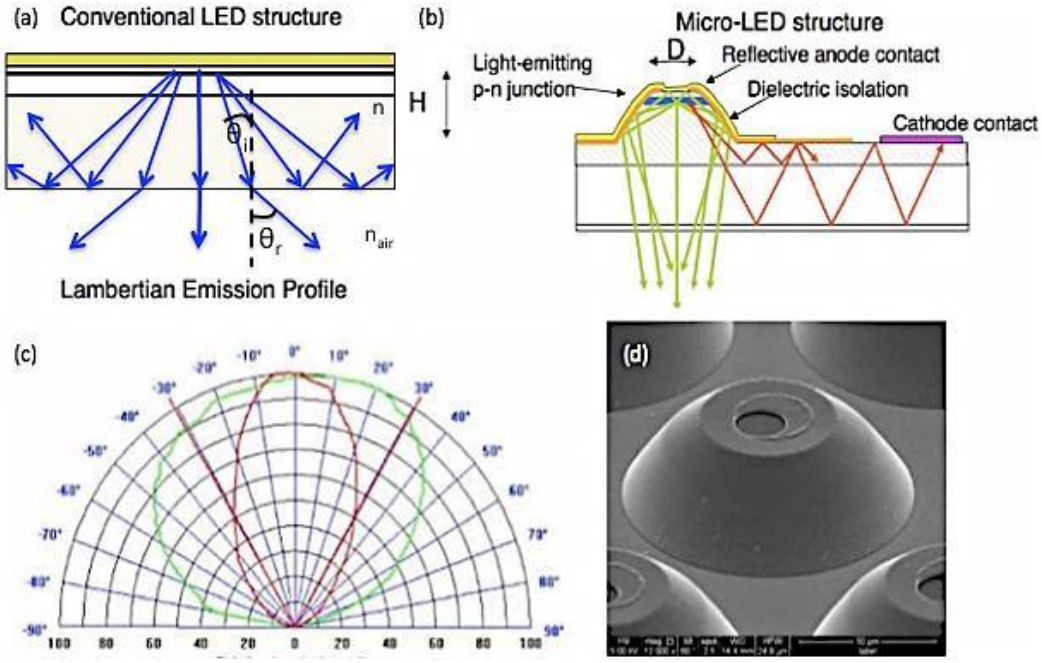

Figure 3-7: Schematics of Tyndall National institute LED

(a) Conventional LED structure, (b) Tyndall's micro-LED structure, (c) Comparison of the light distribution (green: Lambertian and red: Tyndall LED) and (d) Parabolic reflective anode[94]

3.2.2 Micro-LED arrays (MLA)

MLA have been of interest in recent decades mostly due to their potential to be used for applications such as micro-displays and biological applications. In Optoneuro, they are used to stimulate ChR2 with a peak of emission at 470 nm.

Advantages

Compared to broad area LEDs, much higher current densities are obtained with MLAs[79]. The size of an LED emitter influences its response time. This means that MLA devices have therefore a faster response time than broader LEDs and a much faster response than LCD and OLED devices. They can also be controlled temporally and spatially. They are now used in biology to measure fluorescence lifetime of biological samples, where ns to fs light sources are required[95], and in optogenetics for in vivo neural stimulation, where compactness is necessary for micro-LEDs to be inserted on a probe [96].

MLA were first developed with a top-emission structure. However, the power output of those devices were limited by the small emission area and the light absorption in overlying electrical connections[97]. Flip-chip bonding allowed improvements to be made in these areas, as well as allowing them to be placed closer to each other as contacts are on the back of the LEDs and no wire bonding is necessary. Using this technique N. Grossman reported an increase of the current density from 5 to 43A/cm^2 and of the optical power from 0.21 to 1.31µW[39].

Driving MLAs

MLAs are employed for micro-displays where they are driven either in a multiplexed scheme or directly. In a multiplexed driving design, a common anode is used for each column and a common cathode for each row. Each element in a row of the MLA is addressed by applying a bias voltage across the row electrode and by sinking a constant current on each corresponding column. Any imaged pattern can be displayed by raster scanning down the rows one at a time. The intensity can be controlled through pulse width modulation (PWM), another advantage of the fast response time of LED devices. This approach has the advantages of being low cost and easy to manufacture. The disadvantage of the raster scanning technique is the lower output power as the rows are scanned one at a time. Additionally, the necessary drive electronics are placed around the chip, increasing its size.

For our project we use a direct driving design, which provides a higher refresh rate and pixel brightness. Each micro-LED shares the same cathode ground but has an independent anode. This anode is connected to a transistor based on a silicon CMOS integrated circuit[79]. The micro-LED and the MLA cannot be fabricated together on Si integrated circuits. However, hybrid integration is possible via Flip-chip bonding. The flip-chip bonding minimizes the micro-display driver module size, which controls the LEDs as a CMOS backplane is connected directly on the back of each MLA. The MLA and its CMOS driver module are bonded through gold and epoxy bumps [79].

3.2.3 Micro-LED arrays in OptoNeuro

In optogenetics, blue MLAs are used to stimulate ChR2 expressing neurons, generating action potentials and therefore modulating neural activity. The OptoNeuro project goal is to exploit this technology to develop a simple tool for neurophysiology experiments and more particularly to develop a new type of eye prosthesis.

Previous technology

As part of a previous project, a multiplexed, high power, matrix of 64x64 micro-emitters GaN LEDs was developed and tested on hippocampal neurons expressing ChR2. The diameter of the micro-emitters was 20µm and they had a 50µm pitch[39]. The MLA had a peak around 470nm, which is similar to the absorption of ChR2 (see Figure 3-8 (A)). A 1:1 imaging system and on-sample irradiance is shown on Figure 3-8. The MLA could generate patterns that could be controlled spatially and temporally with pulse width around the ms and a rate up to 40 images per second.

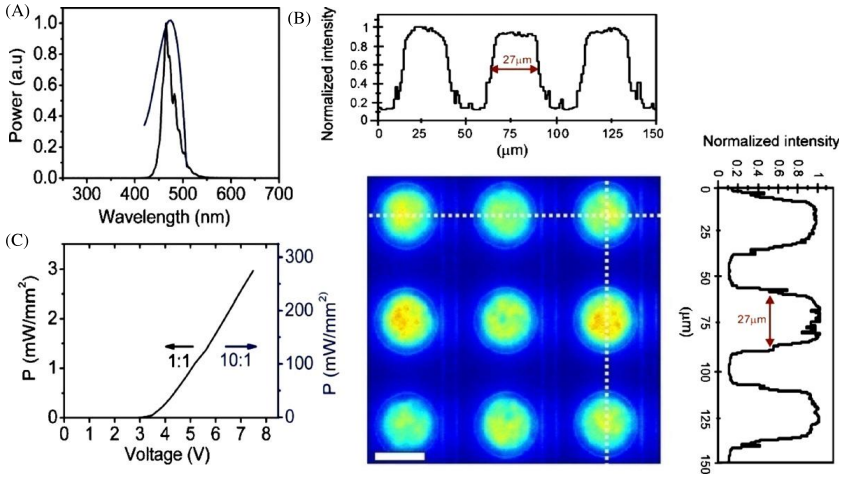

Figure 3-8: Characteristics of on-sample illumination [60]
(a) Emission spectrum of a single blue micro- LED and action spectrum of ChR2 (above the emission spectrum)[45]. (b) Intensity map of 3x3 micro-LEDs with graphic view of the intensity profile along the white lines. Scale bar 25μm. (c) On-sample irradiance from a single emitter as a function of bias voltage. At the left is the scale for a 1:1 imaging, and at the right, for a 10:1[27][98].

An MLA was imaged on neurons using a 1:1 imaging configuration and it was aligned via fluorescence imaging in order to have one spot centered on the soma of a ChR2-YFP-encoded hippocampal neuron[60]. In that example, the best spiking was obtained when stimulating the soma and one of the dendrites together (see Figure 3-9), though clearly here the issue of fill factor and non-uniform irradiance of the sample can be seen.

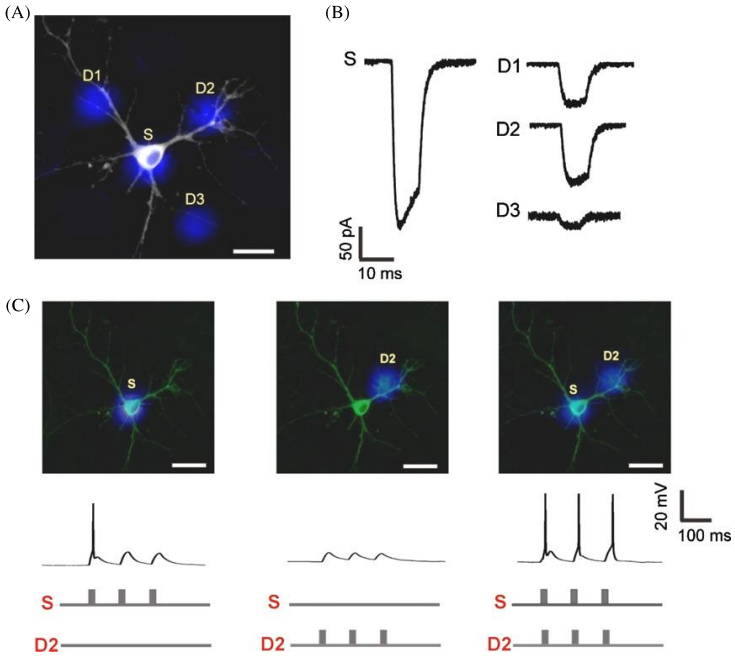

Figure 3-9: Dendritic excitation [60]
(a) Illumination (1:1) of three proximal dendrites and cell soma of ChR2-expressing hippocampal neuron. (b) Currents evoked by 10 ms of 1mW.mm−2 illumination. (c) ChR2-evoked input currents synchronized to maximize spiking[60]

N. Grossmann at al. deduced that in order to be able to stimulate the retina safely and reliably a minimum source radiance of L_{min} = 5mW.mm^{-2} is necessary. They based this result on the measurement of the minimum and maximum cell irradiance needed to stimulate a neuron expressing ChR2 (~0.1 mW.mm^{-2} and ~10mW.mm^{-2}) (see Figure 3-10). This provides us with a proof-of-concept of a novel two-dimensional photo-stimulation tool based on a MLA[4].

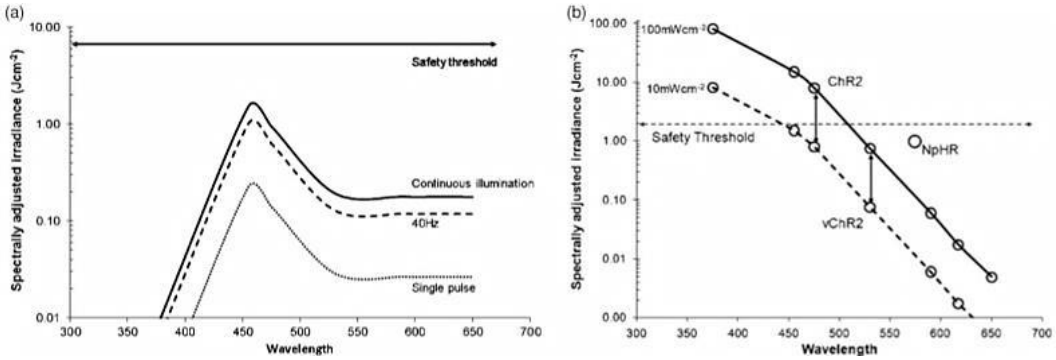

Figure 3-10: Spectrally weighted irradiances and their relationship with thermal and photochemical safety margins.

(a) For LEDs emitting 100 mW.mm-2 on 10% of the retina with different peak intensities. The safety margin is not reached here. (b) For a single LED emitting 5ms pulses at 40Hz on 10% of the retina, the photochemical damage limit could be reached at 10mW.mm^{-2} or 100 mW.mm-2. NpHR (Halorhodopsin) is outside the curve as is the ion pump[4].

However, the system suffers from several limitations. The MLA can't emit light continuously as it has a multiplexed drive and imaged patterns are displayed by raster scanning down rows. The solution is to use a direct driving MLA to drive each micro-emitter separately. This kind of driver implies the use of a CMOS backplane, which is already a well-known technology for DLPs and Spatial Light Modulators (SLM). It means enough power has to be supplied to the CMOS, as well. As seen before, the flip-chip bump bonding technique is used to integrate the MLA and CMOS together. This technique requires a minimum 80 to 150µm spacing between contacts and therefore will limit the pitch between each micro-LED. A 50µm pitch, as was described above, is not yet possible. The micro-emitters will therefore need to be as efficient as possible to improve the optical characteristics compared to what has been obtained before (a collection efficiency of 2% and a fill-factor of ~10% with a 1:1 set-up).

Technology used

The micro-LED arrays developed by Tyndall have their pixels/LEDs driven independently to increase the quantity of light emitted as well as the MLA efficiency. They are made using the flip-chip technique. The III-V materials used here are GaN/$In_{0.25}Ga_{0.75}N$. The main material is GaN with 5 quantum wells formed by thin layers of InGaN with GaN between each layer (for more detail about the design see Chapter 7:).

The first arrays developed were 16 by 16 LEDs with 150µm pitch (see Figure 3-11). The size of the emitter can vary. The LED made by Tyndall, using a conventional design, without a reshaped back reflector has a 25µm diameter. In the case of the LED with the reshaped back reflector, which we are using for our project, the quantum layers, where the light is emitted in the LED, have a diameter around 10µm. They emit light in all directions. The back reflector, within which the quantum layers are, recycles the light emitted backward and sideway to redirect it forward through a 25µm aperture, which results in an LED with an apparent diameter of 25µm (see Figure 3-7).

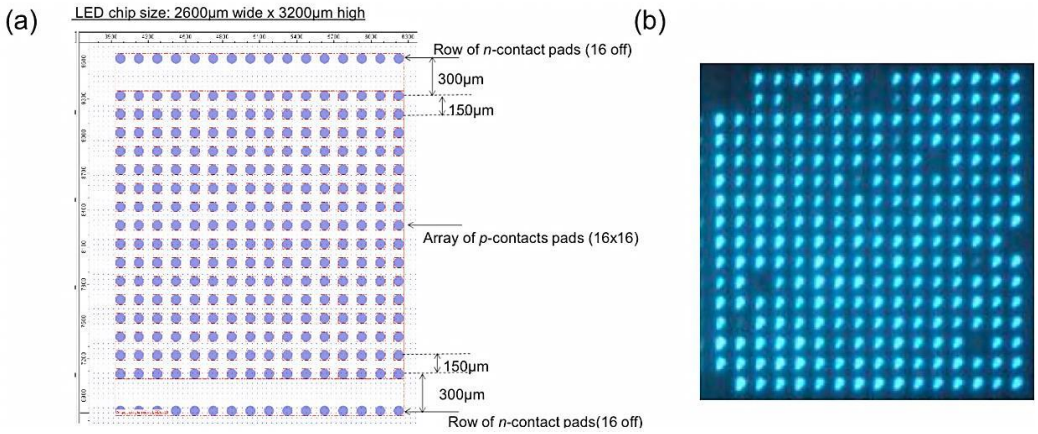

Figure 3-11: 16 by 16 MLA
(a) Bond pad arrangement: 16x16 array with 150µm pitch. (b) Flat emitter MLA

MLA development

From the original design with single emitter and flat back surface, two main issues appeared:

- The total quantum efficiency is low because of the internal reflections of the light inside the LED due to the difference of refractive index between each layer of the micro-LED and the air (from n_{GaN}=2.4 at 470nm to n_{Air}=1).
- A low fill-factor (2.2% of the total area) because of the 150µm spacing of the micro-leds (see Figure 3-11(b)), limited and the size of the CMOS electronics required between each LED in order to achieve low enough drive resistance.

The total external quantum efficiency was improved by reshaping the back reflector, which is used to recycle the light that should have been lost due to internal reflections. The effect of this is that the emission does not follow the Lambertian emission law anymore but has a lower angle of view. Defining the angle of view as the angle between the maximum and 50% intensity, where most of the light is emitted. The Lambertian emission law gives an angle of view of 60°, whereas with our reshaped back reflector we now have an angle of view of ~30°. This will affect the numerical aperture (NA) of LEDs ($\mathrm{NA_{LED}} \approx \sin(\text{Angle of view})$). The amount of light collected by the collecting optics is proportional to the square of the NA of this optics over the square of the NA of the LED. It can be estimated that this new LED design increases the quantity of light onto the biological sample by at least 4 fold.

The second issue, the fill-factor, can be improved in two ways, either by increasing the emitting area or by using micro-optics (see section 3.1).

In parallel with our micro-optics developments, Tyndall explored several MLA designs, the single emitter design a 25µm apparent emitter and a reshaped back reflector to be used with optics (see Figure 3-12(a) and Figure 3-13(a)), a single emitter design with an increased emitting area (~90µm diameter) but with a conventional LED design, as reshaping is not possible for this size (see Figure 3-12 (c) and Figure 3-13 (b)) and finally a cluster of 14 20µm diameter emitters with reshaped back reflector driven as one LED (see Figure 3-12 (b) and Figure 3-13(c)). This design allows the use of higher current without damaging the LEDs and keeps the advantages of small emitters and shaped back reflectors.

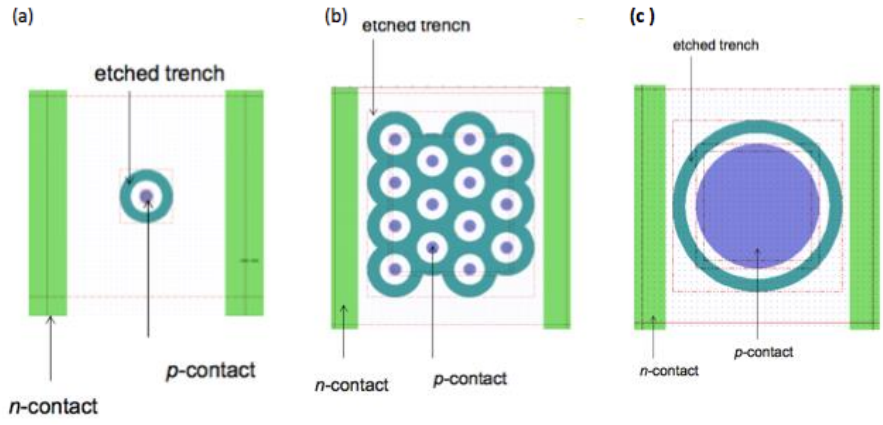

Figure 3-12: MLA emitter design schematics
(a) Single element, (b) Cluster of 14 elements and (c) Large single element

Below is an example of how they look like inside an array:

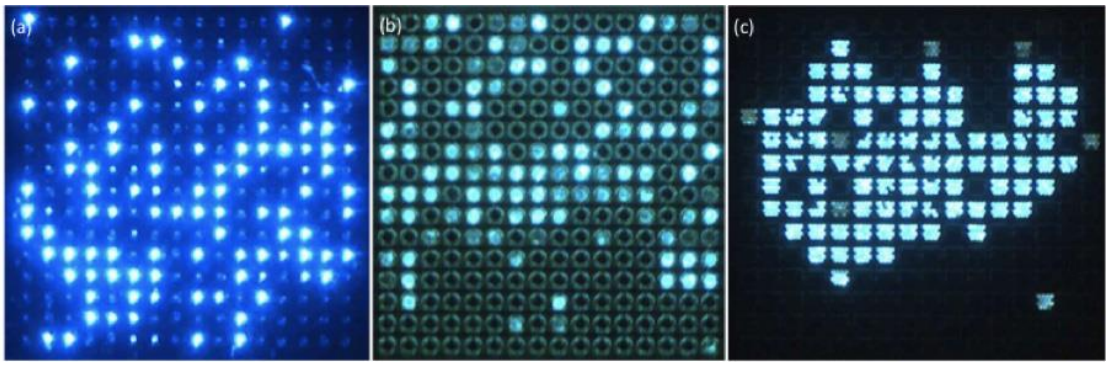

Figure 3-13: MLA designs with 16 by 16 LEDs and 150µm pitch
(a) 25µm diameter single emitters, (b) 90µm diameter single emitters and (c) Clusters of 14 emitters with each small emitter 20µm diameter

In later developments, the sapphire substrate was removed leaving the n-GaN layer directly in contact with the air decreasing the scattering of the light through the LED substrate. The improvement of the driving electronics and the automation of the MLA manufacturing allowed the development of a 90 by 90 LED array with 80µm pitch by the end of the project (see first prototype on Figure 3-14).

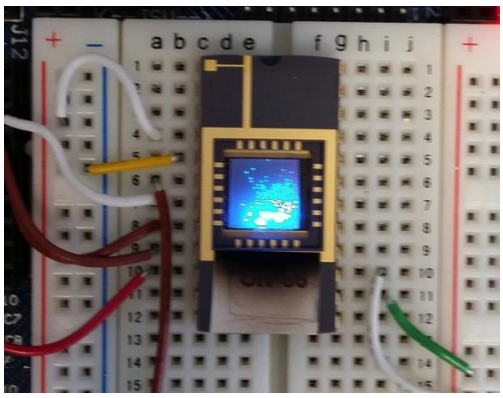

Figure 3-14: 90 by 90 MLA with 80µm pitch

3.2.4 MLA choice

As discussed above, our partner, Tyndall, developed several types of MLA to improve characteristics such as the total emission efficiency of the device by decreasing TIR and decreasing the angle of emission of the light, which allows in turn for more light to be collected by external optics. However, one of the limitations that remain is the fill-factor of the emitting area compared to the total area of the MLA. The most appropriate device without and with micro-optics in the set-up will be discussed here, in order to understand the factors in achieving the highest collection efficiency and fill-factor.

Without micro-optics

Two parameters are actually essential here. First, there is the fill-factor of the MLA, which will be imaged onto the cells and second there is the collection efficiency of the optical system, which depends on the NA or angle of emission of the MLA. Figure 3-15 shows the different MLA designs developed by Tyndall.

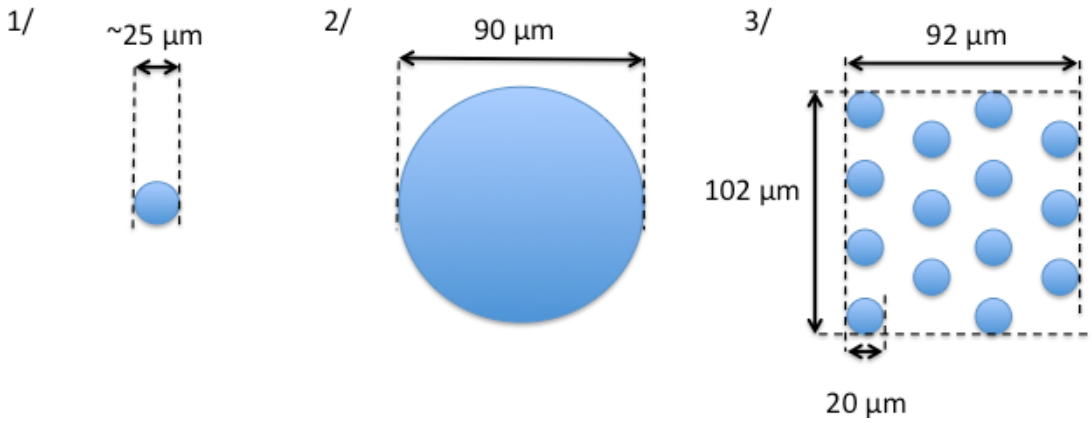

Figure 3-15: Geometric diagram of 1/ a 25µm diameter single emitter, 2/ a 90µm diameter single emitter and 3/ a cluster of 14 emitters 20µm each

The emitting areas were calculated and are summarised below:

	25µm single emitter	90µm single emitter	Cluster of 14 emitters
Number of emitters	1	1	14
Diameter of each emitter (µm)	25	90	20
Emitting area (μm^2)	491	6362	4398
Fill-factor (%)	2.2%	28.3%	19.5%

Table 3-1: Type of MLA emitters and their geometric characteristics

The 90µm single emitter has the largest area and then the cluster, with a slightly smaller emitting area even if it is spread along a larger area. However, their fill-factor is still low (<30%).

The collection efficiency depends on the microscope characteristics and on the NA of the MLA. The smaller the NA, the more will be collected by a microscope system such as the one shown in Figure 3-1. The mathematical expression describing the collection efficiency when the collection NA is smaller than the emission NA is shown below (see appendix A.1):

$$E_{System} = \frac{NA_{Collection}^2}{NA_{Emission}^2} \qquad 3.6$$

Where:

$$NA_{Collection} = \frac{f_{Real\ tube\ lens}}{f_{Reference\ tube\ lens}} . M_{Objective} \quad 3.7$$

The microscope objectives are combined with a tube lens with a specific focal lens. A tube lens with a different focal length modifies the final magnification and NA of the microscope system.

If the NA of the emission is smaller than the NA of the collection optics, then all the light emitted will be collected. The collection efficiency will be identical for the emitters with the same NA even if the sizes of the emitters are different. The Figure below shows the variation of collection efficiency in percentage for MLA with an NA of 0.87, when the distribution is close to a Lambertian distribution, and an NA of 0.375 (22° angle of view, micro-LED with micro-mirrors). Figure 3-16 was plotted for an MLA connected directly to a range of Olympus microscope objectives from 4 to 60 times magnification and a collection NA going from 0.04 down to 0.017. The focal distance of the tube lens used is the one used traditionally with Olympus microscope objectives (180mm).

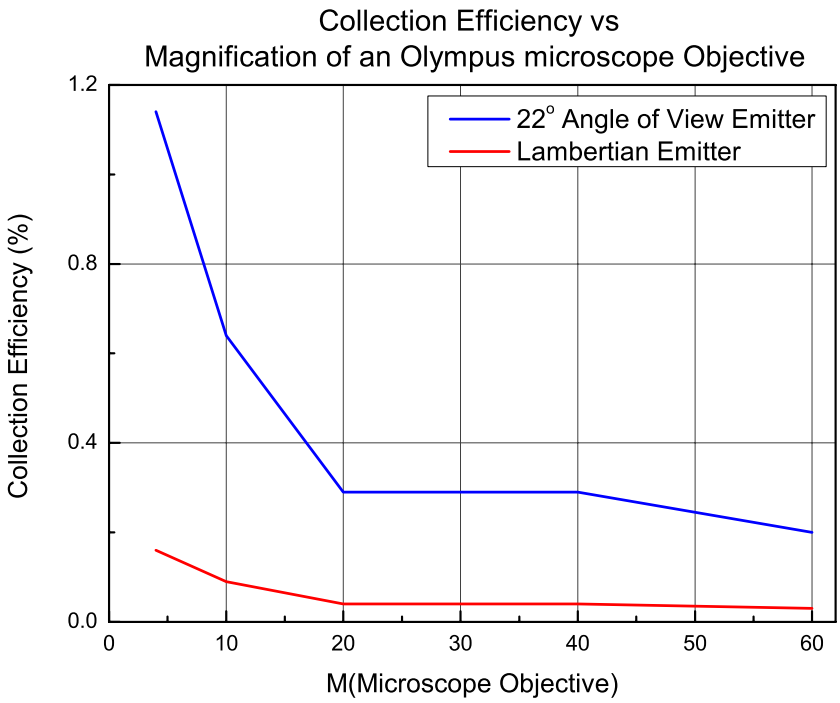

Figure 3-16: Variation of the collection efficiency with the magnification of the microscope objective and two types of light emission for 4x (0.16NA), 10x (0.3NA), 20x (0.4NA), 40x (0.8NA) and 60x (1NA) microscope objectives

Without micro-optics, the cluster of 14 LEDs driven like 1 LED is the most appropriate choice providing the highest fill-factor and a collection efficiency at least 7 times higher than the large Lambertian emitters because of its reshaped back-electrodes that can't be used on a large single emitter. This type of emitter additionally provides the advantage of being able to be driven quicker than a bigger single emitter, however it requires higher current than the small single emitter.

With micro-optics

As described above, and shown in Figure 3-2, we expect to improve performance using MO to collect light from the MLA, which are then imaged on the cells instead of the MLA, which itself is imaged at the pupil of the microscope objective. It may be necessary to use relay optics to match the characteristics of the MLA and MO, such as pitches and the MO focal distance. The difference in pitch will define the magnification of the relay optics and the focal distance, the position of the MLA relative to the MO. This position may be sometimes inside the micro-lens substrate and therefore necessitate the use of an image of the MLA instead. In Figure 3-17, two lenses with different focal distances f_1 and f_2 represent a typical 4f relay optic system.

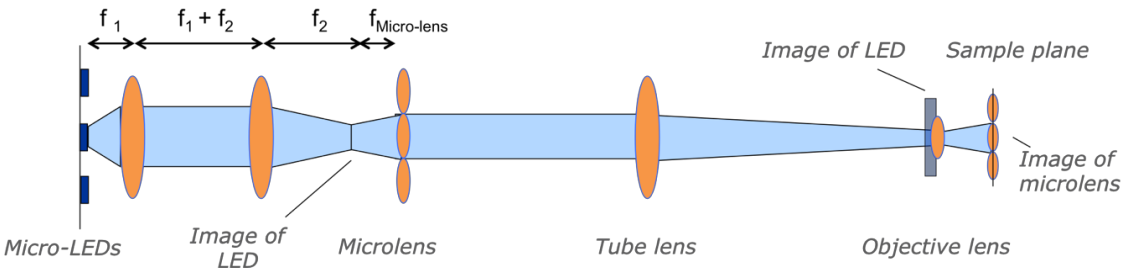

Figure 3-17: Schematic of the MLA coupled with the MO by relay optics

The size of the image at the pupil therefore depends on the emitter size:

$$\emptyset(Pupil\ microscope\ Objective) = \frac{f_2}{f_1} \times \frac{f_4}{f_3} \times \left(\emptyset\ (micro - LED\ emitter)\right) \quad 3.8$$

Where f_1 and f_2 are the focal distances of the lenses in the relay optics with a magnification $M = f_2/f_1$. f_3 and f_4 are the focal distances of the micro-optics and of the tube lens inside the microscope respectively.

The image of the micro-optics is calculated the same way:

$$\emptyset(Sample\ plane) = \left[\frac{f_{Tl1}}{f_{Tl0}} \times M\right] \times \emptyset(microoptics) = M_{Eff} \times \emptyset(microoptics) \quad 3.9$$

Where f_{TL0} and f_{TL1} are the focal distances of the reference tube lens used by microscope manufacturers and of the tube lens used in the system. M is the magnification of the microscope objective and M_{Eff}, the effective magnification of the microscope objective.

To determine how much light is going through the objective, the image of the LED emitter just before the micro-optics (Imaginary source) needs to be compared to the effective NA of the microscope (see A.1.1):

$$\emptyset(Imaginary\ source) = \emptyset(LED\ emitter) \times\ M(Relay\ Optics) \quad 3.10$$

$$NA(Imaginary\ source) = \left[\frac{\emptyset(Imaginary\ source}{2}\right]/(f_3) \quad 3.11$$

Where f_3 is the focal distance of the micro-optics.

$$NA_{Eff} = \frac{NA_{microscope\ objective}}{M_{Eff}} \quad 3.12$$

There is therefore a maximum size for the LED emitter where all the light coming from the micro-optics is going through the microscope objective pupil:

$$\emptyset_{Max}(LED\ emitter) = \frac{2 \times f_3 \times NA_{Eff}}{M(Relay\ Optics)} \quad 3.13$$

Figure 3-18 shows how the collection efficiency varies with the diameter of the emitter and the light emission (Lambertian equivalent or with 22° angle of view) for a system using relay optics with M = 1.67, 1mm focal micro-optics with 250 µm pitch and a 40x microscope objective (NA 0.8) with a 100mm tube lens. For diameters of the emitter above 43µm, the collection efficiency decreases because its image overfills the pupil of the microscope objective.

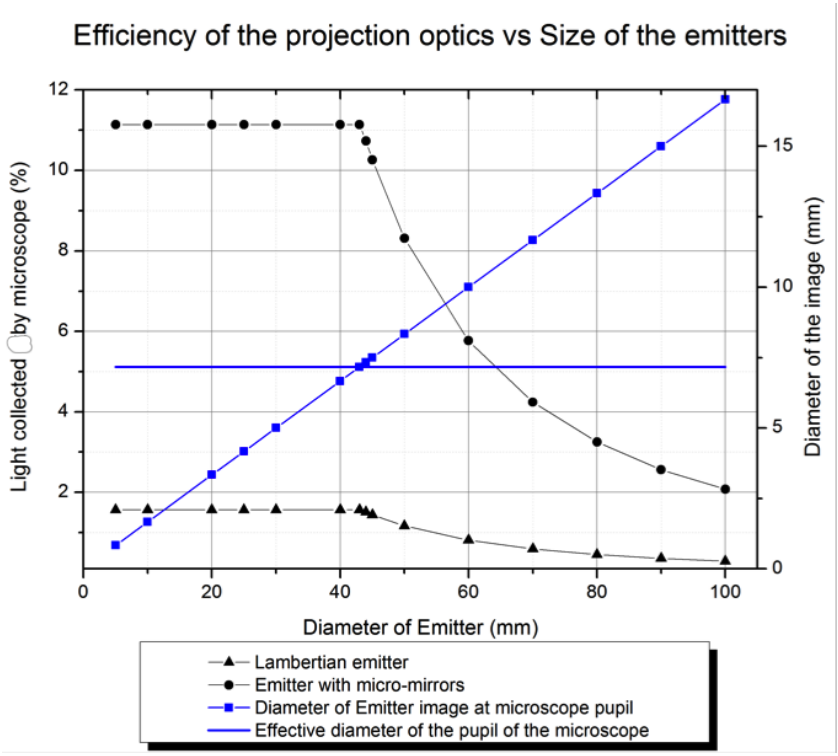

Figure 3-18: Variation of the collection efficiency with the size of the emitters and the type of emission

Additionally the collection efficiency depends on the NA of the emitters, which are collected by the relay optics. The focal distance of the first lens of the relay optics is generally a lot shorter than the one of the tube lens of a microscope and therefore collects more light than without micro-optics.

The four emitters developed by Tyndall are compared for an identical set-up with microscope objectives of different magnifications (see Figure 3-19). The collection efficiency of the small emitters stays constant with the increase of magnification because of its NA, which stays lower than the NA_{Eff} of the microscope objective. However, it decreases for the 90µm emitter and the cluster of emitters because the emitter image is larger than the microscope pupil diameter. The variation with the magnification is due to the fact that at lower magnification, the NA_{Eff} of the microscope objective is actually higher.

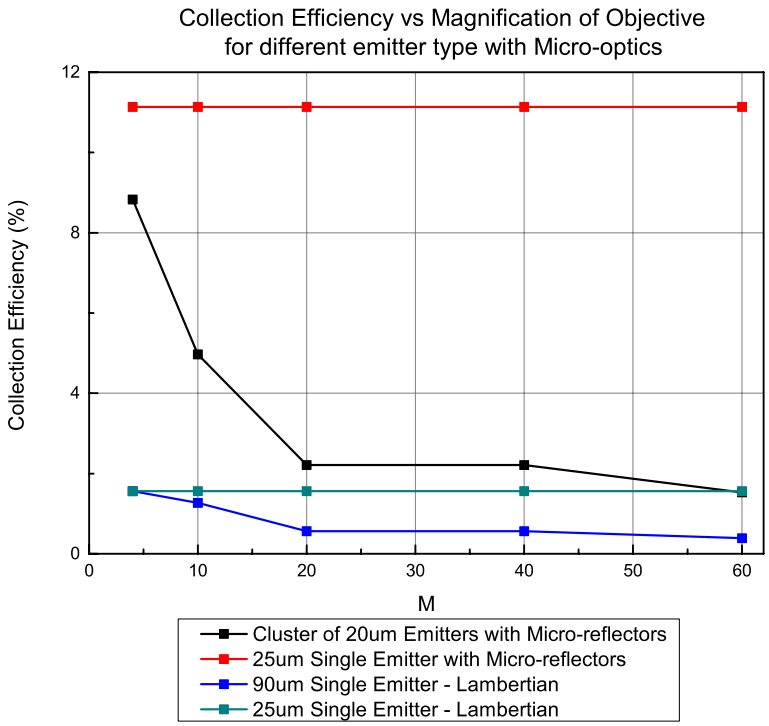

Figure 3-19: Variation of the collection efficiency with micro-optics for Tyndall's MLAs for 4x (0.16NA), 10x (0.3NA), 20x (0.4NA), 40x (0.8NA) and 60x (1NA) microscope objectives

With micro-optics, the 25µm single emitter with reshaped back-reflector is the most appropriate MLA. It allows more light to be collected by the relay optics and has higher probability to not overfill the microscope pupil and therefore let more light through. However, for a longer tube lens and at higher magnification, the NA_{Eff} will be lower and therefore even the small emitter image might overfill the pupil.

3.2.5 Conclusions

MLA qualities are expected to be useful in applications such as optical communications, signal and image processing, optical interconnects and disease detection amongst others[79], [99]. For this project, it will be used and optimised for biology, and particularly Optogenetics.

The device's characteristics like the internal reflections, the collection efficiency and the fill-factor of the emitting area, were modified to correct for issues and limitations caused by the different technology used. The design of the emitters was modified with a reshaped back reflector and different shapes. The space taken by the electronics was progressively decreased. One reason was the optimisation of the micro-LED, with a working voltage going down from more than 7V, which is considered a high voltage and requires specific electronics, to around 3V. The automation of the LED manufacturing allowed an increase of the array size from 256 (16 by 16) to 8100 (90 by 90) LEDs with a pitch going down from 150 to 80µm.

The cluster design provides the same collection efficiency than the single emitter design with a 25µm apparent diameter, but with a higher fill-factor. Without any micro-optics, this design is more suited for biological applications. However, the single emitter design is the best design to be combined with micro-optics to increase collection efficiency and fill-factor at the same time. In the next chapters, it is shown how MLA are combined with micro-optics to be implemented on electrophysiological microscope platforms and integrated into a retinal prosthesis.

3.3 Micro-optics

The use of micro-optics on top of MLA modifies the optical properties of the light emitted to suit the needs of a particular experiment. Above, we saw that the MLA was limited by its internal reflections, angle of view and fill-factor. Most of the LEDs on the market are emitting light with a distribution equivalent to that defined by Lambert. And because light is emitted broadly in the forward direction, only a small amount of light can be collected by optics and a lot of light is lost. In addition, the micro-LED emitters are not filling the whole space in the array and therefore the whole sample plane cannot be illuminated.

The reshaped reflector at the back of the micro-LED emitters developed by Tyndall already improved the light output at a specific numerical aperture (3 times more at 0.5 NA)[94], while partially solving internal reflection problems. However the active matrix MLA from Tyndall still has fill-factor limitations. Micro-optics will help reshape the emitted light, decreasing the NA of the micro-LEDs, and therefore allowing more light to be collected by external optics, while using that extra light to improve the fill factor of the projected image. In the Optoneuro's project, we also want to use this micro-optics to display an illumination pattern as seamless as possible, with as small gaps as possible between the projected pixels.

In this part, a few important rules relevant to micro-optics are outlined, showing the manufacturing methods available as well as the different materials used and describing several applications.

3.3.1 Design theory

Micro-lenses are generally lenses that have a diameter below 1mm. In the Optoneuro project, the goal is to have them fit in the set-up so that they fill most of the space between each emitter: 150 or 80µm.

Optical design rules are also applied on micro-optics. It is useful to recall a few important points about micro-lenses.

In optical design, the image of an object is considered using an array of light rays, instead of a wavefront, to facilitate the mathematical manipulation. The image is calculated either by using the Snell-Descartes law to trace rays through the different surfaces in the system, or more simply by using equations derived from the rays close to 0 (optical axis) to deduce the characteristics of the image in a perfect optical system. This is called first-order, paraxial or gaussian optics and is used to simplify calculations and simulations[15], [100]. On top of this, Seidel's equations help quantify the aberrations generated in an optical system by considering them as higher order perturbations to the first-order calculations. Aberrations are less important with smaller lenses as they effectively scale with the size of the lens and so can quickly become small relative to the optical wavelength. However, they may still have an effect on the set-up we are developing in the scope of the optoneuro project.

Additionally we have to take into account the principle of the Lagrange invariant, which defines that the brightness (power per unit area per unit steradian) of a light source cannot be increased by any optics. It is also linked to the "Etendue", which is defined as the product of the area of the source and the solid angle that the system's entrance pupil can accept. This value is conserved through the entire optical system. The first lens of the optical system fixes the system entrance pupil aperture and therefore determines the value of the Etendue. Generally, a lens can influence the way the rays are distributed, and changes the irradiance on a sample but not the total brightness. This will be the case in our system as well.

The physical characteristics of one micro-lens to be considered are the size (diameter), shape (plan, convex, concave....), with the sag at the lens vertex h_L, the radius of curvature R_C, the conic constant k, the numerical aperture NA, and the refractive index n of the material used. The effective focal distance f_E is important as well. It is defined in the equation 3.14 in function of R_C. A micro-lens array adds more parameters: the size of the array, the pitch, the way they are packed (rectangular, hexagonal…), the micro-lens fill-factor and the micro-lens uniformity[101]. The substrate of the micro-lens array thickness has to be considered too.

$$f_E = \frac{R}{n_1 - 1} \tag{3.14}$$

The other micro-lens array parameters are defined in see A.2.

3.3.2 Manufacturing methods

Different parameters have to be taken into account before manufacturing a micro-lens array. The geometrical and optical characteristics of the micro-lens array and the range of material available to suit its function are important. It can be integrated into another component such as a screen or a LED during the manufacturing process. All of that will influence the cost of fabrication. Many techniques are now available and each of them results in different optical quality and therefore is more suitable for one function or another[102]. Several methods and their evolution in the last 30 last years are shown in Figure 3-20.

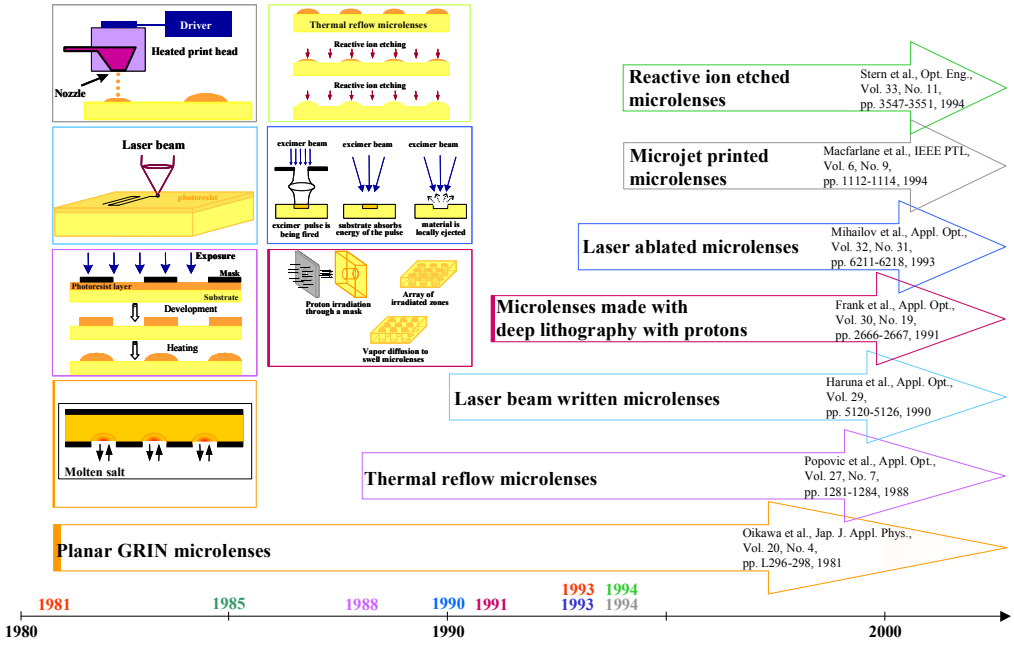

Figure 3-20: The micro-lens techniques and their development timeline[102]

The most current manufacturing method for "off-the-shelf " micro-lenses is the multi-step photolithography process, which generates a multi-level lens structure with 2^n phase levels requiring n-photolithographic and etching processing steps[103]. The main difficulty is to align each mask and the depth of each etching process correctly to get the optical diffraction efficiency. The size of each level is designed to obtain a shape equivalent to a parabola with a low volume difference (~6 %)[104] (See Figure 3-21). Such lenses are generally manufactured on Fused Silica (Quartz).

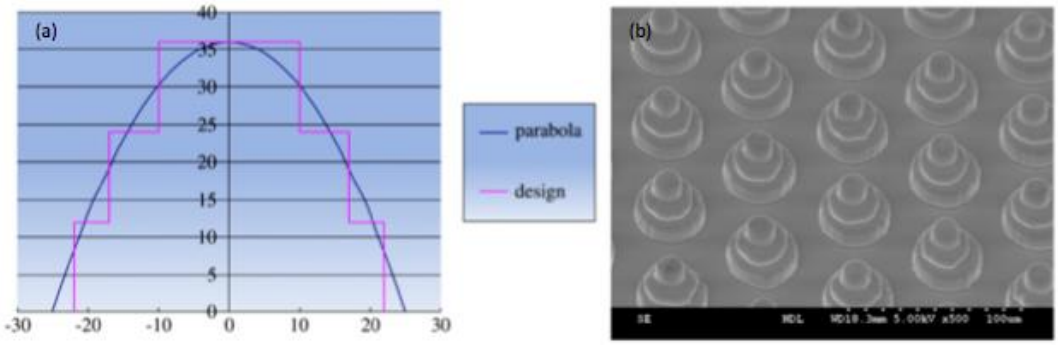

Figure 3-21: Micro-lens array manufactured by multi-step photolithographic process.
(a) Regression curve of a triple-level microstructure for parabolic curve. (b) SEM picture of a triple-level microstructure at the viewing angle of 45° [104]

Another common method is the replication process. A glass plate or a piece of PET is generally used as the substrate. A master, negative mould of the micro-lens array forms the second half of a sandwich with a UV curable lacquer, dispensed between the two before being cured by UV light [105]–[107]. Smoother micro-lenses shapes are thus obtained (see Figure 3-22).

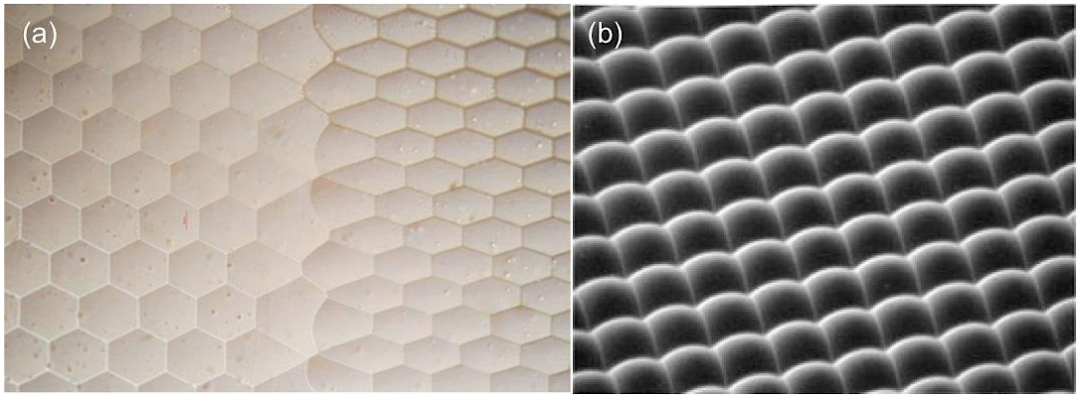

Figure 3-22: Micro-lens arrays made using a replication process at Glyndwr Innovations [108] **((a)) and at RPC Photonics** [109] **((b))**

The master for this previous method is generally laser or diamond machined. It is the most expensive part of the process when applied to custom micro-optics made in small quantities. A method not requiring a master can also be used. A semi-conductor material, SU8, is spin coated on a glass wafer and a micro-lens array is directly laser machined on it. This method is easier, quicker and priced lower for small quantities.

The main materials used to make micro-lenses are glass, plastic or semi-conductor materials. Suss Micro-Optics is manufacturing refractive micro-lenses with fused silica (n=1.458) for deep UV to visible spectrum lenses, or silicon (n=3.478) for wavelengths in the IR. Fused silica is a material that could suit our application as we work in the visible (470nm)[110].

3.3.3 Applications

Micro-lens arrays are widely used in wavefront and image sensing[111], [112],beam shaping, coupling and expansion with different type of light sources, such as lasers, OLEDs[106] and LEDs[113].

The most common microlenses are positive, refractive and plano-convex, though are various other micro-lens designs are reported, with diameters that down to less than 10µm. However specific designs improvements begin to appear with the improvement of the manufacturing process. Bifocal micro-lenses have been produced[114] as well as negative micro-lenses[115]. In addition diffractive optical elements can be used to achieve high projected image resolution in micro-LED applications[116].

Micro-lens arrays are applied to micro-emitters to reshape the beam and modify the extraction efficiency of the micro-emitter array. It was reported in one paper for example, that micro-lenses could be etched into the sapphire substrate of the array, increasing the extraction efficiency of a micro-led array by ~23%. The light cone was more concentrated towards its center with only 20% of it emitted at angles of view above +/-40°[117]. Polymer micro-lenses can also be produced and automatically aligned to UV MLAs by using the UV output light to directly write the micro-lenses into a polymer layer by photopolymerisation. However, in this case the diameter was limited to ~40µm[118], [119].

Micro-lens arrays can also be used in a reverse way for sensing. Instead of having an array of light sources aligned with the micro-lens array and their beam reshaped, the light is focused on a sensor. In Shack-Hartmann wavefront sensors, each lens focuses a wavefront and its local tilt is determined in function of their position on each sensor [120]. It is mainly used to characterize eyes for corneal treatment of complex refractive errors [121]. It is also used in more and more sensors to improve the pixel fill-factor and increase the amount of light on the sensor by collecting wider-angle beams. It was also applied to a light-field camera (Lytro camera) to detect light from more than one direction at a time [122].

3.4 Conclusions

MLA have ideal properties for stimulating the light gated protein ChR2 at 470nm. However, when connected to a microscope platform, this type of light source is limited by its wide angular light distribution and its low fill factor. In this project, a system is developed using micro-optics to collect more of the output light and direct it towards the system pupil improving the optical efficiency of the system. Now the micro-lenses are imaged on the biological cell instead of the MLA, and the fill-factor of the illumination is improved at the same time.

The first MLAs had a conventional design with a light distribution close to a Lambertian distribution and therefore most of this light could not be collected by the system optics. The back of each LED was reshaped into a reflector to redirect light usually lost due to internal reflections and therefore improve the device's external quantum efficiency, while decreasing the angle of view of the emission at the same time. A specific LED design was developed composed of 14 micro-emitters driven in parallel to increase the fill-factor without losing the advantage of using micro-reflectors with the small emitters.

The cluster of emitters is the best MLA to use without MO. However, with it, a single emitter design with an apparent size of 25µm could provide an improvement in collection efficiency and a fill-factor that will depend on the MO fill-factor, potentially close to 100%, which is much higher than the cluster of emitters at about 20%.

Chapter 4: Projection optics with off-the-shelf micro-optics: Basic design principle

The previous chapter explained how MO can be employed to improve the characteristics of the illumination, such as FF and collection efficiency, for experiments with biological samples transfected with the light-gated ion-channel ChR2. Additionally, it described the technology used as well as the most appropriate solutions for this project: 10µm single emitter MLA with reshaped back reflectors, 25µm aperture and 150µm pitch were found to be the best MLA with MO; a replicating manufacturing technique results in MO with spherical shape and highest fill-factor.

This chapter describes the development of projection optics using off-the-shelf MO. Candidate MO are examined and the best choice is justified. The principle of the set-up is explained and its validity is demonstrated experimentally. Finally, a basic optical design for the complete projection optics is presented.

4.1 Projection optics principle with off-the-shelf MO

MO were chosen based on parameters such as the market availability, the manufacturing method, which has consequences on the shape of the micro-lens (see also Chapter 3:) and the requirements of the experiment. They can be made to a specification, but this is expensive. Therefore, for a first attempt, off-the-shelf solutions are investigated, which are a lot less costly.

The MLA has a 150µm pitch. Therefore, MO with an identical pitch were considered. Although some were available, their NA was limited to a value between 0.01 and 0.02 [123]. The NA corresponds in section to the maximum aperture of each micro-lens, not to the maximum square aperture covered by each square containing each micro-lens. A micro-lens array from Thorlabs with an NA of 0.014 was selected and included in the tests. However, with such a low NA the collection efficiency of these MO are expected to be very low (see Chapter 3: and A.1.2). Therefore MO with slightly higher pitch and a lot higher NA were considered as well. Several choices were available with pitches at 222 or 250µm with NAs between 0.1 and 0.22. The 250µm one had the highest NAs with a maximum of 0.22 compared to 0.12 at a pitch of 222µm. With these MO, a relay optic system (RO) is needed to include magnification to match the pitch of the MLA to that of the MO (see section 3.2.4).

The following four micro-lens arrays were selected for testing:

Micro-lens array	Pitch (µm)	Micro-lens diameter (µm)	NA	f (mm)
Thorlabs	150	146	0.014	5.2
Advanced Micro-optics System Gmbh (AMOS) [124]	222	210	0.114	0.92
Flexible OKO Optical [125]	250	250	0.219	0.57
Adaptive Optics Associates (AOA) [126]	250	250	0.125	1

Table 4-1: Micro-lens arrays selected for testing

Figure 4-1 shows micrographs of the micro-lens arrays when illuminated in transmission with white light. Two were made with a multi-step photolithography process ((a) and (b)) and two, by replication ((c) and (d)). The differences are significant as structures can be clearly seen in (a) and (b) and in (a) too the lens diameter is clearly smaller than the pitch. The first one (a) is a circular micro-lens array and thus its maximum fill-factor is $\pi/4 = 78.5\%$. However, the micro-lens has a smaller diameter than the pitch due to a chrome mask that blocks light from being transmitted through the spaces between micro-lenses. Hence its fill-factor is reduced even further to 74.4% for a 146µm diameter lens and a 150µm pitch. The second one (b) looks like a circular microstructure on a square one, as there is one layer less at the edge of each micro-lens. The circular microstructure has a fill-factor of 70.3% (210µm diameter for a 222µm pitch) and no mask. No structures are visible on (c) and (d), and their diameter is nearly identical to the pitch (250µm) with a square shape instead of a circular shape increasing their fill-factor to nearly 100%.

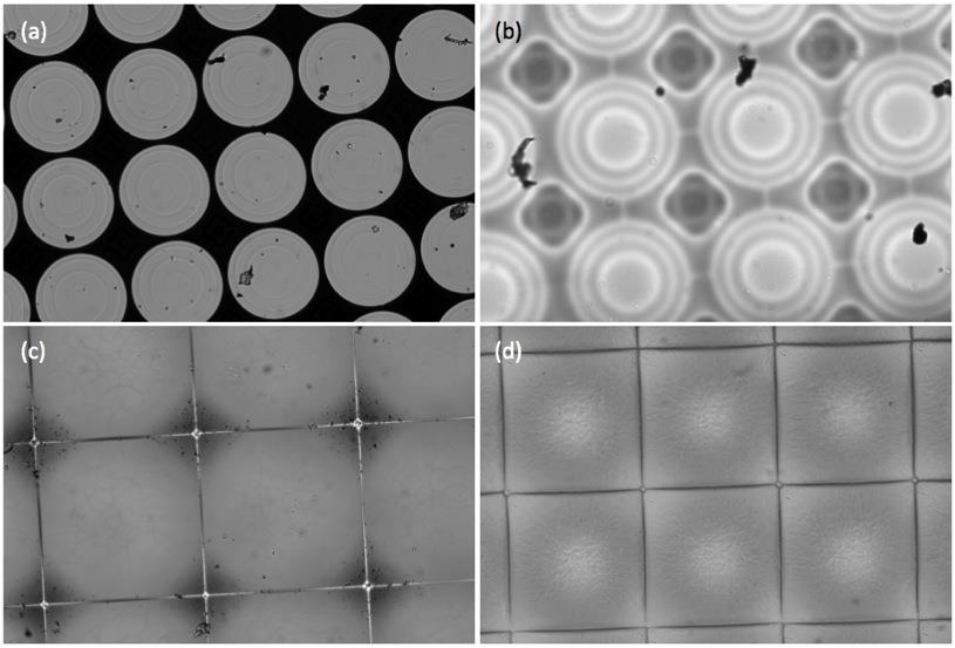

Figure 4-1: Photography of micro-lens arrays with a microscope under white light:
(a) 150 µm pitch and 0.014 NA, (b) 222 µm pitch and 0.11 NA, (c) 250 µm pitch and 0.21 NA and (d) 250µm pitch and 0.125 NA

These micro-lens arrays were all made on glass substrates, which were at least 1 mm thick. Apart from (a) the MO all have a pitch that is different from the MLA and a focal distance equal or below 1mm in air. Relay Optics (RO) are therefore needed to magnify the image of the MLA and set it at the correct focal distance of the micro-optics, which will then be imaged on the cells (see Figure 4-2). The type of relay optics employed is dependent on the choice of micro-lens array and will be described later.

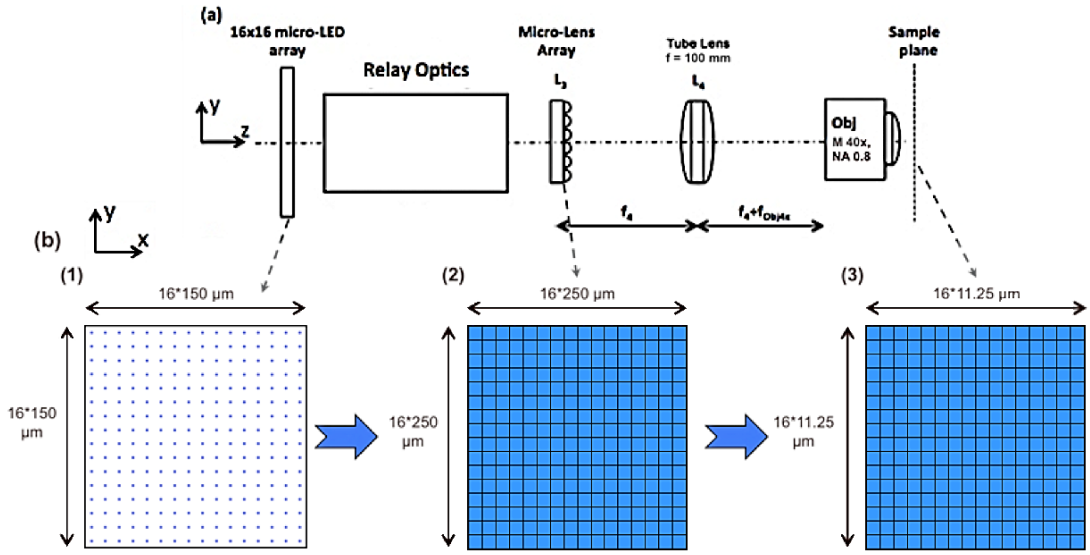

Figure 4-2: Projection optics principle
(a) Schematic of the illumination optics with the projection system, (b) Illumination visible from different point in the optical set-up: (1) MLA (Object), (2) Micro-optics filled with the light from the image of the MLA and (3) Image of the micro-optics onto the sample

Depending on the type of experiment, with microelectrode arrays for multi neuron studies or with a patch-clamp, for single neurons, the requirements are slightly different. It was shown previously using a patch-clamp[60] that the stimulation of a neuron is stronger when the main body of the neuron cell, the soma, is stimulated but optimal when its dendrites are also stimulated. The microscope magnification usually used for such experiments is 20x, 40x and 60x. It was therefore decided that the illumination with a single LED should be able to cover the soma completely, ~10µm (see Figure 4-3). One of our partners, Scientifica, uses an Olympus microscope with a 40x objective that has an NA of 0.8. The Olympus tube lens usually has a focal length of 180 mm, but for their implementation Scientifica have modified the microscope and used a tube lens with a 100 mm focal length instead in order to maximise the field of view when using a camera. This means an effective magnification of 22.22 instead of 40 (see A.1.2). Following these characteristics, a 222µm diameter micro-lens array could produce a 10µm spot and cover the soma with exactly one LED.

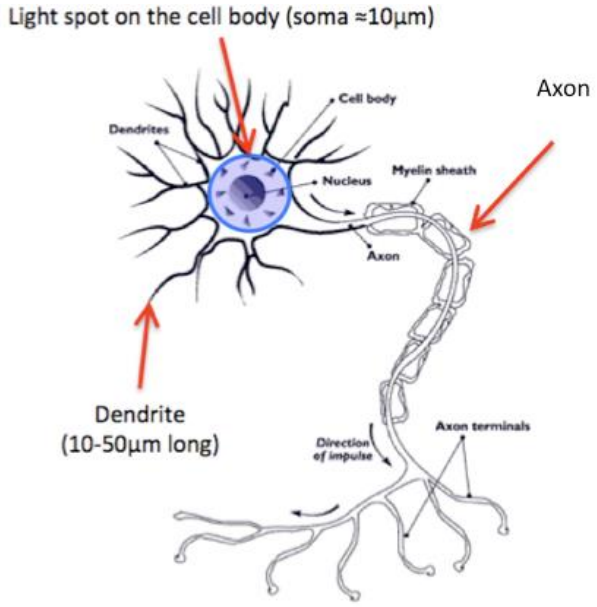

Figure 4-3: Light spot on the cell body

However the 250µm micro-lens arrays were found to be best suited for this set-up as their shape is spherical and continuous, and their fill-factor nearly 100%. They have also the highest NA. In this case, the size of the spot on the sample is still close to the size required at 11.25µm.

As explained above considering that the MLA has a 150µm pitch and the micro-lens array a 250µm pitch a relay optical system with a magnification of 1.67 is necessary to match the arrays to each other. This means the NA of the relay optics at the MLA side needs to be 1.67 times higher than at the micro-optics (MO) side in order to fill each micro-lens to the edge, which corresponds to 1.67*0.219 = 0.365 and 1.67*0.125 = 0.21 for the two different available micro-optics NAs respectively. The lenses used in the relay optics are larger than the micro-lenses (up to 30mm vs 250µm diameter) and therefore will suffer significant optical aberrations (see section 4.2). The larger the NA of the relay optics, the higher is the collection efficiency (see the equation 3.6 in section 3.2.4). With a MLA using micro-mirrors, 95% of the light can be collected by the MO. This quantity is divided by 3 with the lower NA MO. A higher NA requires larger optics for the relay optics, increasing cost and decreasing system compactness. It also means an increase of the amount of optical aberrations and of the difficulty to compensate for it. Taking all these considerations into account the micro-lens array (c) 250µm pitch and 0.125 NA from “Adaptive Optics Associates” was selected to be the most appropriate off-the shelf MO for our system.

4.2 Relay optics (ROs): Theory and proof of principle

The role of the RO is to image the MLA to just before the micro-optics with a specific magnification: 1.67, to fill each micro-lens. Their role is important, as this is where most of the optical aberrations stem from, meaning the quality of the whole system performance is dependent on it. In this section, the validity of this idea will be demonstrated by using simple RO and MO available at the time of the experiment. The method to assess an optical system performance and give an overview of the requirements of the projection optics (RO and MO) is explained. The optical system is composed of RO and a chosen off-the-shelf micro-lens array. Finally, essential optical design theories are reviewed and the choice of an optical design for more advanced RO is justified.

4.2.1 Proof of principle

As a proof of principle, a simple set-up was first implemented with two achromatic doublets and a micro-lens array to verify the validity and potential of this idea when combined with a microscope composed here of a tube lens and microscope objective (see Figure 4-4).

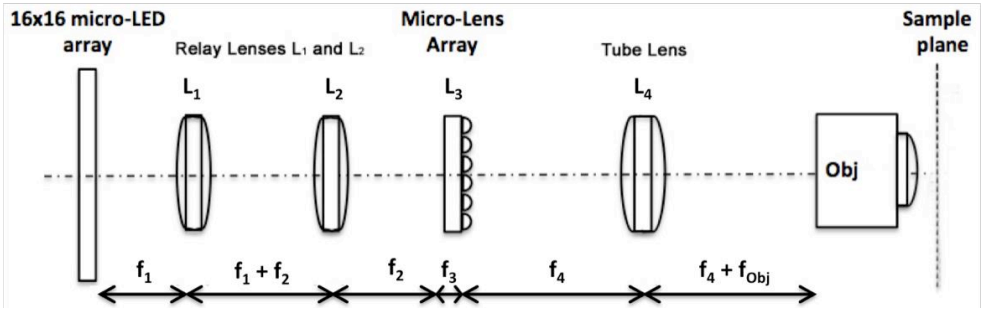

Figure 4-4: Schematic of a simple optical telecentric relay connected to a microscope

As described above the idea was to use a micro-lens array, which could bring gain in collection efficiency and increase the fill-factor. As no 150µm pitch micro-lens array with high enough NA was available to bring a gain in collection efficiency, the 222µm pitch one was first used due to its availability at the time of these basic experiments and fitted these criteria. To adapt to this micro-lens array the magnification of the relay optics was set to be $M = Pitch_{MOs}/Pitch_{MLA} = 222\mu m/150\mu m = 1.48$. Therefore an optical relay with M ≈ 1.50, made of 40 mm and 60 mm focal distance achromatic doublets with 15.8 mm diameter aperture ($NA \approx 0.2$ on the MLA side) from CVI-Melles-Griot, was used (01LAO437 and 01LAO477).

The tube lens had a 100 mm focal distance and the microscope objective M = 20x and 0.4 NA. This has an equivalent entrance pupil to the microscope objective generally used by Scientifica (M= 40x and NA= 0.8). As the resolution of the camera was too small to see the image at the sample plane (Hamamatsu Orca ER: $6.45\ \mu m\ \times\ 6.45\ \mu m$ pixel size[127]), a second microscope was used to image the image of the micro-optics onto the CCD. The size of this image can be increased or decreased by using different magnification objectives. In this experiment, the aim was to look at a few micro-lenses at a time, and so the image needed to be magnified. A 40x microscope objective with 0.75 NA was used, providing therefore 2x magnification, which means an image twice the size of the real micro-lens array on the CCD, or a pitch of 444µm (seeFigure 4-5). The MLA available at the time had a conventional LED design and therefore a distribution close to the one defined by Lambert's emission law.

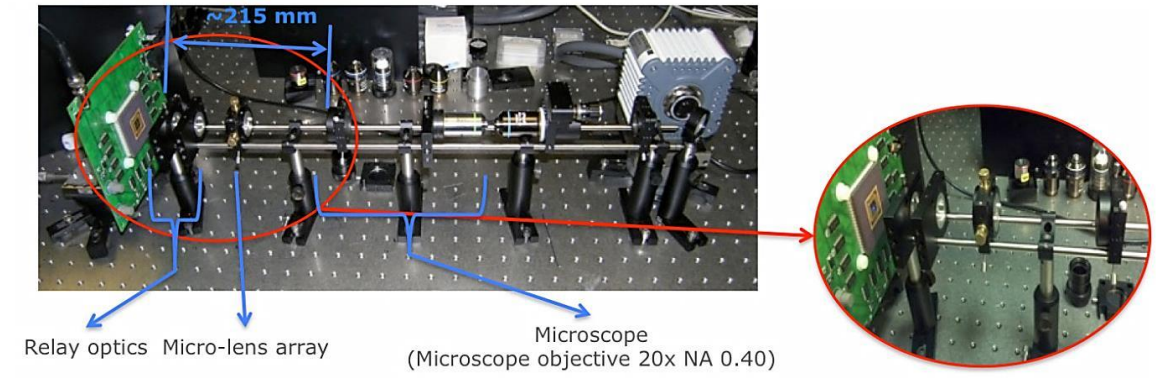

Figure 4-5: Proof of principle: Experimental set-up

Three cases were imaged, first the system without micro-optics, then with the micro-lenses filled and finally with the micro-lenses slightly overfilled (Figure 4-6). These micro-lenses were circular and arranged on a rectangular grid like the MLA. As described above the maximum fill-factor for a circular micro-lens array is 78.5%, however, the micro-lens used had a stepped structure with the largest ring having a smaller diameter than the pitch (210µm vs 222µm), hence a fill-factor of around 70.3%. The micro-lenses could be slightly overfilled to increase the fill-factor at the expense of the collection efficiency.

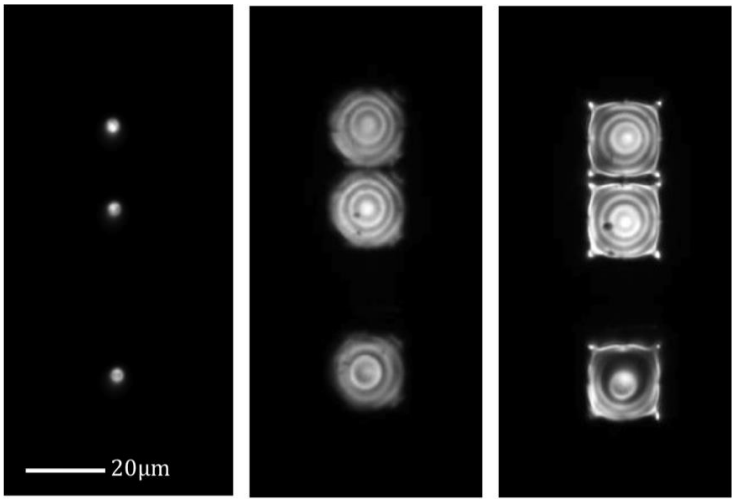

Figure 4-6: Proof of principle: imaging
3 micro-LEDs imaged without (left), with and filling (centre) and slightly overfilling (right) 3 micro-lenses

Figure 4-7 shows the collection efficiencies measured without and with projections optics. Measurements of the intensity were taken at the MLA and after the first microscope objective, where the biological sample would be on a microscope. The collection efficiency was then calculated by comparing these two values. The collection efficiencies without projection optics were in agreement with the theory with results below 0.2%. With projection optics, the collection efficiencies significantly increased. In theory, with a 1.48 optical relay and a 0.11NA micro-optics, the quantity of light that can be collected on the MLA side is $1.48 \times 0.11 = 0.163$ and therefore, if no light is lost at the microscope pupil, the collection efficiency is 2.64% on the sample plane. However, in practice, the results were lower when the micro-lenses were filled or slightly overfilled (1.55% and 0.9%). One of the reasons is that the optical relay is not optimised for the exact correct magnification causing a mismatch in the pitch. This can be solved by adjusting the lens positions to give an exact magnification of M=1.48. The other reason is the shape of the micro-lens, which is not spherical but as described above a stepped structure, which only approximates a spherical shape (see Chapter 3.3).

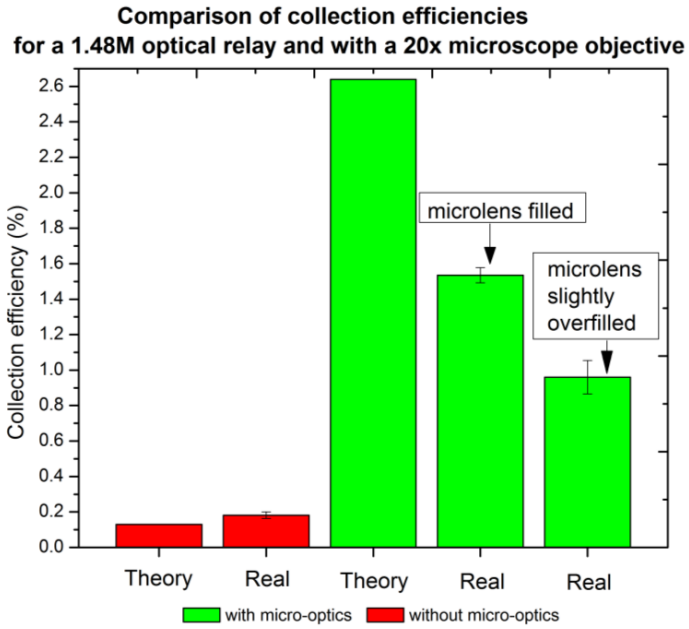

Figure 4-7: Proof of principle: Collection efficiencies measurement

This experiment proved that the fill-factor can be increased using micro-optics (from 2.2% to 70%) as well as its collection efficiency by more than 10 times (from 0.13% to 1.55%). However, the magnification of the optical relay needs to be optimised to fill each micro-lens correctly from the centre of the 16 by 16 micro-lens array to its edge. Additionally, as it was outlined in Section 4.1, the micro-lens shape is not optimised for this experiment, as its shape needs to be continuous to obtain an image with a homogeneous intensity. Another parameter is the micro-lens array fill-factor, which needs to be as high as possible. The micro-lens array that was described above as the best fit for our set-up and that was ultimately used has a square instead of a circular shape. This increases its fill-factor to nearly 100% and thus improving the results considerably.

4.2.2 System performance assessment

Using MO, more particularly off-the-shelf ones, to increase characteristics such as fill-factor and collection efficiency were proven in practice in the previous section. RO were necessary to image the MLA with the correct magnification and at the focal position of the MO. However, the magnification of the simple RO used was slightly high and therefore imaging the entire array was not possible. The RO need to be optimized with the correct magnification to produce a correct imaging of each micro-lens onto the sample plane. Furthermore, the imaging quality is determined by the amount of aberrations in the systems.

Aberrations can be described in two different ways. Wavefront aberrations are the differences between the actual wavefront and the reference sphere. While ray aberrations, caused by the non-spherical wavefronts, correspond to the rays not crossing the optical axis at the paraxial focus. Seidel defined mathematically the third-order lens ray aberrations and put them into several different classifications [100], [128], [129]. There are those obtained with monochromatic light and those obtained with polychromatic light. Table 4-2 summarizes how characteristics of the system influence the magnitude of these ray aberrations.

Aberration	Aperture (Ø)	Field Angle (θ)	Image height (y)
Lateral Spherical	$Ø^3$	---	---
Longitudinal Spherical	$Ø^2$	---	---
Coma	$Ø^2$	θ	y
Astigmatism	Ø	$θ^2$	y^2
Field Curvature	Ø	$θ^2$	y^2
Distortion	---	$θ^3$	y^3
Chromatic	---	---	---

Table 4-2: Variations of Aberrations with Aperture, Field Angle and Image Height

The optical system was developed in an optical design software called Zemax. It enables the modeling of the optical aberrations in an optical system using sequential imaging. Non-sequential imaging lets model non-imaging system with multiple sources, ray splitting, scattering and multiple detectors in a 3D environment. In this project, sequential imaging was first used to develop an optical system then non-sequential was used to generate a model of the optical system within the entire imaging platform.

The development of the system depends on the size of the object and therefore, during modeling, three points on the MLA were studied in respect to aberrations: the centre, A (0,0), one extremity at the edge of the array, B (0, 1.2), and another extremity corresponding to the distance to the corner of the array, (C (0, 1.7)) – all co-ordinates given in mm. These points are imaged to just before the MO plane at: A' (0,0), B' (0, 2) and C' (0, 2.83) (see Figure 4-8). The position C corresponds to the furthest position of a micro-LED on a square array, which is calculated using its diagonal ($1.2.\sqrt{2} = 1.7$). The position at (1.2, 1.2) was not selected as Zemax transverse ray fan diagrams are calculated in x- and y- directions and therefore a measure on the same axis is more representative of the variation between on- and off- axis.

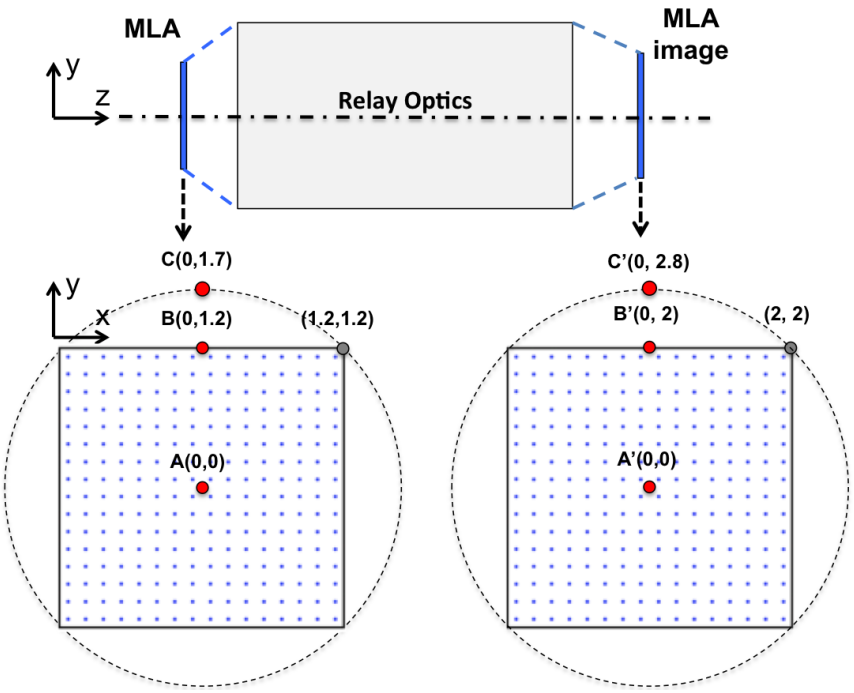

Figure 4-8: Technique to measure the quality of the imaging of the MLA with ROs

When designing an optical system, three important characteristics are tested that will be affected by aberrations: The homogeneity across the entire field, the efficiency of the system and the chromatic aberrations.

Homogeneity across the entire field: It is tested using mainly a Spot Diagram (SD), which provides a good visual indicator of the optical performance of the system in the image space.

Additionally, the geometrical and RMS spot radii are calculated at each field position. The geometrical spot radius only gives information about the one ray that is farthest from the reference point. The RMS spot radius is generally used as it provides an idea of the spread of the rays, since it depends on every ray. The RMS spot radius is defined as:

$$Spot\ Radius_{RMS} = \sqrt{\frac{\sum \Delta r^2}{N}} \qquad 4.1$$

Where Δr is the distance between each ray and the reference point and *N* the number of rays.
This objective is to achieve a relatively low RMS spot radius, which varies as little as possible over the entire field. The simulation of the optical relay system used in the proof of principle showed a 2.4 times difference between the centre and the edge of the array with a spot size going up to 40µm. This system is therefore not optimized for imaging the entire array.

Quality of the system: A ray fan can be used to evaluate the transverse ray aberrations (TRA) and a modulation transfer function (MTF) to evaluate the quality of imaging in an optical system.

The TRA indicates the transverse distance by which the ray misses the ideal intersection with the image surface, which is calculated using the paraxial theory. The horizontal axis in each diagram (*Py* or *Px*) corresponds to the pupil height along the *y*- or *x*-axis. The vertical axis, marked as *ey* or *ex,* stands for the transverse error along the y- or x- axis and defines how far from the z-axis a ray is at the pupil. It is one of the most useful representations of the aberration characteristics of an optical design. In Figure 4-9, the maximum scale was set at 100µm, as transverse ray aberrations stay below 100µm at a maximum distance of 100µm form the pupil centre. On- and off-axis aberrations such as spherical aberrations, astigmatism and coma can be seen.

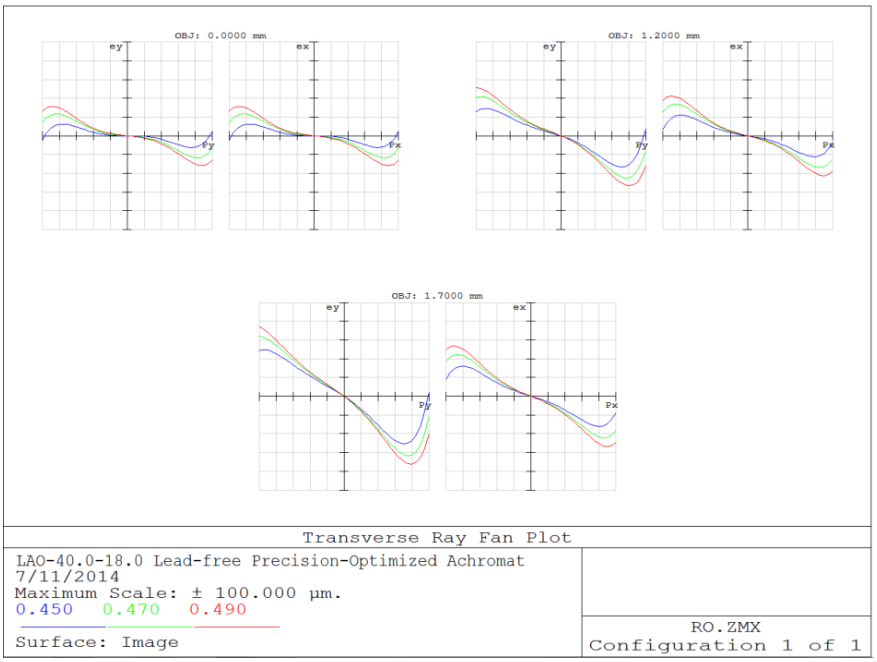

Figure 4-9: Transverse ray fan plots of the RO used within the proof of principle set-up

An MTF is a comprehensive tool that is appropriate to summarize the quality of the image that will be formed by the lens system. The MTF describes the spatial frequency response of an optical system. The modulation (or contrast) is the image contrast expressed in terms of a percentage of the object contrast (100% = white on black, 0% = grey on grey). If we have a pattern of given spatial frequency that is varying sinusoidally in intensity, the modulation can be expressed as:

$$Modulation = \frac{I_{Max} - I_{min}}{I_{Max} + I_{min}} \qquad 4.2$$

Where I_{max} and I_{min} are minimum and maximum intensities.

And the MTF can be expressed as:

$$MTF = \frac{Modulation\ in\ image}{Modulation\ in\ object} \quad 4.3$$

The spatial frequency of the lines in the image space is expressed in terms of line-pairs (cycles) per millimetre (cycles/mm). Calculating the inverse of this frequency gives the spacing of a line-pair in millimetres. The MTF graph shows how at increasingly higher spatial frequencies the modulation is decreased [130].

For a perfect circular lens, the MTF is defined in the following equation and in Figure 4-10:

$$MTF(v) = \frac{2}{\pi}(\phi - \cos\phi \,.\, \sin\phi) \quad 4.4$$

Where:

$$\phi = \cos^{-1}\left[\frac{\lambda v}{2NA}\right] \quad 4.5$$

The diffraction cut-off frequency, which is the maximum spatial frequency where an optical system can transmit information, is given in terms of the NA or the F-Number, N, by:

$$v_0 = \frac{2NA}{\lambda} = \frac{1}{\lambda \times N} \quad 4.6$$

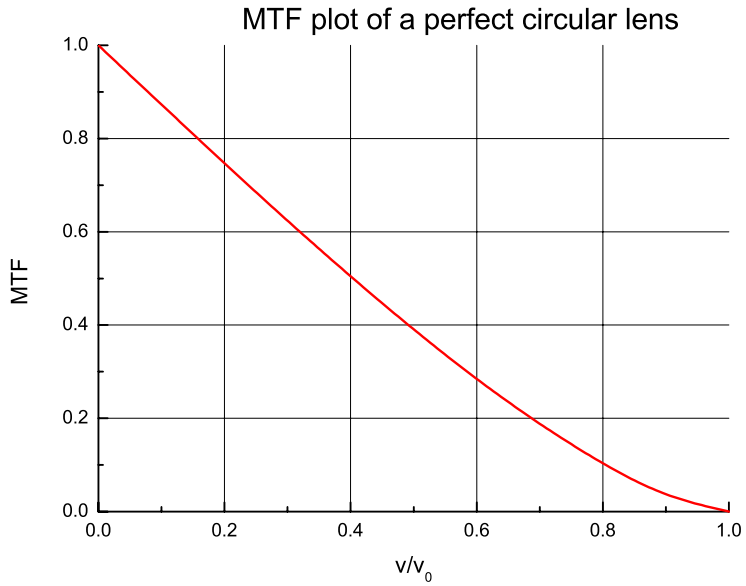

Figure 4-10: MTF plot for a perfect circular lens

A digital sensor, which is pixelated, also limits the resolution. Therefore, a practical resolution limit is generally slightly below the Nyquist frequency. This is defined as $1/(2 \times Pixel\ spacing)$. With the camera used, a Hamamatsu Orca ER, the pixel size is 6.45µm and therefore the Nyquist frequency is 77.5 lines per mm. A 10µm resolution or 50 lines per mm was fixed as the limit of study in this project.

Figure 4-11 shows the MTF, which goes down to 50% at 15 and 5 cycles per mm, demonstrating a low contrast for details smaller than 33 and 100µm at the center and edge of the array, and consequently, this low contrast will be seen on the camera.

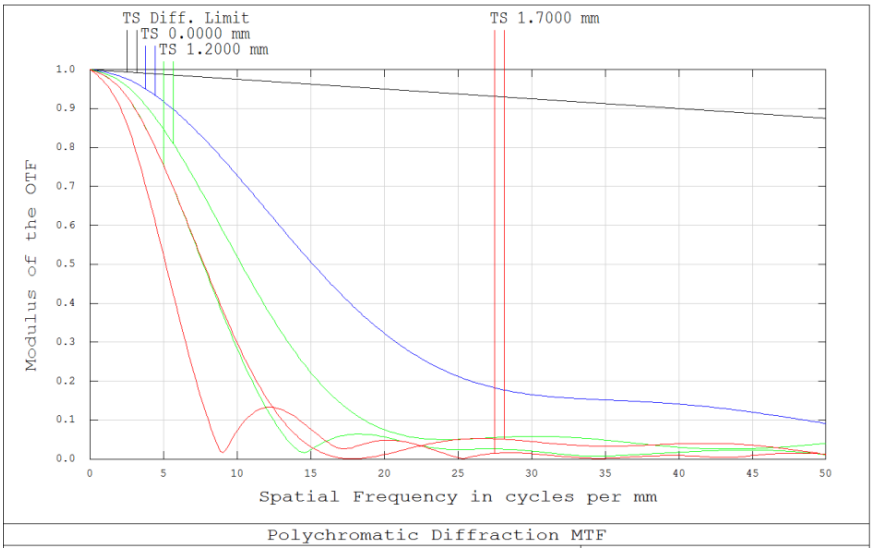

Figure 4-11: MTF of the relay optics used within the proof of principle set-up

Idealistically, the goal is to obtain a homogeneous image of each micro-lens along the entire micro-lens array, which may be difficult as the image of the MLA with the RO is very close to the MO. This means that for example, spherical aberrations may cause high variation of intensity inside each micro-lens, which would have been less important with the image of the MLA further away from them. Spot and TRA diagrams are used to assess the quality of the imaging and the MTF, to confirm it. The goal is to develop relay optics with similar performances along the entire array and therefore a control of the optical aberrations. With a MTF below 50%, details can't be distinguished. Therefore, the goal is to have an MTF at 50% at a spatial frequency close to the Nyquist frequency calculated above for the detector to visualize an image as sharp as could be distinguished by the camera.

Chromatic aberrations: Chromatic errors occur as a consequence of the dispersion of the optical materials for different wavelengths and therefore have a completely different origin and behaviour in comparison to monochromatic aberrations[128]. The longitudinal chromatic aberration occurs because usually materials exhibit higher index of refraction for blue light than for the red light and thus the lens system that has pronounced chromatic aberrations has different focal lengths for various wavelengths. For this project there was a need for an optical system that works for a 40 nm bandwidth (470nm ± 20nm) in order to use the entire output spectrum of the MLA efficiently. Therefore the Chromatic Focal Shift is also measured.

In Zemax, a Merit function is used to optimize the performance of the optical system by modifying variable parameters to reach a set of goals set in it. In this project, the goal is to image an array of micro-LEDs through relay optics with the smallest transverse ray aberration possible. The corresponding default merit function in Zemax is "*Sport Radius*" and defines part of the algorithm used. Weighted operands can also be added to specify other requirements to reach, such as magnification, telecentricity, etc… The lower the Merit function, the better the system performed.

4.2.3 Requirements

To develop ROs, the correct magnification is important as well as the control of the optical aberrations. Taking the considerations described in the previous sections into account the following requirements can therefore be fixed:

- The magnification and NA are set in order to fill the micro lenses (M = 1.667 and NA≥0.125)
- The angular full field of view (FOV) of the relay optics has to be kept low in order to reduce optical aberrations.
- The focal length of the lenses within the relay optics have to be kept small to limit the size of the system
- The lenses have to be nearly telecentric and have low distortion to obtain comparable images at the edge and center of the array, and then fill the MO homogeneously
- The image of the MLA at the entrance pupil of the microscope objective should be smaller than the pupil aperture in order not to lose light (see Chapter 3:).
- The cost has to be taken into account and thus off-the-shelf components are considered where possible

Note that the second and third requirement are interdependent and a good compromise has to be found between the two as the angular full field of view of the RO corresponds to the angle at which the maximum width of the MLA is seen by the lens L_1 at a distance f_{L1} (see Figure 4-12).

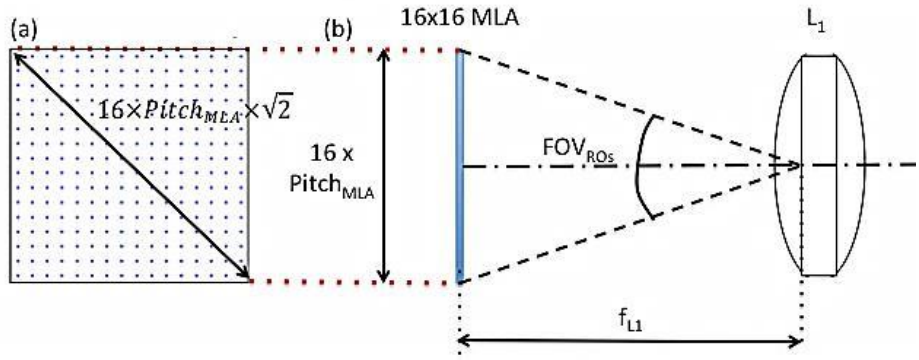

Figure 4-12: Schematic of the angular full field of view
(a)Front view of the MLA and (b) side view of the MLA and first lens of the RO

Mathematically, it is defined in the equation below:

$$FOV_{ROs} = 2 \times \arctan\left[\frac{\left(8 \times Pitch_{MLA} \times \sqrt{2}\right)}{f_{L1}}\right] \approx 2 \times \frac{\left(8 \times Pitch_{MLA} \times \sqrt{2}\right)}{f_{L1}} \quad 4.7$$

Where f_{L1} represents the focal distance of the first lens within the relay optics, $(8 \times Pitch_{MLA} \times \sqrt{2})$ half the diagonal of the entire MLA. Equation 4.8 gives a result in radians and a factor of $(180/\pi)$ must be used to convert this angle to degrees instead. In our project, the pitch of the MLA is 150µm.

For the purpose of our system we have considered three different options:

F_{L1} (mm)	30	60	100
FOV_{RO} (°)	6.48	3.24	1.94

Table 4-3: FOV_{RO} calculated for different lens focal distances

4.2.4 Plausible design solutions

Two directions were taken:

1. To find an already developed solution using lenses from Sill Optics (as had previously been used[60]).
2. To develop our own solution based on the required parameters, such as the FOV and the NA to identify what optical layout might show an acceptable result.

A very useful rough visual guide to the performance of various optical lens system design types is shown in Figure 4-13 [100], [128]. In this case, when selecting the initial layout we are aiming to use a minimal number of optical elements and still have enough degrees of freedom to compensate for the main aberrations.

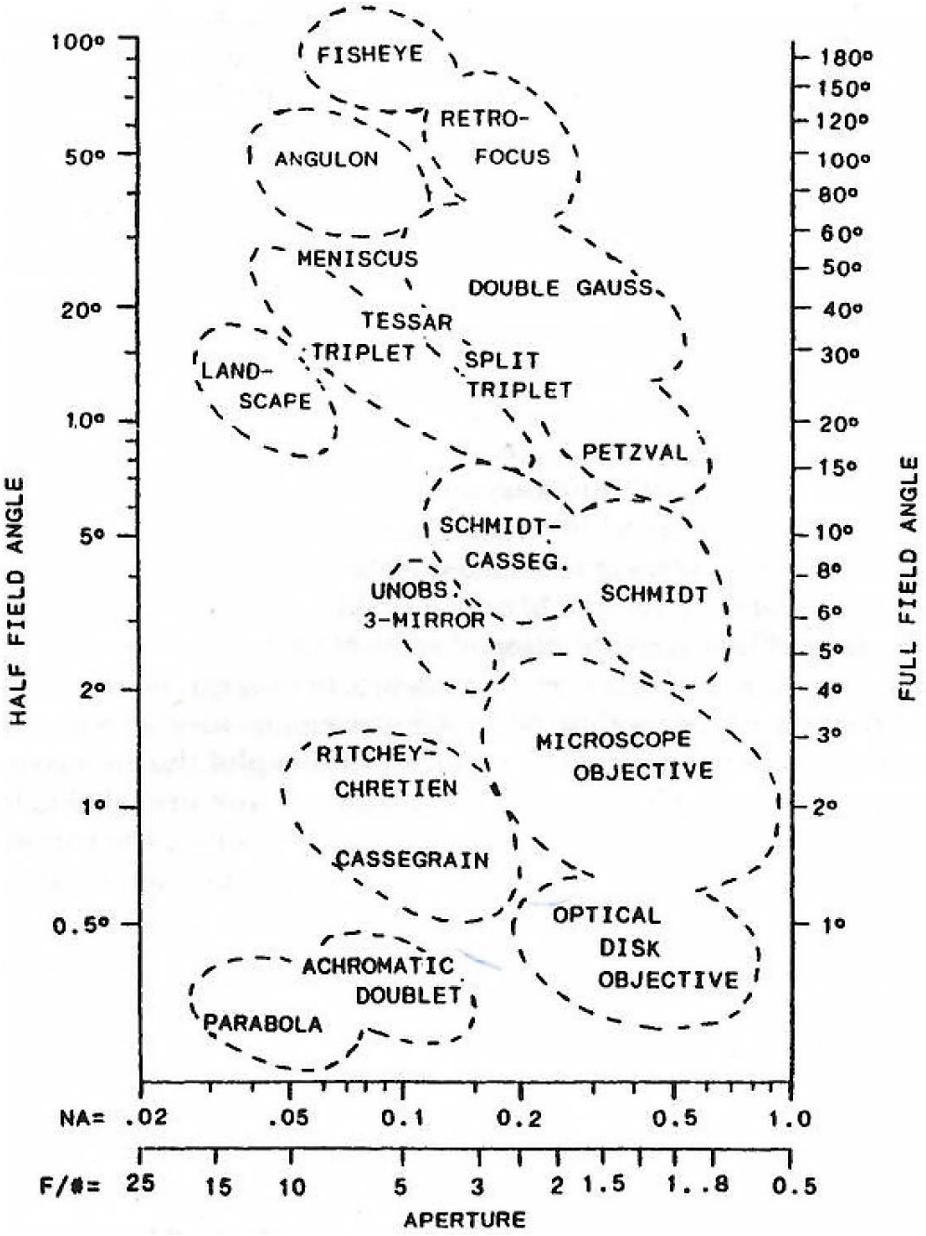

Figure 4-13: Map showing design types commonly used for various combinations of aperture and the field of view [128]

The NA required at the micro-lenses is 0.125, which means that at the entrance pupil the NA equals 0.125 × 1.667 = 0.208. From the schematic above, the microscopic objective design type looks like the best solutions[128]. The simplest development of a microscope objectives from a single achromatic doublet is to add an aplanatic-normal meniscus lens, which allows the NA to be multiplied by the refractive index of the meniscus lens without adding any spherical aberration or coma [100].

In the proof of principle described in Section 4.2.1 only 2 achromatic doublets were used but the design was shown to have its limitations. As a next development an improvement in its optical characteristics are considered by using two "off-the-shelf" achromatic doublets with a magnification M = 1.67 combined with two identical aplanatic meniscus lenses. This ensures that the magnification M is kept the same whilst the NA at each end of the relay is increased by the refractive index of the aplanatic meniscus lenses.

4.2.5 Optical design theory

As described in Section 4.2.2 the Seidel aberrations were described as a way to help quantify the geometrical optical aberrations and therefore the quality of the optical system. Having established that a combination of 2 meniscus lenses and 2 achromatic doublets will form the RO, a number of other aspects have to be considered for the optical design. Below the influence of the focal length of the lenses in the RO and their refractive index is explained, as well as the reason behind the use of aplanatic meniscus lenses.

Influence of the focal length of the achromatic doublets on the aberrations

The focal length of the lenses used in the RO influences the observed aberrations. For a given NA and field image height, low aperture and low field angle cannot be obtained at the same time (see Table 4-1). For example, a 0.21 NA, 30 mm focal length lens will have a 12.5 mm diameter compared to 25 mm for 60 mm focal length.

Choice of a glass Type

There are many types of glass (see A.4), but these are broadly split according to their dispersion properties:

- *Crown glass*: A low dispersion glass with V-Value above 50 when n is higher than 1.6 and above 55 when *n* is lower than 1.6
- *Flint glass*: A high dispersion glass ($V < 50$) for *n*>1.6 or ($V < 55$) for $n < 1.6$.

From the formula of the Bending, the Conjugate and the Seidel coefficients S_I (Spherical Aberration), S_{II} (Coma), S_{III} and S_{IV} (Field curvature and astigmatism), S_V (astigmatism) C_I and C_{II} (longitudinal and transverse chromatic aberrations) [100], it can be derived that with a higher refractive index, the monochromatic aberrations S_I , S_{II} , S_{III} , S_{IV} and S_V are decreased and the polychromatic ones (C_I and C_{II}) increased, when the dispersion is increased. This means that generally, Flint glass will be better for correcting monochromatic aberrations but worse for correcting chromatic aberrations when compared to crown glass. A high refractive index crown glass with an identical refractive index to a flint glass will have a lower dispersion and therefore be more appropriate for a polychromatic system.

Aplanatic-normal meniscus lens

Meniscus lenses can be shaped so that no additional spherical aberration or coma is introduced into the system. The first surface of the lens is aplanatic and refracts a beam of light perpendicularly to the second surface, where no refraction therefore occurs. This shape is called the aplanatic-normal form. The magnification is then equal to the reciprocal of the material index of refraction. The parameters are therefore dependent on the first surface, which is aplanatic (see Figure 4-14).

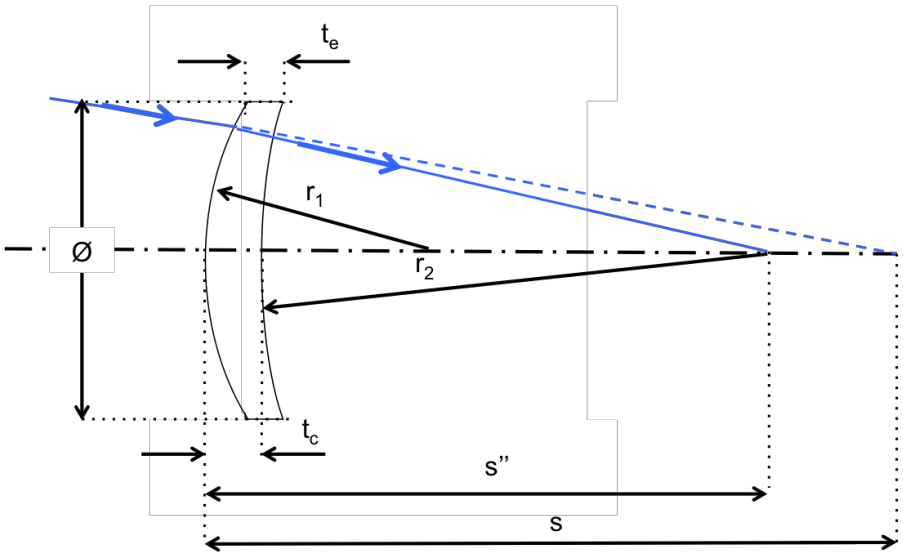

Figure 4-14: Aplanatic meniscus lens with index of refraction n

A positive aplanatic meniscus lens has a front radius given by:

$$r_1 = \frac{s}{n+1} \qquad 4.8$$

The image position *s''* can be deduced:

$$\frac{n}{s''} - \frac{1}{s} = \frac{1}{f} = \frac{n-1}{r} = \frac{n^2-1}{s} \Longrightarrow \frac{n}{s''} = \frac{n^2}{s} \Longrightarrow s'' = \frac{s}{n} \tag{4.9}$$

The Magnification *M* is then:

$$M = -\frac{1}{n} = \frac{s''}{s} \tag{4.10}$$

The second radius of the meniscus lens is given by:

$$r_2 = s'' - t_c \tag{4.11}$$

The focal distance of the meniscus lens was calculated using the thin lens and thick lens theory in A.5. The second model was used develop custom aplanatic meniscus lenses[130].

Table 4-4 shows how optical aberrations change for an achromat with either a fix aperture or a fix imaged NA when an aplanatic meniscus lens is used. If the same lens aperture is used without and with an aplanatic meniscus lens, then the lateral ray aberrations are reduced by a factor of the magnification $M = n$. However, the field of view is increased by an identical factor $M = n$ that might increases the other aberrations depending on the field angle only. If an identical image NA is looked for, the aplanatic meniscus lens will allow to use a smaller lens aperture. Lateral ray aberrations and coma are therefore diminished and distortions are increased.

Optical aberration	**Aperture dependence**	**Field angle dependence**	**Operation at same lens aperture**	**Operation at same image NA**
Lateral spherical	ϕ^3	1	$\div n$	$\div n^4$
Spherical (S_1)	ϕ^3	1	1	$\div n^4$
Coma (S_2)	ϕ^2	θ	$\times n$	$\div n^2$
Astigmatism (S_3)	ϕ	θ^2	$\times n^2$	1
Field Curvature (S_4)	ϕ	θ^2	$\times n^2$	1
Distortion (S_5)	1	θ^3	$\times n^3$	$\times n^2$

Table 4-4: Variations of Aberrations with Aperture, Field Angle, an identical lens aperture or image NA used without and with an aplanatic meniscus lens

Table 4-5 shows where aberrations appear at each surface of the aplanatic-normal meniscus lens and how they vary over the entire lens. While this lens does not add any spherical or coma itself it can add significant astigmatism and field curvature, and as a singlet will certainly add chromatic aberration. The characteristics of the lens such as focal distance and material characteristics (refractive index n and Abbe parameter V) determine the quantity of aberrations added. A longer focal length means less achromatic aberrations. A higher dispersion (higher V) decreases the chromatic aberrations.

Optical aberration	Aplanatic surface	Zero Marginal ray (beam normal to the surface)	Aplanatic-Normal meniscus lens
Spherical (S_1)	0	0	0
Coma (S_2)	0	0	0
Astigmatism (S_3)	0	- (Field curvature)	$\div f$
Field Curvature (S_4)	≠ 0	≠ 0	$\div f$
Distortion (S_5)	≠ 0	≠ 0	$\div f^2$
Chromatic (Axial) (C_1)	≠ 0	0	$\times f/V$
Chromatic (Lateral) (C_2)	≠ 0	≠ 0	$\times f/V$

Table 4-5: Variations of Aberrations of an aplanatic-normal meniscus lens at each surface of the lens and for the lens itself

4.3 Conclusion

There is a variety of off-the-shelf MO on the market, however, only a few suit our application. The replication process allows the manufacturing of square lenses with spherical shapes and fill-factors close to 100%. NAs high enough are needed to improve the collection efficiency at the MLA plane. Additionally, the thinnest substrate on which off-the-shelf MO are replicated is 1mm thick. RO are therefore necessary to magnify the image of the MLA and place it at the focal distance of the MO, which may be inside the substrate if the NA is high enough. RO magnify the image of the MLA by a factor M on the MO side. However collecting more light means increasing the NA and potentially adding more optical aberrations, which need to be corrected. Therefore a compromise was chosen between improvement of the collection efficiency and the possible amount of optical aberrations. A micro-lens array with 250µm pitch and 0.125 NA was selected.

A simple optical relay system was prepared to demonstrate the feasibility of such a system, demonstrating the restrictions as well. RO have to follow specific requirements such as an exact magnification (1.67), a NA of at least 0.21 on the MLA side, telecentricity etc. and must have optical aberrations controlled to obtain a correct patterning of the MLA and a homogeneous filling of the MO from centre to edge.

With all these parameters in mind, and considering cost, an optical design was selected as the base for RO development. Achromatic doublets coupled with aplanatic meniscus lenses allow for an increase of the NA similar to the refractive index of the meniscus lens without adding either spherical aberration or coma.

In the next chapter, the multiple steps to develop and implement this reference design into a first PO system, called “PO 1” are described.

Chapter 5: Design and implementation of the basic design: "PO 1"

After having proven the feasibility of the concept and having established the basic requirements for the design of the system in the previous chapter, the development of a PO made of a RO system based on a microscope objective design made of achromatic doublets and aplanatic-normal meniscus lenses (see Figure 4-13), coupled with MO is described. A solution based on lenses that are available on the market and easy to implement is first shown. Then the methods to develop an in-house design are explained. Modelling is used to demonstrate the advantages of meniscus lenses with the development of their characteristics to obtain the best results over the entire field. Finally, the set-up "PO 1" is implemented and tested to confirm the modelling results, including a number of experiments on biological samples.

5.1 Off the shelf RO design

The characteristics and costs of the design selected were compared using an Optical design Software (Zemax[131]), and lens data provided by the supplier. The system was set at $M = 1.667$, $NA = 0.125$ (on the MO side), telecentricity and length (≤ 300mm).

The company Sill Optics[132] was identified as a good candidate for the provision of suitable off the shelf lenses. It has two CCD lenses with high resolution and designed for infinity that can be used in nearly telecentric condition (S5LPJ1446 and S5LPJ1475). They have 46 and 75mm focal distances and their f-number is 1.4, which corresponds to $NA_{Max} = 1/(2 * f_{\#}) = 0.36$. Modeling was done with a protected design called Black box design in Zemax. This means that the models of the two CCD lenses can be used to simulate a relay optical system, however, the specific design of each lens can't be seen and/or modified.

Figure 5-1 shows the Spot Diagrams for the RO based on the CCD lenses from Sill optics. The root mean square (RMS) spots at the three points measured have an average of 7.5µm with a standard deviation (STD) below 0.2µm (see Table 5-3).

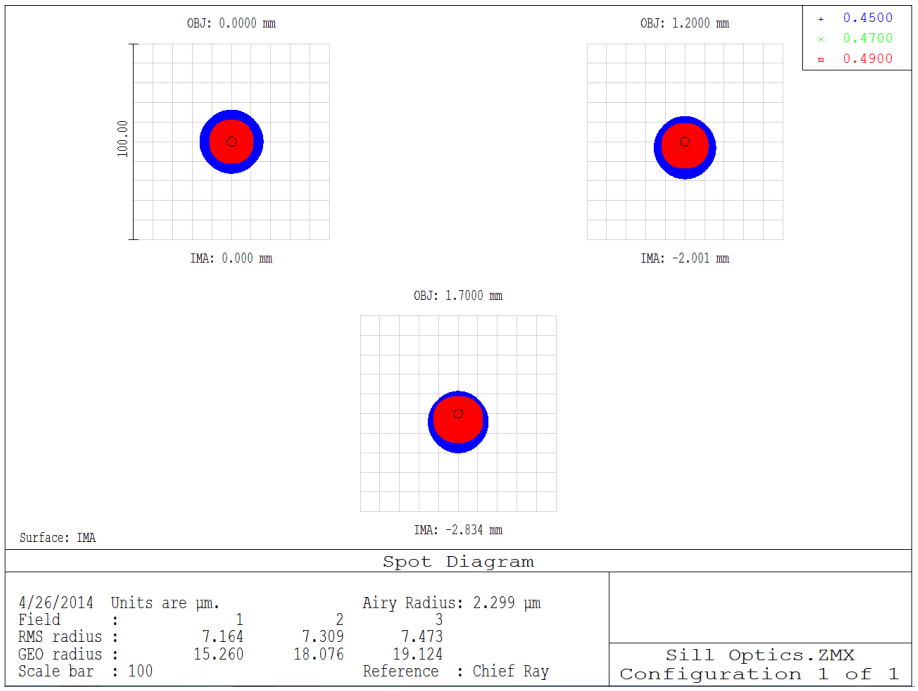

Figure 5-1: Sill Optics Relay Solution Modelling Results: Spot Diagram
These spot diagrams are for fields at the center and at the edge of an imaged array. The imaging is homogeneous along the entire array with a RMS radius around 7.32±0.15µm

The homogeneity over the entire field is also noticeable on the ray fan and MTF diagrams with no significant differences between the measured points (see Figure 5-2 and Figure 5-3). The MTF is around 60% at 30cy/mm. The main aberrations are spherical aberration (SA) and distortion. The modelling reveals that the distortion is far below 0.1% (~0.01%) at the edge of the field of view. There is also a slight Coma, which is off-axis.

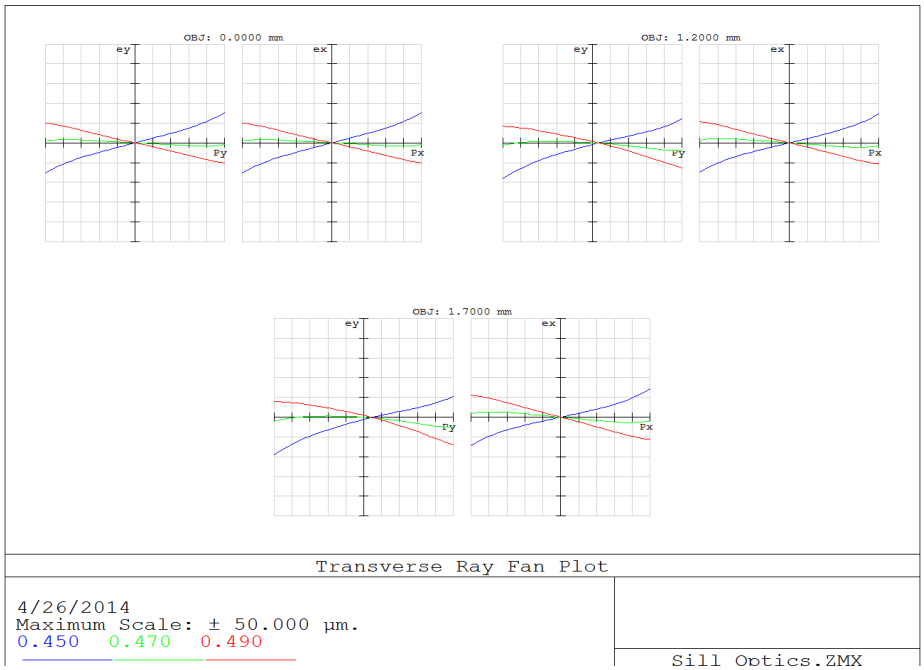

Figure 5-2: Sill Optics Relay Solution Modelling Results: Ray Fan
Transverse ray fan plots at the center and edge of the image. The optical aberrations do not change over the entire field. This is optimized for 470nm. At the other wavelengths, SA and field curvature are noticeable

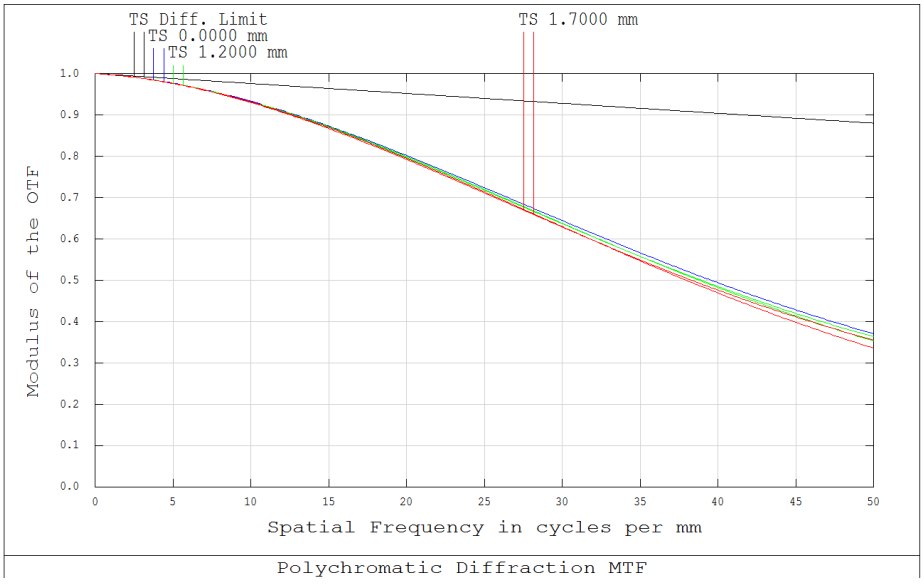

Figure 5-3: Sill Optics Relay Solution Modelling Results: MTF
The MTFs along the entire field are above the reference criterion (50% at 30lpm and 30% at 50lpm)

The monochromatic requirements are reached with this solution, however Figure 5-4 shows that chromatic aberrations are high (~169µm) as these lenses are optimised for the entire visible spectrum or for use at longer wavelengths than 470nm.

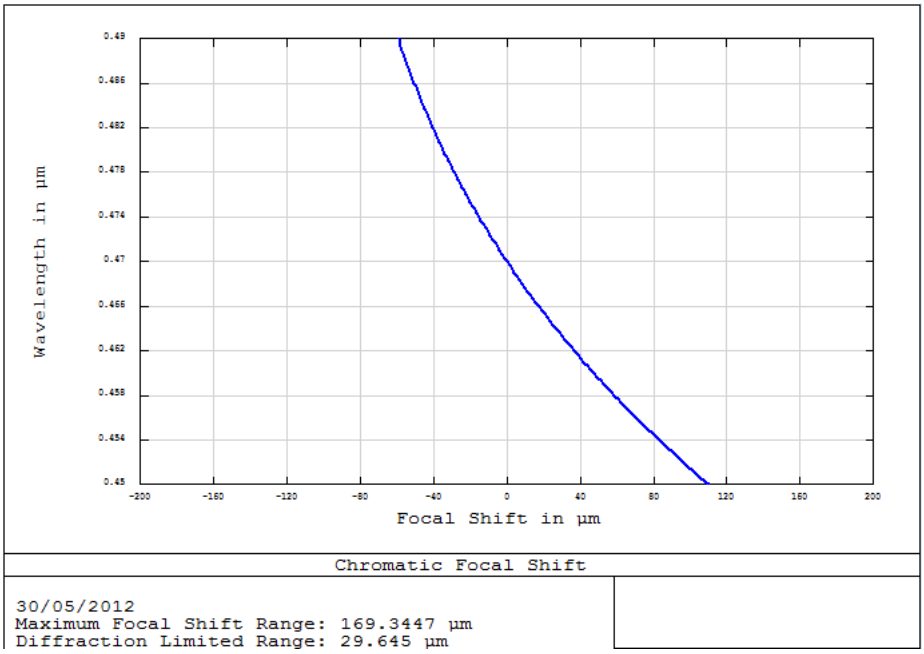

Figure 5-4: Sill Optics Relay Solution Modelling Results: Chromatic Focal Shift
The CFS is large for a 40nm bandwidth monochromatic source.

This off-the-shelf solution proves to be suitable for applications in the visible spectrum or at longer wavelengths with a good control of the aberrations but not at the wavelengths used in this project, where chromatic aberrations are high. However, the cost is high (~£2000), which justifies the development of an in-house design that would cost less, be optimised for 470nm and if possible has even less optical aberrations.

5.2 In-house optical design of ROs

The development of an in-house design necessitated optical modeling in Zemax, construction and testing. The process was separated into several steps, which are presented here. Firstly, optical systems are compared with achromatic doublets coupled without and with aplanatic-normal meniscus lenses. Secondly, the final design is simulated. Thirdly, the complete final design is modeled with micro-lenses, implemented and compared to the experimental results. Finally, a few experiments and results with a biological specimen are shown.

5.2.1 RO with and without aplanatic-normal meniscus lenses

A 60-100 mm focal length system of achromatic doublets was chosen as it gave a good compromise in terms of aberrations (see Figure 5-8(a)), being dominated by neither spherical and coma nor astigmatism and field curvature. Additionally, it has already been shown that their performance can be improved, with the addition of aplanatic-normal meniscus lenses. These require a distance s from the original focus point: $BFL_{Lens} \geq s_{Meniscus}$, where BFL_{Lens} is the back focal length of the original achromatic doublet lens (see Chapter 4:). A pair of achromatic doublets from CVI-Melles-Griot (01LAO479 and 01LAO524) was selected because of its higher performances across the field over other available lenses. Note that a compromise had to be made between performances on and off axis. The back focal length of the 60mm focal length achromatic doublet is 53.5mm. A minimum space of 1mm is necessary between the aplanatic-normal meniscus lens and the achromatic doublet. Therefore the custom meniscus lens should have an object distance $s \leq 52.5$ mm. The 100mm focal length achromat, however, has a back focal length of 95.5mm and so here the meniscus should have an object distance of $s \leq 94.5$ mm. Both meniscus lenses should be made from the same glass so that the same increase in NA is achieved at each end of the relay.

Inserting an aplanatic-normal meniscus lens ensures that the same NA at the object or image plane is maintained but this then leads to a smaller illuminated area on the achromatic doublets and therefore reduces spherical aberration (SA) and coma (see table 4.2 and Table 4-4). Alternatively the aplanatic-normal meniscus lenses can be used to increase the NA of the system by maintaining the same illuminated area on the achromats. In this case the NA is increased to $NA_{with\ ML} = n_{ML}.NA_{Without-ML}$. The quantity of SA and coma wavefront aberrations is not increased, though the transverse SA ray aberration is decreased by a factor n_{ML} because of the change in magnification at the object and image planes. However, in both cases the meniscus lens can add aberrations of its own such as curvature of field, astigmatism, distortion and chromatic aberrations.

Here, first the achromatic doublet with f = 60mm is compared without and with an aplanatic-normal meniscus lens made with the crown glass N-BK7 for an identical aperture. Then, the RO without these meniscus lenses at $NA_{without\ ML} = NA_{RO\ with\ ML}/n_{ML} = \frac{0.208}{1.523} = 0.137$ is compared to the RO with meniscus lenses respecting the aplanatic-normal conditions at $NA_{RO\ with\ ML}$ = 0.208. The RO is optimized for telecentricity. Two identical meniscus lenses were used on each side of the system to keep the same system magnification and the cost of manufacturing low. These comparisons are done to verify how the aberrations vary when an aplanatic-meniscus lens is added and the aperture kept constant.

In the first set-up, the achromatic doublet with f = 60mm, used in the RO, is compared without and with an aplanatic-normal meniscus lens. The same 20mm aperture, wavelengths (450, 470, 490nm) and image positions (0, 1.2mm, 1.7mm) are used (see Figure 5-5).

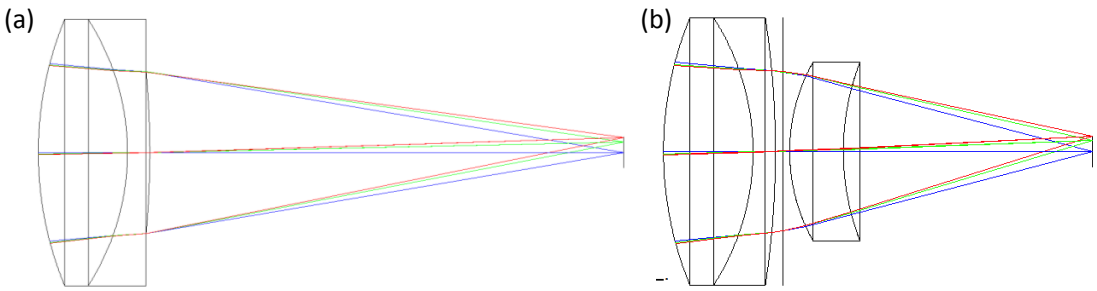

Figure 5-5: Schematic of an achromatic doublet (f = 60mm) without and with an aplanatic-normal meniscus lens

Figure 5-6 shows the ray aberrations at the three image positions. Spherical aberrations are the main aberrations here. There is also a small amount of coma, astigmatism and field curvature, which causes the ray fan to rotate in x and y, when measured off-axis (field curvature), and to be slightly modified in the y direction (coma and astigmatism).

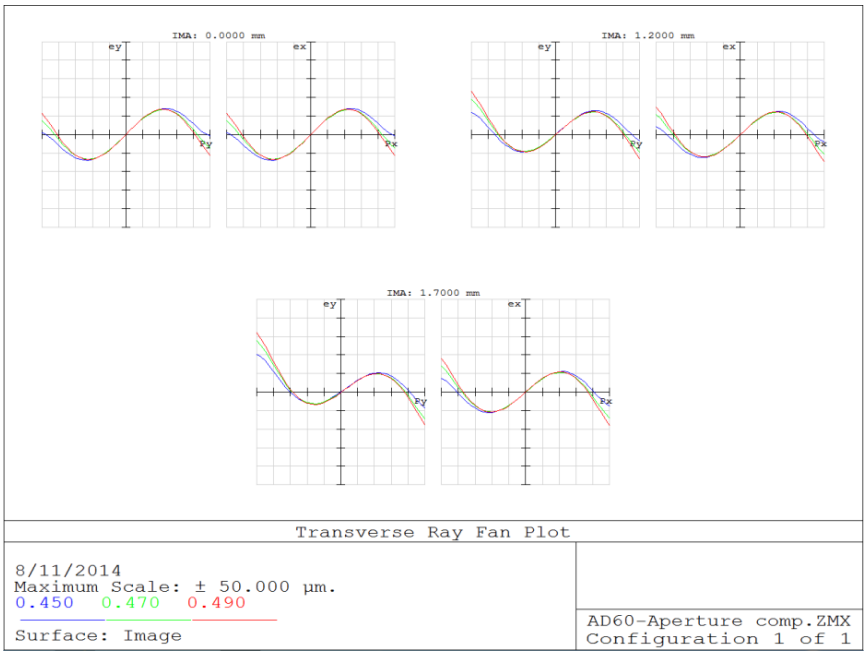

Figure 5-6: Ray diagrams for the f = 60mm achromatic doublet at 0, 1.2 and 1.7mm from the center

Figure 5-7 shows the ray diagrams of the same achromatic doublet coupled with an aplanatic-normal lens at identical image positions. The quantity of spherical aberrations is nearly unchanged as expected. However, the other achromatic aberrations are increased. The effect of astigmatism, coma and field curvature can be seen off-axis. Chromatic aberrations are also higher. The diagrams for each wavelength are now completely distinguished from each other.

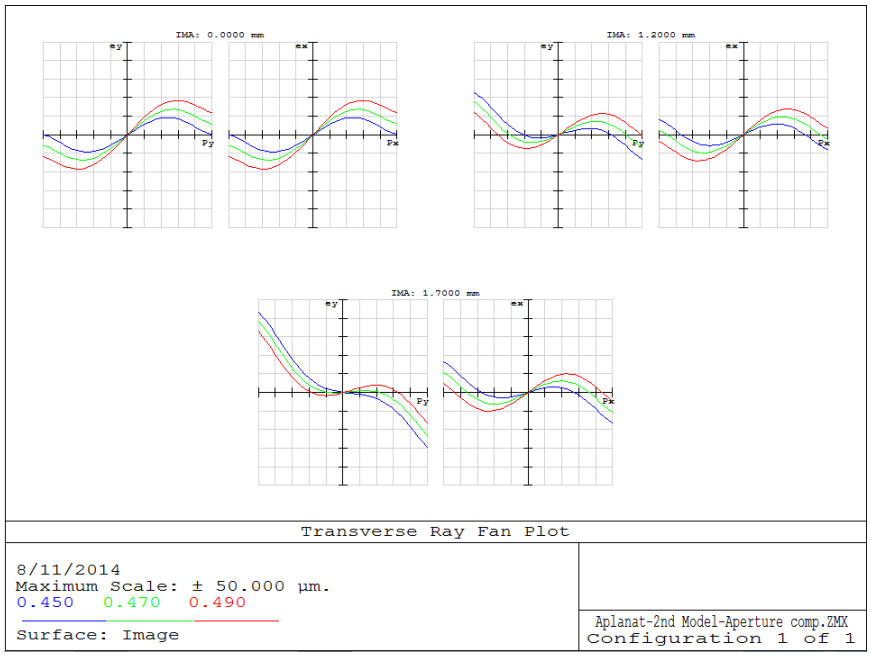

Figure 5-7: Ray diagrams of the f = 60mm achromatic doublet coupled with an aplanatic-normal meniscus lens at 0, 1.2 and 1.7mm from the center

Table 5-1 shows the variations of optical aberrations for the achromatic doublet between the two optical systems obtained using modelling in Zemax and the Seidel equations (see also Table 4-4). The variations match, when the lens is at the stop.

Ray aberration	Zemax - Modelling	Seidel equations - Theory
Lateral Spherical	0.656	$\div n$
Spherical (S_1)	1	1
Coma (S_2)	1.525	$\times n$
Astigmatism (S_3)	2.327	$\times n^2$
Field Curvature (S_4)	2.327	$\times n^2$
Distortion (S_5)	3.551	$\times n^3$
Chromatic (Axial) (C_1)	1.005	1
Chromatic (Lateral) (C_2)	1.526	$\times n$

Table 5-1: Variations of Aberrations of an achromatic doublet (f = 60mm) without and with an aplanatic-normal meniscus lens

The aplanatic-normal meniscus lens also adds aberrations such as astigmatism, field curvature, distortion and chromatic aberrations (see Table 4-5). Spherical aberrations are not added by the meniscus lens as expected; however, the increase of the other aberrations may deteriorate the off-axis behavior of this system at large aperture.

Figure 5-8 shows the schematic of relay optics using the two achromatic doublets selected, coupled and optimised together without and with meniscus lenses respecting the aplanatic-normal condition to obtain a telecentric optical system with a magnification *M = 1.67*. With meniscus lenses, the total length of the system is decreased as the focal distance of each lens group containing each an achromatic doublet is decreased by n_{ML}.

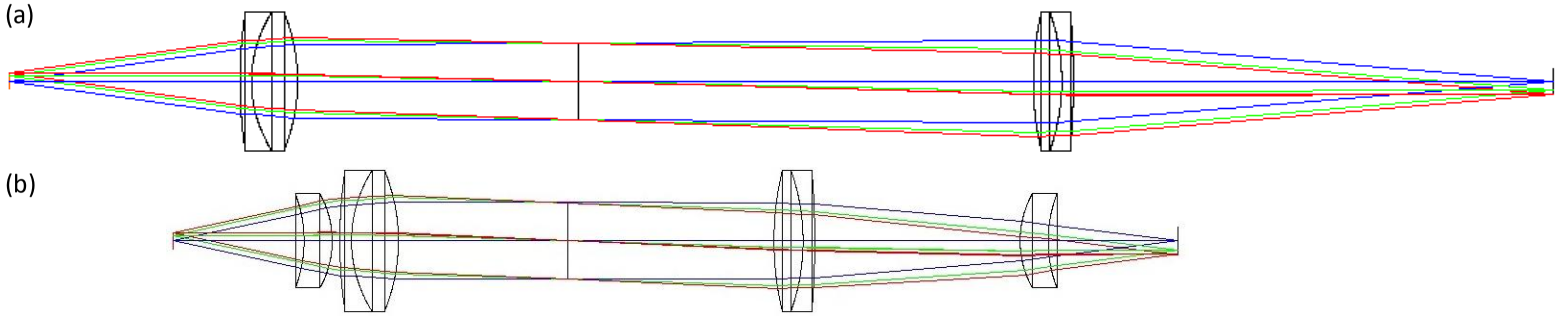

Figure 5-8: Layout of the RO without (a) and with aplanatic-normal meniscus lenses using N-BK7 glass (b)
A meniscus lens was coupled with each achromatic doublet on (b), respecting first the aplanatic condition to increase the NA by the refractive index of the meniscus lens without adding SA and coma. Then, the meniscus lenses positions are optimized away from the aplanatic condition to provide with homogeneous imaging along the entire field

Figure 5-9 shows the ray diagrams for object positions 0, 1.2 and 1.7mm and therefore their corresponding images positions, *M=1.67* times higher. The amount of spherical aberrations is of the same scale than with the achromatic doublet modelled in Figure 5-5(a), as this lens introduces most of the spherical aberrations. A shorter focal distance means a shorter radius of curvature, which then causes more aberrations such as spherical ones.

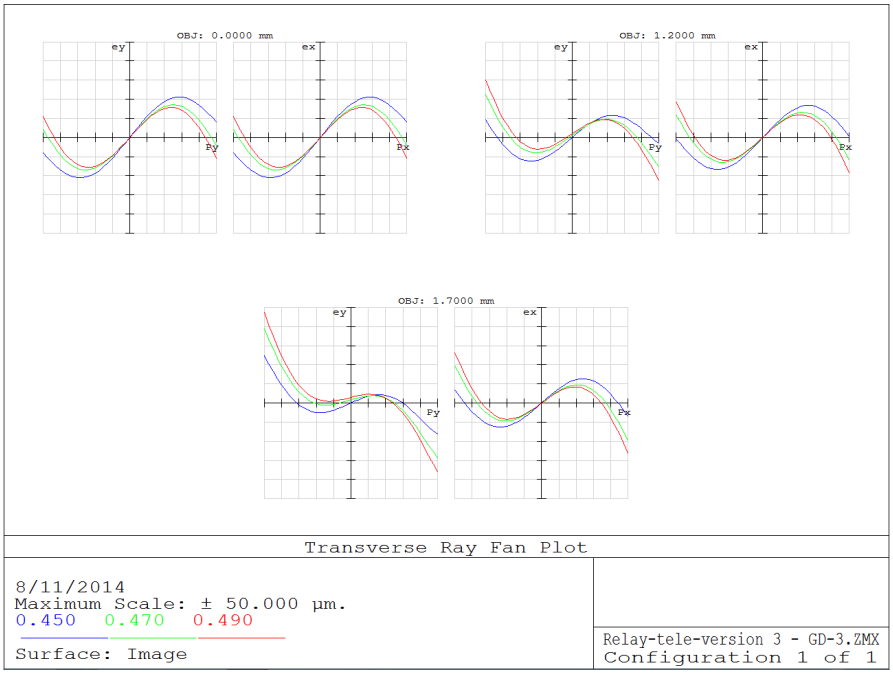

Figure 5-9: Ray diagrams for the relay optics without meniscus lenses

Figure 5-10 shows the ray diagram when the achromatic doublets are coupled with an identical meniscus lens respecting the aplanatic-normal condition. The distance between the two achromatic doublets was optimised for telecentricity. On-axis achromatic aberrations are very close, as neither the achromatic doublets nor the meniscus lenses should add spherical aberrations. However, chromatic aberrations are increased. Off-axis aberrations are also increased to more than 50µm.

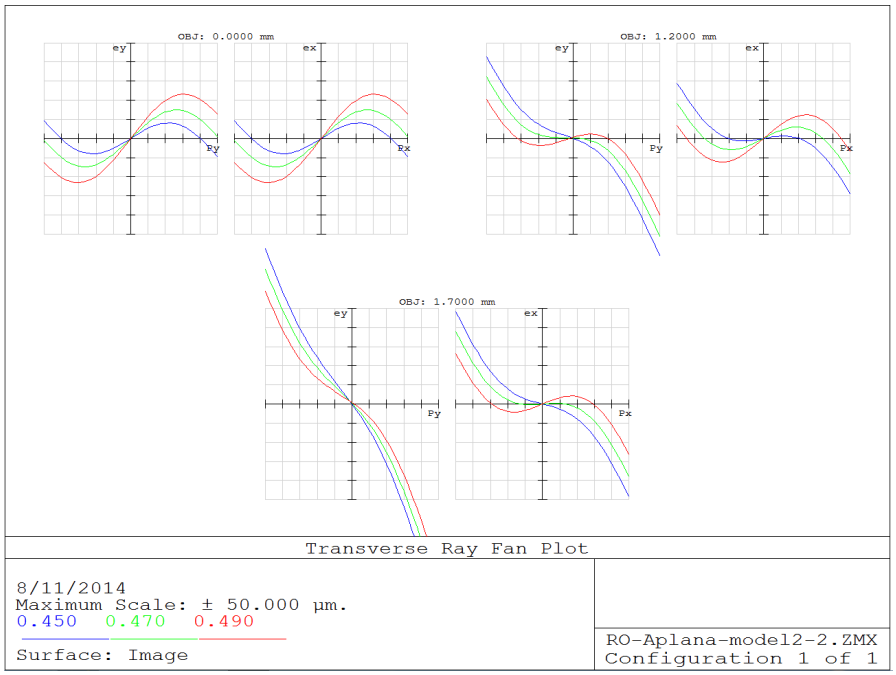

Figure 5-10: Ray diagrams for the relay optics with aplanatic-normal meniscus lenses

Table 5-3 shows the aberration differences of the achromatic doublets between the two systems. The modifications of the aberrations differences, such as coma, astigmatism, distortion and lateral chromatic, are the result of the shift of the stop relative to each surface [100]. The stop was moved during the optimization of the relay optics telecentricity. The other aberrations are close to the values expected, as the differences should not change with the stop shift. The noticeable small differences are caused by a small increase of the beam height at the first achromatic doublet surface.

Ray aberration	Zemax - Modelling	Seidel equations - Lens at the stop	Seidel equations – Lens away from the stop
Lateral Spherical	0.783	$\div n$	-
Spherical (S_1)	1.201	1	-
Coma (S_2)	9.100	$\times n$	$\neq 0$
Astigmatism (S_3)	1.933	$\times n^2$	$\neq 0$
Field Curvature (S_4)	2.353	$\times n^2$	-
Distortion (S_5)	3.68	$\times n^3$	$\neq 0$
Chromatic (Longitudinal) (C_1)	0.810	1	-
Chromatic (Axial) (C_2)	0.482	$\times n$	$\neq 0$

Table 5-2: Variations of Aberrations of two achromatic doublets (f = 60mm and f = 100mm) without and with identical aplanatic-normal meniscus lenses

The previous simulations in Zemax agree with the theory explained at the end of chapter 4. It also shows that an aplanatic-normal meniscus lens can improve the NA collected by an achromatic doublet by its magnification $M = n$ for an identical lens aperture filled without adding any spherical aberrations and coma. However, other aberrations, which have an effect on off-axis behavior, are increased at the achromatic doublet and added by the aplanatic-normal meniscus lens. In the relay optics, aberrations, such as coma, astigmatism, distortion and axial chromatic, are dependent on the position of the stop and therefore its position has to be taken into account when optimizing the system.

The relay optics coupled with aplanatic-normal meniscus lenses allow to collect more light and decrease the system size without adding any spherical aberrations. However, other aberrations are not well controlled. The system performance on and off axis depends on parameters such as the meniscus lens material, focal length, the position of each lens and the position of the stop. In the next section, an in-house design is modeled by optimizing these parameters.

5.2.2 In-house design final optimization

Meniscus lens characteristics

The meniscus lens has a high influence on the optical relay optics behavior. The choice of its material and focal distance determines how it may fare. As outlined in 4.2.5, crown glass lenses have generally smaller refractive index than flint glass lenses but larger Abbe number. They are better at correcting chromatic aberrations (see Table 4-5) but not as good as correcting the monochromatic ones. A crown glass such as N-LAK7 with a refractive index of 1.661 at 470nm of the same scale of flint glasses was therefore chosen as it combines the advantage of the two types of glass with a better monochromatic behavior as well as an optimised polychromatic behavior. Table 4-5 shows also that a higher focal distance decreases monochromatic aberrations but increases chromatic ones.

The complete bandwidth of the micro-LED array is roughly 40nm with a peak at 470nm. It is not monochromatic, but the bandwidth is not large either. The main priority is to decrease the monochromatic aberrations as much as possible and then control the chromatic aberrations in order for them not to be visible.

Optical relay design

The design was modified and optimized to obtain the best behavior on and off axis at $NA = 0.208$ when using the same aperture of the achromatic doublet than the system without an aplanatic meniscus lens with *NA = 0.208/n_{ML}*. Parameters like the distances between the achromatic doublets and the meniscus lenses were modified, moving away from its original aplanatic position, and the pupil positions were adjusted to maintain telecentricity in object and image spaces. The maximum total length of the RO was set at 200mm because of space restrictions on our partner's microscope platforms.

During optimisation, the N-LAK7 meniscus lens should have been designed with the highest focal distance possible to be able to respect the aplanatic-normal condition and being set as close as possible to the achromatic doublet (1mm). However, due to a miscalculation, it was designed with a slightly lower focal distance (79.4mm instead of 92.3mm) and had to be set at ~10mm from the achromatic doublet with the shortest focal distance achromatic doublet (f = 60mm). It was noticed after the custom meniscus lenses were ordered and therefore were used during the optimisation. Figure 5-11 shows the final design of the RO that is then coupled with a micro-lens array to form the projection optics (PO 1).

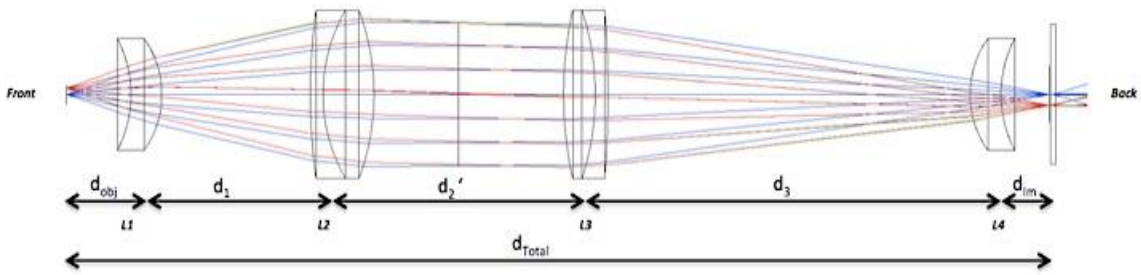

Figure 5-11: Layout of the RO design

Table 5-3 shows that the RMS spot radiuses in this design are lower the ones in the original set-up with aplanatic-normal meniscus lenses seen in 5.2.1. Its standard deviation is also much lower. This demonstrates the performances of the RO on and off axis. The performances are similar to the relay optics without meniscus lenses and at a NA *n* times larger.

Relay Optics	Numerical Aperture (NA)	Average RMS spot radius (µm)	Maximum on transverse ray fans (µm)	Chromatic Focal Shift (µm)	MTF(%) at 30 cy/mm	Maximum Distortion (%)
Sill Optics	0.208	7.32±0.15	20	169	60	0.01
CVI-MG (NA/(n(N-BK7))	0.136	13.62±2.68	50	88	10	0.35
CVI-MG (NA/n(N-LAK7))	0.125	11.59±2.66	40	88	20	0.35
CVI-MG & N-BK7 meniscus lens in aplanatic-normal condition	0.208	23.16±8.80	75	242	0	0.25
PO 1 (N-LAK7 ML)	0.208	11.33±1.6	40	77.6	23	0.04

Table 5-3: Summary of relay optics modelling results

Figure 5-12 shows the spot diagrams obtained on and off axis. The average spot radius is larger than the ones from the Sill Optics RO and less homogeneous on and off-axis (see Figure 5-1).

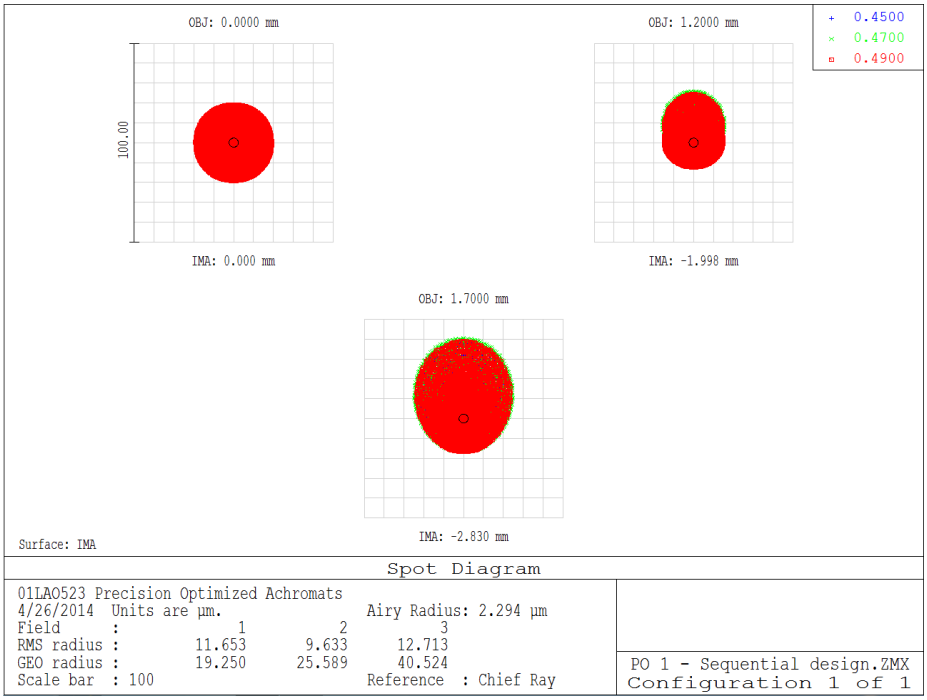

Figure 5-12: RO analysis: Spot Diagram
The average RMS spot radius is 11.3±1.6µm over the entire field.

In Figure 5-13, SA is visible as well as field curvature as the curves are identical on x- and y- off-axis diagrams, and the curves seem rotated off-axis. Coma and astigmatism are not visible here, which means that this set-up provides a behaviour on and off axis very close to its version without meniscus lenses (see Figure 5-9). Chromatic aberrations are however better controlled here.

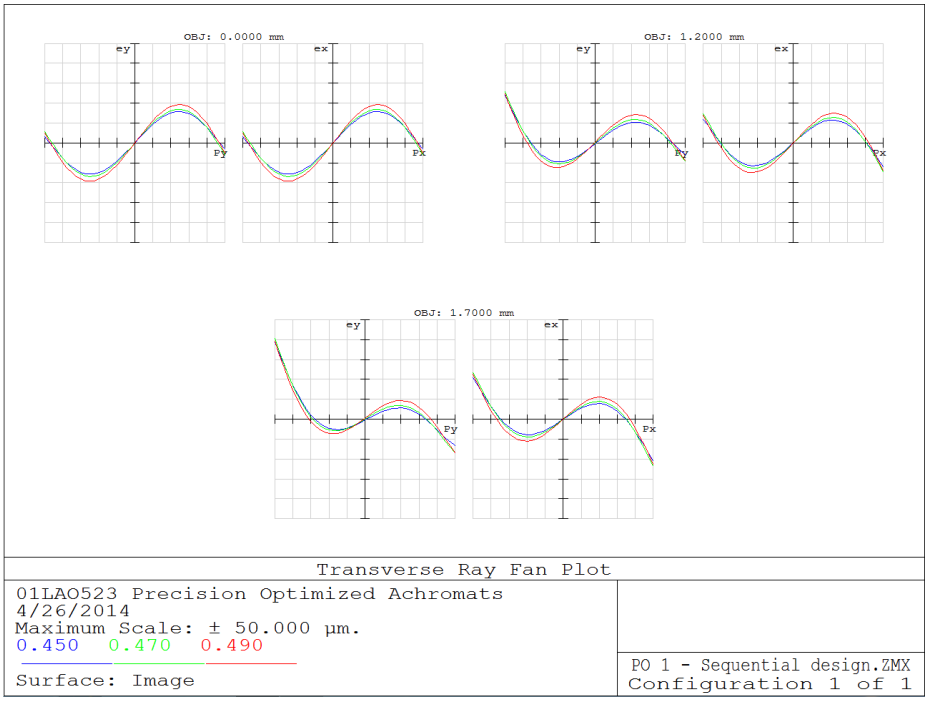

Figure 5-13: RO analysis: Transverse ray fan

In Figure 5-14, the contrast is lower at the centre than at the edge of the system. Compared to the Sill Optics system (see Figure 5-3), the MTF is lower and behaves differently on- and off- axis.

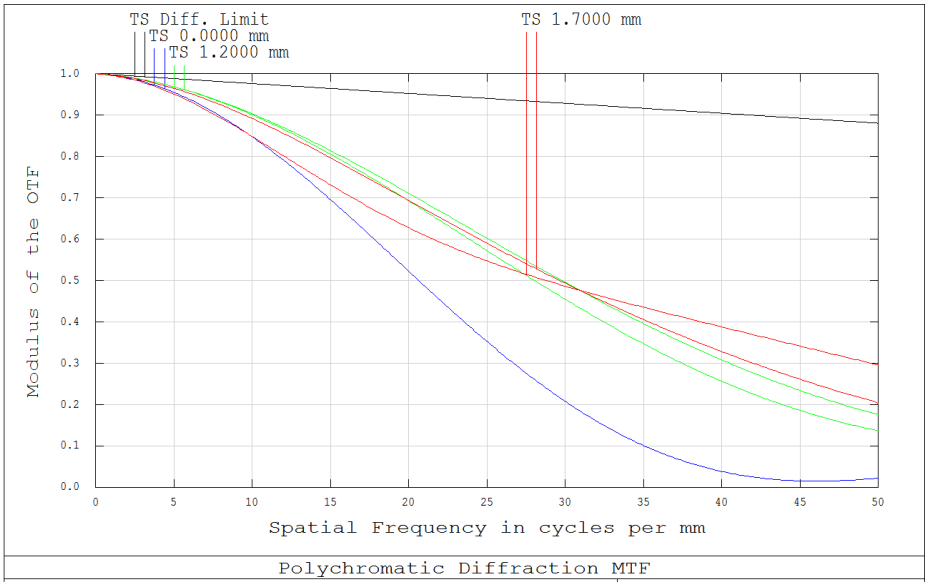

Figure 5-14: RO analysis: MTF

In Figure 5-15, the chromatic shift is lower and it is optimised for a lower wavelength instead of the entire visible bandwidth with Sill optic lenses.

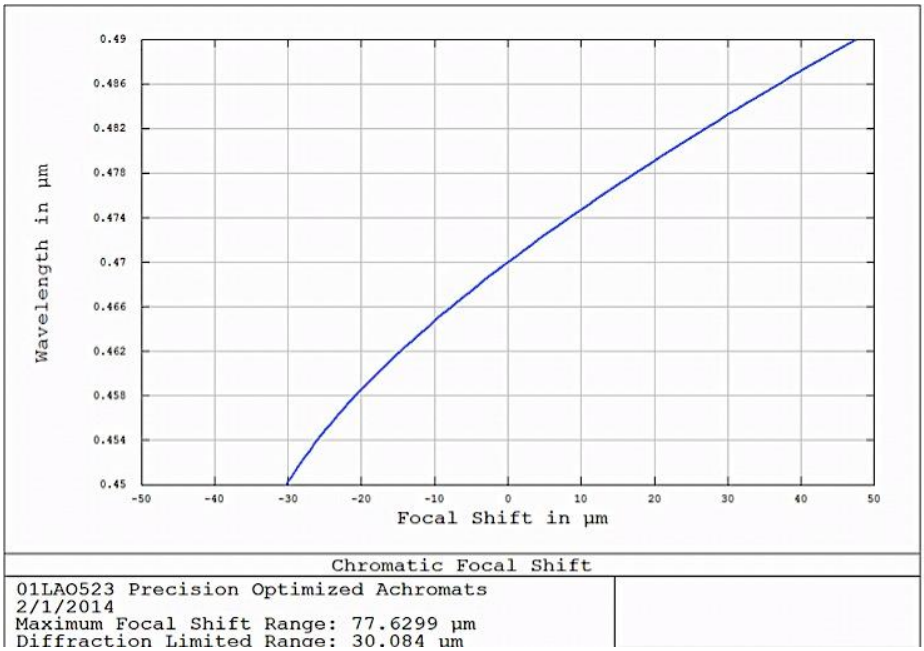

Figure 5-15: RO analysis: Chromatic focal shift

The final design started from the aplanatic-normal principle and was optimised away from it to provide performances on- and off- axis similar to the system without meniscus lenses for a NA n times higher (0.208 vs 0.124). The chromatic behaviour of the RO was also improved for 470nm.

5.2.3 Simulation of the MO imaging with the final in-house design

To simulate the imaging in Zemax the two systems were integrated with micro-optics inside a similar set-up described in Chapter 4: (see Figure 5-16). An aperture equivalent to a pupil of a microscope objective with 40x magnification and 0.8 NA replaced the microscope objectives. Using models of real tube lenses or paraxial lenses does not change the quality of the imaging, as the NA of the light going through it is low.

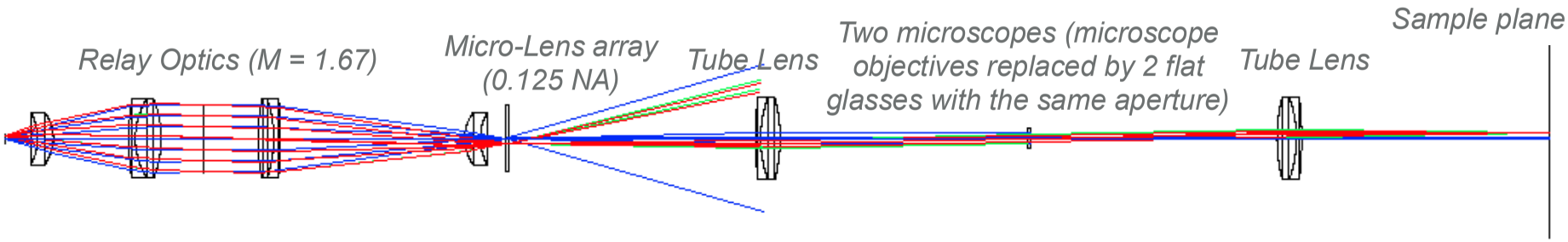

Figure 5-16: Experimental set-up modelled in Zemax
A MLA, RO and MO are modeled with the equivalent of two microscope set-ups, composed, each, of a tube lens and an aperture, identical to the pupil of a microscope objective. The MO are imaged on the sample plane.

In this modelling, the sequential mode was used to optimise and determine the amount of optical aberrations in the system. The non-sequential mode allows an opto-mechanical modelling in 3-D and a more realistic simulation of the imaging. It was used here to test the entire imaging system and compared to the modelling.

Figure 5-17 shows the results of simulations of the image at the sample plane without and with MO, and also an irradiance cross-section measured on the centre of the image obtained with projection optics. The fill-factor is improved to nearly 100% with each micro-lens filled similarly over the entire array. However, there are high intensity variations between the centre and the edge of each micro-lens image. Therefore the main visible optical aberrations are spherical aberrations, which are on-axis. This demonstrates that for this particular application, a telecentric, and therefore more homogeneous system, can be obtained respecting the requirements set at the beginning.

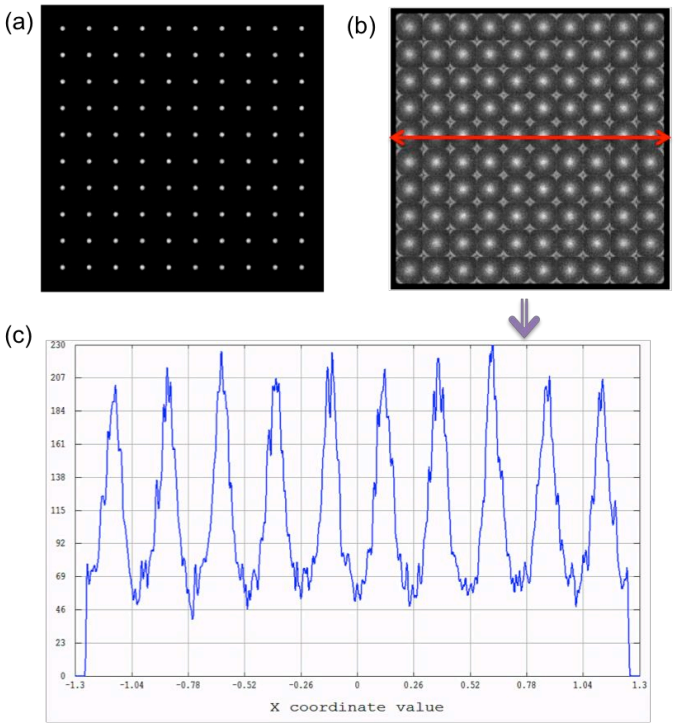

Figure 5-17: Simulated imaging with the projection optics (PO 1)
The image at the sample plane (a) without micro-optics, (b) with the micro-optics and (c) the irradiance cross-section with micro-optics.

5.3 Testing of "PO 1"

5.3.1 Testing of POs

The designs modelled in 5.2.2 were implemented and tested in a similar way. Figure 5-18 shows the recorded image at the sample plane for optical systems without and with POs, therefore without and with MO. Additionally, a cross-section of the intensity is displayed. The MLA provided by Tyndall was flawed which explains the black spots in the image where some of the LEDs were not functioning. A 10 by 10 array was used here as it was judged enough to demonstrate the advantage of a system compared to the other. Only rows where all the LEDs were in working order were used for the measurement of the cross section. This enabled us to compare the results of the two systems to each other as well as to the simulations.

The results were found to be very similar to the simulations. The micro-lenses are filled similarly through the entire array. The intensity difference between the centre and the edge of each micro-lens is high as expected confirming that the most important aberrations are spherical.

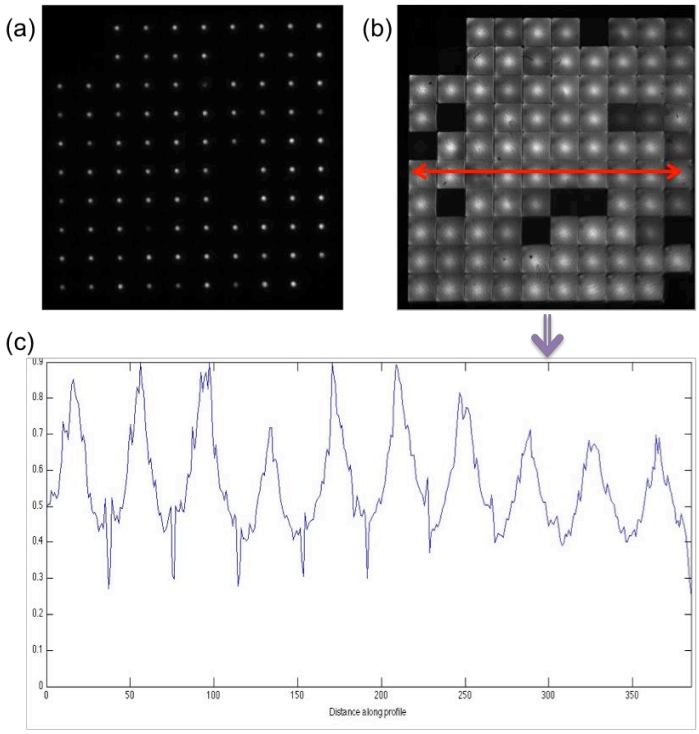

Figure 5-18: Imaging with a conventional design MLA with PO 1
With the image at the sample plane (a) without micro-optics, (b) with the PO and (c) the irradiance cross-section with PO. The dark noise was not subtracted on (a), (b) and (c).

In Figure 5-16, an equivalent of two microscopes are put front to front to image the MLA or MO on a plane that was called “sample plane”. On the microscope platform, only one microscope is used to illuminate a biological specimen on a plane between the two microscopes. Intensities were measured with a power meter just above a MLA, still using a conventional design, and at the true biological specimen plane. Collection efficiencies were calculated. These measurements were then compared to the theory (see Figure 5-19). The experimental result is less than half the collection efficiency expected in the theory (1.76% vs. 4.3%). This was probably caused by imperfections in the optical materials, imperfect alignment and optical aberrations. A slight decrease of the intensity at the edge of the array is observed (see Figure 5-18(b)). Additionally, the system may lose more light at the pupil of the microscope objective and at the micro-lens array. This result is still an important improvement over systems without MO. The collection efficiency is more than 12 times higher that without any micro-optics and provides an illumination with a nearly 100 % FF.

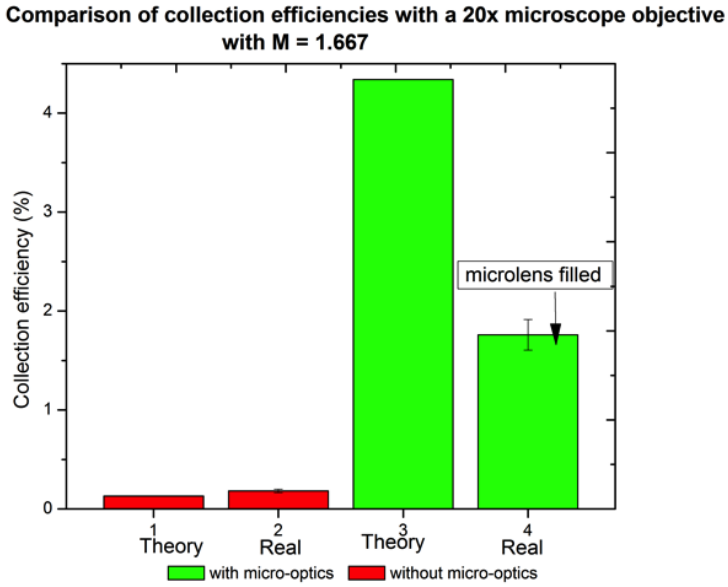

Figure 5-19: Compact PO: Comparison of collection efficiencies measurements with the theory

5.3.2 Integration into Scientifica microscope platform

The chosen design, called “PO 1”, was then integrated within an upright modified Olympus microscope, such as the ones Scientifica is using in their SliceScope systems. Olympus microscopes share similar modular components to reduce cost. At Imperial College, an Olympus microscope BX41 was used with a universal reflected light illuminator BX-URA2, which is also part of the SliceScope. “PO 1” was implemented into the microscope that was also equipped with shorter focal tube lens (100 mm) (see Figure 5-20). This was first tested at Imperial College then on a SliceScope at Newcastle University.

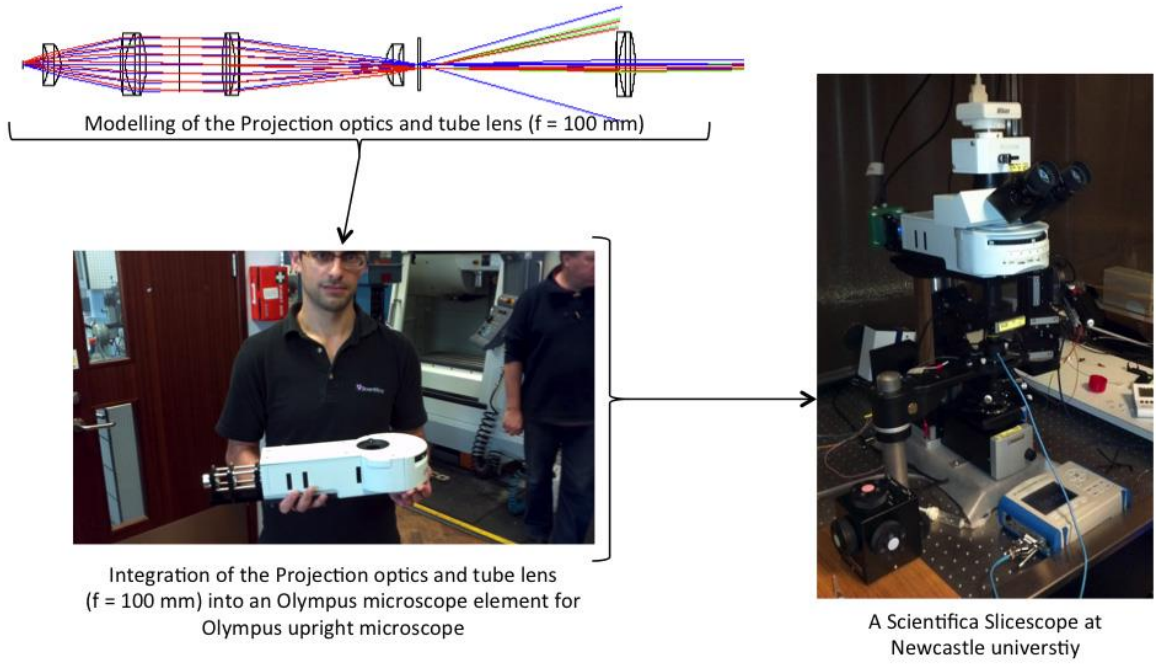

Figure 5-20: PO 1 integration into an Olympus and Scientifica upright microscope
Top-left) Sequential modeling of PO 1 with 100 mm focal tube lens, Bottom left) Integration of PO 1 into a universal reflected light illuminator BX-URA2 and Bottom right) Scientifica’s SliceScope

In order to ensure the smallest possible distance between the first ML and the MLA to allow a better control of the optical aberrations, as per the PO development, the ML was placed directly into the mount connecting the MLA housing to the PO. This was possible because the aperture of the MLA housing developed by Scientifica is 28 mm. This is larger than the 15 mm needed to allow a 0.208 NA on the MLA side of the ROs.

In the same way, better results were be obtained by keeping the distance between the last ML and the micro-lens array small. However, a minimum distance was required as ML and MO were in different mounts and holders. The thickness of the mechanical components was at least of 3 to 5 mm. The micro-lens array was placed in x-y positioner from Qioptiq.

The 2 achromatic doublets were attached to 30mm cage mount rods, from Thorlabs and Qioptiq, just outside the universal reflected illuminator, allowing an adjustment of the magnification of the RO during the experiment.

5.3.3 Imaging tests with an Olympus microscope

As described above "PO 1" was integrated into a universal reflected light illuminator BX-URA2 and first tested in an upright Olympus microscope (Olympus BX41). A fluorescence slide and a cell on a transparent slide were used for the imaging. Figure 5-21 shows the MLA pattern on both a) the fluorescent slide and b) the cell. The advantage of using an MLA compared to a single source is clearly shown in this figure as well. The spatial control over the MLA makes it possible to target specific portions of the biological samples by simply switching the relevant LED on or off. It allows the stimulation of specific areas with a fill-factor close to 100% and an increase of collection efficiency.

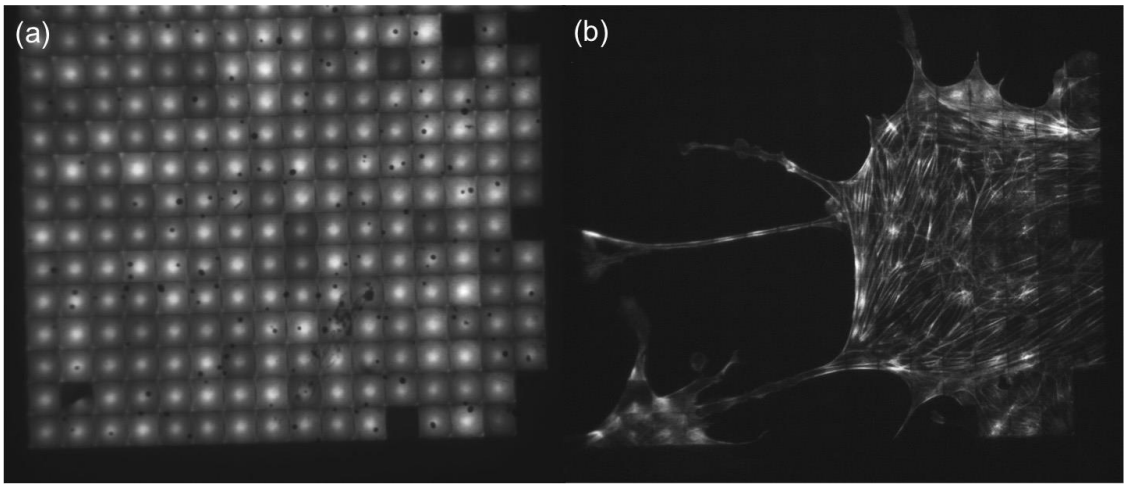

Figure 5-21: Fluorescence imaging using PO integrated into an Olympus microscope BX41
(a) Imaging of the micro-lens array with a microscope objective 20x NA 0.4, LED pixel size 22.5µm at sample and 360µm field of view, and (b) Imaging of a biological sample with microscope objective 40x NA 0.75, LED pixel size 11.25µm at sample and 180µm field of view

5.3.4 Biological experiment

The first experiment on biological specimen was done at our partner's laboratory in Newcastle University. This experiment was done on a patch-clamp platform using a SliceScope from Scientifica (see Figure 5-20). Its goal was to compare an MLA of single emitter micro-LEDs with reshaped back electrodes without and with the integrated PO and a shorter tube lens (f =100 mm instead of f=180mm) by measuring the power at the MLA and at the sample plane. An additional goal of these first experiments was to stimulate a fluorescence sample.

Collection efficiency measurement:

Measurements were done without and with the PO with different microscope objective magnifications to compare the different results to each other and to the theory (see Table 5-4). The 10x microscope objective has 0.3 NA, the 20x, 0.4 NA and the 40x, 0.8 NA. More light can be collected with the 10x microscope objective than with the 2 others, which have the same aperture.

Note that the two set-ups were integrated at the same time on the microscope platform, one on the fluorescence arm (without MO) and one on the camera side (with MO). The usual 180mm focal tube lens had to be used on the camera side as this system was not adjustable. The 100mm focal tube lens was used with the PO on the fluorescence arm. The collection efficiency is estimated to be reduced by a factor of 3 (see A.1.2) on the camera side. This means that the results obtained have to be corrected by a factor of ~3.

Without PO, the collection efficiency difference between 10x and 20x is in theory a factor of 2.2. In practice, the collection efficiency of the 20x was 1.42 times higher than the 10x. With the 10x microscope objective, one fifth of the light was collected compare to the theory. With the 20x microscope objective, one third was collected. This difference between theory and practice is most probably caused by losses at the pupil of the microscope objective.

With the PO, there are no obvious differences as expected. Collection efficiencies are all measured around 11.5%. The difference between measurements and theory is lower compare to no MO (~2.5 times vs 3 or 5 times). This decrease of light losses is probably caused by the optimisation of the imaging at the microscope pupil aperture. Without POs, the image of the MLA at the pupil is a lot larger than the pupil aperture. With PO, this image is smaller than this aperture, which explains that there are no differences between the 3 objectives. The other losses are probably caused by optical aberrations, materials imperfections and imperfect alignment.

Magnification Obj/Tube lens focal	Collection efficiency (%)		Theory Coll Eff (%)	
10x/180mm	0.132%		0.64%	
20x/180mm	0.093%		0.29%	
10x/100mm (with excitation filter)	7.865%	~ 32.5% loss with excitation filter	24.032%	in theory 22.3% loss
10x/100mm	11.538%		30.929%	
20x/100mm	11.239%		30.929%	
40x/100mm	11.758%		30.929%	

Table 5-4: Collection efficiency measurements comparison with the theory

With PO, the collection efficiency is ~11.5% which is 29 times and 41 times higher than without PO for 10x and 20x magnification respectively (after correction for the tube lens). For our experiments the power per area is important. For a system without PO only a small area is illuminated in the centre of the pixel, but the power per area is relatively high. With PO we found that the power per area for the entire pixel, has not decreased significantly and is close to the original power per area. An average of 4 times less power per area was observed over the whole pixel.

Fluorescence stimulation

The second step consisted in stimulating action potentials in neurons. To help targeting the neurons correctly, it is common to use fluorescence markers such as green fluorescence proteins (GFP) that can be excited around the same wavelength than ChR2. We imaged an astrocyte and neurons with a 60x microscope objective (1.0 NA) (see Figure 5-22).

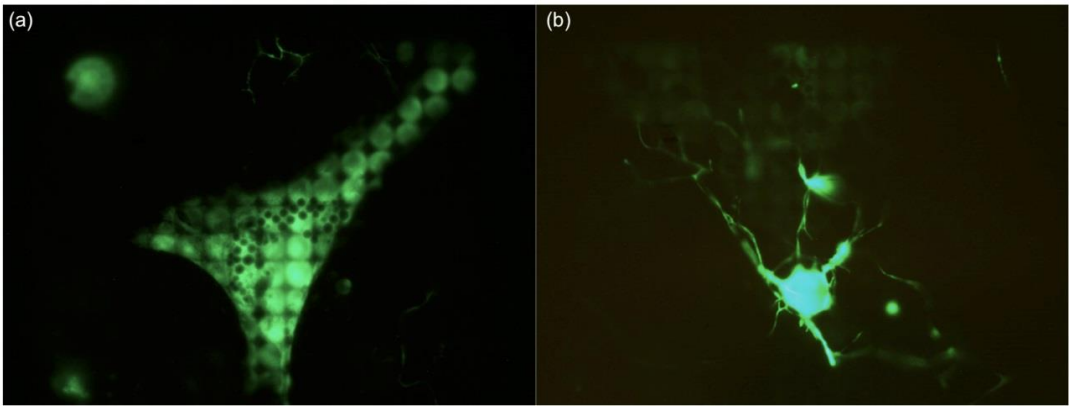

Figure 5-22: GFP stimulation and imaging with a 60x NA1.0 microscope objective and a blue MLA
(a) Astrocyte and (b) Neuron

This experiment showed that there is enough light to generate a high fluorescence response from the cells with GFP markers in it. Unfortunately, the MLA malfunctioned which made it impossible to measure action potentials stimulation during this experiment. The constant use of the MLA constantly at a high current for an extended amount of time caused contacts to burn and an inconstant behaviour of the MLA. Part of this problem was solved later by making the device more efficient. This device was used with a maximum voltage between 4 and 5 V and it was decreased later to 2.5/3.5 V. In MLA with LED clusters, a fan was added to cool the chip and avoid this problem.

This experiment outlined that this first implementation of the PO into a microscope platform had mechanical limitations as well. First, the x-y positioner was not good for this application as it was rotating when it was adjusted, and therefore had to be realigned manually often by opening the side of the universal reflector illuminator or by rotating the MLA. Secondly, the optimisation of the RO magnification was not easy because of the imprecise adjustment of the two achromatic doublets at the back of the microscope that was in a Faraday cage. And thirdly, by replacing a complete component of the microscope, it means that the electrophysiology platform had to be reset correctly after adding it. This is not practical, if several types of light sources are to be used on the same platform. It is practical only, if the PO is to be integrated permanently on it.

5.4 Conclusion

A compact and cheap PO (~200 mm and ~500£), composed of 2 identical custom meniscus lenses from Knight Optical and 2 achromatic doublets from Melles Griot, was developed, using Seidel equations and the optical modelling software Zemax, with an homogeneous illumination along the entire array, and implemented into an electrophysiological platform from Scientifica. Although the system has higher fill-factor and higher collection efficiency than one not using PO a problem was identified, the illumination is not homogeneous in each micro-lens due to a high amount of spherical aberrations in the RO, which are more visible on the MO as the image of the RO is very close to the MO. There is a slight decrease of the intensity at the edge of the array as well. On-axis (SA, Astigmatism) and off-axis (Coma, Field-curvature and Distortion) optical aberrations need to be decreased to improve the quality of the imaging. Sill Optics provides an optical system with higher performances than “PO 1”. But the cost is more than 4 times higher.

The PO “PO 1” was integrated into an Olympus microscope element with a 100mm focal tube lens in it. The 100mm focal tube lens allows for more light to be collected compared to the traditionally used tube lens in Olympus microscope (180mm) as expected. This first implementation of the PO into a microscope platform showed mechanical limitations.

Chapter 6: Advanced design and implementation: "PO 2"

In the two previous chapters, the reasons behind the selection of a basic optical design for RO were explained. Then the development of a first PO, "PO 1", was described. It was shown that the RO performance was not enough to provide a homogeneous illumination in each micro-lens over the entire field, due mainly to residual primary spherical aberration. Furthermore, the opto-mechanical design had limitations. In this chapter, the development of a more advanced RO, and therefore PO, "PO 2", using modelling and experiments is shown. It is followed by its implementation by Scientifica and Imperial College for integration in Scientifica's SliceScope and in a variety of microscope platforms used by Optoneuro's partners.

6.1 Design

The main problem with PO1 is that there is residual spherical aberration in the design. This is manifested by the fact that there is intensity variation across the micro-lenses as they are close to the focus of the relay optics. The main effort here therefore is to correct that spherical aberration by changing the shorter focal length achromat to a custom design and to combine it with an off the shelf plano-convex lens in order to reduce its required power. In addition there is also longitudinal chromatic aberration in PO1 caused by the fact that the doublets are optimised to operate across the entire visible spectrum and so are best corrected chromatically in the green, but then also because this is then over-compensated by the meniscus singlet lenses (Figure 5-15). Finally, we find that the system suffers from curvature of field, which is to be expected, as the majority of the elements in the system are positive, but it was largely hidden in PO1 by the spherical aberration. So we include a plano-concave field flattener lens just before the micro-lens array. In general a positive lens placed at the stop will exhibit positive astigmatism, but here none of the lenses are placed at the stop and so we expect the optimisation process to be able to control astigmatism. Finally it is important that distortion is minimised in the design and also that telecentricity is maintained at both the input and the output planes. Again here optimisation constraints are used in the design process.

In “PO 1”, there are restrictions that are purely mechanical. The first meniscus lens was first in a mount that was then connected to another mount holding the MLA housing. Its position was therefore set at ~12mm, which corresponds to the distance between the MLA and the edge of its housing and the thickness of the meniscus lens mount. Now in PO 2, the meniscus lens is integrated directly into the mount holding the housing. It allows for possible optimisation to shorter distances between the MLA and the meniscus lens. On the MO side of “PO 1”, the meniscus lens and the MO are in two different mounts. The concave side of the meniscus lens is toward the MO. The minimum distance is therefore around 10mm. In “PO 2”, they are integrated into the same mount thus increasing flexibility and enabling us to decrease this distance if we observe an improvement in with shorter distance. This way, the PO have four separate groups (first meniscus lens, Achromatic doublet group 1, Achromatic doublet group 2 and Second meniscus lens group with MO) instead of five, simplifying its set-up (see Figure 6-1).

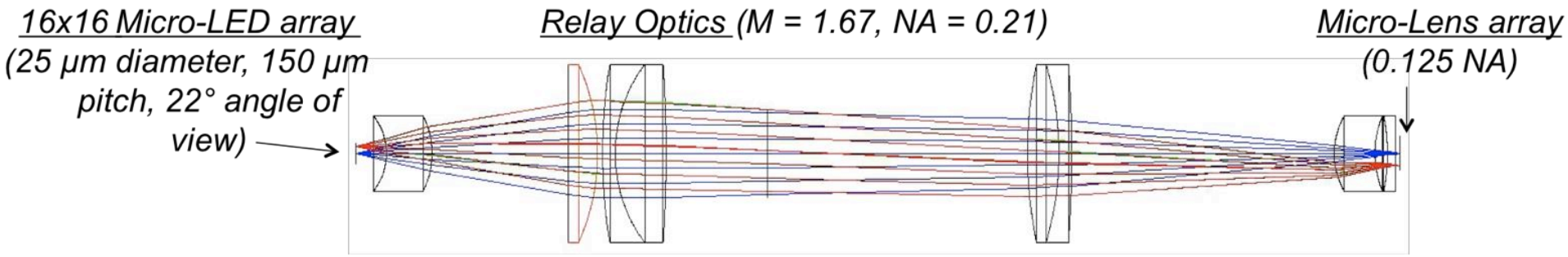

Figure 6-1: Schematic of "PO 2"
Schematic of the Improved version of the PO. Three off-the-shelf and three custom lenses are used in this design.

With all these parameters and cost in mind (see A.3), the system was optimised (see Figure 6-1 and A.6). The first achromatic doublet (f = 60 mm) is causing most of the spherical aberrations and therefore, its power is now split in two lenses. Additionally the achromatic doublet is customised and thus optimised compared to the off the shelf lens used before. The first lens, a plano-convex lens, adds positive SA and coma (surfaces 3 and 4 of Figure 6-2) and the achromatic doublet compensates with negative aberrations (surfaces 5, 6 and 7 of Figure 6-2). A plano-concave lens was added between the last meniscus lens and the MO. It is used as a field lens and it improves curvature of field. These meniscus lenses were re-optimised separately to obtain best performance. The plano-convex and plano-concave lenses were initially optimised but then equivalent off-the-shelf lenses were chosen as close matches were available. The meniscus lens on the MLA side was re-optimised as well. The aberrations could be decreased by slightly increasing the thickness and radius of curvature of the meniscus lenses. However, this is limited by mechanical and manufacture constraints. The total RO has now 6 lenses instead of 4 and 3 custom lenses (one a doublet) instead of 2.

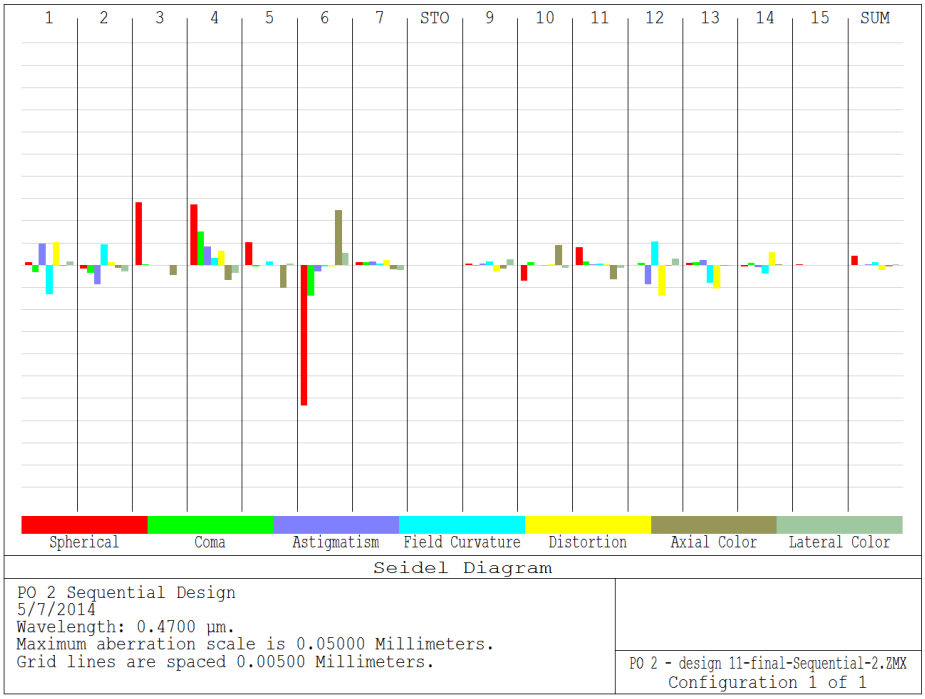

Figure 6-2: Seidel diagram of "PO 2", note that this diagram only includes primary aberrations
This diagram summarizes the optical aberrations added by each surface and the total at the end of the RO

The transverse ray fan shows (see Figure 6-3) that on-axis aberrations were decreased by nearly a factor of 10. Note that the maximum scale on these figures is 5µm compared to 50µm shown in the previous chapter. There is still some high order spherical aberration, and some high order astigmatism, field curvature and distortion that cause the difference between the centre and edge of the array. The system is nearly diffraction limited with geometric spot sizes close to the Airy radius (see Figure 6-4 and Figure 6-5). The chromatic focal shift is divided by 3 fold compared to "PO 1" (25 vs. 77µm) (see Figure 6-6 and Table 6-1).

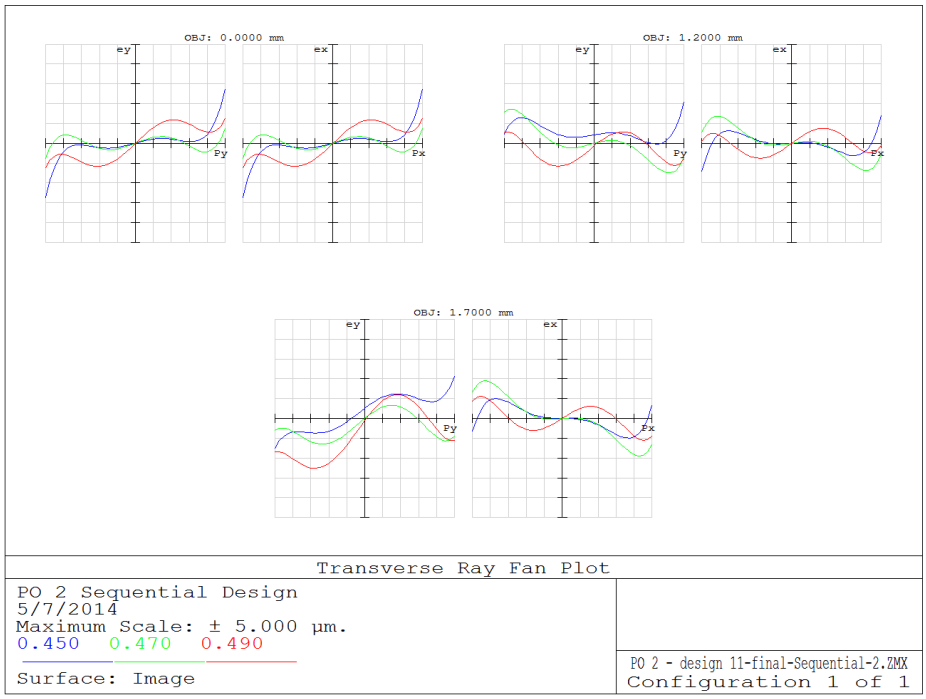

Figure 6-3: "PO 2" Zemax sequential analysis at 0.208 NA: Transverse Ray Fan, note the residual aberrations are generally higher order, particularly second order spherical is apparent.
The ray fans are showing the presence of SA and FC in the RO.

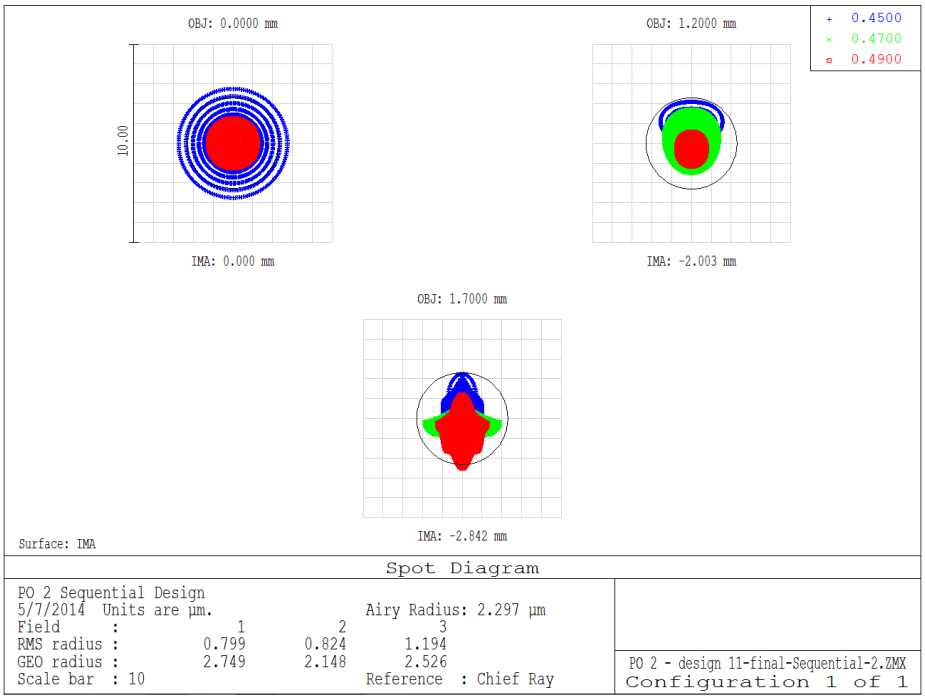

Figure 6-4: "PO 2" Zemax sequential analysis at 0.208 NA: Spot diagram
The RMS spot radius is 0.9±0.2µm and the geometrical radius 2.5±0.3µm, which is very close to the airy disk size.

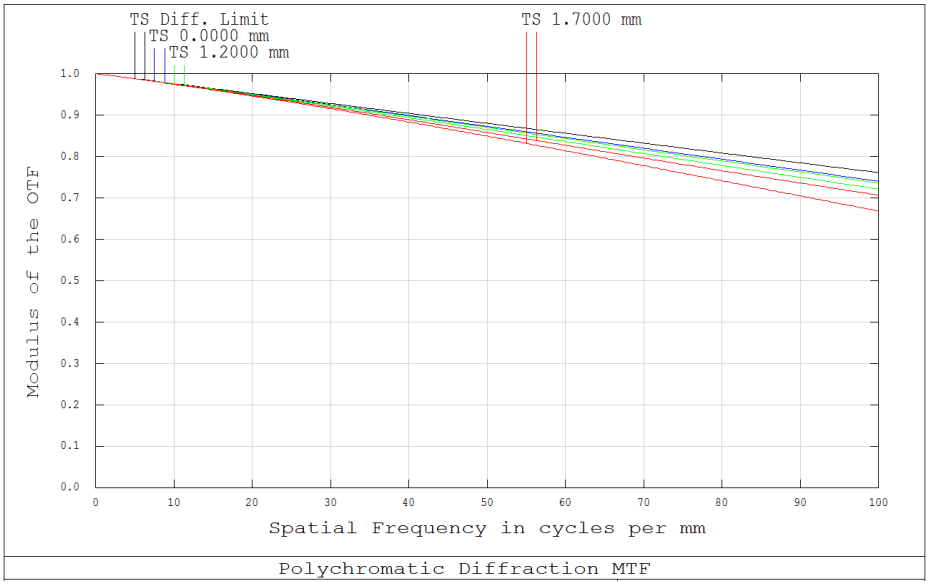

Figure 6-5: "PO 2" Zemax sequential analysis at 0.208 NA: MTF
The MTF was traced up to a spatial frequency of 100lpm instead of 50lpm with "PO 1" to demonstrate the improvement of this RO. Its MTF is higher than 50% at 100lpm, which means that the image will still be sharp at a 5µm resolution. In PO 1 (see Figure 5-14), the MTF goes below 50% before reaching 30lpm.

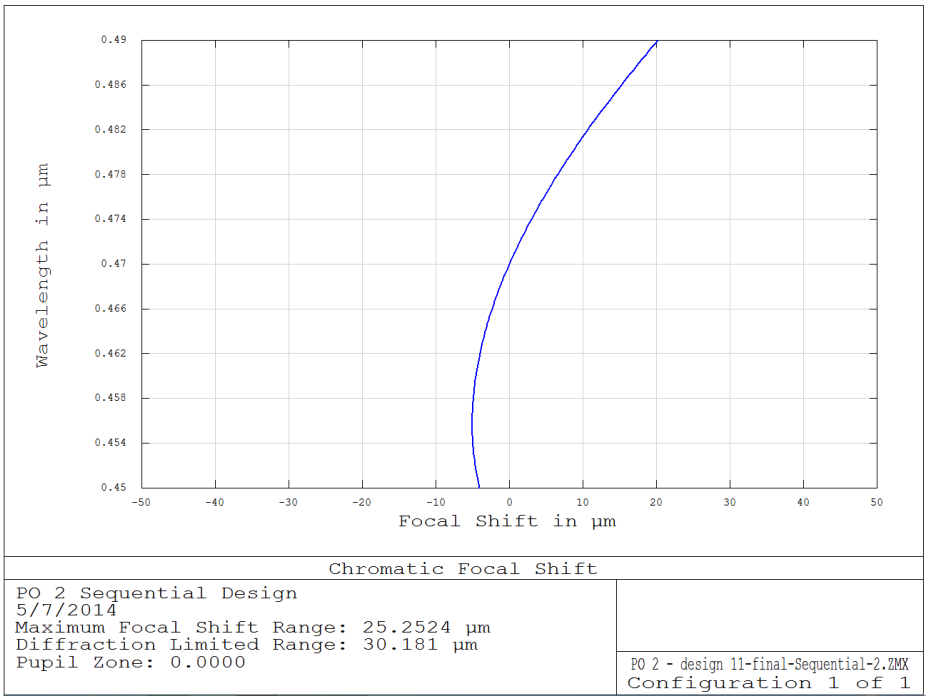

Figure 6-6: "PO 2" Zemax sequential analysis at 0.208 NA: Chromatic focal shift
The chromatic focal shift is divided by 3 compared to the one obtained in "PO 1" simulation (~77µm). This means that chromatic aberrations, due to the wide bandwidth of the MLA (470±20nm), are decreased. It has therefore decreased its effect on the quality of the illumination

The field curvature was one of the main reasons behind the decrease of intensity at the edge of the array in "PO 1". In "PO 2", It was decreased by ~5 fold (see Figure 6-7). The plano-concave lens added at the end of the system is largely responsible for this as it is the only element with negative field curvature aberrations.

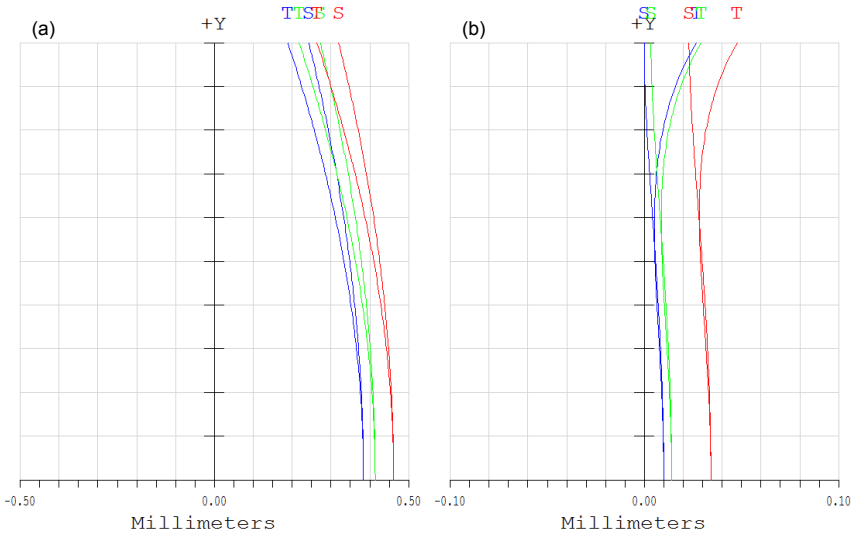

Figure 6-7: Comparison of the field curvatures of the RO developed, note also the large defocus in PO1, which is indicative of compensation for primary spherical aberration.
(a) "PO 1" and (b) "PO 2"

"PO 2" was then modelled in non-sequential Zemax, to simulate the distribution of light coming from the MLA and its interactions through all the parts of the PO such as internal reflections, which are not shown in the sequential mode. The MLA was modelled as a 25µm disk emitting light either with a Lambertian distribution or with the 22° angle of view distribution supplied by Tyndall (see Chapter 3:). Imaging was simulated for the scenario where the entire array is switched on and for one where every second LED is switched on (chequerboard illumination) to verify that a good contrast ratio was being achieved. This simulation shows an increase of the homogeneity for each micro-lens with a much-reduced difference between the lower and maximum intensity compared to "PO 1" (see Figure 6-8 (a)). Very little light is observable in neighbouring micro-lenses (see Figure 6-8 (b)). However, there is still a slight decrease of intensity at the edge of the array.

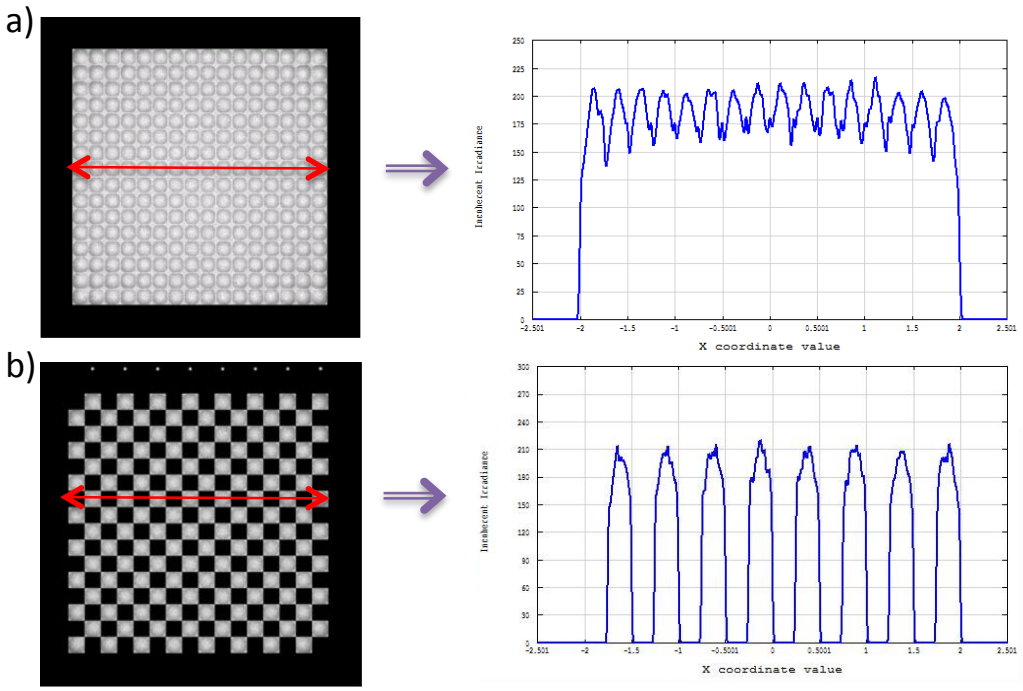

Figure 6-8: Simulated imaging of "PO 2" (left) and an irradiance cross-section of it (right)
Of (a) a complete illumination of the 16 by 16 MLA and (b) a check-board illumination

Table 6-1 summarizes the results of the relay optics modelling. As described before "PO 1" behaved less well than the Sill Optics Set-up across the board, with a higher RMS spot radius and STD and a lower MTF. In contrast "PO 2" has much reduced RMS spot radius and STD. Its MTF is around 92% and 85% at 30 and 50lpm respectively. Chromatic aberrations are as well much more controlled and it therefore decreases any focal shift that can be caused by the wide bandwidth of the MLA (470±20nm). Furthermore, "PO 2" performs a lot better than the Sill optics lenses for half the price (see A.3). The goal to develop a system performing better than a reference design for a lower price was therefore reached. The experimental tests performed to corroborate the simulations are described in the next section.

Relay Optics	Average RMS spot radius (µm)	Maximum on transverse ray fans (µm)	Chromatic Focal Shift (µm)	MTF (%) at 30 cy/mm	Maximum Distortion (%)
Sill Optics	7.32±0.15	20	169	60	0.01
PO 1 (N-LAK7 ML)	11.33±1.6	40	77.6	23	0.04
PO 2 (N-LAK7 ML)	0.94±0.22	2.5	25.3	92	0.009

Table 6-1: Summary of relay optics modelling results at NA = 0.208
Generally, telecentric RO have distortion ≤0.1 %. The maximum transverse ray aberrations can be seen on the transverse ray fans.

6.2 Focus and magnification adjustment

Ideally the opto-mechanical mechanical design should be identical to the model however each step of the manufacturing of the optics and of the mechanics adds errors. Therefore, two groups of lenses were set on z-translation stage to compensate for focus and magnification.

In Figure 6-9, the schematic of the relay optics used in PO 2 is shown with each important distance. d_{Object} is the distance between the MLA and the centre of the first lens of the relay optics and d_{Image}, the distance between the last lens and the image of the MLA. The micro-lens array is set at its nominal focal distance from this image (~0.3mm from the back of the micro-lens substrate). d_1, d_3 *and* d_4 are the distances between each lens group. Each lens group is mounted inside a mechanical mount. d_2 and d_5 are the distances between the lenses in lens group 2 and 4. In the lens group 2, the lenses were optimised for a distance of ~6mm between the edges of the lenses to include 3 two mm thick locking rings that were available in Thorlabs. d_5 was optimised for the two lenses to be next to each other.

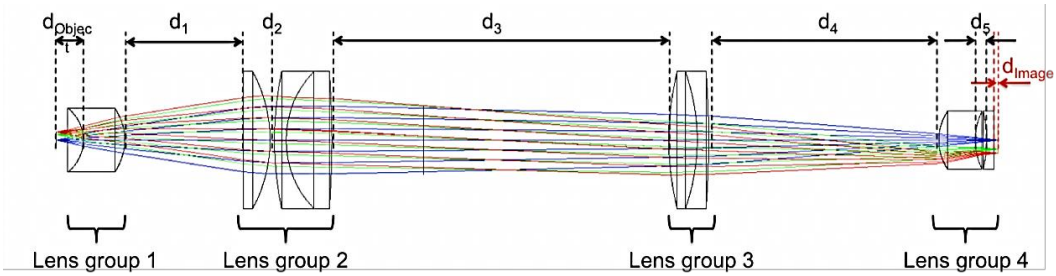

Figure 6-9: RO used in PO 2

In PO 2, the first lens (or Lens group 1) is integrated into the mount that connect to the MLA housing developed by Scientifica to permit a closer positioning of this lens to the MLA, which improves the control of the Seidel aberrations. The lens group 4 is integrated inside the same mount of the micro-lens array for the same reason. The Lens groups 1 and 4 are therefore fixed in z-.

Adjustments are therefore done by moving lens group 2 and lens group 3 to optimise the magnification and focus to compensate for any variations due to the manufacturing tolerances. These two lens groups are therefore integrated onto separate z-translation stages. In this section, a Monte-Carlo simulation is done in Zemax to study the consequences of the variation of d_1 ($\Delta(d_1) = \pm 2mm$) over the exit pupil, magnification and on- and off- axis Strehl ratio. The Strehl ratio corresponds to the peak intensity of the diffraction point spread function divided by the peak intensity of the diffraction point spread function in the absence of aberrations. For each simulation, the relay optics is re-optimised using d_3 as compensators and a merit function to reoptimise for the best spot radius. d_4 is modified accordingly to keep the total length of the system constant. Two other Monte-Carlo simulations were done when the image is at ±0.5mm from its original position.

Figure 6-10 shows the variation of d_3 (Δd_3) in function of the variation of d_1 ($\Delta(d_1)$. It shows that d_3 will increase with d_1, causing a decrease of d_4, which is equal to: $\Delta d_4 = -(\Delta d_3 + \Delta d_1)$.

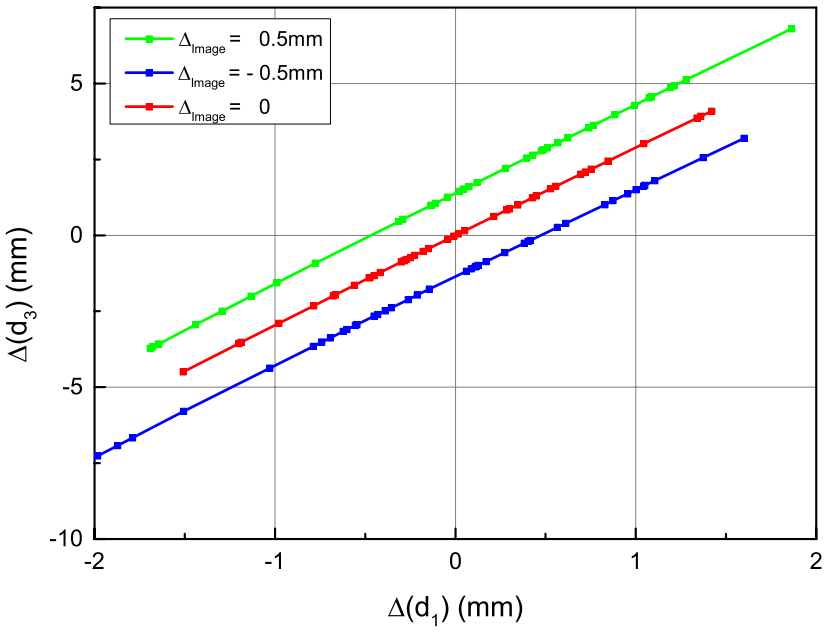

Figure 6-10: Variation of d_3 with d_1

Figure 6-11 shows the evolution of the inverse of the paraxial pupil position, which should be zero when the system is telecentric. The system is set with an entrance pupil at the infinite and optimised for an exit pupil at the infinite. The system can be kept nearly telecentric for these variations of d_1. The variation of the position of the image does not change very much at the reference position of d_1. However this difference increases when d_1 is increased positively.

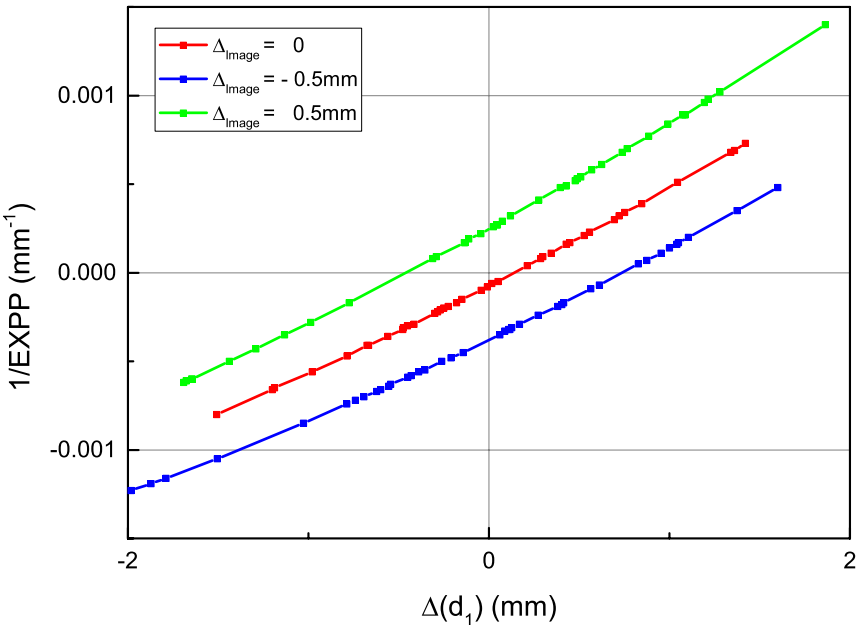

Figure 6-11: Variation of the inverse of the exit pupil (EXPP) with d_1

Figure 6-12 shows the variation of the magnification caused by the change in the lens group 2 and 3 position. There is only one position where the correct magnification is obtained (-1.667). A variation of the image position and therefore d_{Image} means that d_1 is modified slightly and may cause a slight decrease of the system performances.

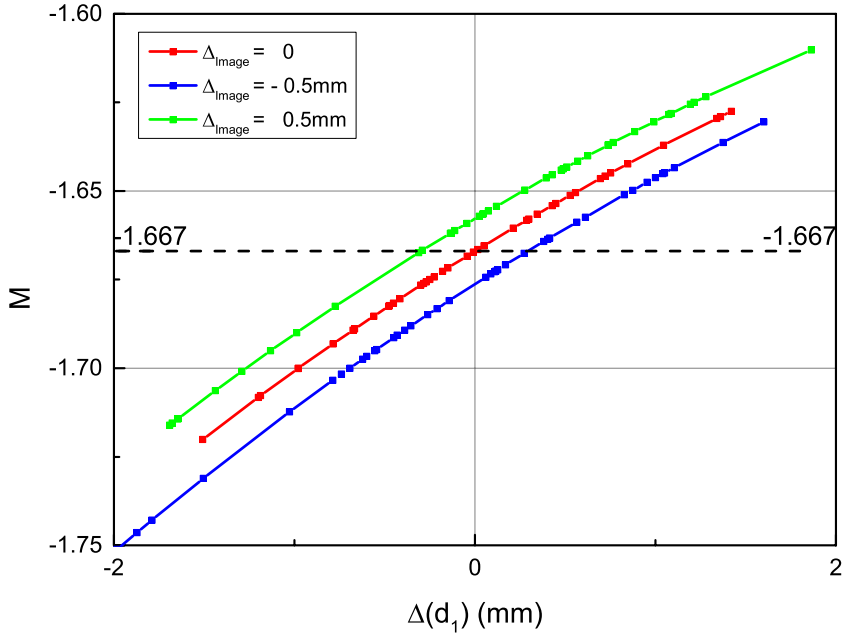

Figure 6-12: Variation of the magnification *M* of the relay optics with d_1

Figure 6-13 shows the evolution of the Strehl ratio with *Δd1* for three fields studied on- and off-axis (see Figure 4-8). The airy disk, which gives the point spread function, corresponds to the image of a point source through a uniform aperture, when there is no aberration. A system is considered diffraction limited when its strehl ratio is above 0.8, which is when its point spread function closely resembles the Airy disk. In the reference position (Δd_{Image}=0 and Δd_1=0), field 1 and 2 are diffraction limited and the third one, which is the furthest off-axis, is slightly below the diffraction limit criterion. This position corresponds to the best compromise for performances on- and off-axis. The on-axis strehl ratio can be slightly increased by decreasing d_1 at the detriment of the off-axis performances, and the off-axis strehl ratio can be improved by increasing d_1 at the detriment of on-axis performances. Performances can be also slightly improved to be diffraction limited over the entire field, when the distance to the image is decreased. However, technically it is almost impossible to decrease it due to the space required by the opto-mechanics.

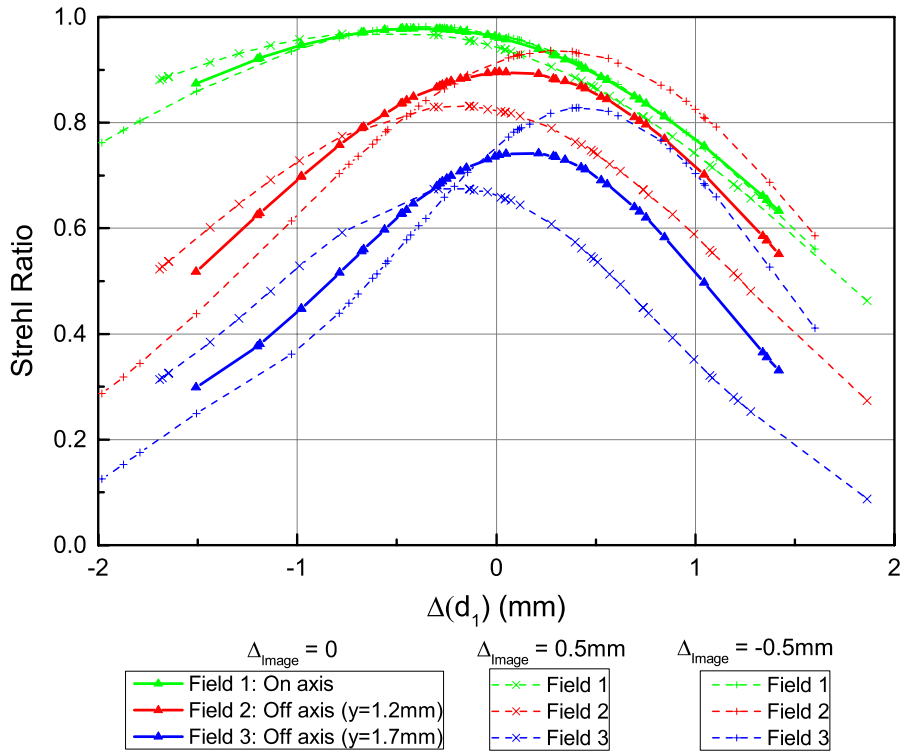

Figure 6-13: Variation of the Strehl ratio for fields on and off axis with d_1

The diagrams above demonstrate the importance of the possibility to vary the lens group 2 and 3 positions to allow a setting at the correct magnification and therefore an alignment of the image of the MLA with the MO. It also shows that for variations of d_1 below ±1mm, the performances are not decreased too much. However, performance off-axis are decreased the further away from the reference position we go.

In practice, translation stages with ±10mm movement were used to allow for more flexibility when each lens is integrated within its lens group and mount and attached to opto-mechanical platform.

6.3 Testing

This system was tested with MLA with reshaped back-reflectors, as these are the ones that are used in all the experiments that followed. In theory, compared to MLA with a conventional design, this means a 7-fold increase of the quantity of light collected at the sample. The tube lens used in this first experiment was identical to the one used with "PO 1" (f = 100 mm) (see Figure 5-16).

Two different microscope objectives were used in this experiment (10x 0.3 NA and 40x 0.75 NA). Figure 6-14 shows the results of the first measurements. The red bars represent the theory and measured results for both microscope objectives without MO and the green bars represent theory and results for the system with MO. When there are no PO, the collection efficiency will be affected by the change of microscope objective. According to the theory without POs, the 40x microscope objective should collect only 38.9% of the light that is collected with the 10x microscope objective (0.81%/2.08%=0.389). This was confirmed in the measurements; with 1.14% and 0.44% collection efficiency measured (see Figure 6-14 - red bars), which shows that the 40x objective collects 38.6% of the light compared to the 10x objective. For both objectives the difference between the theoretically calculated collection efficiency and the measurements one is of a factor of 1.8.

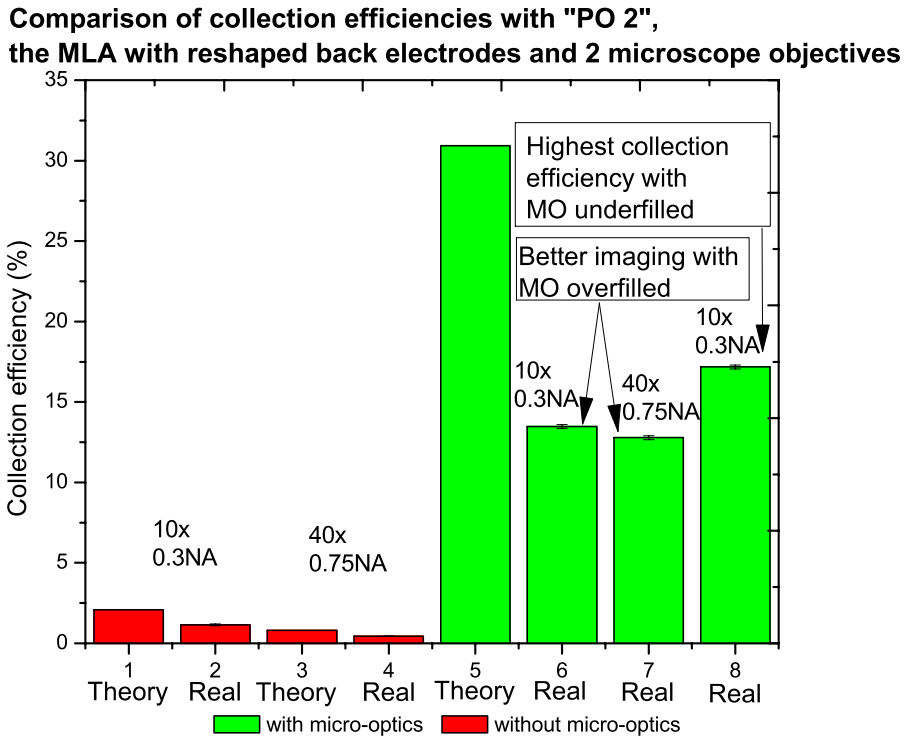

Figure 6-14: Collection efficiency measurements for two microscope objectives (10 and 40x) without and with MO

The collection efficiency should not change when the two microscope objectives are interchanged (see A.1.2), when "PO 2" is used (30.929% collection efficiency). This is confirmed by the measurements as well. 13.5% and 12.8% were measured with the 10x and the 40x, showing that 40x objective collects 94.8% of the light compared to the 10x objective. The green bars in Figure 6-14 show this result, which was obtained for slightly overfilled micro-lenses. The final green bar represents the results obtained for under filled micro-lenses.

The first set of measurements was made having optimised the imaging (see Figure 6-15 (a)). The illumination looks even more homogeneous than from modelling. There is no peak of intensity at the centre of each micro-lens (see Figure 6-15 (b)). The difference of intensity is due to the variations between pixels of the MLA itself.

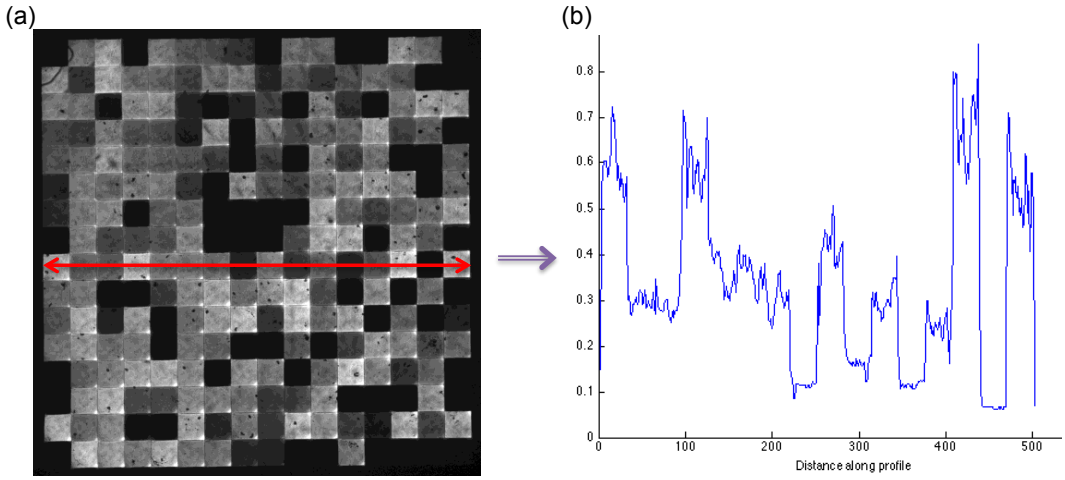

Figure 6-15: Imaging of a MLA using "PO 2"
With (a) the image at the sample plane and (b) the irradiance cross-section. The dark noise was not subtracted on (a) and (b).

A difference of focus between each side of the array can be noticed on Figure 6-15 (a). It is caused by the position of the MLA, which is slightly at an angle and the short depth of field, which is defined as:

$$\Delta z = \frac{\lambda}{2.NA^2} = \frac{0.47}{2.0.21^2} = 5.43\mu m \qquad 6.1$$

The difference between theory and the highest value obtained in practice is a factor of 1.8. This is identical to the one obtained without the PO as described above.

These results are 7 to 9 fold higher than with “PO 1” because MLA with reshaped back reflectors were used here. Compared to the MLA without POs, the collection efficiency with “PO 2” is 15 to 39 times higher, with nearly 100% FF.

6.4 Opto-mechanical design

This PO system has four lens groups. This is one less than “PO 1”. Two design types can be implemented, a straight one, or a folded one, which is less long and should be easier to use on an electrophysiological platform where space is limited. Opto-mechanical platforms were developed by Scientifica to be integrated into their SliceScope and by Imperial to be connected to the different platforms used by the project partners. These are described in the next section.

6.4.1 Development of a multi-platforms set-up with “PO 2”

At Imperial College, the same principle was used to develop and implement two designs with quick prototyping in mind. A simpler design was done with precise tolerances. The main mounts were attached to a metal plate by screws and dales to fix them at the same precise positions. Components that were available on the market like kinetic mounts, x-y positioner or z translation stage were used and modified for these designs.

Straight design

This design uses an x-y positioner from Qioptiq (see Figure 6-16) to position the MO. This x-y positioner is of higher specification and so does not have the problem of the one used with “PO 1”, where the inside of the mount was rotating and therefore rotating the MO. It is used in an experiment with virtual reality optics at Newcastle University where this system is not connected to a microscope and therefore does not have limiting space requirements.

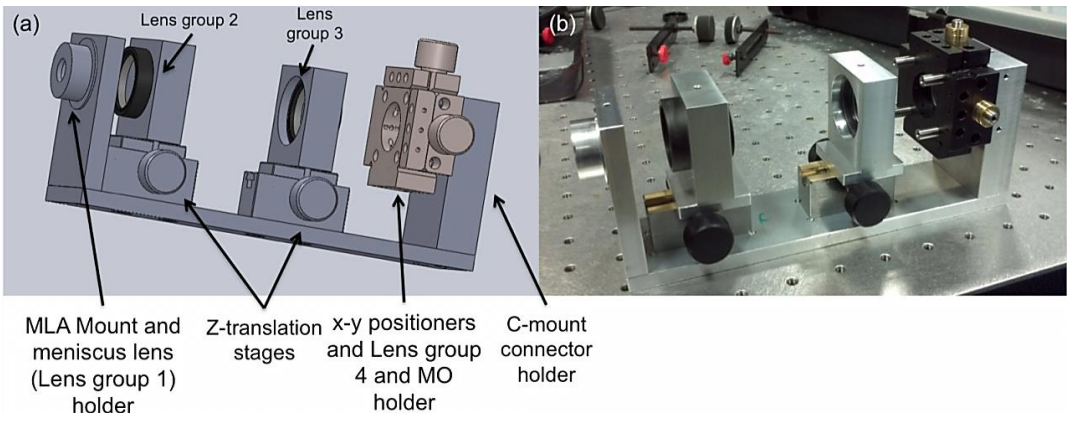

Figure 6-16: Straight design developed in house
(a) SW design and (b) Prototype

In “PO 2”, Lens group 2 and 3 do not require too tight tolerances. The distance between the two lenses in the lens group 2 can be increase from 1 to 1.3 mm, without much changing the image at the end of the system. Tight tolerances are required for the lens group 4 where the distance between the last lens of the 4th lens group and the back of the MO is 1.29 mm. The MLA orientation is important as well as if it is not exactly parallel to the lens planes, its image won’t be parallel to the MO plane and therefore won‘t fill the micro-lenses homogeneously. The short depth of field of the system at the MO causes this (see Equation 6.1). The micro-lens array is fixed at one angle. Therefore, rotating the MLA box on the MLA mount is used to achieve the alignment between MLA and MO in rotation.

Folded design

The folded design was first prototyped because of its compactness easing its use on microscope platforms where space is limited. A kinematic mount with a mirror was added between the lens groups 2 and 3 to align the MLA and the MO laterally (see Figure 6-17). In rotation, the alignment between MLA and MO is achieved by fixing the angle of the MO and rotating the MLA box on its mount. Two Z-translation stages from Edmund Optics were used to adjust the RO magnification. Most of the custom lenses were developed with diameters similar to the off-the-shelf lenses (30 mm diameter for the lenses of the groups 2 and 3 and 0.5 inch diameter for the lens group 4). Only the meniscus lens in lens group 1 was developed with a specific diameter (14 mm), as it is integrated inside the MLA mount. The other lens holders are standard for tube lenses from Thorlabs. The holder for the lens group 4 was modified to fit the MO holder to achieve a 1.29 mm distance from the MO.

This system is used as a stand-alone set-up that could easily be connected to any microscope ports. Camera ports with a C-mount are generally used. A tube with C-mount connection was therefore adapted to fit the 4th lens group post holder. Retractable feet were added on the other side of the set-up to hold it in position, as the first version of this system was heavy. The base plate had a thickness of 13mm. A second version was built with an 8mm base plate to decrease the weight.

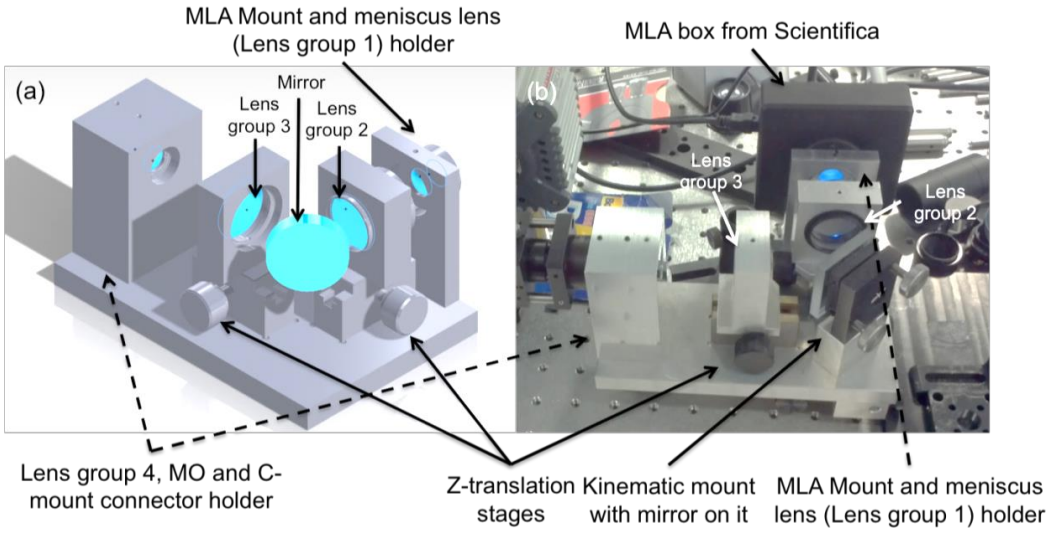

Figure 6-17: Folded design developed in house
(a) SW design and (b) Prototype with the MLA connected to it

6.4.2 Integration of "PO 2" into Scientifica platform

The main difference with the previous set-up is that it is developed more like a stand-alone part that can be connected easily to different microscopes and where the internal workings of the optics are hidden from the user and so will remain clean. The 2nd and 3rd group of lenses (see Figure 6-1) can now be adjusted more precisely and more easily than in "PO 1" using the adjustment rings and fixed to this position if necessary (see Figure 6-18). The 4th lens group is in the same mount than the MO, simplifying the assembly and allowing the 4th lens group to be as close as possible to the MO. This mount is rectangular to be fixed at the same angle when it is moved laterally by two thumbscrews. They are easily accessible to allow for correct lateral alignment of the MO with the MLA. In rotation, alignment is achieved by rotating the MLA box on its mount.

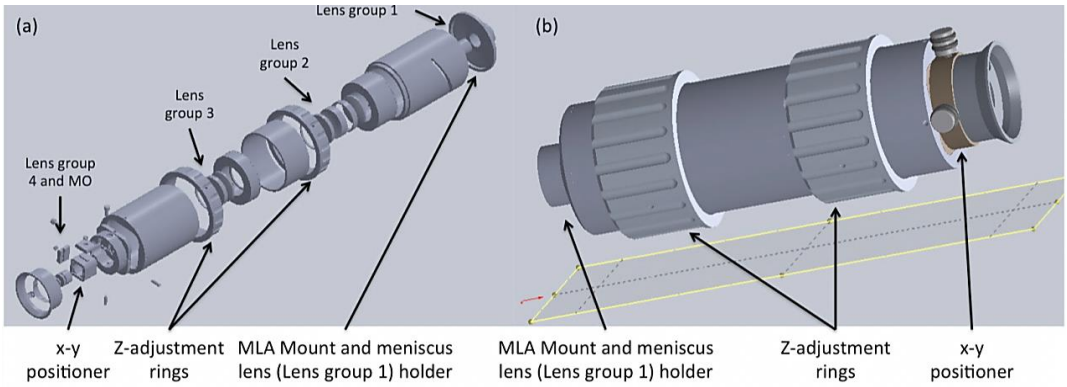

Figure 6-18: Solid Words design schematics of the straight design by Scientifica
(a) Exploded view of the first version of the design. (b) Second and last version of the design with larger adjustment rings and a modified x-y positioner compare to the first version.

Scientifica's priority is in the straight design as it could be easily implemented into their SliceScope platform. After several iterations and testing at Imperial and Scientifica, a final design was manufactured (see Figure 6-19).

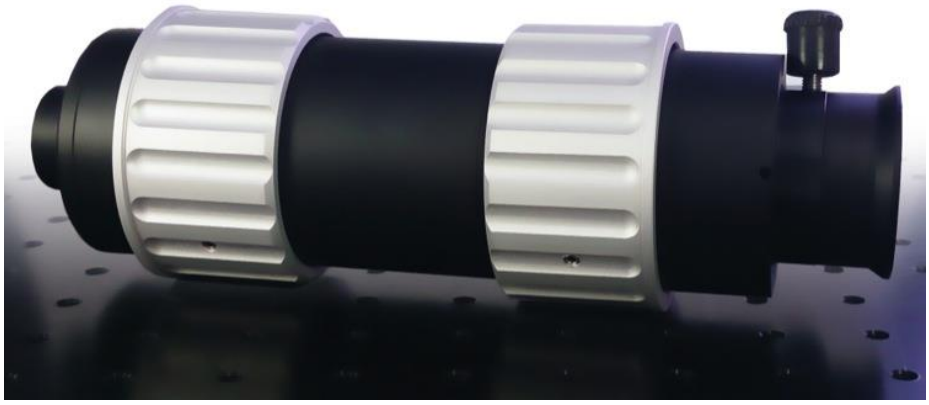

Figure 6-19: Scientifica final opto-mechanical design

6.4.3 Set-up optimisation

The optical system has been designed such that in conjunction with the tube-lens an image of the micro-LEDs is formed at the back aperture of the microscope objective when the micro-lens array is placed at the front focus of tube lens, and with the back aperture at its back focus. In typical infinity corrected microscopes however, the distance between the tube lens and the objective can be variable, especially on the camera output ports. When this is the case a correcting field lens can be placed just next to the micro-lens array in order to correctly focus the micro-LEDs onto the microscope objective pupil.

Figure 6-20 demonstrates this process. In Figure 6-20(a) the output is viewed as though a 160mm tube lens is used placed at exactly 160mm from the microscope pupil (see Figure 5-16). However if this lens is replaced by an 80 mm tube lens then an in focus image can still be obtained with the tube lens 80mm from the micro-lens array but now 240mm from the objective pupil (which has not been moved). In this case the image in Figure 6-20(b) results, and actually a magnification of 2x is achieved in the image plane, but vignetting by the microscope objective pupil causes loss of light in the corners of the array.

However, this can be corrected exactly by placing an f=-40mm focal length lens immediately after the micro-lens array will bring the image of the micro-LEDs exactly back onto the objective pupil. In reality a similar result is also attained by placing a slightly longer focal length lens (-50mm) a few mm after the micro-lens array as shown in Figure 6-20(c).

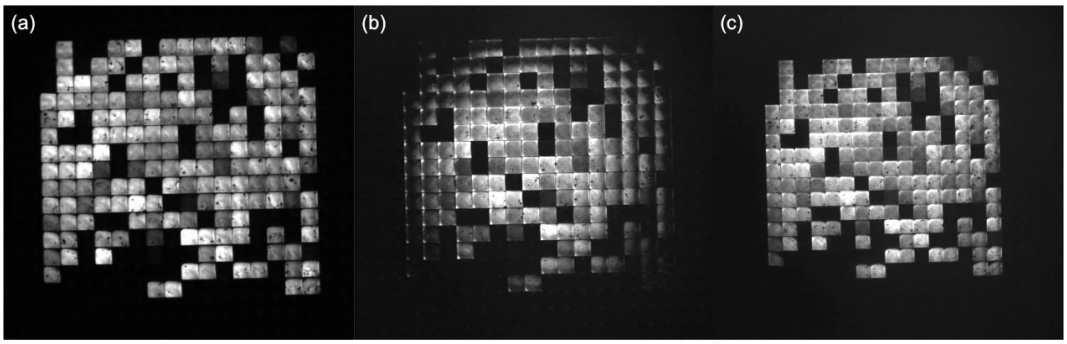

Figure 6-20: MO imaging on a CCD camera with tube lens with different focal distances
a) With 160 mm focal tube lens, b) with 80 mm tube lens, c) with 80 mm tube lens and a 50mm plano-concave field lens added next to the MO. Vignetting can be seen on (b).

These tests were done as our partner at MPI in Frankfurt uses a Zeiss microscope with a 0.5x adapter on the camera port where the PO will be connected. The 0.5x adaptor demagnifies the microscope image at the camera by two and therefore multiplies the image of the MO on the sample by two. This may cause some vignetting, as there is no requirement for the 0.5x adaptor to be telecentric at the camera plane and there might be vignetting at the pupil of the microscope.

6.5 Conclusion

The new MLA allows 7 folds increase of the collection efficiency. But the major breakthrough is brought by the PO that brings an increase of the collection efficiency to more than 13 % and even up to 17 % with a nearly 100% FF. Its development shows that for half the price of an off-the-shelf system (2 Sill Optics lenses), a RO with higher performances was developed.

The intensity is homogeneously spread along each micro-lens and the entire array, although the modelling was showing a less homogeneous spread in each lens than was observed in practice. It is due to the model of the MLA used in NSC Zemax, which is a simplified model. Its light distribution, measured by Tyndall, was associated to an area corresponding to the top of an LED, where the light is homogeneously emitted. However, the light repartition on this surface is probably not homogeneously spread along the entire area in reality. A more accurate model is developed in the next chapter.

A Monte-Carlo study of the variation of the position of the second lens group was done to show how magnification, telecentricity and aberrations were changing. It was also compared when its image position was modified to ±0.5mm demonstrating that even if the micro-optics position is not exactly at the wanted position, d_1 can be modified slightly to optimised the magnification without modifying the coma and only slightly increasing or decreasing the astigmatism and the spherical aberration. It demonstrates the importance of being able to modify the position of the lens group 2 and 3 to compensate for any opto-mechanical errors and optimise its magnification to align perfectly the image of the MLA with the MO.

The single emitter MLA coupled with “PO 2” was implemented into a stand-alone set-up that can be attached to different microscope platforms and optimised easily to obtain an illumination with a nearly 100% fill-factor and an improved collection efficiency on the cell. With our partner, Scientifica, we have made a more advanced set-up for integration into their SliceScope platform.

Chapter 7: Custom micro-optics development for direct integration onto micro-LED arrays

The projection optics “PO 2” developed previously improved fill-factor and collection efficiency, with off-the-shelf and custom macro-optics components for less than a thousand pounds, and with off-the-shelf MO. However, this system is limited by its size and therefore can’t be integrated into an eye-prosthesis for example. Integrating the MO directly on the MLA is the only solution.

No off-the-shelf MO, with a high enough NA or a thin enough substrate (with f < 1 mm), are available on the market. Therefore the design needs to be custom-made. Additionally, the performance of the MO depends on the MLA itself. Models and simulations of the MO are carried out taking into account the specific design of the MLA made by Tyndall.

In this chapter, the principles of this system composed of an MLA and MO are explained. Then, the reasons behind the choice of the manufacturer are described. Finally, the different steps of the design of this system in Zemax are shown and the final results compared to the previous models with off-the-shelf MO and no MO.

7.1 Principle and Requirements

7.1.1 Principle

The principle does not change with the integrated MO compared to the systems described before. Each LED needs to be at the focal distance of each micro-lens and then each micro-lens is imaged onto a sample (see Figure 7-1). The fill-factor will therefore be determined by that of the micro-lenses. Additionally, the amount of light collected from the MLA will depend on the NA of the MO. The pitch of the MLA and the MO need to be identical to allow a correct alignment. However, if there is a slight difference in pitch, the MLA image on the system pupil will be moved. This may be corrected with a field lens after the micro-lens array.

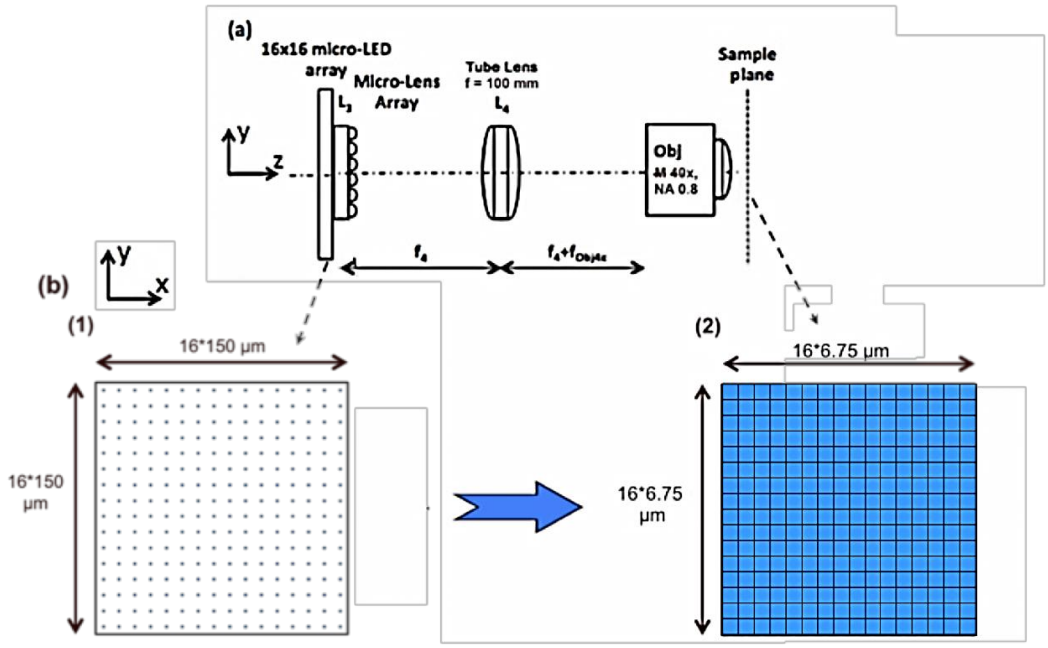

Figure 7-1: Principle of the integrated MO on the MLA

While more reliant on alignment during manufacture, this system is easier to use and simpler to develop than "PO 2" as there are no RO between the MLA and the MO and therefore they have an identical pitch. This characteristic means that the main optical aberrations are coming from the MO only, which, because of the size of the micro-lenses in the MO (150 or 80µm pitch), should be small.

7.1.2 Technology and requirements

Each micro-lens is placed at the focal distance of each micro-LED, which corresponds to the distance between the bottom principle plane of the micro-lens to the quantum layers of the micro-LED, which is where the light is emitted in every direction in the LED. shows the design schematic of the bottom of a micro-LED emitter with the quantum layers next to the p-contact. It has a mesa shape. The "flat" emitter from Tyndall has this shape, however the ratio of the etch depth over the diameter of the mesa is very low (~0.09) just as the mesa angle θ. Micro-LED emitters with reshaped back electrode have a ratio above 0.3 and a higher mesa angle θ.

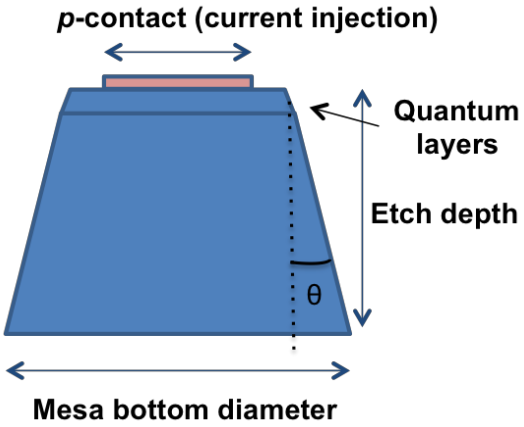

Figure 7-2: Schematic design of a micro-LED emitter.
The light is emitted at the quantum layers, which are placed just below the p-contact. The variation of etch depth, mesa top diameter and bottom diameter influences the light emission distribution

When the back electrode is flat, the light distribution approximates well that defined by Lambert's law, with a high percentage of the light lost inside each layer of the LED due to internal reflection. The reshaped back electrode developed by Tyndall allows of part of the light, which would be generally lost, to be recycled and it also decreases the angle of emission (22° angle of view)[94]. This light distribution was measured and supplied by Tyndall. A micro-lens is placed on top of each micro-LED to collimate the light outside the LED even further so that it can be projected into the following system aperture.

The position of the micro-lens relative to the LED quantum layers depends on each layer of the LED and micro-lens (see Figure 7-3). The materials used for each micro-LED are Gallium nitride (GaN), InGaN and Fused silica, which is an amorphous (non-crystalline) substrate. The p-contact is made of Palladium and the fused silica has a Titanium coating on the back. The quantum layers are made of $In_{0.24}Ga_{0.76}N$ and GaN layers. Tyndall's fabrication process fixes the thickness of nearly all the layers, apart from the thickness of the GaN. The GaN wafer thickness is either 350µm or 320µm, when unpolished, though it can be polished down to 100-150µm. Below this thickness, the material becomes too fragile. This parameter influences the light distribution obtained and it will be used to optimise the coupling with the MO. The modelling does not take into account the electronic and thermal interactions happening within the quantum layers and the rest of the LED that may have an incidence on the way the light is emitted.

Figure 7-3 shows a schematic of the MLA and micro-lens. The micro-lens is composed of two parts, its substrate that can be made of glass or plastic (PMMA, PET…) and the micro-lens itself, made of a UV curable lacquer (see Chapter 3:). Some parameters, such as the substrate thickness, the substrate's and UV-lacquer's refractive indexes, depend on the manufacturer. The micro-lens parameters, such as the radius of curvature and therefore the focal distance, are the key parameters that can be chosen.

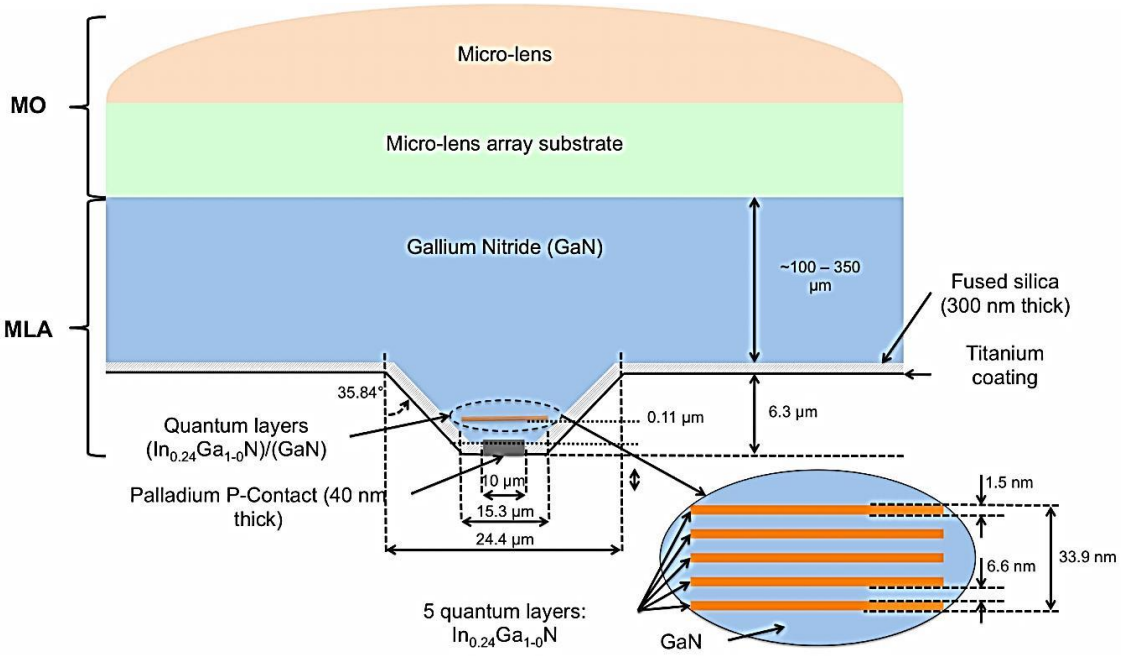

Figure 7-3: Schematic of the MLA and MO integrated together

Therefore, the variables for this system are:

- MLA: GaN layer thickness: between ~100 and 350µm
- Micro-lens substrate: Material (refractive index n) and thickness
- Micro-lens: Material (refractive index n) and radius of curvature (and therefore focal distance and NA)

Tyndall developed two types of MLA. The first is a 16 by 16 array with 150µm pitch that was used since the beginning of the project. The second one is a 90 by 90 LED array with 80µm pitch. It was chosen, as it was the smallest pitch that could be manufactured and bonded to a CMOS substrate reliably by Tyndall. The emitter size and geometry is identical in the two designs (see Figure 7-4). But the fill-factor of the emitting area at 80µm is increased by a factor $\sim(150/80)^2 = 3.5$. Additionally, for an identical focal distance, a micro-lens would have its NA decreased by a factor of $\sim(150/80) = 1.9$.

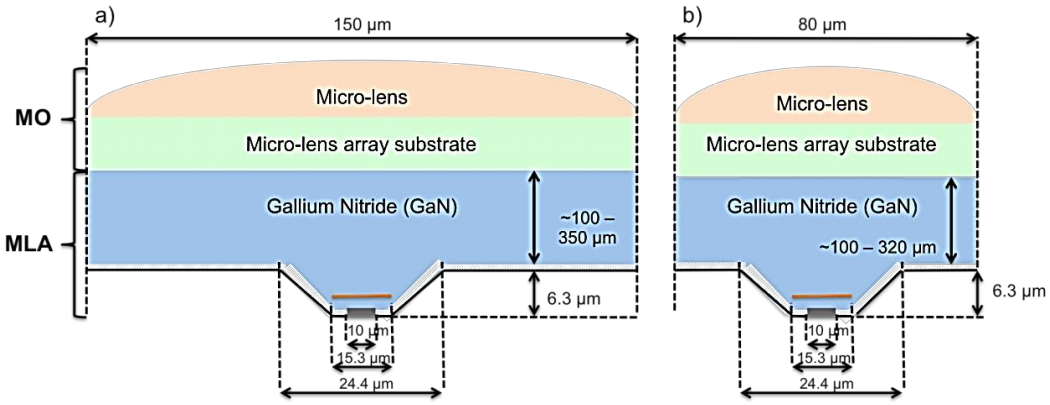

Figure 7-4: Size of single emitter MLAs
a) 150µm width and pitch LED with integrated MO and b) 80µm width and pitch LED with integrated MO

Tyndall has a second possible design for the MLA with 80µm pitch. This design uses a thinner layer of GaN (~6.3µm) and a layer of Sapphire instead of a thick layer of GaN (see Figure 7-5). The refractive index of the sapphire is 1.67 and that of the GaN is 2.47. Therefore, the sapphire will be optically thicker than the GaN. However the Sapphire suffers the same fragility as the GaN when the thickness goes down to below 100µm. The starting Sapphire wafer thickness is 440µm. The design of the micro-lenses should fit both these two possible MLA designs.

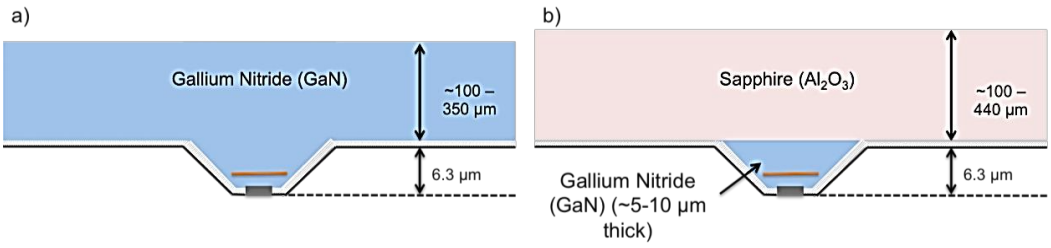

Figure 7-5: Schematic of 80um pitch single emitter MLAs
a) Traditional GaN MLA structure and b) Backup wafer (Al_2O_3) with a thin layer of GaN

The idea for the integrated micro-optics is to attach it to a microscope system first. As the focal length of the micro-lens is limited by the micro-lens diameter (150 and 80µm) and by the difficulty of manufacturing lenses with high curvature, the micro-lens focal distance was optimised such that the image of the micro-leds will fill the aperture of a low magnification microscope objective (4x, 0.16NA). For higher magnification lenses the objective pupil will in general be smaller and so modifications to the projection system from the MO to the objective pupil might be necessary – effectively reducing the tube-lens focal length – so that the image of the micro-led still passes through the objective pupil. Most of the lacquers and micro-lens substrates have refractive indexes that are around 1.5-1.6. Using the characteristics of the material used in the off-the-shelf MO used in "PO 2", a focal length of around 0.3mm with 0.25 NA was calculated.

A simple relay may be used to decrease the image of the MLA at the pupil of the microscope objective, increasing at the same time the image at the sample. Its magnification M corresponds to the magnification of the image at the sample. The NA of the collimated beam is relatively close to zero and therefore nearly little optical aberration is added by basic relay optics and no complicated designs are necessary. Table 7-1 shows how the magnification of a basic relay optic system can modify the size of a pixel at the sample for 150 and 80µm pitch MLA with different microscope objectives.

M (microscope Objective)	NA (Microscope Objective	M (Relay Optics)	Pixel Size for a 150µm pitch Micro-LED array (µm)	Pixel Size for a 80µm pitch Micro-LED array (µm)
4	0.16	1	37.5	20
10	0.2	2	30	16
20	0.4	2	15	8
40	0.8	2	7.5	4

Table 7-1: Variation of the size of the pixel size with the use of relay optics between the integrated micro-optics and a microscope

7.2 Micro-lens array fabrication

In Chapter 3:, the embossing method was described and its choice justified. Three MO manufacturing companies were investigated:

- Epigem.ltd (UK)
- Crealas (CH)
- Glyndwr Innovations (UK)

Epigem and Crealas are working together, as Crealas is making the master and the nickel shim, used on the replication process, for Epigem. The two are using glass substrates and would make a single sample available at a time. One of the possible drawbacks of this method is the resulting thickness of the glass substrate.

Glyndwr Innovations is doing master drums instead of the flat masters supplied by the other suppliers. The master drums are steel with copper plating. Depending on its thickness, the drum may be used two or three times before being re-plated. Concave shapes are cut into the drum to be able to replicate convex shapes. A flexible material, such as a plastic sheet (PET or PMMA), needs to be used here as the micro-lens substrate. Here, an A4 size PET sheet is used. The lens patterns are hand-casted casted on 30*55mm strips. These dimensions correspond to the most practical size as the drum rotates.

The first solution described above was quoted between £12000 and £20000 for only a few samples for each of the micro-lens. The solution proposed by Glyndwr Innovations is quoted at £8000 for 3 sheets (30*55mm) for each pattern, providing more than 200 and 28 samples for the 16 by 16 (150µm pitch) and 90 by 90 (80µm pitch) micro-lens arrays. The thickness of the PET substrate can vary between 0.175 and 1mm, as the material needs to be flexible.

This second solution was therefore chosen for the micro-optics development. The substrate thickness was fixed at 175µm by the end of the development, as Glyndwr Innovations supplier was not manufacturing other thicknesses of this material anymore. This particular PET substrate was developed with a coating that improves the adhesion of the UV-lacquer on the PET.

7.3 Modelling

The modelling was separated into three parts and is described in this section. First, the MLA was modelled and the results compared to measurements with a real device. Then, the MO were considered and their integration onto the MLA was modelled. Finally, the different systems, without MO and with off-the-shelf and custom MO and RO, were compared.

7.3.1 Micro-LED model development

All the Tyndall micro-LED designs used the same materials to emit at 470 nm apart from one where most of the GaN layer was replaced by an aluminium oxide (Al_2O_3) (see 7.1). The emitting layers are composed of 5 layers of $In_{0.25}Ga_{0.75}N$ and GaN. Light is emitted when a current is passed through them in forward bias. The P-contact is made of Palladium (Pd). Below the GaN and around the P-contact is an insulating layer of 300nm thick silica layer (as an electrical insulator) with a titanium (Ti) coating on the outer side. The refractive indices and absorption coefficients for each material were found on the website: http://refractiveindex.info or supplied by Tyndall, such as eg for $In_{0.25}Ga_{0.75}N$ and Al_2O_3.

Modelling in non-sequential Zemax

Tyndall supplied the geometry of the micro-LED with a reshaped back electrode. It is identical at 150 and 80µm pitches. The software "Zemax" is used to model the LED. The non-sequential mode (NSC) was mainly used as light is allowed to propagate in all directions in this mode, and therefore reproduces behaviour closer to reality, like internal reflection inside the LED, the reflection of the light on the reshaped back electrodes and the shape of the emitter, which is a volume that could emit in every direction and from every position in it.

Most of the required geometries can be created in directly within Zemax, however CAD designs can be added for specific shapes such as for the silica and GaN (see Figure 7-3). Apart from silica, all the materials have to be created in Zemax. Values of the refractive index from ~400-450nm to 700nm are entered and then values like n_d, V_d and the coefficients of the dispersion formula are calculated in the software to determine the behaviour of the light in a specific material. The fitting formula used is called the Sellmeier equation and is one of the most used formulas to define the dispersion of light in a transparent medium as a function of "n" and "λ" (see A.7) [131]:

$$n(\lambda)^2 - 1 = \frac{K_1\lambda^2}{\lambda^2 - L_1} + \frac{K_2\lambda^2}{\lambda^2 - L_2} + \frac{K_3\lambda^2}{\lambda^2 - L_3} \quad 7.1$$

Where $K_{1,2,3}$ and $L_{1,2,3}$ are Sellmeier coefficients.

The modelling was limited to a 3x3 micro-LED array due to the complexity of the design, the number of sources, the number of objects and the number of rays used for the simulation, as the simulations need a lot of computer resources to run. Typically of order 5 million rays would result in acceptable model performance.

The emitting layers of the micro-LED

The aim of the following simulations is to determine the most efficient and easy way to design a MLA that gives a result close to the distribution measured with the real device. The Zemax simulations are used to test the different solutions in order to design a system. The emphasis is placed on finding a working solution and no importance is placed on the mechanism applied by Zemax to determine the solution at this stage. There are two ways to design the emitting layers. Either the 5 layers of $In_{0.25}Ga_{0.75}N$ and those of the GaN are designed separately as shown in Figure 7-3, or these layers are regrouped in one layer and an equivalent refractive index is calculated as a function of the volume occupied by each of the materials. The diameter of the emitting layers is modelled as being the same as the P-contact, 10µm (see Figure 7-3). From the data given the five layers consist of 28.4% $In_{0.25}Ga_{0.75}N$ and 71.6% GaN. The variation of refractive index in the visible is then calculated as $0.716*n_{GaN}+0.284*n_{InGaN}$ and is shown in see Figure 7-6.

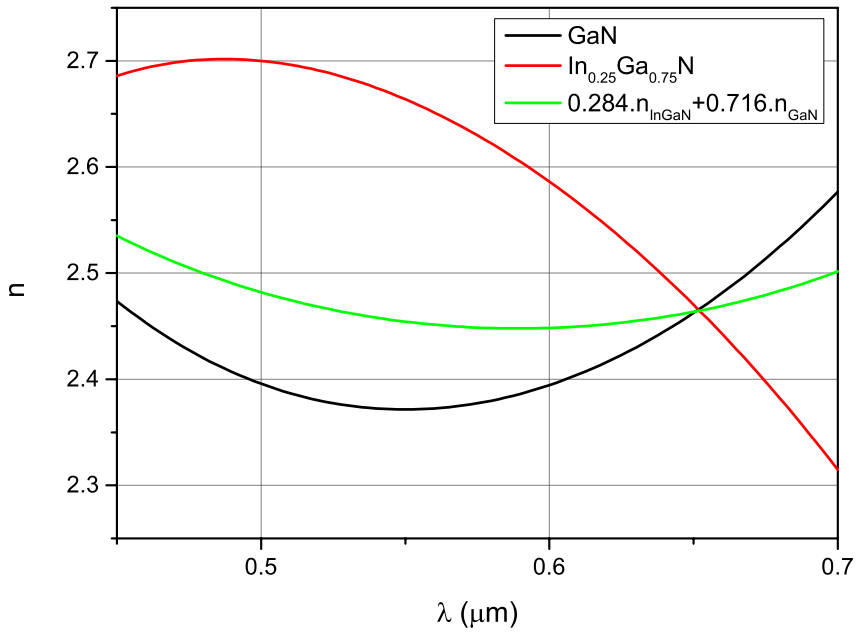

Figure 7-6: Refractive index variation in the visible for GaN, In0.25Ga0.75N and a combination of the previous layers in one layer (28.4% of In0.25Ga0.75N and 71.6% of GaN)

These two designs were simulated. A chequerboard illumination was chosen, as it is useful to see how the micro-lenses are filled and if there are issues with crosstalk from on-pixels to off-pixels. In order to reduce computer memory requirements and computation time a 3 by 3 LED array was modelled to see how the micro-LEDs were behaving together.

The design with separated emitting layers, which is closer to the real one, gave a result nearly identical to the distribution measured and supplied by Tyndall on the real device (see Figure 7-7). The other approximate model gave a wider angular distribution that was far from the reality.

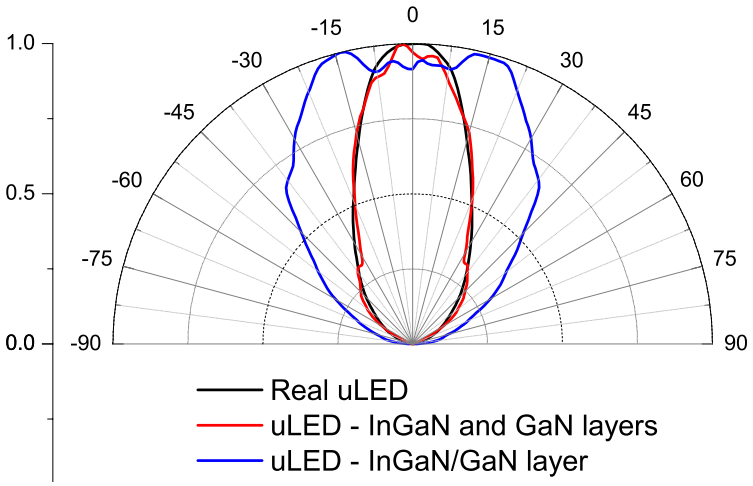

Figure 7-7: Light distribution at 470nm of the real MLA and of the simulated MLA designs

To understand how this is happening, the number of InGaN layers was modified from one up to 5, the number of InGaN layers used in reality, to see how the distribution varied. Figure 7-8 shows that the number of layers does not influence the light distribution when their thicknesses are not modified.

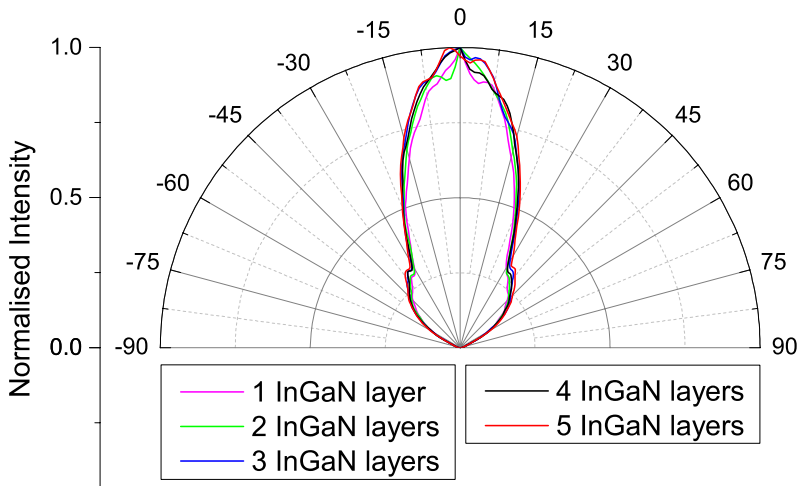

Figure 7-8: Variation of the distribution with the number of identical layers of InGaN

The number of layers does not seem to influence the distribution, but the thickness of the layers does. Therefore, the thickness of one InGaN layer was varied from the original thickness (1.5nm) to a maximum thickness equal to the total thickness of the block of layers in the real model (33.9nm). Figure 7-9 shows that the distribution becomes wider with the increase of its thickness.

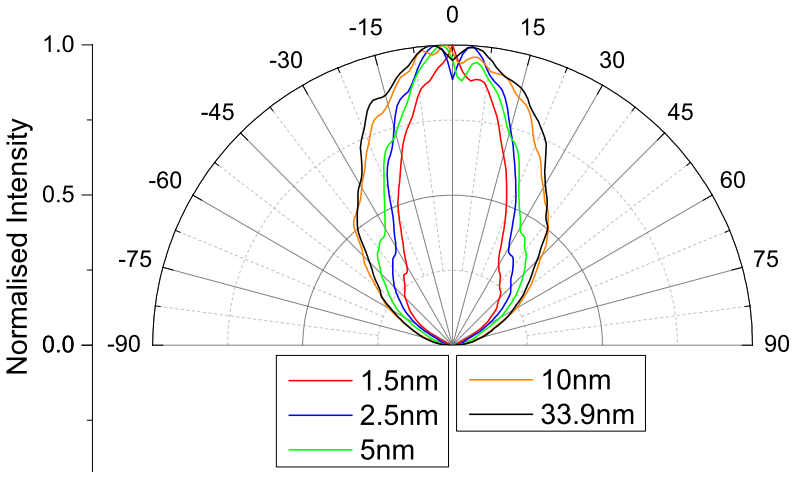

Figure 7-9: Variation of the light distribution with the thickness of one layer of InGaN

The thickness of the InGaN layer influences the distribution in Zemax. This explains the wider distribution obtained in Figure 7-7 even so the percentage of InGaN and GaN was kept identical in the material created. The simplest way to design this LED is therefore to use one layer of InGaN with 1.5nm thickness.

When imaged, the correct model gives an image very close to the one obtained in reality (see Figure 7-10). Furthermore, another important characteristic of the illumination is shown: that the image now has significant structure in it. This was not the case in the previous simplified model, where the light source was emitting light homogeneously over its entire area. In the inhomogeneous case the disk of light at the centre corresponds to the emitting layers. The ring of light at the edge, which is brighter, corresponds to the light reflected on the reshaped back-reflector. This light is redirected forward instead of being totally reflected, decreasing the effect of light lost due to TIR in the device and increasing the efficiency compared to micro-LEDs with a conventional design.

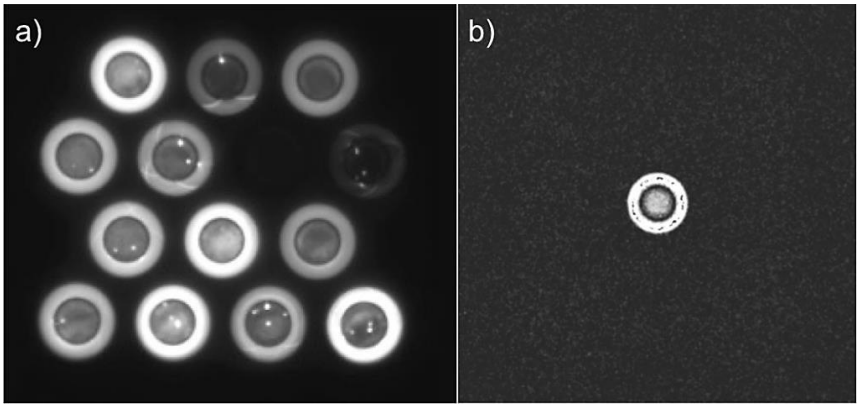

Figure 7-10: Imaging of a real cluster of LEDs (a) and of simulated LED (b)

Modelling of an emitter following the Lambert's emission law

In addition, a more traditional design of an LED with a flat back electrode was modelled in Zemax (see Figure 7-11). The emitter is designed to have the same apparent diameter as that with the shaped back reflector, where the emitter has a 10μm diameter but an apparent diameter of 24μm due to the reshaped back electrode. Therefore the emitter layers have a diameter of 24μm.

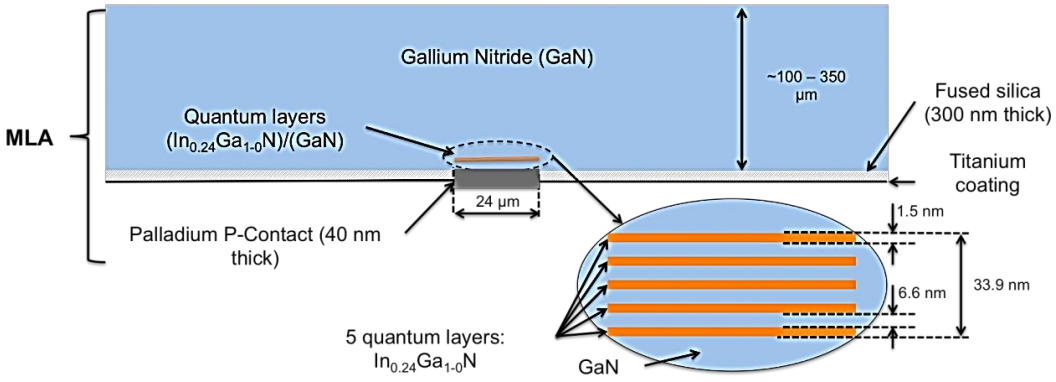

Figure 7-11: Flat LED design schematic

The simulated distribution obtained is close to a Lambertian distribution and to the one demonstrated using the Snell-Descartes's law (see (see Section 6.2.1.4 and Figure 7-12). It proves that these models give realistic results.

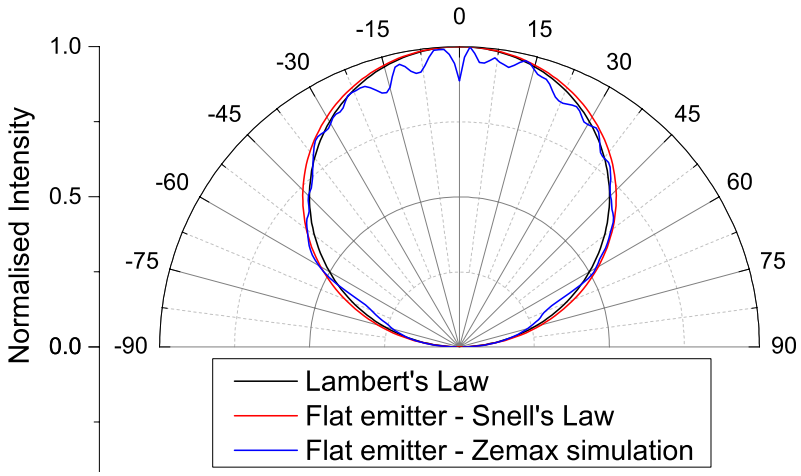

Figure 7-12: Light distribution of a simulated flat LED

The flat emitter and the shaped emitter were compared for the same internal power output. For similar characteristics, such as the GaN thickness (100µm), Tyndall's shaped LED design is more efficient with ~1.4 times more light measured outside the MLA (11.22W vs 7.83W) and a peak of intensity ~4 times higher than with the conventional emitter (29.8 vs 7.41 kW/cm^2). Less light is lost on the edge of the MLA as well (see Figure 7-13). The fact that the difference between peak intensity is higher than the total amount of light outside the MLA shows that a lot more light is emitted in a forward direction from the light recycled on the back-reflectors.

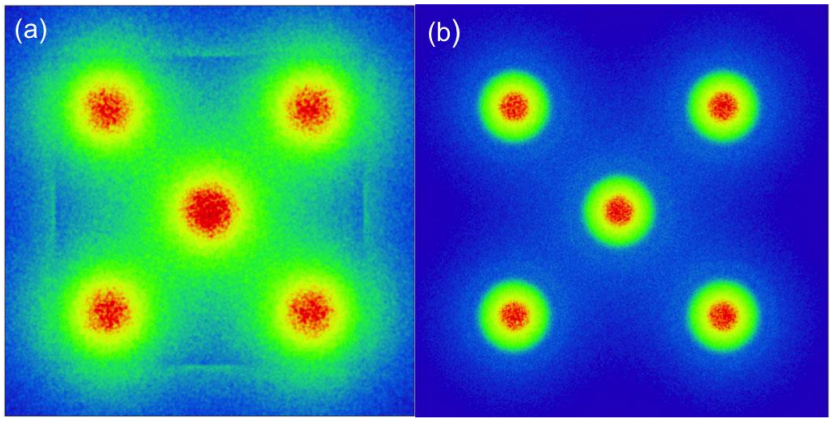

Figure 7-13: Light distribution at the surface of a MLA using a 100µm GaN substrate
(a) Lambertian emitters and (b) Tyndall new emitter with 22° angle of view for an identical thickness of material

Modelling of the LED arrays developed by Tyndall

As outlined in 7.1, the two MLAs have been designed with pitches of 150µm of 80µm. The small pitch size was chosen to give as many pixels as possible on the device (90x90), but was ultimately limited by the smallest pitch that could be flip-chip bonded. Additionally, Tyndall chose to use sapphire (Al_2O_3) as a possible back-up solution if the usual structure of the LED were to cause problems (see Figure 7-5). Here the light distribution of these 3 designs is compared. The simulation is showing similar light distributions at 150 and 80µm pitches (see Figure 7-14). The third design, composed of a thin layer of GaN and a thicker sapphire layer to keep the optical path length constant, gives a distribution that nearly matches the two previous designs. It differs only at wide angles, where the intensity is less important. The difference of refractive index between these two materials at 470nm (1.67 and 2.45 for Al_2O_3 and GaN) is high enough to cause TIR of the widest-angle beams at the interfaces GaN/Al_2O_3 and Al_2O_3/air instead of only the GaN/air interface. The light is then recycled by the back reflector and emitted forward. In the simulation, the peak intensity simulated on top of the MLA reached 6.1 W/cm^2. This is nearly twice the peak obtained for the design with only GaN (3.35 W/cm^2). It confirms that this design allows for more light to be recycled.

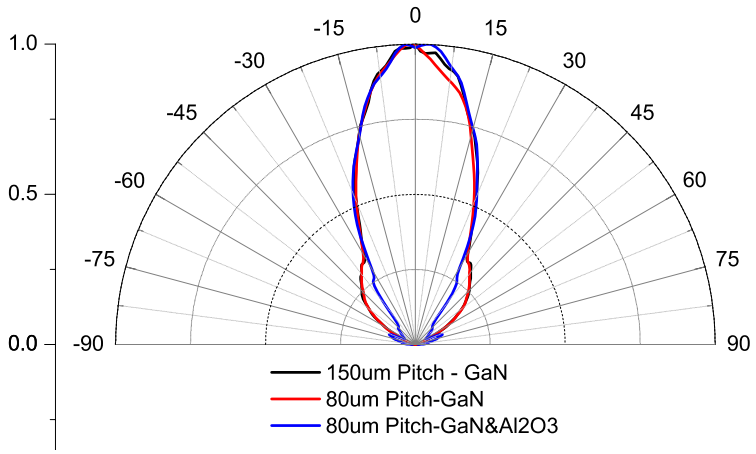

Figure 7-14: Light distribution of the MLA developed by Tyndall

The 150µm pitch 3x3 MLA was modelled with the specific design from Tyndall and it matches well the characteristics of the real device. Additionally, a 150µm pitch 3x3 MLA with a conventional LED design was modelled and it matched the expected distribution, close to the one defined by Lambert's emission law. The other Tyndall MLA design models are therefore expected to match the real devices. This is useful for the optimisation of the design of these MLAs, when coupled with MO.

7.3.2 Micro-optics model development

The goal of the MO here is the same as before (see 7.1). However its optimisation requires the modelling of the MLA that is coupled with it. One parameter is modifiable in the MLA, the thickness of the GaN or sapphire layer. The MO characteristics should ideally have been all variables, but some of them were fixed due to manufacture constraints. Choosing a specific radius of curvature set its focal distance. The choice is made using three criteria. The first is the fact that the lens can't be more than half a sphere. The second is the increase of manufacture tolerances for high radius of curvature lenses. The third is chosen so that light goes through the objective pupil.

The MO will be first tested on a microscope platform. It is therefore optimised for a 4x microscope objective with a 0.16NA operating with a standard tube lens. Other objectives with higher magnification (which would generally have a smaller physical aperture) can be easily accommodated either by decreasing the tube lens focal length or by including a simple set of relay optics. Note that in this case the demands on the relay optics are much reduced compared to those in chapters 5 and 6 as the light is now nearly collimated and hence has a low NA. It is important that the projected image of the micro-LEDs must be smaller than the objective pupil as the results shown in Figure 7-10 indicate that the bulk of the power is in a ring at the edge of the micro-led image. First, the method used to calculate each parameter to obtain a collimated beam outside the system MLA/MO is explained. Then, the materials used and the different limitations set by the manufacturers are described. Finally, the resulting simulations for each MLA designs from Tyndall are shown.

Theory

Choice of the MO parameters:

The calculations to find the best MO follows the same principle as in Chapter 3:. The microscope characteristics are used to deduce the optimised micro-lens characteristics.

The diameter of the pupil of the microscope objective corresponds to the maximum filling of this aperture by the MLA image. Larger images will mean losses at the objective pupil. The *focal length of the micro-lens array* $f_{\mu L}$ for this diameter is calculated using the formula below:

$$f_{\mu L} = \frac{\emptyset_{\mu LED}}{\emptyset_{IP}} * f_{TL} = \frac{\emptyset_{\mu LED}}{2.f_{TL}.(NA/M)} * f_{TL} = \frac{\emptyset_{\mu LED}}{2.(NA/M)} \qquad 7.2$$

Where $\emptyset_{\mu LED}$ and $\emptyset_{IP}$ are the diameter of each micro-LED and of the pupil of the microscope objective for a particular magnification *M*, *NA* and tube lens. f_{TL} is the focal of the manufacturer's standard tube lens inside the microscope used. $\emptyset_{IP}$ can be calculated with f_{TL}, *NA* and *M*.

A 4x (0.16NA) objective was chosen for the design. Material parameters, such as the refractive index of the lacquer used for the MO: n_{470nm} = 1.518, are described later in this chapter. $f_{\mu L}$ will therefore be 305µm.

The sag at the centre of the lens was calculated for a circular and a square micro-lens. For our system, a square micro-lens is developed. As shown below, the sag of the square micro-lens is higher as it is calculated for a diameter equal to the diagonal of the micro-lens square ($\emptyset_{\mu L} * \sqrt{2}$).

$$Sag_{Circular-\mu L} = R_C - \sqrt{{R_C}^2 - \left(\frac{\emptyset_{\mu L}}{2}\right)^2} \quad 7.3$$

$$Sag_{Square-\mu L} = R_C - \sqrt{{R_C}^2 - \left(\frac{\emptyset_{\mu L} * \sqrt{2}}{2}\right)^2} \quad 7.4$$

The maximum NA of a micro-lens is, in theory, when the micro-lens shape is half a sphere. The radius of curvature of the micro-lens R_c is then equal to the radius of the micro-lens. The maximum R_C for circular MO is therefore 75 or 40µm for 150 and 80µm diameter MO, respectively. For square MO, the maximum R_c corresponds to the diagonal of the square lens. Therefore, R_c is $r_{\mu L}(square) = r_{\mu L}(circular) \times \sqrt{2} = (150/2) * \sqrt{2} = 106.1\mu m$ or $r_{\mu L}(square) = (80/2) * \sqrt{2} = 56.6\mu m$. The minimum focal distances for square MO are therefore $f_{\mu L} = R_C/(n_{\mu L} - 1) = 0.204$mm and 0.109mm with $n_{\mu L}$ the refractive index of the lacquer. Our preferred focal length of 0.305mm is therefore larger than this and the lenses can be manufactured.

This system has the same limits as the projection optics developed in the previous chapters. Most of the losses occur at the MO pupil and at the pupil of the microscope objective. Figure 7-15 shows the evolution of the theoretical collection efficiency at the sample with the focal distance of 150µm pitch MO, with a 4x/0.16NA microscope objective. For a homogeneous illumination, the optimal position is found when both MO and objective and pupils are overfilled. However in the real device, the illumination is not homogeneous with most of the light emitted at the edge of the apparent emitter (see Figure 7-10). The focal distance of the MO is therefore optimal when the objective pupil is filled or slightly under-filled.

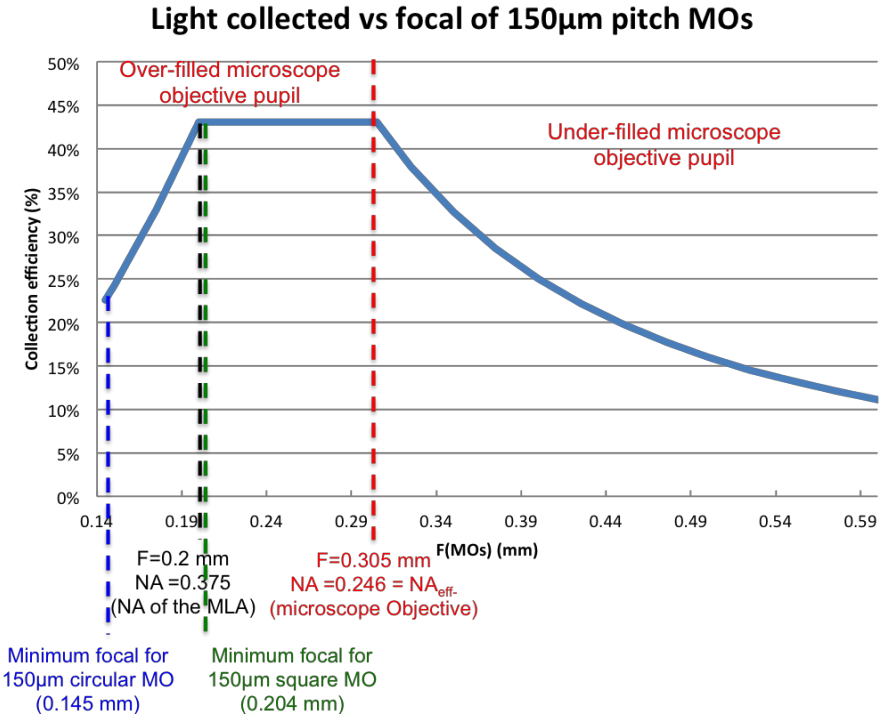

Figure 7-15: Calculation of the variation of the quantity of light on the sample plane with the focal length of the MO for a homogenous illumination with a 4x (0.16 NA) microscope objective

The MO are optimised for a low magnification microscope objective. The NA of the MO would need to decrease to fit the aperture of a microscope objective with higher magnification (see A.8). A relay optical system can be added between the system MLA/MO and the microscope to decrease the size of the image of an LED at the pupil of the microscope objective. The magnification necessary for the relay optics (M_{RO}) can be calculated by comparing the size of the image of the LED at the pupil of the microscope objective (I_{Pupil}) to the pupil's actual size ($\emptyset_{Pupil}$). M_{RO} is deduced from the formulas below:

$$I_{Pupil} = \frac{f_{TL}}{f_{\mu L}} . \emptyset_{\mu LED} \qquad 7.5$$

$$\emptyset_{Pupil} \approx \frac{NA}{M} . f_{TL} . 2 \qquad 7.6$$

$$M_{RO} = \frac{I_{Pupil}}{\emptyset_{Pupil}} = \frac{M . \emptyset_{\mu LED}}{f_{\mu L} . NA . 2} \qquad 7.7$$

Where $\emptyset_{\mu LED}$ and $f_{\mu L}$ are the diameter of a micro-LED emitter (24µm) and the focal length of one micro-lens of the MO, M and NA, the magnification and the NA of the microscope objective and f_{TL}, the focal of the tube lens in the microscope.

With a 40x (0.8 NA) microscope objective and a standard 180mm tube lens focal length, the image at the pupil is two times bigger than the pupil aperture of the microscope objective and therefore relay optics with two times magnification is necessary. It multiplies by two the sizes of the micro-lens array on the sample (see Table 7-1). The light outside the MLA and MO is nearly collimated and therefore the NA very low. Thus, the quantity of optical aberrations introduced by the optics here will be very low. A simple RO made of two achromatic doublets will be sufficient.

Thickness of each layer in the MLA/MO system

An important parameter to take into account in the development of this system is the thickness of each layer of material the beams are going through. Our goals for the beam at the edge of a micro-lens can be summarize as shown below:

- The exit beam should be collimated
- This collimated beam should be at the edge of the micro-lens, as the micro-lens needs to be filled.

These parameters need to be estimated before beginning any simulation in sequential or non-sequential Zemax. The method used for this estimation is explained in A.9. The thickness of the GaN layer is determined using either paraxial rays or with a marginal ray using trigonometry and the Snell's-Descartes law. The final angle in the air is fixed at 0, as the beam should be collimated. The source is considered a point source for these calculations. The two values obtained are different as one puts the paraxial rays in focus and the other puts the marginal rays in focus, therefore this gives a range of values that should be close to the optimised thickness obtained with a wider light source.

Note that the schematic in A.9 shows a MLA/MO system composed of three layers (MLA substrate, MO substrate, MO polymer). However, the number of layers may be increased when sapphire is used as the MLA substrate, as GaN is still present around the emitters. The number of layers might also have to be increased to compensate for the manufacturing limitations of the MLA and MO substrates thicknesses. The company manufacturing the MO ultimately only had a 175µm thick substrate and the thicknesses of the unpolished wafers used for the different MLA were: 350 or 320µm for the GaN wafer and 440µm for the sapphire wafer. This means that a 4th layer of material may be necessary to obtain a collimated beam outside the MO and therefore have the emitting layers at the focal distance of the MO. The calculation principle stays the same whether three or four layers are used.

MO Materials

MO are composed of two materials, a substrate and a polymer layer. The substrate used is Polyethylene Terephthalate (PET) with a refractive index of $n_{PET} = 1.608$ at 470nm (see dispersion diagrams in A.10). A client of the company manufacturing the MO developed the polymer and the datasheet was not available. A few centilitres of the lacquer were sent to us. However, this lacquer must be cured with UV light to transform it into a solid sample with a refractive index equal to that of the MO. Thin flat, transparent films are required to measure the refractive index of the material with an abbe refractometer. The measurement is done with a matching fluid to improve the contact between the thin film and the refractive prism of the device.

The Abbe refractometer gives a reading of the refractive index n_d and dispersion value *Z*. The refractive index n_d corresponds to the refractive index of the material at the Sodium line (589.3nm). Several values are taken for each; their average calculated and values *A*, *B* and M are principal dispersion coefficients deduced from a dispersion table supplied by the Abbe refractometer manufacturer [133] using n_d to determine *A* and *B*, and *Z* to determine *M*. $(n_F - n_C)$, which is called the principal dispersion, can then be calculated with the formula:

$$n_F - n_C = A + B.M \qquad 7.8$$

Where n_F is the refractive index at the Hydrogen F line (486.1nm), n_C, the refractive index at the Hydrogen C line (656.3nm)

The dispersion of the material as described by its Abbe value can then be calculated using:

$$V_d = \frac{n_d - 1}{n_F - n_C} \quad 7.9$$

Light dispersion in the visible can also be described using the Cauchy law.

$$n(\lambda) = C + \frac{D}{\lambda^2} \quad 7.10$$

Where $n(\lambda)$ is the refractive index for a wavelength λ, and C and D are coefficients that can be determined for a material by fitting the equation to measured refractive indices at three known wavelengths.

Combining equation 7.10 with equation 7.8, we get.

$$n_F - n_C = \left[C + \frac{D}{{\lambda_F}^2}\right] - \left[C + \frac{D}{{\lambda_C}^2}\right] = D.\left[\frac{1}{{\lambda_F}^2} - \frac{1}{{\lambda_C}^2}\right] \quad 7.11$$

The factors C and D can then be deduced as:

$$D = \frac{n_F - n_C}{\left[\frac{1}{{\lambda_F}^2} - \frac{1}{{\lambda_C}^2}\right]} \quad 7.12$$

$$C = n_d - \frac{D}{{\lambda_d}^2} \quad 7.13$$

Four samples were measured and an average refractive index was obtained (see Figure 7-16). From the equations 7.12 and 7.13, D was found to be $(5.249 \pm 0.088).10^{-15}\text{m}^2$ and C, 1.4941 ± 0.0003. The Cauchy formula for this material is therefore:

$$n(\lambda) = (1.4941 \pm 0.0003) + \frac{(5.249 \pm 0.088).10^{-15}}{\lambda^2} \quad 7.14$$

Hence, its refractive index at 470nm is: $n(470nm) = 1.5179 \pm 0.0007 \approx 1.518 \pm 0.001$.

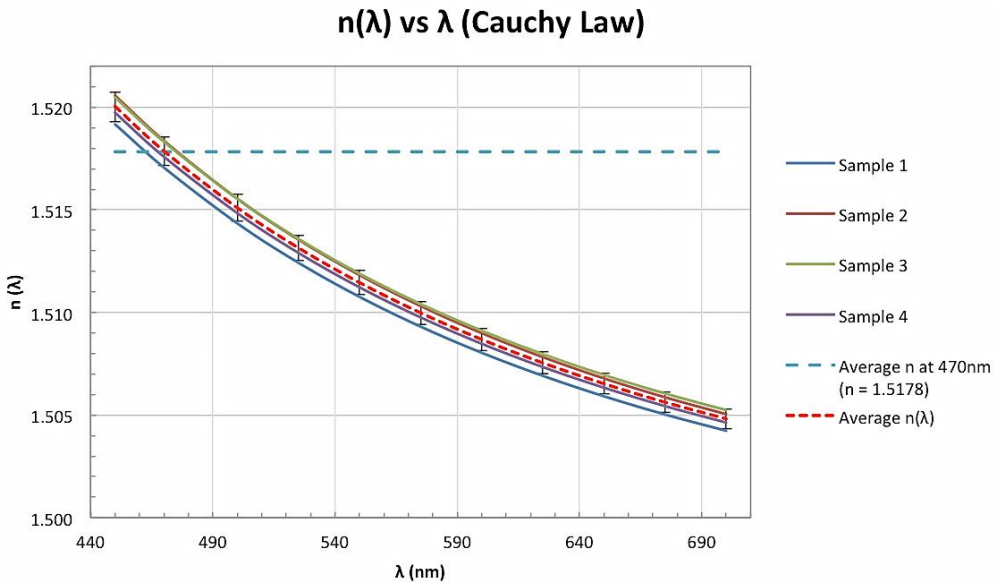

Figure 7-16: Dispersion diagram for the MO UV cured polymer material

As explained just before, a spacer may be required to set the MO at the correct distance from the MLA emitting layers. Glass cover slips from VWR made of Borosilicate glass (Schott D263) (see dispersion diagram in A.10) are available with different thicknesses (130 and 160µm) and can be used as a spacer. The refractive index is $n_{D263} = 1.531$ at 470nm.

Modelling

There are three MLA designs. The design of the custom integrated MO is therefore separated in three sections. The first and second ones are for the 150 and 80µm pitch MLA with a substrate made of GaN only. The third one is for the 80µm pitch MLA with a substrate made of GaN and Sapphire (Al2O3). During the development, two important limiting parameters were added due to manufacturing requirements:

- MO substrate (PET): Fixed to 175µm thickness
- GaN wafer: An unpolished wafer, 350µm thick, was used with the 150µm pitch MLA and a 320µm thick one was used with the 80µm pitch. These wafers are polished when integrated in a MLA package. This means that the real maximum thickness for these wafer are 20 to 50µm thinner.

In sequential Zemax, a micro-lens can be optimised alone or within an array for an approximate distribution and an estimation of the aberrations can be made. In non-sequential Zemax, details such as light distribution, size of the sources and interactions between each surface are taken into account, allowing a representation closer to the real device. As with the projection optics system, "PO 2", the integrated MO system was integrated to a double microscope system with an aperture equivalent to the pupil of an Olympus 40x (0.8NA) microscope objective (see Figure 5-16). A 3x3 MLA was modelled with every second LED switched on in a chequer board pattern (see Figure 7-17).

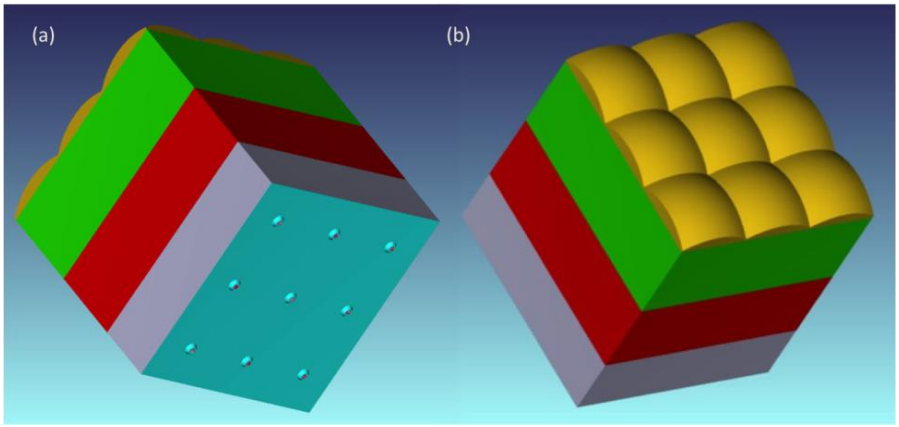

Figure 7-17: Model of a 3x3 GaN 150µm pitch MLA with integrated MO
The back of the model is shown in (a) with the fused silica and titanium back reflectors (blue). The MO are shown in (b) (Yellow). The GaN material (grey), the spacer (red) and the glass substrate (green) can be seen as well.

150µm Pitch GaN MLA

Tyndall optimised the MLA without MO and thinned the GaN wafer to 130µm, limiting the number of variables to the MO only. Additionally, the MO substrate thickness was restricted to 175µm. It leaves only the MO polymer thickness. Using the paraxial formula, a radius of curvature $Rc \approx 85.4\mu m$ is calculated if no spacer is used. This is below the minimum Rc feasible ($106.1\mu m$) and would in any case over-fill the objective pupil. Therefore, a spacer is necessary between the MLA and the MO to be able to manufacture the system thicknesses for an optimal focal length of 306µm ($Rc = 159\mu m$). The sag at the centre of the micro-lens was calculated at 40.4µm, and the residual thickness of lacquer below the shaped micro-lens is generally under 10µm.

The thickness of the polymer was fixed to 45µm, 40.4 for the micro-lens and the thickness left for the thin layer below it. As for the spacer, a cost effective and quick solution can be a thin glass plate. Cover slips from VWR are made of borosilicate glass (D263 Schott) and have thicknesses at a range of values below 200µm. The spacer thickness was then optimised with the same material and values between 128 and 217µm were obtained with the Snell-Descartes law (marginal focus) and the paraxial formula. With a circular lens, the value is closed to 152µm. A common cover slip thickness (160µm) was then selected between these two values. The radius of curvature of the micro-lens was therefore re-optimised for best focus with this spacer thickness using Zemax in sequential mode, where paraxial rays and marginal rays are considered simultaneously. In this model, the MLA/MO system was modelled in reverse with a collimated light beam directed on a micro-lens, which then focused it through the different layers of the system to a point corresponding to the point source (LED emitter). Values between 154 and 165μm were obtained for the optimal radius of curvature.

The simulation was therefore set with these parameters directly in NSC Zemax as nearly all parameters were fixed apart from the focal distance of the MO. The MLA/MO system was added within the experimental set-up used with the previous projection optics (see Figure 5-16). A constant power of 1W was fixed per source emitting layer with 5 micro-LEDs switched on and five emitting layers per micro-LED, making it a total power of 25W. The power was measured at the sample plane and compared for Rc between 156 and 166µm using 250000 rays for each simulation. The highest total power was obtained at $Rc = 162\mu m$ (see Figure 7-18).

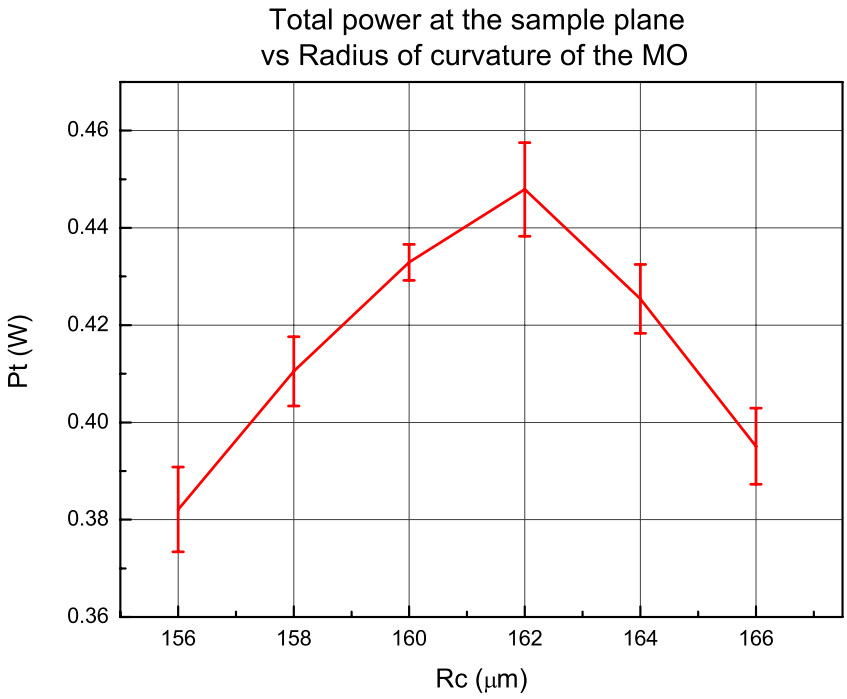

Figure 7-18: Simulated total power variation at the sample plane of the experiment set-up (see Figure 5-16) with the MO radius of curvature

The parameters were fixed and the number of rays increased to 10 million. The images of the MLA obtained before and after the pupil of the microscope objective (see Figure 7-19) shows that the system is optimised to go through the pupil of the objective without much loss. Additionally, the inhomogeneity of the micro-LED illumination distribution can be observed.

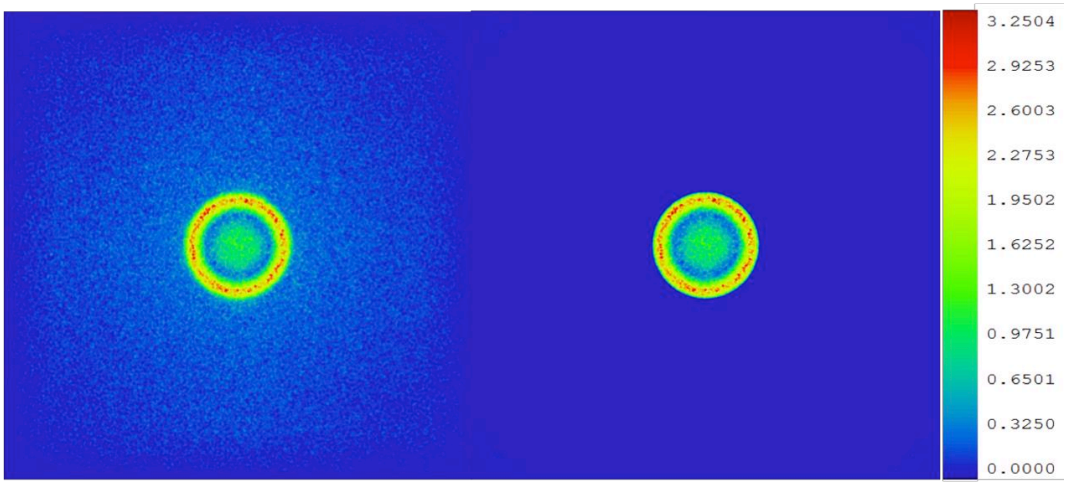

Figure 7-19: NSC modelling of the 150μm MLA image before and after the pupil of the microscope objective (left and right)

On the sample plane, the MO is imaged. The result with custom MO is homogeneous over each micro-lens apart from a slight decrease of the intensity in the corners. This is due to the optical aberrations that are larger at the corners (see Figure 7-20) where the marginal ray focus differs most from the paraxial focus.

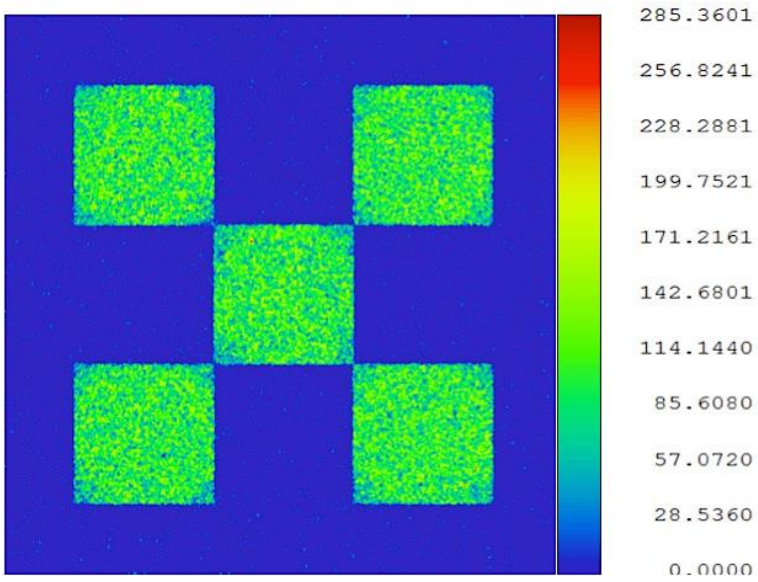

Figure 7-20: NSC modelling of the 150µm pitch MO on the sample

The far field light distribution for the MLA/MO system was simulated. The entire intensity is emitted through a cone of angles close to zero compared to that of the bare MLA. This shows how the light is nearly collimated outside the MLA as expected.

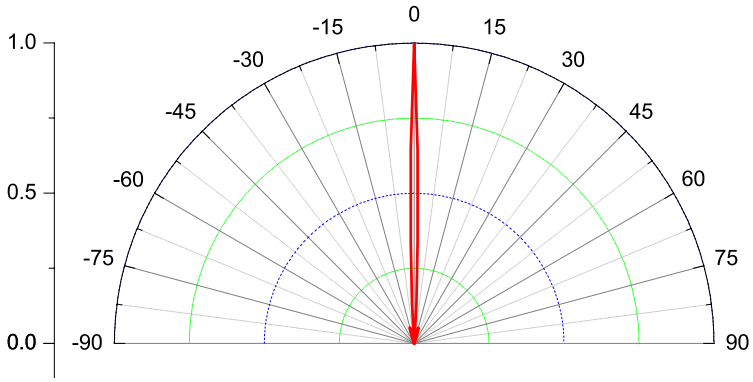

Figure 7-21: Far field light distribution of the MLA/MO system

The MO were ordered following the previous simulations. However, there is a parameter that was not taken into consideration and may influence the final result. A spacer was added between the MLA and the MO. In reality, an UV curable adhesive is necessary between the MLA and the spacer, and the spacer and the MO. A few flat films were made using a UV curable lacquer that can be attached to glass and plastic (Norland NOA-68). The sample thicknesses obtained were measured between 5 and 10µm. This means that the real system may be between 10 and 20µm thicker than in the simulation, and that a slightly thinner spacer might be required.

80 µm Pitch GaN MLA

With the GaN MLA, the wafer used was not polished to a fixed thickness and therefore it could be optimised for values between 100 and 280µm, as the unpolished wafer is 320µm thick. The MO substrate thickness was fixed (175µm). To make a set of tooling for a drum on which the MO are replicated, there is one important parameter, the radius of curvature (R_C). Different micro-lens diameters can be made with one set of tooling thus reducing the cost considerably. The radius of curvature was therefore fixed to the value obtained for the 150µm pitch MO optimisation, 162µm.

The only variable left is the GaN wafer thickness. The thickness of the MO was fixed at 14µm, as the sag of the lens is 10.2µm. The required GaN thickness was calculated to be above 400µm, which is more than the wafer thickness. A spacer is therefore essential to collimate the light.

The maximum thickness of the other wafer available (Sapphire) was not known at the time of the development, and in consequence, the same minimum and maximum thicknesses were set for the two wafers (between 100 and 280µm). 280µm was not thick enough with the two wafers, even though the Sapphire (Al_2O_3) wafer was 1.46 times optically thinner than the GaN wafer. A spacer was therefore required. A cover slip from VWR was selected. Two thicknesses were available, 130 and 160µm. With a 130µm spacer, a GaN wafer with a thickness between 248 and 260µm is required and a Sapphire wafer with a thickness between 174 and 183µm. With a 160µm spacer, thicknesses of ~205 and ~145µm were calculated. The first spacer was selected as the sapphire becomes fragile at thicknesses around 100-150µm.

In NSC Zemax, the thickness was varied between 210 and 280µm to obtain the highest power at the sample (see Figure 7-22). With these MO, the NA is lower than before because of the lower diameter of each micro-lens. The power expected should therefore be: $NA_{150\mu m}{}^2/NA_{80\mu m}{}^2 = 0.24^2/0.128^2 = 3.52$ times lower than with 150µm pitch MO. The difference obtained during the modelling is $0.4479/0.135 = 3.32$, which is very close to the value expected. The best result is obtained with a thickness around 246µm. However, the values obtained for thicknesses between 225 and 255µm are close and therefore it means that the ± 10µm manufacturing tolerance won't be a problem.

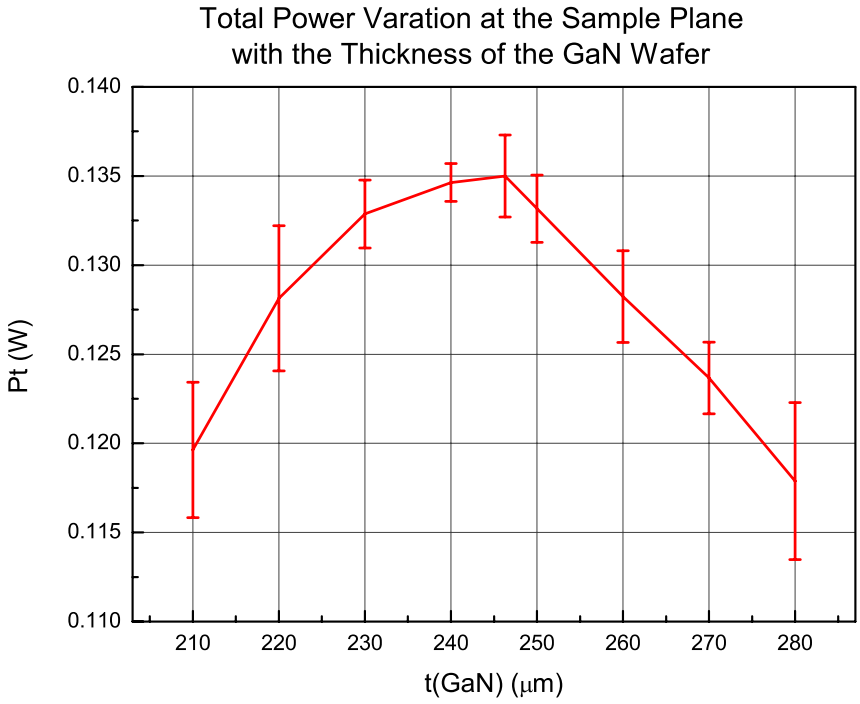

Figure 7-22: Modelling of the total power variation at the sample plane with the thickness of the GaN wafer

The set-up was imaged following the same method as that used with the 150µm pitch MO and the results looks similar (see A.11).

80 µm Pitch GaN&Sapphire MLA

The wafer thickness with the sapphire is 1.46 times thinner than with the GaN. It was optimised in Zemax to be between 316 and 325µm, which is feasible as the thickness of the unpolished wafer was revealed to be 440µm, not 320µm. No spacer is therefore required. This was calculated for the case where the GaN is completely replaced by the Sapphire. However, there is still a thin layer of GaN (6.3µm thick) where the light is emitted and the sapphire thickness required is therefore slightly lower (~316µm).

In Zemax, this thickness was varied from 270 to 340µm. The highest power was obtained between 290 and 310µm (see Figure 7-23). 300µm was therefore chosen as the thickness of the Sapphire (Al_2O_3). The ± 10µm manufacturing tolerance should not be a problem with this wafer.

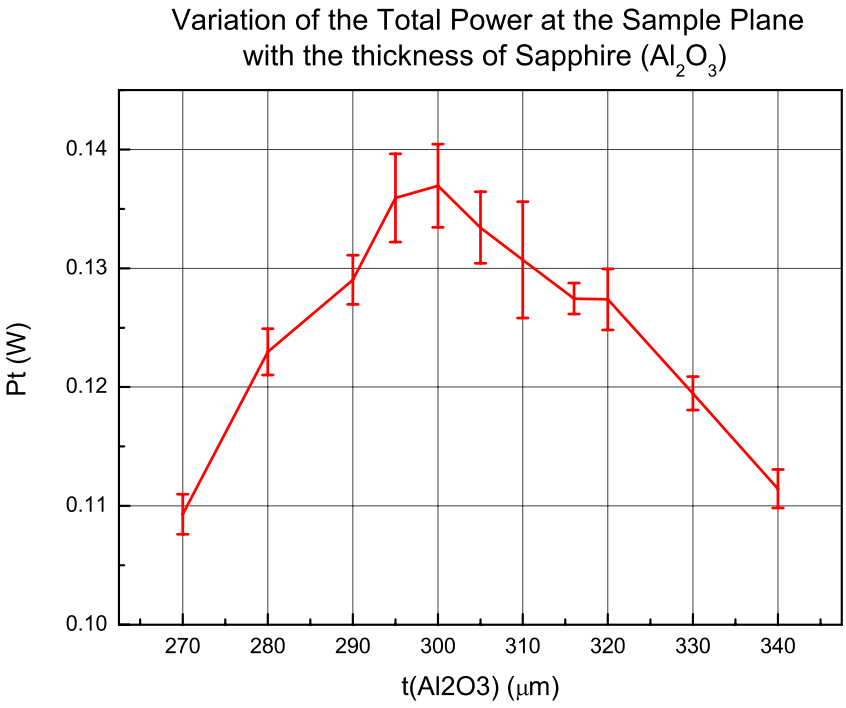

Figure 7-23: Modelling of the total power variation at the sample plane with the thickness of the Sapphire (Al_2O_3) wafer

The results look similar to the previous ones obtained with the 150 and 80µm MO with an MLA using a GaN wafer and are summarized in A.12.

The performances are expected to be higher with this MLA as no spacer is needed and therefore only one layer of the UV curable glue (Norland NAO-68) is necessary between the sapphire and the PET substrate of the MO, instead of two with the spacer. It means there is only one 5-10µm layer with a refractive index of 1.555 at 470nm.

Summary of MLA/MO designs

Three MLA/MO systems were developed for the MLA developed by Tyndall. The MO have all the same R_c (162µm) and therefore the NAs of these systems are $NA_{150\mu m} = 0.24$ and $NA_{80\mu m} = 0.128$. The difference is caused by the diameter of the micro-lenses in the MO (80 and 150µm). A spacer is needed for the GaN MLA as the wafer is not thick enough. The GaN/Sapphire MLA uses a thicker unpolished wafer, which is thick enough for the optimisation with the MO. Therefore no spacer is necessary with this system. The UV curable glue that will be used to stick together each device (MLA, spacer, MO) is from Norland [134] and glues both plastic and glass. Adding it adds another thickness (5-10µm) per applied layer.

7.3.3 Comparison of the MLA without MO, with PO (off-the-shelf MO) and custom integrated MO

In this section the simulation results obtained in sequential Zemax with a point source and in NSC Zemax with a model of the single emitter MLA with a light distribution close to the real one measured on a the real device from Tyndall are summarized and compared. The 150µm pitch MLA with reshaped back reflectors was used with the off-the-shelf MO in "PO 2". Thereby, systems using this MLA were compared. The MLA alone, with PO 2 and with custom integrated MO are studied.

First, the integrated MO is compared with PO 2 in sequential Zemax to see how they are performing at the pupil of a microscope pupil when coupled with a 180mm focal length paraxial lens similar to the tube lens used in Olympus microscope and a point source. The position of the furthest point for analysis was modified slightly to align it with a micro-lens in the array. The ray fan plots show that the achromatic aberrations are of the same order (<1000µm). However, in PO 2, high orders SA are seen and in the integrated MO, third order SA (see Figure 7-24 and Figure 7-25). Additionally, there is a small amount of off-axis aberrations in PO 2, which is not present in the other system.

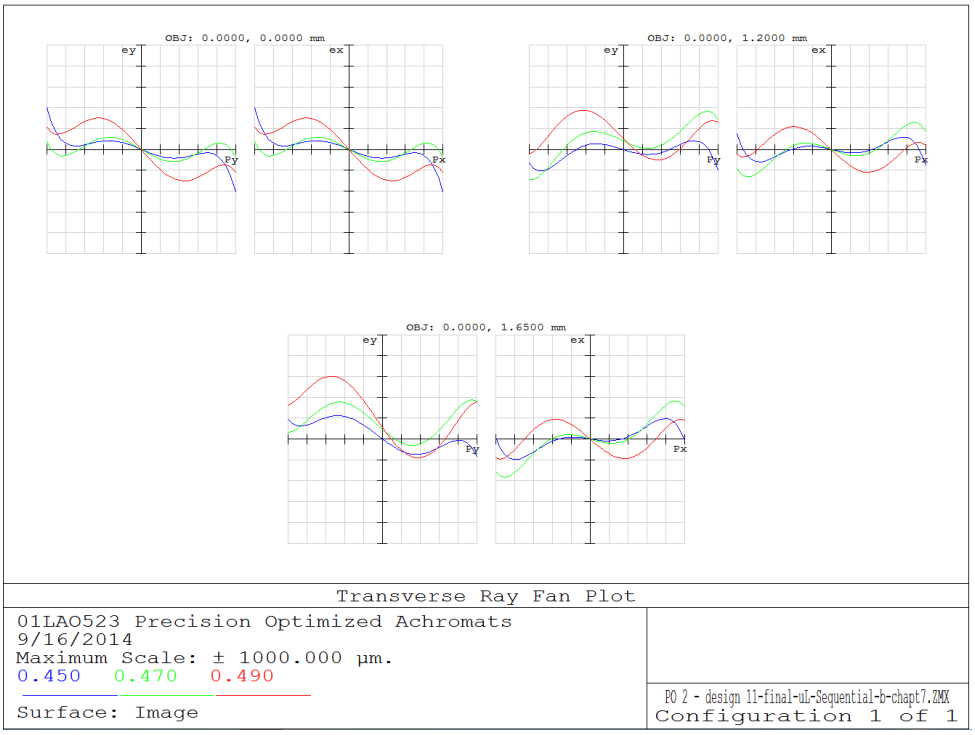

Figure 7-24: Transverse ray fan for PO2 (RO and MO) with a 180mm focal paraxial lens at the centre and edge of the field of illumination

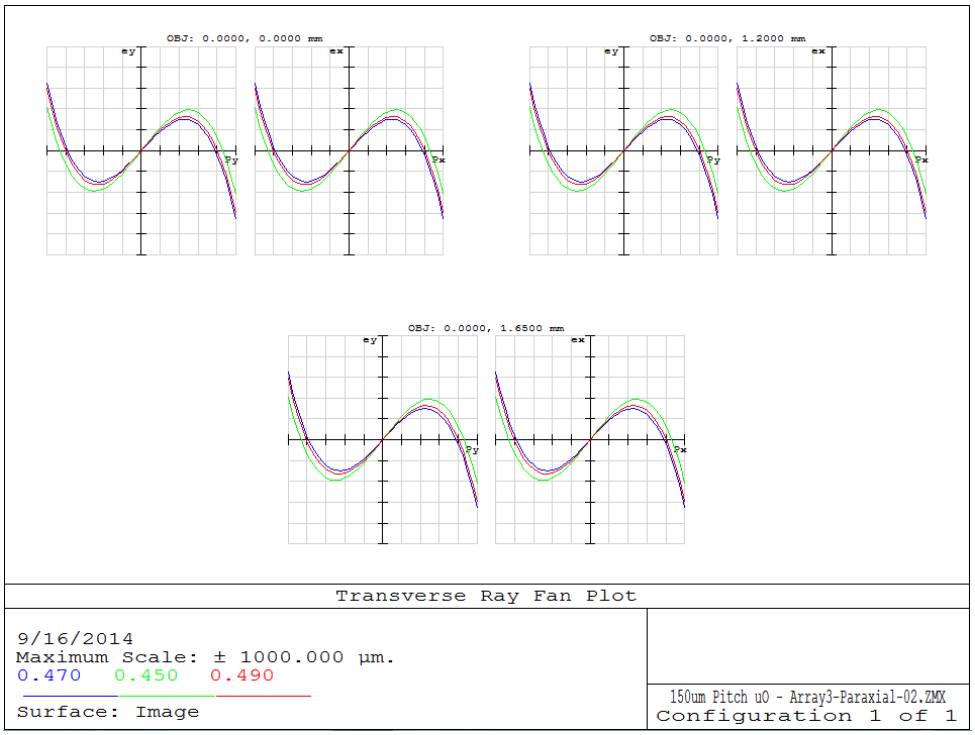

Figure 7-25: Transverse ray fan for the integrated MO with a 180mm focal paraxial lens at the centre and edge of the field of illumination

In NSC Zemax, the different designs are validated with the real MLA distribution connected to a microscope platform with a 40x/0.8NA objective. MO improved the illumination effectively by increasing its FF to nearly 100% (see Figure 7-26(b), (c) and (d)) compared to without it, where there is a high portion of the area that is not illuminated (see Figure 7-26(a)). The illumination looks slightly more homogeneous with the integrated MO.

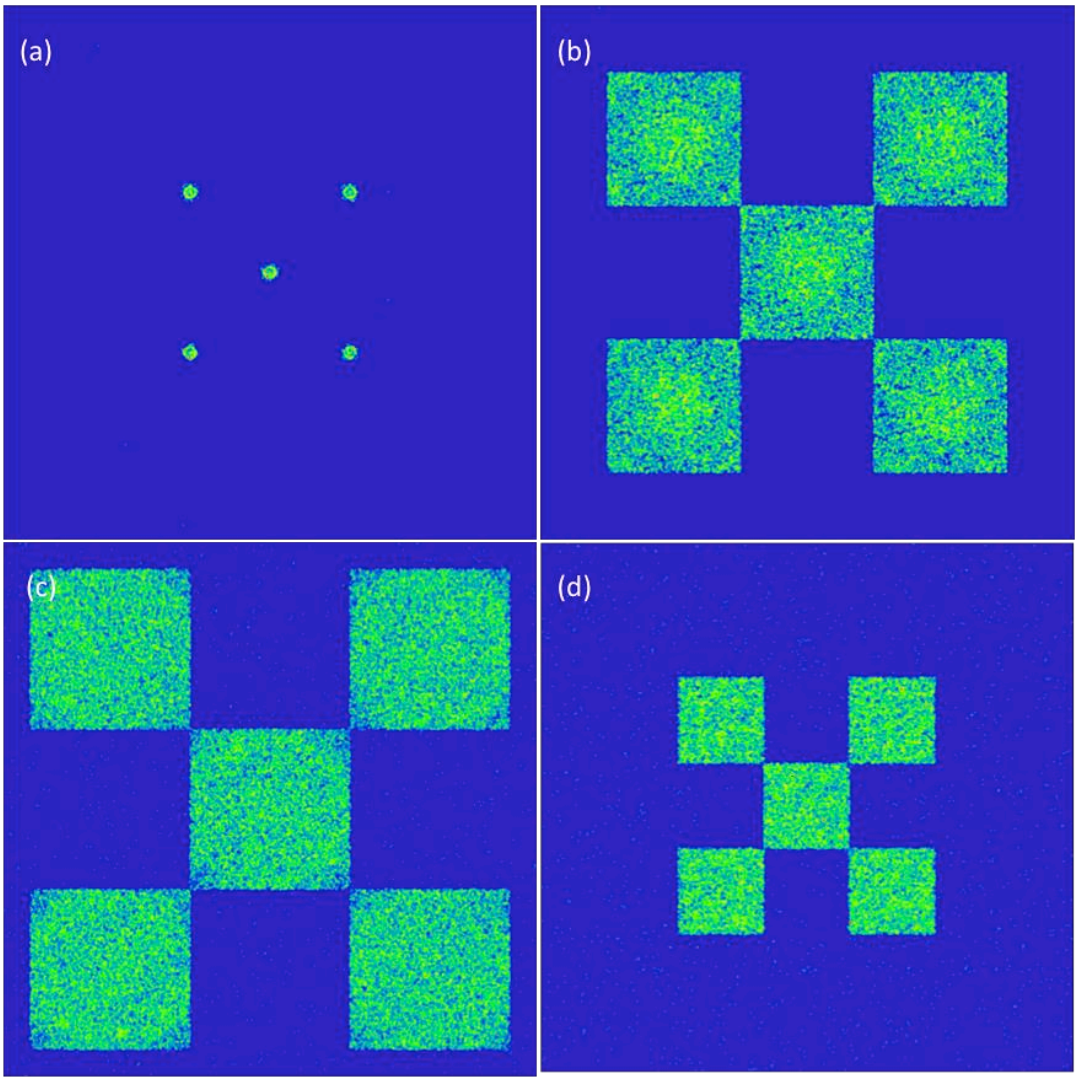

Figure 7-26: Modelling of the image at the sample plane for the systems without and with MO
MLA without MO (a), with "PO 2" (RO and off-the-shelf MO) (b) and with integrated MO (c). The scale is identical for the three images (25µm x 25µm). The image is smaller in (a) because the exact pitch of the MLA (150µm) is imaged. In (b), the image is larger as the MO has a pitch of 250µm, which is 1.67 time larger than (a), and here the MO is imaged instead of the MLA. In (c), it is larger still, even though the MO has the same pitch as the MLA, An extra stage of the relay optics is required between the MO and the tube-lens, increasing the magnification at the sample by 2 to let all the light through the pupil of the 40x/0.8NA objective. In (d), the MO is down to 80µm x 80µm to match the smaller MLA pitch. An extra stage of the relay optics between the MO and the tube-lens is required as in (c). The pitch on the sample for these four cases is therefore (a) 3.75µm, (b) 6.25µm, (c) 7.5µm and (d) 4µm.

Additionally, the simulated power obtained at the sample plane is multiplied by 64 times with PO 2 compared to the MLA without it, when a 40x/0.8NA objective is used, and 136.6 times with the integrated MO. It demonstrates that MO allow a high increase of the system efficiency.

7.3.4 Conclusion

Table 7-2 shows characteristics of these systems, such as expected collection efficiency, fill-factor, the size of the system and its cost. With a 40x/0.80NA, MO allow at least a 100 times improvement of the collection efficiency, to up to 140 times. With a 4x/0.16NA, the difference goes from 25 to 35 times. The collection efficiency without MO varies with the size of the pupil of the objective. This is not the case with the MO as there are optimised to not overfill the aperture of the pupil. This is important, as it means that the MLA won't need to be run as hard as without MO, generating therefore less heat and increasing the lifetime of the device at the same time. A high difference can be seen in the simulations with an improvement in system efficiency up to 136 times.

System	Micro-optics	Numerical aperture at MLA	Efficiency 4x/0.16NA objective (%)	Efficiency 40x/0.8NA objective (%)	Fill-factor (%)	System length (mm)
Bare MLA	-	0.04 (4x) or 0.02 (40x)	1.10	0.29	~2.2	<1
MLA + PO	Off-the-shelf ~€1400 each	0.208	30.90	30.90	~100	200
MLA + integrated MO (150µm pitch)	Custom ~€300 each at ~100 of	0.243	41.00	41.00	~100	<1
MLA + integrated MO (150µm pitch)	Custom ~€300 each at ~100 of	0.131	12.18	12.18	~100	<1

Table 7-2: Expected characteristics of the three different systems based on 16x16 micro-LED arrays (MLA)
Either bare, with a projection system to micro-lenses (PO) or with integrated micro-lenses (MO). Values for typical microscope objective lenses (40x/0.8NA and 4x/0.16NA) are shown.

Additionally the fill-factor is increased to nearly 100%, allowing a uniform illumination. PO 2 is generally bulkier and less easy to use than the integrated MO, which does not need a RO between the MLA and the MO to be adjusted. However the integrated device will require more precise alignment at the assembly stage. Relay optics can be used with the integrated MO system at higher magnification (M_{Obj} > 4x/0.16NA objective) to allow for all the light to go through. But it does not need to be as precisely adjusted as the RO of "PO 2", and a simple design suffices, as the NA needed is very low. In this case, the two system lengths should not be very different. As for the cost, price is generally higher for the integrated design as £9000 is necessary to manufacture a large array of custom micro-lenses compare to £1000 for the off-the-shelf MO. However, around 150 micro-lens arrays can be made from the custom arrays ordered for £9000 compared to 4 for the off-the-shelf array. This makes the price per MO for the custom-made arrays lower.

The modelling and characteristics summarized above demonstrate the advantages of integrating MO directly onto the MLA. It allows a higher NA to be used and therefore increases the collection efficiency of the system. As soon as the MLA and MO are assembled together, the system becomes a lot easier to use than the projection optics with off-the-shelf MO. Additionally, it can be coupled with simple RO to match the NA of the objective and therefore does not lose any light with the decrease of the effective NA of the objective.

Two versions of the 80µm pitch MLA were developed, one with a GaN wafer and one with GaN and Sapphire (Al_2O_3) wafer. Without MO, the last design seems to be slightly more efficient with less light lost at wider angles. However, with MO, no real differences were observed. The advantage of the Sapphire is here its maximum thickness (440µm), which is enough for its optimisation by polishing without the need of a spacer. Adding a spacer means that two layers of UV curable glue are necessary instead of one.

7.4 Integration onto the MLA

The custom MO were delayed and arrived only by the end of April. They are therefore not yet integrated onto MLA. However, several samples were provided as stated at the beginning of this chapter. Some were already given to our partner Tyndall for testing on the MLA using a sapphire substrate, which do not need a spacer.

The quality of the samples was tested and a few faults were noticed when imaged with a microscope (see Figure 7-27). The spot at the centre is caused by a limitation of the tooling used, which is a spherical shaped drill. At the centre the tool speed is essentially zero and so imperfect shaping always occurs here. A second fault can be seen only on the Figure 7-27(b) with the 150µm microlenses. Here it appears that there has been an issue of judder as the tool has been used to drill the deeper holes required for these larger pitched lenses. It is not clear yet how significant these issues are optically.

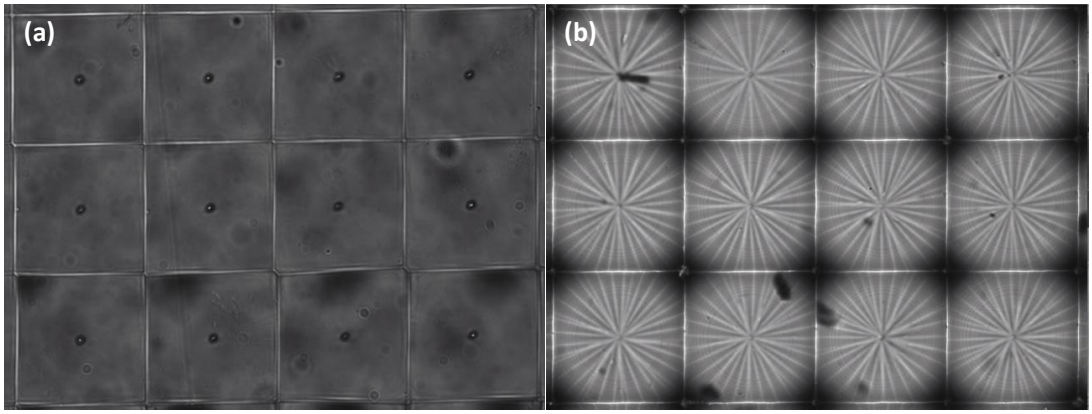

Figure 7-27: Manufactured custom MO
Pictures of (a)a 80µm pitch MO taken with a 20x (0.4NA) microscope objective and (b)a 150µm pitch MO taken with a 10x (0.16NA) microscope objective

7.5 Conclusion

In this chapter, the description of precise models of the MLA in NSC Zemax has been presented. The layer thicknesses in the MLA are optimised at the same time as the MO layers to collimate the light exiting the MLA and MO. The model of the 150µm MLA with a GaN wafer was compared to the real device and the far field and angular distributions matched closely, reproducing the increased but inhomogeneous illumination in the image of the MLA caused by the back-reflectors. Additionally, the Zemax simulations demonstrated the advantages of the MLA with back reflectors over the conventional design. Two 80µm pitch MLA designs were also produced. The MLA using a GaN and sapphire (Al_2O_3) wafer has a distribution that is slightly modified at wide angles. But otherwise, the distribution is similar to the one with the GaN wafer, which is identical to the design with a 150µm pitch.

The MLA and MO were coupled and optimised as a whole. $Rc = 162\mu m$ was fixed for all the MO as tooling for its manufacture is dependant on Rc and not the diameter of each micro-lens. Therefore the NA at 150 and 80µm pitch MLA and MO are: $NA_{150\mu m} = 0.24$ and $NA_{80\mu m} = 0.128$, which means that the collection efficiency will be divided by ~4 with the smaller diameter. No real difference was observed in the light distribution between the two different wafers available for 80µm pitch MLAs.

The different systems developed during this project, “PO 2” and the integrated MO system, were compared to the MLA without any MO coupled with a microscope system and the equivalent of the 40x/0.8NA objective. It was demonstrated that adding MO increases the collection efficiency and therefore allows the system to be used at lower current, thereby generating less heat and increasing its lifetime. The two systems using MO give a similar amount of optical aberrations. However, MO can be developed with higher NA as optical aberrations depend on the size of the lens and therefore, the integrated MO were optimised for a 4x/0.16 NA objective with an NA of 0.24 compare to 0.208 in “PO 2”. The collection efficiency should therefore be higher with the integrated MO.

Once assembled, the integrated MO system is a lot smaller and easier to use than “PO 2” as the MO is already aligned with the MLA and the magnification does not need to be adjusted in the RO as the MO have the same pitch as the MLA. It can be coupled to a simple RO with low NA to collect the collimated light from the MLA/MO system to match the effective NA of the microscope objective used and therefore not loose any light. This is due to the fact that the integrated MO is optimised to closely match the aperture of the 4x/0.16NA microscope objective.

The custom MO were received at the end of April. Preliminary observations of their quality were carried out before being coupled with spacers and then sent to Tyndall for coupling with the 16x16 150µm pitch and 90x90 80µm pitch MLA. The next steps will consist in testing the device MLA with integrated micro-optics and compare them to the theory (imaging quality and collection efficiency). Future work will involve further biophotonics experiments in conjunction with the project’s partners such as MPI, Newcastle University and FMI.

Chapter 8: Biological experiments

In the previous chapters, the development of two set-ups using MO was shown to improve specific characteristics of an illumination with MLA connected to a microscope platform, such as fill-factor and collection efficiency. The higher fill-factor means a more homogeneous illumination. The increase of the collection efficiency means that the MLA can be used at lower current. The end goal of all the development and implementation is to improve the stimulation of nerve cells transfected with ChR2. Patch-clamp and multi-electrode array (MEA) experiments were devised at our partner's labs at MPI, Newcastle University and FMI.

These experiments will help demonstrate the feasibility of an eye stimulation prosthesis by experimenting with virtual reality optics, eye models and by stimulating the retina of a living animal.

In particular the specific kinds of experiments that are typically undertaken at the three laboratories are:

1. *Max-Plank Institut (MPI) for Biophysics, Frankfurt*: Microscopy experiments investigating the temporal and optical characteristics of novel optogenetic constructs in cell culture. Recent developments in the Bamberg lab have shown promising new constructs either with enhanced temporal properties or sensitivity as well as tandem constructs including both excitatory and inhibitory pathways addressed with different wavelengths. We have designed and constructed a system specifically tailored for use in their conventional microscopy environment.
2. *Department of Electrical Engineering, Newcastle University*: Using optical models of the eye with extracted retinas and direct multi-electrode array recording. These experiments aim directly to test the principles of prosthetic sight restoration by optically stimulating opto-genetically modified retinas from mouse models. The experiments will use direct electrical recording of retinal neuron responses and optical stimulation via virtual reality optics such as might be used in a compact, wearable vision prosthesis.
3. *Friedrich Miller Institute (FMI), Basel*: In-vivo experiments exploring the spatio-temporal stimulation of vision impaired mice transfected to render parts of the retinal neural circuits light sensitive, and to track their stimulation back to the visual cortex. Important aspects of this work are the additional integration of the micro-LEDs with a fundus camera projection system to enable targeting of specific areas of the retina with defined moving patterns of light.

8.1 MPI experiments: Stimulating cultured cells in a conventional microscope

At MPI, one of the groups of the biophysical chemistry department directed by Prof. Ernst Bamberg is focusing its research on the study of the functional and structural analysis of the retinal binding protein channelrhodopsin 2 (ChR2) and its application in neuro and cell biology. This group was the first to describe ChR2, which has since become an essential tool in neurobiology. The genetic code for this protein can be inserted into neural cells in culture or in living animals and the ChR2 protein produced in the cells as a result can be stimulated by light alone in a non-invasive manner.

The micro-LED array allows both spatial and temporal control of the ChR2 stimulation. An experiment was therefore devised to verify if the micro-LED array coupled with projection optics (PO 2) could generate light induced current in a human embryonic kidney (HEK) cell transfected with ChR2, as measured with a patch-clamp set-up. The micro-LED array coupled with the projection optics was developed as a stand-alone kit that can connect directly on a microscope mount. If successful, the second step of this experiment is to stimulate action potentials with neurons transfected with ChR2.

8.1.1 Microscope set-up

The folded design was selected for this experiment, as space is limited on the microscope platform, which is inside a Faraday cage to allow for measurements of very low electrical signals without being perturbed by outside signals. In Figure 8-1, the schematic shows the microscope used by MPI and how it is coupled with the light illumination and the detection. The PO and a camera are connected to a beam splitter box (50/50 in Transmission/Reflection), connected itself to the camera port. This camera port is on the front of the microscope, a Zeiss Axiovert 40. A 0.5x converter was added originally to image the entire field of view on a 35 mm film camera.

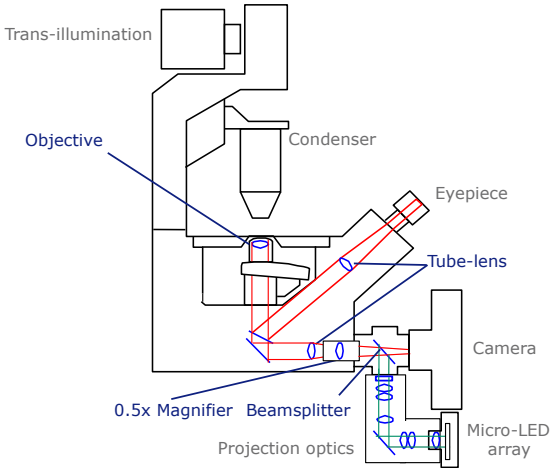

Figure 8-1: Schematic of the MPI experimental set-up using a Zeiss Axiovert 40 microscope

Figure 8-2 shows the set-up mounted at the MPI in Frankfurt.

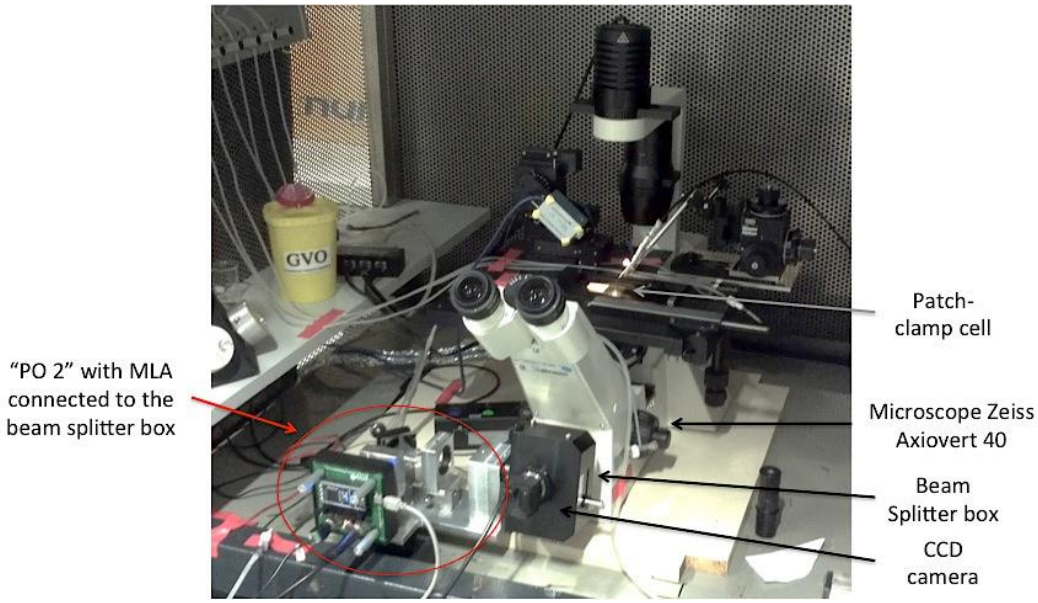

Figure 8-2: MPI patch-clamp platform with a Zeiss Axiovert 40 microscope and the PO attached to it

In this experiment, a cell is studied. Its size is in the order of 10s of µm and therefore 10x (NA 0.25), 20x (NA 0.3) and 40x (NA 0.5) microscope objectives were used with a preference towards 20x and 40x magnification. The beam splitter box has two positions. The first one uses a 50/50 beam splitter to split the image between the camera and the PO. It was helpful during the patch-clamp proceedings and the setting up of the PO. The second uses a mirror, which reflects 100% of the light from the PO.

With the 0.5x adaptor, vignetting could be noticed and therefore a plano-concave field lens (f = -100 mm) was used to correct it successfully (see Chapter 6.4.2 and Figure 8-3(a)). However, the imaging on the cell using illumination light from the PO was limited by internal reflection inside the 0.5x adaptor (Figure 8-3(b)). Additionally, the imaging quality was lower than expected with a high focusing difference across the array. It was therefore used on the first experiments but not on the latter ones.

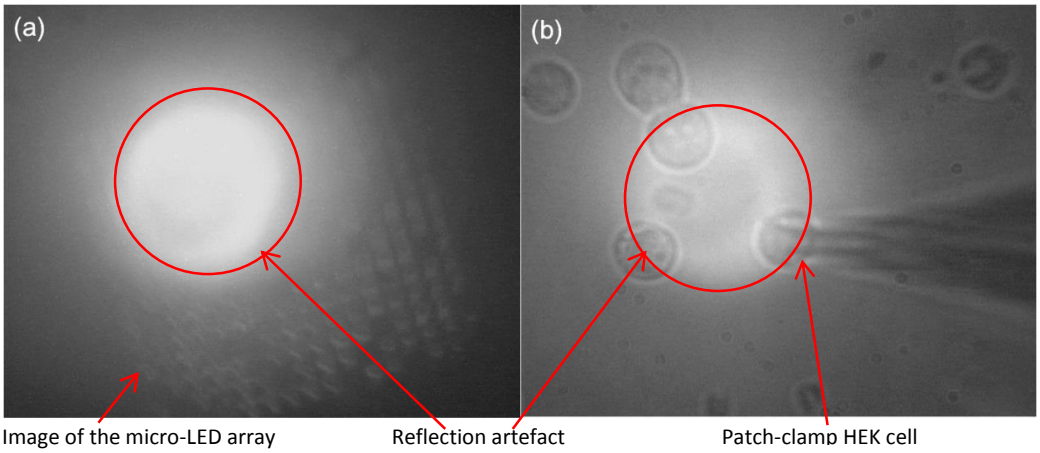

Figure 8-3: Internal reflections caused by the 0.5x adapter on the Axiovert 40
(a) Imaging of the MO on a fluorescent slide and (b) on a slide with HEK cells. Reflection artefacts inside the 0.5x adaptor are seen on the sample.

Without the 0.5x adaptor, the pattern was correctly imaged on the cell and less internal reflections was visible (see Figure 8-4). In Figure 8-4 (b) and (c), a second image of the micro-LED array is nearly visible on the right of the main image. It corresponds to the reflection of the light from the back surface of the beam splitter. The diffused light around the micro-LED array is caused by reflections at the air-glass interface of the glass slide where cells are sitting on within a solution. This reflection happens twice with the light illuminating the cell and the light reflected by the cell toward the camera causing a reflection of $R = [(n_2 - n_1)/(n_2 + n_1)]^2 \approx 4\%$ twice. It is still expected that the illumination at the sample is of high quality and that these artefacts are only a result of imaging through the same port as the illumination.

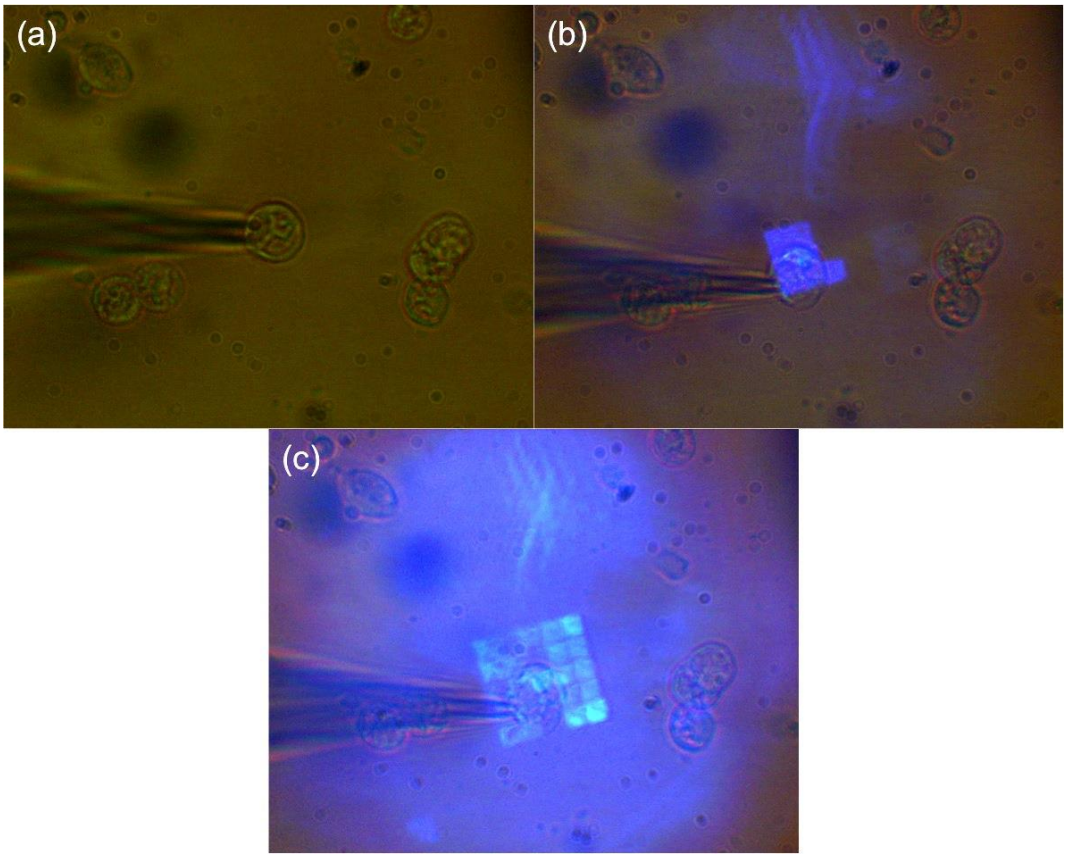

Figure 8-4: Patch clamp cell stimulation with a blue MLA
(a) Patch-clamp cell, (b) patch-clamp cell stimulated with 3 by 3 LED array with 7 LEDs working and (c) with 5 by 5 LED array covering the entire cell with 22 LEDs working.

8.1.2 HEK cells stimulation

Human embryo kidney cells (HEK cells) were used for this experiment as ChR2 is highly expressed in this type of cell. They do not fire action potentials, but they are used to verify how the light-induced current is modified by a specific stimulation in the so-called voltage – clamp mode, where the voltage over the membrane is controlled. Normally this is used to evaluate the performance of different light gated ion-channels and light activated ion-pumps, but here we use it to evaluate the performance of our illumination.

The light intensity variation has consequences on the strength of the peak of current. Figure 8-5 shows the results obtained in these experiments. The peaks represent the signals from the cell. Figure 8-5 (a) looks at the change in signal current with change of MLA drive voltage (note that a beam splitter is used here). The signal increases to a maximum value with the application of a reference laser pulse delivered from an optical fibre positioned above the sample, after which the targeted cell died or the patch clamp stopped functioning.

Figure 8-5 (b) shows the results using a 4x4 MLA switched on and off and driven at 3.5V through either a 50/50 beam splitter or a mirror. It was compared to a reference blue laser stimulation applied at a time point of just after 30 seconds. The first five peaks were measured with the beam splitter and are lower than the light–induced current generated just after by the laser pulse. The illumination of the MLA was then switched to the mirror. The power at the cell should therefore be multiplied by two. However, no signals were seen. Illuminating with a 14 by 14 LED array restored the signal to the same level it has with the beam splitter. The mirror position is therefore assumed to be aligned differently to the beamsplitter such that the image shifts by at least 37.5µm, making it difficult to target the cells precisely with the mirror.

The advantage of the MLA is the possibility to switch the LEDs to match the cell position, covering the cell properly without simulating neighbouring cells and therefore optimising the stimulation. In Figure 8-5 (c) we looked at the effect of changing the size of the array, from a 3x3 array, to 5x5 then 16x16 all driven at 3.5V and compared it to a laser reference. There is an increase of the light induced current between the 3x3 and 5x5 arrays. However, the signal remains nearly the same between the 5x5 and 16x16 array as the cell is already effectively illuminated.

The large signal that can be seen in Figure 8-5 (b) and (c) stems from the laser, which was used as a reference here. It is much stronger but not by a 100 times as suggested by the power measured at the sample plane (7.6µW vs 11.6mW). It's the signal response from the cell that depends on the intensity per area and the area illuminated by the laser is a lot larger than that illuminated by the MLA and PO. With a 40x and 0.5NA microscope objective, the power per unit area from the MLA was: $7.6\mu W/(4/40)^2 = 76mW/cm^2$.

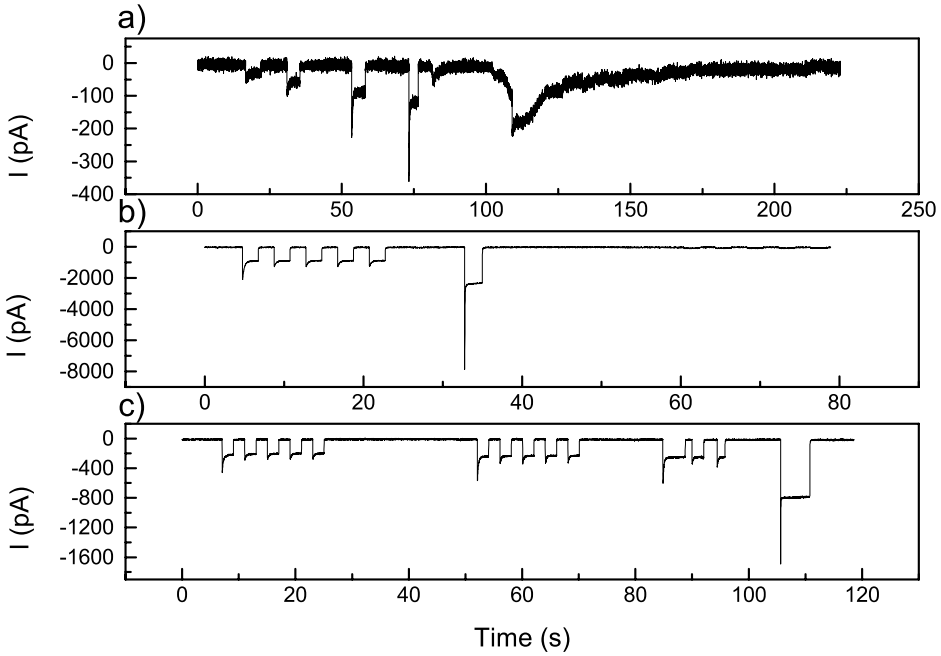

Figure 8-5: Cell stimulation: $I_{membrane}$ = f(time)

In (a) The entire MLA was switched on and its voltage increased from 2.75 to 3, 3.25 and 3.5V to stimulate a HEK cell transfected with ChR2. The increase of the light-induced current can be seen on the four pulses on the left of the diagram. After, the targeted cell died or the patch clamp stopped functioning. In (b), 4 x 4 LEDs from the MLA were switched on and driven at 3.5V. They were covering the entire HEK cell, generating a variation of the current in the membrane. The current variation generated by a reference laser pulse delivered from an optical fibre positioned above the sample is higher. After 40s in the measurement, the beam splitter box was switched from a 50/50 beam splitter, to target precisely the MLA on the cell, to a 100% mirror to increase the intensity of the light on the cell. No signals are then seen. This indicates that the position of the mirror is probably slightly off compared to the beam splitter position. In (c), the size of an array of LEDs switched on, on a MLA driven at 3.5V, is increased from 3x3 to 5x5 and 16x16. Several pulses are generated for each array, followed by a laser pulse. The light induced current increases with the size of the array until it covers the cell more or less completely.

These experiments show that the MLA with PO provides enough power to stimulate light-induced current in a HEK cell transfected with ChR2.

8.2 Newcastle University: MEA measurements and virtual reality (VR) optics

The experiment was carried out in the Neuro-prosthesis lab, which is a part of the µSystems group at the Newcastle School of Electrical and Electronic Engineering in partnership with the Newcastle Institute of Neuroscience. The Neuro-prosthesis lab primary interest is in developing neural stimulators and state of the art implantable systems for the field of optogenetic neuroprosthesis. The goal is to both generate new understanding in core neurobiology and use neuroinspired designs to make better circuits and systems. As for the institute of neuroscience, particularly Dr Evelyne Semagor's lab, the main focus is in neuroprosthetics & brain-machine interfaces and on testing the optogenetic prosthetic technologies developed in living retinal tissue.

The goal of this experiment was to use the single emitter MLA coupled with PO ("PO 2") to stimulate ganglion cells though a virtual reality lens (VR) and an eye model to reproduce the stimulation of ganglion cells inside the eye. Ganglion cells from intact mice retinas were used. They were set in an oxygenated solution to be kept alive during the experiment, which was placed on the top of a multi-electrodes array (MEA), where the potentials of each neuron close to each electrode are measured. The MEA is 8 by 8 electrodes with 200µm pitch. Four electrodes were not working, leaving 60 functioning electrodes.

Imaging through VR optics

The first step was to couple the MLA and PO with VR optics. Figure 8-6 shows a schematic of the set-up that is used to stimulate ganglion cells from a mouse eye. The MLA is coupled with the projection optics PO 2. Then an achromatic doublet lens is used to image the micro-lens array at the object plane of the VR optics (WF05 prism module), which then project an image of it on the back of the eye. Here, the ganglion cells on the MEA are placed at the back of the eye model. The MEA is placed horizontally so as to contain the liquid solution with the retina. Therefore the system was set to emit light vertically outside the VR optics using a mirror.

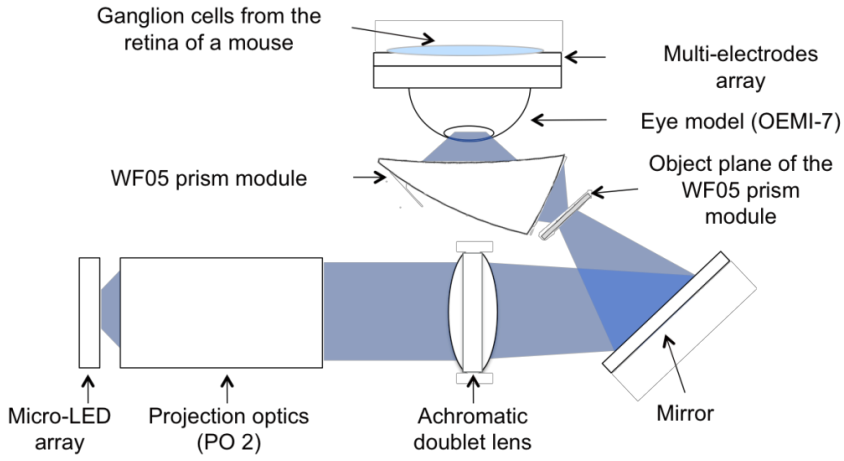

Figure 8-6: Schematic of the set-up used to stimulate Ganglion cells from a mouse eye

Figure 8-7 shows the WF05 prism module from *eMagin* [135]. It provides a lightweight solution for near-eye viewing devices. It is made of plastic and optically designed to correct for geometric aberrations. Normally, it is used with an OLED microdisplay in eMagin's Z800 3D Visor. Its folded optical path and short focal length allow the single-element optical design to deliver nearly 40° field of view. This module has a 22mm focal length and 27mm eye relief that corresponds to the position of the front of the eye from the VR optics.

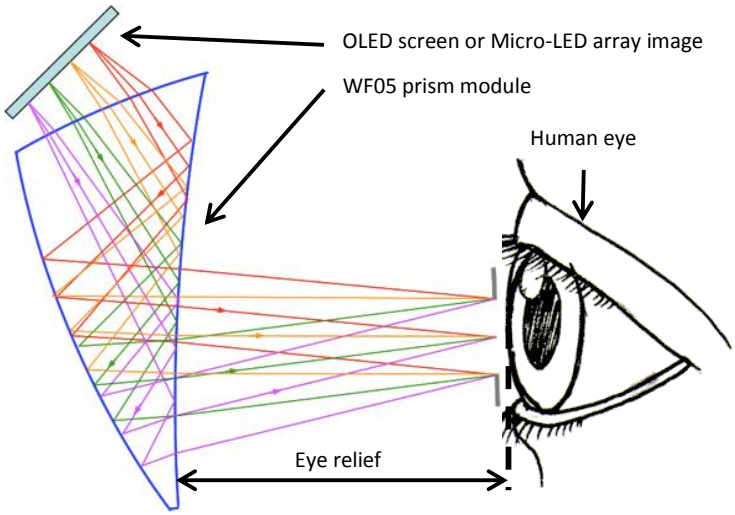

Figure 8-7:WFO5 prism module (eMagin) schematic of an OLED display imaged inside a human eye

Figure 8-8 shows the resulting set-up with the trajectory of the light through the optics up to outside the VR optics.

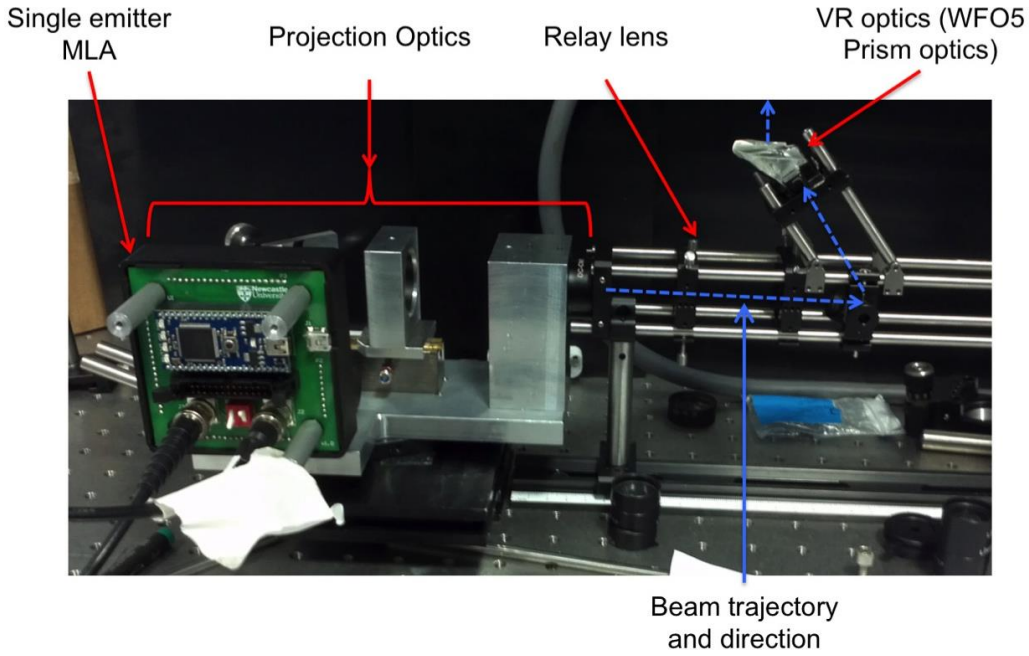

Figure 8-8: MLA and PO coupled with VR optics

The image can be visualized quickly and easily by placing the eye above the VR optics at low intensity (V_{MLA}<2.6V). The achromatic doublet lens and the position of the WF05 prism can be moved to modify the magnification of the micro-lens array image. Lenses of focal lengths between 40mm and 80mm were selected to be able to modify the size of the image at the pupil of the eye and then on the retina or, in this experiment, on a 1.6x1.6mm^2 MEA (see Figure 8-9). In A.13, the track length variation and the pupil shift for the four lenses tested are shown on diagrams for magnification between 0.1 and 3. The highest magnification possible is limited at 2.25 by the field aperture of the VR optics. It demonstrates that the longer the focal length of the achromatic doublet lens, the longer the track length and the larger the pupil shifts from the design position of the VR optics. Actually a good range of magnifications, 0.5x-2.5x, can be achieved with just the $f_1 = 80\,mm$ achromat. With this lens over this range of magnifications the track length, provides enough space to move the lenses around, it also does not vary much and the pupil shift is manageable.

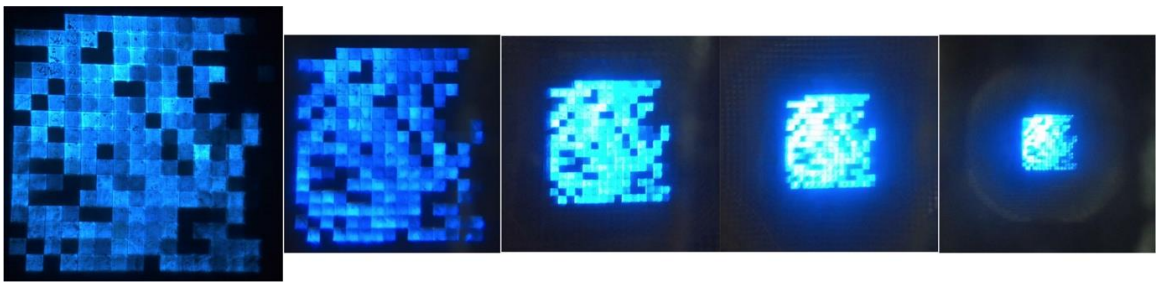

Figure 8-9: Variation of magnification with 40, 50, 60 and 80mm focal distances achromatic doublets.
The smallest magnification was obtained with f_{AD}=80mm

Implementation with an eye model and MEA

The MLA, PO and VR optics were then coupled to an eye model OEMI-7 from *Ocularinc* [136]. The imaging eye model reproduces natural surfaces of the human eye such the cornea, crystalline lens and retina, which is non-flat. The back of the eye model, the part containing the false retina, was replaced in this experiment with a small aperture where the MEA amplifier and a flat MEA sit (see Figure 8-10). The image at the MEA may be deformed as this eye model is optimised for a curved surface (the retina) not a flat surface.

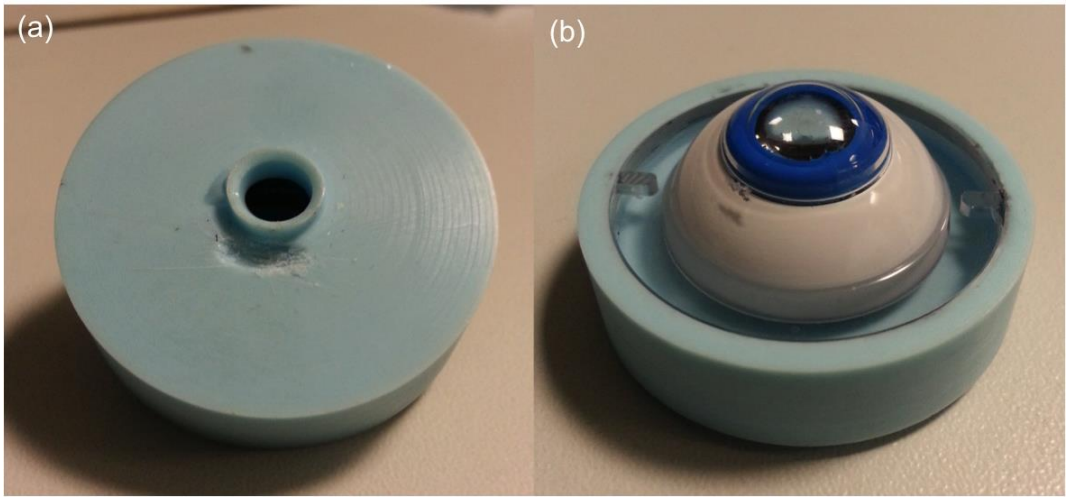

Figure 8-10: Imaging Eye Model (OEMI-7) from Ocularinc modified to fit an MEA mounted over the hole in the grey resin part added at the back.

Due to the restricted output pupil position of the VR lens, the eye model and MEA were placed on a 3-D positioner. The eye model position can therefore be optimised relative to the VR lens (see Figure 8-11).

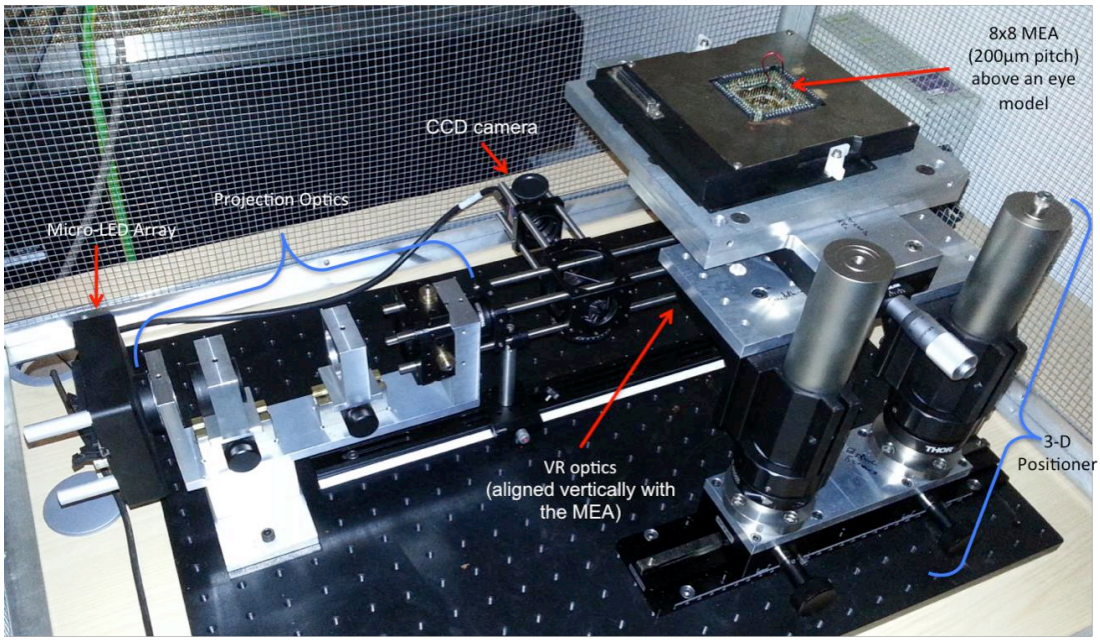

Figure 8-11: Ganglion cell stimulation and measurement set-up with a MEA, VR optics, MLA and PO

A 80mm focal length achromatic doublet was chosen to relay the image of the MO to the VR lens and then to the MEA, producing a projected MLA size slightly larger than the MEA to stimulate all the ganglion cells in the retina (see Figure 8-12).

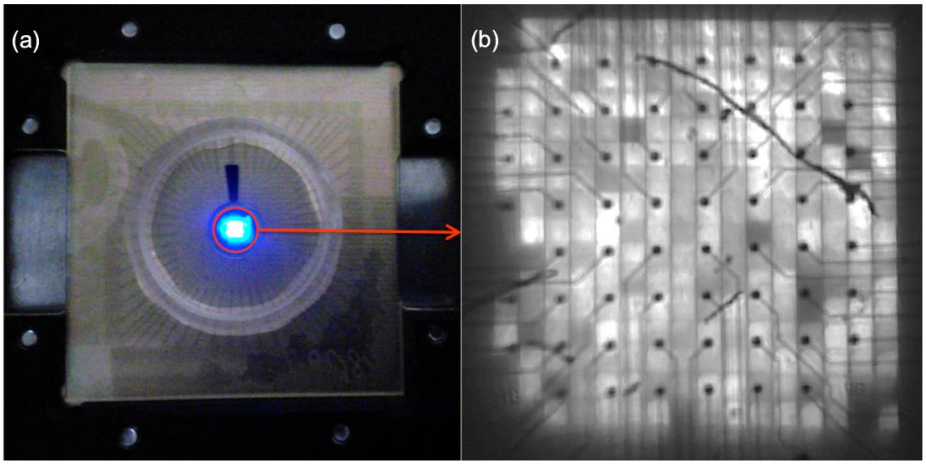

Figure 8-12: MO imaged on the MEA
(a) MEA with image of the MO at its center. (b) MO image focused and aligned with the MEA

The size of the image of the MO was then deduced from the size of the MEA. $Pitch_{MOs} \approx Pitch_{MEA}/1.3 = 153.8\mu m$. Thus the size of the total array is $16 \times Pitch_{MOs} = 2.46mm$. A power of 86.6µW was measured on top of the MLA at a drive voltage of 4V with all LEDs turned on. Therefore, the power per unit area is 1.43mW/cm^2.

Experiments

The experiments were carried out with a whole retina with ganglion cells transfected with ChR2 extracted from genetically modified mice. The retina was added in fluid on top of the MEA and left for two hours to settle on the top of the electrodes. The photoreceptor mediated light responses were tested with green light from a broad area LED to verify how close the retinal circuitry is to the electrodes. Then, a drug made of 10µM DNQX and 20µM D-AP4 is added to block these responses and leave only the possible response from stimulations of ChR2 by blue light.

The goal of this experiment is to verify the firing response of neurons transfected with ChR2 when the width of the MLA pulse is varied from 10 to 100ms every 2 seconds. The MLA (model ON-54) was driven at 4V to be able to stimulate action potentials with the MEA. Peristimulus-time diagrams are used in Figure 8-13. Each peristimulus diagram shows the timing of the spikes and also the number of spikes per stimulation, called firing rate. In Figure 8-13, the firing rate is increasing with the width of the pulse demonstrating an improved stimulation of the retina when the quantity of light on the retina is increased next to the electrode used for the measurement. Similar results were obtained with some of the other electrodes in the MEA proving that the results are repeatable.

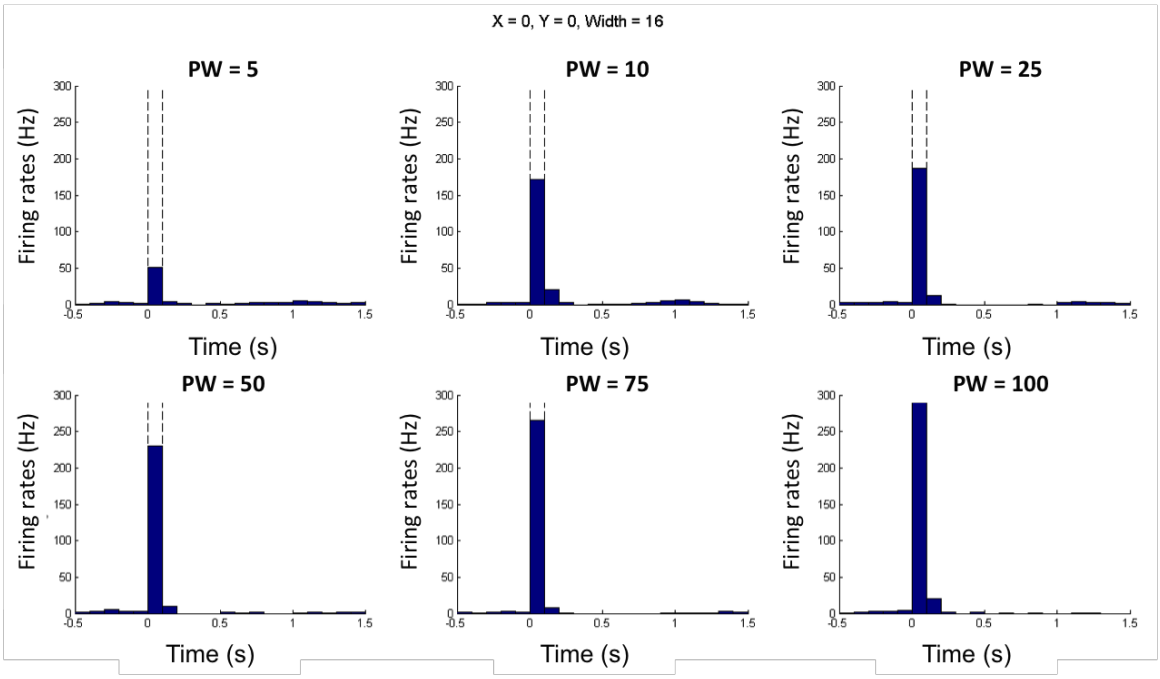

Figure 8-13: Peristimulus-time histograms for different pulse widths (5ms (a), 10ms (b), 25ms (c), 50ms (d), 75ms (e) and 100 ms (f)) generated every 2s for a channel of the MEA

Figure 8-14 shows more detailed peristimulus-time diagrams. Most of the responses happen within 0.1s of the stimulation with a tendency to be higher closer to the stimulation.

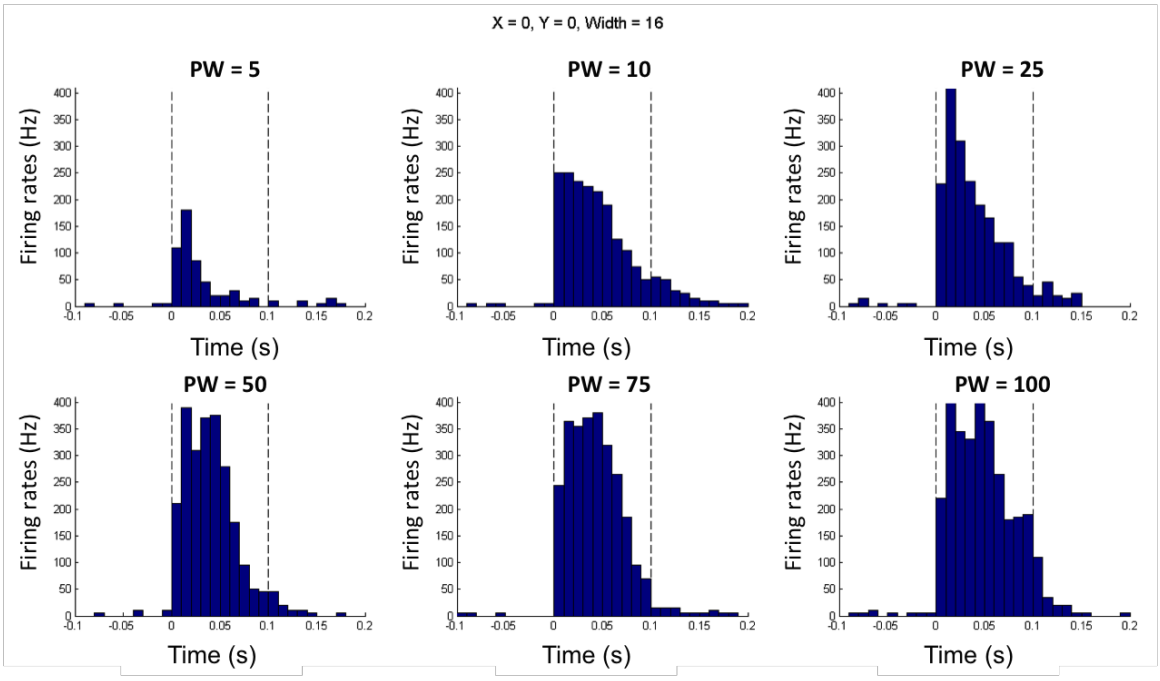

Figure 8-14: Detailed peristimulus-time histograms of the main responses to light stimulation for different pulse widths (5ms (a), 10ms (b), 25ms (c), 50ms (d), 75ms (e) and 100ms (f)) generated every 2s for a channel of the MEA

This experiment shows that action potentials could be stimulated with a power per area lower than the minimum power per area measured in the paper "Optobionic vision-a new genetically enhanced light on retinal prosthesis" [4] (5mW/cm^2 vs. 10mW/cm^2 in the experiment and reported in the paper respectively). However, the power may be higher inside the solution in which the ganglion cells are kept, as there may be extra losses as the light is transmitted through the MEA, which has indium-tin-oxide conductors, towards the point where the power was measured with a power meter. Additionally, the fact that the FF of the illuminating area is nearly 100%, the stimulation of the neurons may be more efficient and therefore happen at lower power per unit area.

It was determined that the width of the MLA pulses has consequences on the frequency of the responses. The minimum pulse width where there is 50% probability of a response occurring on one of the neuron is ~25ms.

Strong responses were obtained in this experiment with the MLA driven at 4V. The micro-LED array using clusters of emitters without the PO had to be driven at 6V at least to fire action potentials. The single emitter MLA coupled with PO have an increased FF and collection efficiency that in turn allows it to stimulate enough neurons transfected with ChR2 to fire action potentials at a lower drive voltage.

8.3 In-vivo stimulation of a living mouse retina

These experiments were carried out in the Botond Roska group, which is part of the neurobiology department at the Friedrich Miesher Institute for biomedical research in Basel. Its primary interest is in studying the structure and function of neural circuits, to understand how neurons interact in local neuronal networks to compute visually and behaviourally relevant functions. In OptoNeuro, the biological and optoelectronic technology developed is used to explore the science of the retina.

Typically for in vivo stimulation experiments with vision-impaired mice, they transfect retinal circuit cells with ChR2, to render them light sensitive, and co-transfect with green fluorescence protein (GFP) to help visualize which cells have ChR2 in them. However, in live mice it was difficult to see the GFP labelling. The aim of this experiment is therefore to develop a set-up, which allows spatio-temporal stimulation of these mice where the stimulation can be mapped to known parts of the retina, such that this stimulation can be tracked back to the visual cortex of the brain. A micro-LED array combined or not with projection optics is used to stimulate the retina and a fundus camera is used to visualize the retina by scattered light to reveal the optic disc and blood vessels. As the MLA also excites GFP, it should be possible to visualize the successfully transfected cells. This should enable more precise targeting of the stimulation on the retina. The next step is to study how the mouse reacts with defined moving patterns of light.

First, the theory behind the fundus camera is explained. Then, the set-up is described. Finally, its testing with an array of cluster of emitters are shown and compared to the single emitter MLA coupled with “PO 2”.

8.3.1 Principle of a fundus camera

A fundus camera is composed of two parts. Imaging of the fundus on a camera can be carried out using similar optics as are used to project the micro-LED array on the retina. However, illuminating the fundus so that the optical disk or the blood vessels can be seen is difficult due to the particular shape of the eye and the scattering and reflections on and inside the eye. Carl Zeiss Company introduced the first fundus camera in 1926 for ophthalmic applications. It offered a 10° retinal field and required manual exposure using flash powder and colour film [137]. Since then, their capabilities have improved with electronic illumination control, automated eye alignment and high-resolution digital image capture. Fundus photography is now a standard ophthalmic practice for detecting and documenting retinal disease.

The fundus illumination uses two optical principles, the Köhler illumination and the principle of geometric pupil separation. The first is most often used with microscopes as it provides a homogeneous illumination. Here the light source is imaged onto the optical pupil of the imaging system, such that the illumination in the object field is uniform. The same principle was used previously with the micro-optics, which image the individual micro-LEDs onto the microscope or eye pupil.

The second principle is the one of geometric pupil separation, which states that the illumination and observation beam paths should be geometrically separated in all locations where scattering and reflections occur [138], other than at the plane to be imaged. This principle was formulated by Alvar Gullstrand applying it in 1911 into the Zeiss ophthalmoscopes [139]. The separation of the path means there is no interfering reflection or scattering light generated inside the eye, such as corneal reflections and eye lens scattering, observed in the fundus image and therefore impairing it. Slit and annular illuminations were developed with this principle in mind [140].

Fundus imaging is generally performed with white light to obtain colour images of the fundus. It can be operated in different imaging modes to expand the diagnostic options. Filters can be used to do monochromatic observations. Blue light increases the visibility of the anterior retinal layers. Around these wavelengths, the light is absorbed by the retinal pigmentation and blood vessels, providing a dark background against which specular reflections and scattering in the anterior layers of the fundus is enhanced. However, the contrast at the shortest wavelengths can be severely reduced by the high scattering of semi-transparent structures, such as retinal folds, nerve fibre layers etc... Therefore, blue-green filters centred at 490nm are often used. Green light is also absorbed by blood, but is only partially reflected by the retinal pigmentation. There is therefore less scattering than in the blue and generally higher contrast imaging of the fundus results. The green light enhances the visibility of the retinal vasculature and helps find thicknesses, such as haemorrhages. Additionally, the spectral sensitivity of the eye peaks in the green around 540nm. Filters with wavelengths between 540 and 570nm are therefore easy to view and focus with when using optical instruments by eye. Red light (>590nm) reveals more of the choroidal pattern, as the retinal pigmentation appears progressively lighter and more transparent. The rest of the eye structures are less visible as their colours are close to that of the illumination and therefore the contrast of the fundus imaging is greatly diminished. The most common filters used have peaks between 625 and 640nm [138].

8.3.2 Set-up

Figure 8-15 shows a schematic of the set-up developed for this experiment.

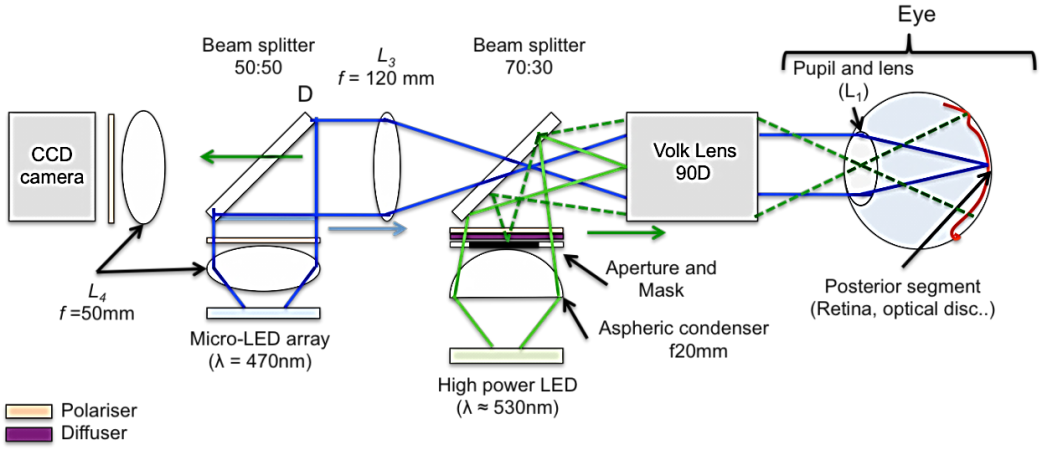

Figure 8-15: Schematic of the set-up developed for stimulation of the retina and its visualization with a Fundus camera

The micro-LED is imaged on the retina through two relay optics, L_4 and L_3, and the Volk lens and the lens of the eye. The high power LED is imaged on the Volk lens and the aperture and mask on the pupil of the eye. The polarizers on the illumination arms and detector arms are perpendicularly crossed to decrease any unwanted reflections from any intermediary optics.

The whole system combines MLA excitation and the fundus illumination and imaging arms. Two illumination sources are therefore used. The MLA is spatio-temporally controlled to stimulate the ganglion cells transfected with ChR2 on the retina at ~470nm. The fundus illumination is constant in both time and space, and should not stimulate the ganglion cells transfected with ChR2. These cells are also labelled with GFP, which has a peak of absorption at 475nm and a fluorescence emission peak at 516nm. This is used to find their location on the retina. A green high power LED from Thorlabs (M530L3) with a peak at 530nm and a maximum power of 350mW is therefore used with the fundus camera. This wavelength gives a high contrast image of the fundus without stimulating the ChR2. Light from the MLA itself is used to excite GFP

A condenser lens (Thorlabs ACL2520) collects as much light as possible from the green LED onto a mask with a 16mm diameter added in front of the condenser lens to create an annular illumination. The image of the annular illumination is projected by the Volk lens onto the eye pupil. This images needs to be either less than 7mm for the pupil of a human eye or 3mm for that of a mouse eye. Its size can be modified by moving the condenser lens and LED source. A diffuser was added between the condenser and the objective to homogenise the illumination on the retina.

The non-contact slit lamp Volk lens[141] is a double aspheric and it has the advantage of being a single element compared to an eyepiece, which is composed of several elements, thus decreasing the chance of reflections occurring within the objective.

The eye is optimised for projecting images onto the fundus. This means that it is already optimised for imaging onto a curved surface. The Volk lens is developed for the human eye. The experiments will be with mice, which have a much smaller pupil and retina. The human eye has a 22mm diameter, the mouse eye a 3.32mm one. The human retina area is over 1000mm^2, which is nearly 10 times larger than that of the mouse [142]. The focal distances of each eye are 23mm and 3mm and their pupil diameter ~7mm and ~2mm for the human and mouse respectively. The lens chosen for this experiment (90D) therefore has to illuminate the central retina of a human eye, and simultaneously allows examination via a small pupil for mouse work. The field of view of this lens is greater than 70° and it has a 7mm working distance.

The imaging section of the fundus system is used to visualize the fundus as well as the area of the fundus that fluoresce because of illumination from the MLA imaging and MLA stimulation, which are therefore following an identical optical path.

An image of the entire array on the mouse retina around 2mm size was requested by the biologist at the FMI, as the retina is ~5 x 5mm^2. Therefore a relay optics composed of a 50 and 120mm focal length , giving 2.4x magnification was combined with the 90D ($f = 1/90 = 11.1$mm) and the 3mm focal length of the mouse eye. This corresponds to a total magnification of the MLA at the retina of: : $M_{MLA} = 2.4 \times (3/11.1) = 0.65$ (see Table 8-1). The projected MLA images on the retina will therefore be 1.56mm with a bare MLA or 2.6mm with the MLA coupled with "PO 2". The field of view of the MLA images are well below the 90D Volk lens field of view (74°), which means that the entire array will be seen on the camera.

Type of Subject	Light source	F_{eye} (mm)	$FoV_{Volk\ lens}$ (°)	M_{MLA}	S_{Object} (mm)	I_{Retina} (mm)	FoV_{Retina} (°)
Human	MLA	23	74	4.97	2.4	11.93	29.1
	MLA & PO 2				4	19.9	46.8
Mouse	MLA	3		0.65	2.4	1.56	29.1
	MLA & PO 2				4	2.6	46.8

Table 8-1: Summary of theoretical image dimensions and field of view (FoV) for a human and a mouse eye for a first relay optics using *f* (L_4) = 50mm and *f* (L_3) = 120mm.
Two types of light sources are used to stimulate the retina, the MLA and the MLA with the projection optics PO 2. The size of the object imaged on the retina, S_{Object}, changes with each source because of the 1.67 magnification introduced by the projection optics "PO 2". Image size (I_{Retina}) and field of view (FoV_{Retina}) on the retina are therefore also multiplied by 1.67 with "PO 2".

The system will give an image of the MLA on the camera with the same scale as the original MLA as the relay optics are the same in both the MLA stimulation and the imaging arms. However, the total field of view illuminated with the fundus camera corresponds to the maximum field of view of the Volk lens. The maximum field on the retina is ~4.52 and ~34.66mm on the mouse and human eye. This means the total field is ~6.97mm on the detector. The Hamamatsu camera used for testing (Orca ER) has an effective area of 8.67x6.60mm (1344x1024) pixels and therefore the entire camera field of view is properly illuminated.

Beam splitters are used to combine the fundus illumination, the imaging and the MLA stimulation. A 50/50 (Transmission/Reflection) beam splitter was used in front of the MLA and detector. A 70/30 (Transmission/Reflection) was used in front of the fundus illumination with the illumination on the reflection side, as there is enough power coming from this LED. However, it is important that as much light as possible is imaged from the MLA on the retina to stimulate it. A 50/50 beam splitter means that 25% of the light emitted by the MLA goes to the retina instead of 35% with the chosen beam splitter. The power on the detector is decreased the same way and it needs to be as sensitive as possible to detect the MLA excitation of GFP on the retina.

Polarizers were added on each illumination path and set perpendicularly to that next to the camera to filter any unwanted reflections and scattering. This helps to improve the contrast of the imaging.

An Imaging Eye Model (OEMI-7), from *Ocularinc* [136] was used to verify the quality of the imaging. This eye model corresponds to a human eye, which should behave in a same way to a mouse eye even if the dimensions are different.

Figure 8-16 shows the implemented system. The system can be rotated to fit in a tight experimental platform and translated to place it precisely in front of the mouse eye, and the MLA positioned precisely to target specific area of the fundus. The Hamamatsu camera was later replaced by a more compact camera (Ximea MQ013MG-E2 1.3MP Monochrome Camera). In Figure 8-16(a), a MLA using cluster of emitters without projection optics is used. In Figure 8-16(b), a single emitter MLA coupled with the projection optics “PO 2” is tested.

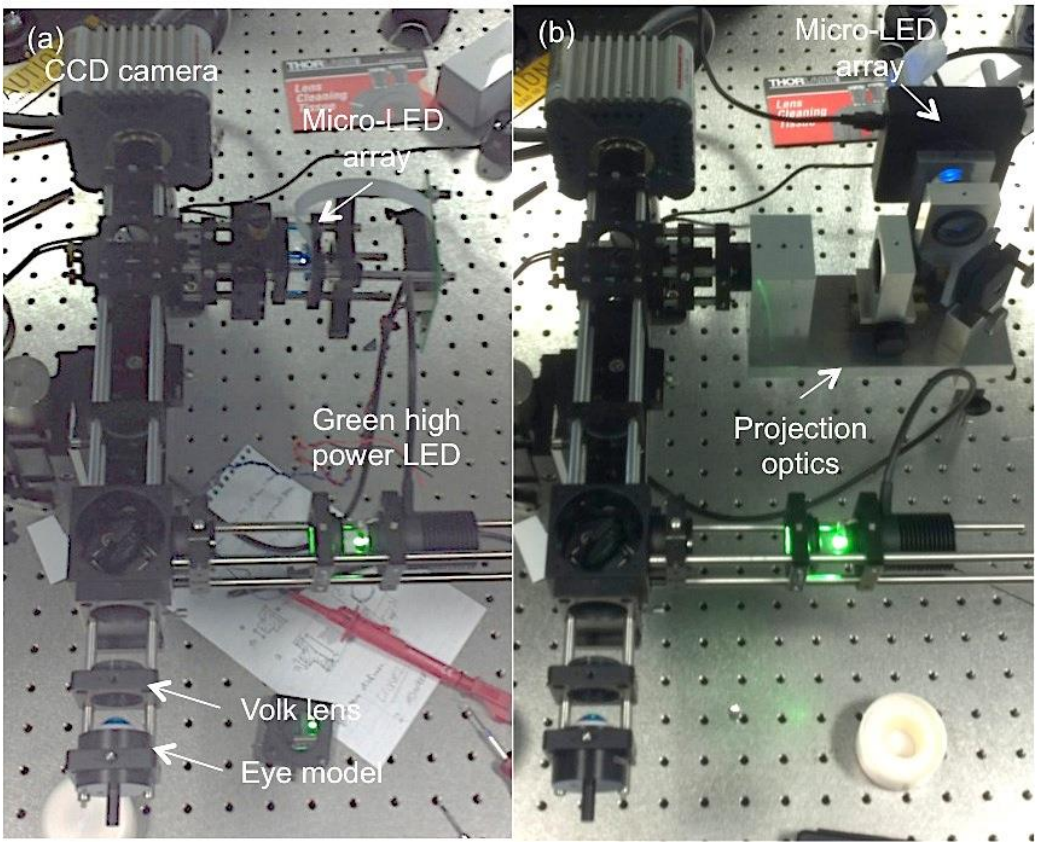

Figure 8-16: In-vivo mouse retina stimulation and visualisation with a MLA and fundus camera
(a) Stimulation with cluster of LEDs MLA and (b) with a single emitter MLA with "PO 2"

8.3.3 Testing and Experiments

The array of cluster of MLA was imaged on the CCD camera with the retina. The fundus camera is working, as the fundus is visible (blood vessels and optical disc) (see Figure 8-17). The power of the MLA had to be increased to at least 4-5V to see an image of the array of cluster of LEDs on the optical disc of the eye model. This optical disc has some fluorescent qualities in the eye model, which explains why the image is more visible on the optical disc than on the blood vessels or retina.

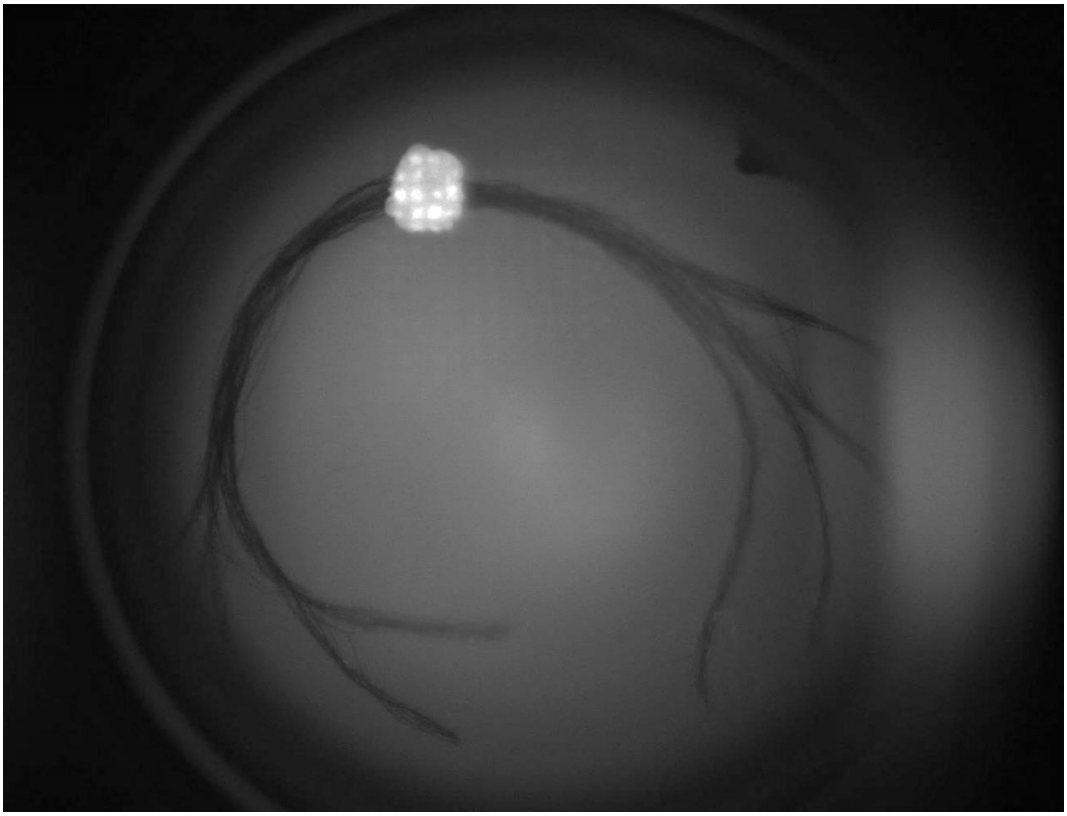

Figure 8-17: Visualisation of the Fundus with a fundus camera and of the MLA stimulation
Several Clusters of LEDs can be seen better than the rest of the array because they are imaged on the optical disc, which is fluorescent. The image of the array covers a small area of the retina.

The same experiment was repeated with the single emitter MLA coupled with “PO 2”. The size of the apparent MLA, which is imaged later on the retina, is multiplied by 1.67 because of the PO and is therefore 4mm wide instead of 2.4mm (see Figure 8-18). The MLA image occupies a larger area of the fundus as expected in Figure 8-18.

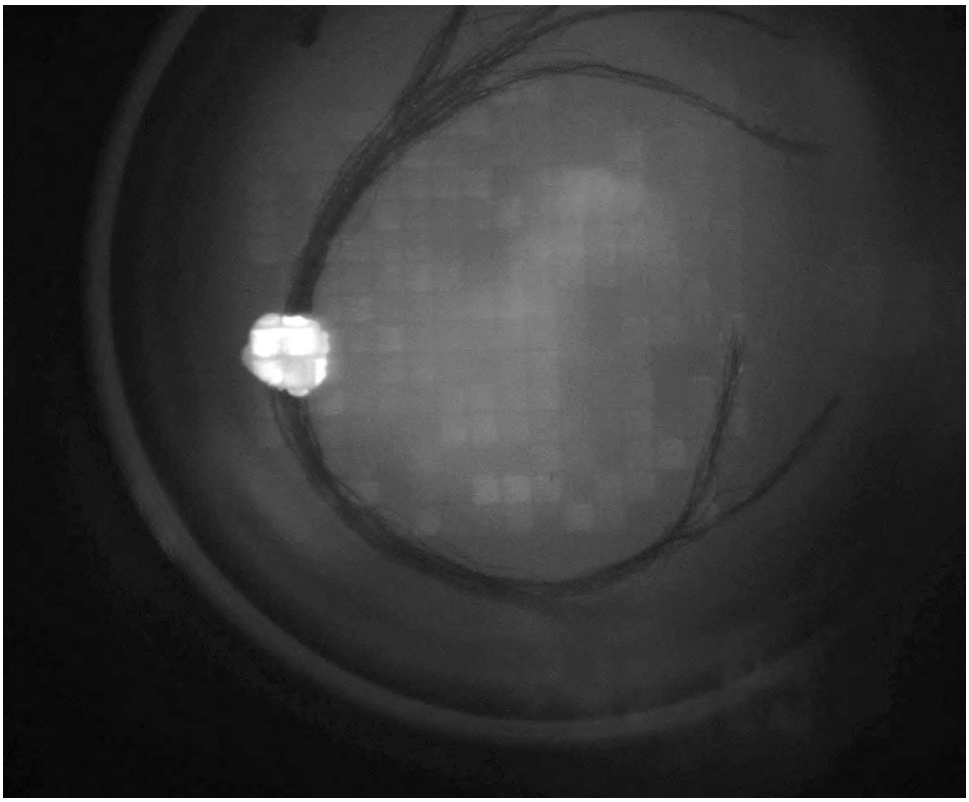

Figure 8-18: Visualisation of the Fundus with a fundus camera and of the MLA coupled with "PO 2" stimulation
The MLA can be seen here all over the retina, not only on the optical disc. The area covered on the retina is larger than with LED clusters array because of the projection optics magnification.

Preliminary measurements showed a difference of power between the two systems at the eye of a factor 1.8 (1.47 vs 2.61µW). The difference was expected to be higher as the MLA with projection optics provides a nearly collimated beam of light, instead of a beam with the MLA distribution, increasing the collection efficiency of the optical system used in the fundus camera set-up.

The next step is to experiment with a mouse eye with both the array of cluster of LEDs as well with the single emitter MLA with integrated MO. It won't have the limitation caused by the size of the image as the MO is the same size that the MLA. It should therefore increase the efficiency of the stimulation. Additionally, this system can be realistically added to the set-up and tested with a mouse, as it is not as bulky as "PO 2".

8.4 Conclusion

The system was generating enough power to stimulate current peaks in the HEK cell. On MEA, the stimulation was strong enough to stimulate neurons to fire action potentials with a power per area lower than the value of the minimum requirement reported in a previous paper[4]. It may indicate that the power is higher in the cell than at the detector, and that power is lost at the interface liquid/air due to TIR. It also indicates that an illumination where the FF is higher stimulates the cells more efficiently.

In addition the high collection efficiency of the PO means that the MLA can be driven at only 4V to stimulate neurons to fire action potentials. This is significantly lower than the minimum of 6 V driving a MLA without PO that is usually needed to observe action potentials. This increases the lifetime of the LEDs as less heat will be generated and the damage will thus be reduced.

A set-up was developed to stimulate in-vivo and visualize the retina of a living mouse with ganglion cells transfected with ChR2 and GFP. The GFP is used for the visualisation of the MLA stimulation. A Fundus camera was coupled with it to improve the targeting of the stimulation. The stimulation was implemented in a compact way to be integrated onto an experimental platform where space is limited. An eye model was used to validate the effectiveness of the set-up, however, an experiment with mouse will allow us to check if the stimulation is high enough to stimulate the GFP to be seen by the CCD camera, ChR2 to trigger action potentials.

Chapter 9: Conclusion and future work

The goal of this thesis was to design and implement an optical set-up to improve the transfer of light from micro-structured Gallium-Nitride LEDs to biological samples transfected with an optically gated ion channel protein, ChR2, using micro-lens arrays. This project was undertaken in partnership with Newcastle University, Tyndall in Ireland, Scientifica in the UK, MPI in Frankfurt and FMI in Basel as part of a FP7 European project, OptoNeuro.

In chapter 2, the field the project is applied to was defined, Optogenetics. This field opened several doors to the understanding of the way neurons interconnect and function. Its four main components were described. They are based on control, targeting, illumination and measurement. In this project, we deal mostly with an optically gated ion channel protein, ChR2 that is transfected in genetically modified mice neurons. A patterned illumination, with spatio-temporal control on sub-millisecond timescales, is used to target and stimulate specific neurons. The evolution of the technology, micro-structured Gallium-Nitride LED Arrays (MLA), is shown through this thesis as well as its effects on neurons measured using multi-electrode arrays, patch-clamps or in exciting fluorescence markers, such as GFP. Optoneuro's interest is oriented toward the development of a non-invasive retinal prosthesis to stimulate ON-bipolar cells that will induce light-evoked spiking activity in ganglion cells and then restore partial visual function. However, this field also has other neuroscience applications, such as optical control of movement and locomotion, and the probing of neuronal circuits for studying pathologies such as Parkinson's disease.

ChR2 stimulation with a GaN MLA was previously demonstrated in Vincent Poher and Nir Grossman's works. However, their systems were limited by different aspects of the technology as stated in chapter 3. The flip-chip technology was already used. But, the array was driven using a multiplexed raster scanning and therefore the efficiency of the emission was limited. In this project, each LED is driven individually allowing a better brightness and control of the illumination. The second limitation was the emitter itself. Conventionally designed LEDs have light distributions close to the one defined by Lambert's emission law. They are extended sources with wide divergence and therefore conventional optics collect only a small part of what is emitted.

Tyndall improved the design by reshaping the back reflector behind the emitting layers to recycle the wide-angle beams and redirect them in a forward direction, increasing the efficiency of the device as well as decreasing its angle of emission. In this way, a higher percentage of the light can be collected by external optics. Arrays of 16x16 single emitters with 25μm diameter and 150μm spacing were first produced and then array of 16x16 clusters of 14 emitters were developed. This last design provided an increase of the total emitting area over the entire area of the device when connected to a microscope. However, the collection efficiency was still limited to values around 2% and below depending on the magnification used on the microscope. In that kind of system, losses are important at the tube lens, which has a low numerical aperture, and at the pupil of the microscope objective.

The principle of this project is to improve the apparent illuminated area at the sample as well as the total efficiency of the system using a micro-lens to collect the light coming from each micro-LED, then collimating it and finally imaging the micro-lens instead of the micro-LED on the sample. The principle is similar to a Kohler illumination, where the source, a micro-LED in our case, is imaged onto the objective pupil by the combination of the micro-lens and tube-lens, resulting in a uniformly filled image of the micro-lens on the sample. In collecting more light from the micro-LED, that light is delivered to the sample and effectively used to improved the fill factor of the illumination. The size of the emitter is therefore important as, if above a certain size, no extra light is delivered to the sample as it is blocked by the objecting pupil. For this reason the array of single compact emitters is more appropriate, with added advantage that less electrical current is needed to supply a given area of the sample and so also the thermal load on the micro-LED array and drive circuit is reduced.

This project followed two directions. The first one consisted in using off-the-shelf micro-optics combined with projection optics to image light from the MLA to the micro-lenses, and the second one using custom developed micro-optics integrated directly onto Tyndall MLAs.

During the course of this project, competing technologies have been developed, such as a high fill factor micro-LED array [143] or improved, such as DLP technology (see 2.6.2). High fill factor micro-LED arrays provide a uniform illumination but require much higher current to drive them, increasing the thermal load and therefore decreasing their lifetime. The light emission distribution is close to the one defined by Lambert's emission law and therefore a large percentage of the light emitted can't be collected by optics. Also, these high fill factor emitters can't use MO as efficiently as Tyndall MLA (see 3.2.4). The DLP technology is the strongest competing technology as it provides high power and multi-wavelength illumination, and is already available on the market. However, it is not as power efficient as micro-LED arrays with a high percentage of the light emitted lost at the DMD, and bulkier, making it difficult to apply it to optogenetic retinal prosthesis.

In chapter 4, the choice of a micro-lens array is explained. It is manufactured following a replicating process using UV curable lacquer and a mould, with a 250µm diameter and 0.125 NA. This manufacturing method was the only one available on the market providing micro-lenses with a spherical shape. A diameter that was different from that of the MLA (150µm) was chosen, as the off-the-shelf MO available at the matching diameter did not have a high enough NA to provide a real gain in collection efficiency. The second reason behind this choice is the fact that at the MLA end of the relay optics, the collection NA would be 1.67 x 0.125 = 0.208 because of the required magnification of 1.67x to match the image of the MLA with the MO. At high NA, macro-optics can be limited by Seidel aberrations, which justifies the choice of this particular NA. Additionally, this image may be projected inside the substrate of the micro-lens array as the thicknesses available were of the same order than the micro-lens focal distance (~1mm), which would otherwise have made direct integration impossible.

A simple set-up with off-the-shelf lenses was first implemented to verify our idea. A filled lens could be imaged with an increased collection efficiency of ~1.55% compared to values below 0.2% without it. The fill-factor (FF) and the collection efficiency were therefore shown to be improved. However, it also showed the limitation of such a simple set-up. The magnification needs to be optimised to fill each micro-lens uniformly, also it highlighted the importance of telecentricity and off axis optical aberrations.

In chapter 5, the relay optics are therefore optimised with a design close to that used in simple microscope objectives. Meniscus lenses were combined with achromatic doublets to increase the maximum NA of the system without increasing some of the aberrations. It was applied to a first set-up developed in-house, composed of two off-the-shelf achromatic doublets and two identical custom meniscus lenses. This set-up showed improved performance, but suffered from high spherical aberrations leading to a high variation of the intensity from the centre to the edge of each micro-lens (between 2 and 3 times). But despite this fault, it improved the collection efficiency to 11% when combined with the MLA with back-reflectors. This is nearly a 100 times higher than without MO and the back reflector behind the MLA.

In chapter 6, the development of a more advance set-up, called “PO 2”, is described, in which the faults of the first design are addressed. “PO 2” has 6 lenses. 3 are off-the-shelf optics and 3 are custom-made. The price was kept at half the price of an existing solution on the market from Sill optics, and had better performance. Modelling in non-sequential Zemax showed an improved homogeneity of the imaging of each micro-lens with only a small difference between centre and edge. In practice, the experimental results were even more promising with no significant difference observable in intensity across the micro-lens apertures. The collection efficiency reached 13% when the imaging was optimised and 17%, when the micro-lenses were slightly underfilled.

This set-up was implemented into an opto-mechanical platform to allow an easy coupling onto our partner’s microscope platforms. Scientifica developed a compact opto-mechanical design to be integrated in their SliceScope.

In chapter 7, the different steps that brought me to the final design of the custom MO for direct integration are explained. A model matching the real device with back reflectors was constructed in non-sequential Zemax before coupling it with a model for the MO. This was applied to the design with a 150µm spacing first and then to two different designs with a smaller spacing, 80µm. One of these two designs is the traditional design, which uses a GaN wafer as a substrate for the MLA. In the second, the thickness of GaN is below 10µm and it is combined with a Sapphire (Al_2O_3) wafer substrate.

The custom micro-lens array designs, replicated on PET substrate, were optimised to nearly fill the pupil of a 4x/0.16NA microscope objective with a singlefront surface radius of curvature of 0.162mm. At 150µm spacing these lenses would have a numerical aperture of 0.24NA to maximise the efficiency of the system. This efficiency can be kept at this level with a higher magnification objective with the use of relay optics to match the NA of the objective pupil. These MO should increase the collection efficiency of the system by a factor of ~1.3 compared to "PO 2". Additionally, this system is a lot more compact and easier to use as MLA and MO are aligned during the manufacturing.

In chapter 8, different optogenetic applications of this set-up are shown. The projection optics are used successfully to stimulate light induced current in a cell transfected with ChR2, and measured with a patch-clamp. The projection optics was coupled with virtual reality optics and a modified eye model to stimulate ganglion cells in an ex-vivo mouse retina on a multi-electrode array. Action potentials were generated and measured for the MLA driven at voltages a lot lower than without any MO (3.5~4V vs 6V). This reduction in drive voltage and hence current causes a decrease of heat production for the same light delivered to the sample and allows an increase of the lifetime of the device. A projection system, coupled with a fundus camera for navigation was developed to be used for in-vivo experiments with mice. The first experiments with the eye model showed the MLA stimulation projected onto the retina. A proper in-vivo experiment on a mouse should confirm the preliminary results.

In this project, MLA were successfully coupled with MO to improve parameters, such as fill-factor, to nearly 100%, and collection efficiency, to more than 13%. Different systems were developed with off-the-shelf and custom-made MO. However, the most promising solution is the custom one, which is integrated and optimised with the MLA. The finished product is as compact as the MLA without MO and is easy to use, making it an ideal solution for electrophysiological platform and/or eye prosthesis.

The next step of this development would be to do more experiments to verify the utility of the systems with "PO 2" and the integrated MO for neuroscience applications and potentially their feasibility for use in a retinal prosthesis. Additionally, the quality of this last solution needs to be characterised and compared to the modelling. A new 90x90 MLA was developed in this project but not yet tested. This new array needs to be tested and its performance compared to that of the 16x16 MLA with MO. Most importantly, these solutions will have to be applied in optogenetics experiments to compare them with the different solutions available on the market and demonstrate their qualities and potential market opportunities.

In many respects the optical designs presented here do not represent the ultimate performance that could be achieved. For instance it should be possible to design more compact forms of the “PO 2” system, but which might required more custom optics. Likewise, the integrated micro-lens design is spherical, because this is easiest to manufacture, and there is already evidence that spherical aberrations are an issue. A micro-lens array with an aspheric front surface would address these issues. Finally there is a fundamental issue in that current GaN family of LED semiconductors performs optimally in the blue, where ChR2 is optimally excited, but poorly, if at all, in the yellow where halorhodopsin is optimally excited. For full optogenetic control with micro-LEDs, new semiconductor technologies and/or new ion pump constructs are needed to take the field forwards.

Publications/ Presentations

1. J. Barret, **L. Chaudet**, Pr. M. Neil, N. Dong, X. Sun, E. Semagor, P. Degeenar, *Combining An Optical Eye Model and MEAS Recordings For Testing Of Retinal Prostheses*, Proceedings for John Barret presentation, 9th International Meeting on Substrate-Integrated Microelectrode Arrays (MEA 2014)
2. **L. Chaudet**, *Optical Designs to improve Optoelectronic Neural Stimulation with Micro-LED arrays*, Poster, Optical Design Meeting 2013 at Rutherford Appleton Laboratory (RAL Space), Kidger Optics associates, 19/09/2013
3. **L. Chaudet** and al., *Development of optics with micro-LED arrays for improved opto-electronic neural stimulation*, Proceedings of the SPIE, Volume 8586, id. 85860R 7 pp. (2013).
4. **L. Chaudet** and al., *Improving Opto-electronic Neural Stimulation with Micro-LED arrays and Optics*, Talk, Young Researchers Futures Meeting on Neural Engineering, 24/09/2012
5. **L. Chaudet** and al., *Optical Designs to improve Opto-electronic Neural Stimulation with Micro-LED arrays"*, Poster, Photon 12, IOP, 2012

Bibliography

[1] R. Tate, L. Smeeth, J. Evans, A. Fletcher, C. Owen, and A. Rudnicka, "The prevalence of visual impairment in the UK: A review of the literature," *London Unpubl. Rep. Comm. by RNIB*, 2005.

[2] C. F. Inglehearn, "Molecular genetics of human retinal dystrophies," *Eye*, vol. 12, no. 3b, pp. 571–579, May 1998.

[3] D. M. Brown, P. K. Kaiser, M. Michels, G. Soubrane, J. S. Heier, R. Y. Kim, J. P. Sy, and S. Schneider, "Ranibizumab versus Verteporfin for Neovascular Age-Related Macular Degeneration," *N. Engl. J. Med.*, vol. 355, no. 14, pp. 1432–1444, Oct. 2006.

[4] P. Degenaar, N. Grossman, M. A. Memon, J. Burrone, M. Dawson, E. Drakakis, M. Neil, and K. Nikolic, "Optobionic vision-a new genetically enhanced light on retinal prosthesis," *J. Neural Eng.*, vol. 6, no. 3, p. -, 2009.

[5] L. Greenemeier, "FDA Approves First Retinal Implant," vol. Nature New, no. Feb 15, 2013.

[6] R. L. Fork, "Laser Stimulation of Nerve Cells in Aplysia," *Science (80-.).*, vol. 171, no. 3974, pp. 907–908, 1971.

[7] J. Wells, C. Kao, P. Konrad, T. Milner, J. Kim, A. Mahadevan-Jansen, and E. D. Jansen, "Biophysical mechanisms of transient optical stimulation of peripheral nerve.," *Biophys. J.*, vol. 93, no. 7, pp. 2567–80, Oct. 2007.

[8] M. Banghart, K. Borges, E. Isacoff, D. Trauner, and R. H. Kramer, "Light-activated ion channels for remote control of neuronal firing.," *Nat. Neurosci.*, vol. 7, no. 12, pp. 1381–6, Dec. 2004.

[9] M. Volgraf, P. Gorostiza, R. Numano, R. H. Kramer, E. Y. Isacoff, and D. Trauner, "Allosteric control of an ionotropic glutamate receptor with an optical switch," *Nat Chem Biol*, vol. 2, no. 1, pp. 47–52, Jan. 2006.

[10] D. M. Berson, "Strange vision: ganglion cells as circadian photoreceptors.," *Trends Neurosci.*, vol. 26, no. 6, pp. 314–20, Jun. 2003.

[11] L. Buchen, "Neuroscience: Illuminating the brain," *Nature*, vol. 465, no. 7294, pp. 26–28, 2010.

[12] O. C. M. and J. U. Adams, *Essentials of Cell Biology, Unit 4.3: Ion Channel Receptors Generate Electrical Signals in Response to Chemical Signals*, Cambridge. NPG Education, 2010.

[13] K. X. (Georgia S. U. Charand, "Bioelectricity: Action Potentials," *HyperPhysics - Biology*. [Online]. Available: http://hyperphysics.phy-astr.gsu.edu/hbase/biology/actpot.html.

[14] N. Franks and S. Brickley, *Biophysics of Nerve cells, Physics Lecture Year 4*. Imperial College London, 2007.

[15] J. W. Smith, *Modern optical engineering*, Fourth., vol. Fourth Edi. SPIE Press, 2008.

[16] P. H. Raven and G. B. Johnson, “Sensory systems,” in *Biology; Part XIV Regulating the animal body*, 6th ed., Mc Graw Hill, 2002.

[17] H. Tomita, E. Sugano, Y. Fukazawa, H. Isago, Y. Sugiyama, T. Hiroi, T. Ishizuka, H. Mushiake, M. Kato, M. Hirabayashi, R. Shigemoto, H. Yawo, and M. Tamai, “Visual properties of transgenic rats harboring the channelrhodopsin-2 gene regulated by the thy-1.2 promoter.,” *PLoS One*, vol. 4, no. 11, p. e7679, Jan. 2009.

[18] P. Degenaar, “Optoneuro, Platform for OPTOgenetic NEUROn stimulation,” *2010*. [Online]. Available: http://www.optoneuro.eu/.

[19] F. Zhang, J. Vierock, O. Yizhar, L. E. Fenno, S. Tsunoda, A. Kianianmomeni, M. Prigge, A. Berndt, J. Cushman, J. Polle, J. Magnuson, P. Hegemann, and K. Deisseroth, “The microbial opsin family of optogenetic tools.,” *Cell*, vol. 147, no. 7, pp. 1446–1457, Dec. 2011.

[20] K. Deisseroth, “Optogenetics,” *Nat. Methods*, vol. 8, no. 1, pp. 26–29, 2011.

[21] M. Baker, “Light tools,” *Nat Meth*, vol. 8, no. 1, pp. 19–22, 2011.

[22] P. Hegemann and A. Moglich, “Channelrhodopsin engineering and exploration of new optogenetic tools,” *Nat. Methods*, vol. 8, no. 1, pp. 39–42, 2011.

[23] K. M. Tye and K. Deisseroth, “Optogenetic investigation of neural circuits underlying brain disease in animal models,” *Nat Rev Neurosci*, vol. 13, no. 4, pp. 251–266, Apr. 2012.

[24] X. Han, X. Qian, P. Stern, A. Chuong, and E. S. Boyden, “Informational lesions: optical perturbation of spike timing and neural synchrony via microbial opsin gene fusions ,” *Frontiers in Molecular Neuroscience* , vol. 2 . 2009.

[25] E. Pastrana, “Optogenetics : controlling cell function with light,” *Nat. Methods*, vol. 8, no. 1, pp. 24–25, 2011.

[26] K. Deisseroth, “http://optogenetic.org/,” 2011. [Online]. Available: http://optogenetic.org/.

[27] O. C. M. and J. U. Adams, *Essentials of Cell Biology, 4.2 G-Protein-Coupled Receptors Play Many Different Roles in Eukaryotic Cell Signaling*, CambridgeM. NPG Education, 2010.

[28] R. D. Airan, K. R. Thompson, L. E. Fenno, H. Bernstein, and K. Deisseroth, “Temporally precise in vivo control of intracellular signalling,” *Nature*, vol. 458, no. 7241, pp. 1025–1029, 2009.

[29] Z. Melyan, E. E. Tarttelin, J. Bellingham, R. J. Lucas, and M. W. Hankins, “Addition of human melanopsin renders mammalian cells photoresponsive,” *Nature*, vol. 433, no. 7027, pp. 741–745, 2005.

[30] V. Poher, “Microscopic Imaging and Photo-stimulation using Micro-structured Light Emitting Diodes,” *Imp. Coll. London, Dep. Phys. , Photonics Gr.*, no. PhD Thesis, 2008.

[31] S. Hughes, T. S. Watson, R. G. Foster, S. N. Peirson, and M. W. Hankins, “Nonuniform Distribution and Spectral Tuning of Photosensitive Retinal Ganglion Cells of the Mouse Retina,” *Curr. Biol.*, vol. 23, no. 17, pp. 1696–1701, 2013.

[32] S. Sekaran, R. G. Foster, R. J. Lucas, and M. W. Hankins, “Calcium Imaging Reveals a Network of Intrinsically Light-Sensitive Inner-Retinal Neurons,” *Curr. Biol.*, vol. 13, no. 15, pp. 1290–1298, 2003.

[33] OpenOptogenetics, “Opto-XRs,” 2014. [Online]. Available: http://www.openoptogenetics.org/index.php?title=Opto-XRs.

[34] K. Lugo, X. Miao, F. Rieke, and L. Y. Lin, “Remote switching of cellular activity and cell signaling using light in conjunction with quantum dots,” *Biomed. Opt. Express*, vol. 3, no. 3, p. 447, Feb. 2012.

[35] A. Stark, “Flipping a Light Switch in the Cell: Quantum Dots Used for Targeted Neural Activation,” *OSA (The Opt. Soc.*, pp. 1–2, 2013.

[36] S. Kleinlogel, U. Terpitz, B. Legrum, D. Gokbuget, E. S. Boyden, C. Bamann, P. G. Wood, and E. Bamberg, “A gene-fusion strategy for stoichiometric and co-localized expression of light-gated membrane proteins,” *Nat Meth*, vol. 8, no. 12, pp. 1083–1088, 2011.

[37] M. Baker, “The Author File Ernst Bamberg,” *Nat. Methods*, vol. 8, no. 12, p. 985, 2011.

[38] T. G. Oertner, “The Lego-logic of optogenetics,” *Nat. Methods*, vol. 8, no. 12, pp. 1011–1013, 2011.

[39] N. Grossman, K. Nikolic, V. Poher, B. McGovern, E. Drankasis, M. Neil, C. Toumazou, and P. Degenaar, “Photostimulator for Optogenetic Retinal Prosthesis,” *2009 4th Int. Ieee/Embs Conf. Neural Eng.*, pp. 68–71 746, 2009.

[40] S. J. Chinta and J. K. Andersen, “Dopaminergic neurons,” *Int. J. Biochem. Cell Biol.*, vol. 37, no. 5, pp. 942–946, 2005.

[41] V. Gradinaru, K. R. Thompson, F. Zhang, M. Mogri, K. Kay, M. B. Schneider, and K. Deisseroth, “Targeting and readout strategies for fast optical neural control in vitro and in vivo,” *J. Neurosci.*, vol. 27, no. 52, pp. 14231–14238, 2007.

[42] T. Kim, J. G. McCall, Y. H. Jung, X. Huang, E. R. Siuda, Y. Li, J. Song, Y. M. Song, H. A. Pao, R.-H. Kim, C. Lu, S. D. Lee, I.-S. Song, G. Shin, R. Al-Hasani, S. Kim, M. P. Tan, Y. Huang, F. G. Omenetto, J. a Rogers, and M. R. Bruchas, “Injectable, cellular-scale optoelectronics with applications for wireless optogenetics.,” *Science*, vol. 340, no. 6129, pp. 211–6, Apr. 2013.

[43] A. M. Aravanis, L. P. Wang, F. Zhang, L. A. Meltzer, M. Z. Mogri, M. B. Schneider, and K. Deisseroth, “An optical neural interface: in vivo control of rodent motor cortex with integrated fiberoptic and optogenetic technology,” *J. Neural Eng.*, vol. 4, no. 3, pp. S143–S156, 2007.

[44] Y. Iwai, S. Honda, H. Ozeki, M. Hashimoto, and H. Hirase, “A simple head-mountable LED device for chronic stimulation of optogenetic molecules in freely moving mice,” *Neurosci. Res.*, vol. 70, no. 1, pp. 124–127, 2011.

[45] M. Choi, J. W. Choi,, K. Seonghoon, S. Nizamoglu, S. K. Hahn, S. H. Yun, and *, “optogenetic synthesis in vivo,” *Nat. Photonics*, vol. 278, no. October, pp. 1–8, 2013.

[46] J. G. McCall, T. Kim, G. Shin, X. Huang, Y. H. Jung, R. Al-Hasani, F. G. Omenetto, M. R. Bruchas, and J. a Rogers, “Fabrication and application of flexible, multimodal light-emitting devices for wireless optogenetics,” *Nat. Protoc.*, vol. 8, no. 12, pp. 2413–2428, Nov. 2013.

[47] A. M. Packer, B. Roska, and M. Häusser, “Targeting neurons and photons for optogenetics.,” *Nat. Neurosci.*, vol. 16, no. 7, pp. 805–15, Jul. 2013.

[48] S. Peron and K. Svoboda, “From cudgel to scalpel: toward precise neural control with optogenetics,” *Nat. Methods*, vol. 8, no. 1, pp. 30–34, 2011.

[49] K. Wang, Y. Liu, Y. Li, Y. Guo, P. Song, X. Zhang, S. Zeng, and Z. Wang, “Precise spatiotemporal control of optogenetic activation using an acousto-optic device.,” *PLoS One*, vol. 6, no. 12, p. e28468, Jan. 2011.

[50] H. Wang, J. Peca, M. Matsuzaki, K. Matsuzaki, J. Noguchi, L. Qiu, D. Wang, F. Zhang, E. Boyden, K. Deisseroth, H. Kasai, W. C. Hall, G. Feng, and G. J. Augustine, “High-Speed Mapping of Synaptic Connectivity Using Photostimulation in Channelrhodopsin-2 Transgenic Mice,” *Proc. Natl. Acad. Sci. U. S. A.*, vol. 104, no. 19, pp. 8143–8148, 2007.

[51] O. et al. Ayling, “Automated light-based mapping of motor cortex by photoactivation of channelrhodopsin-2 transgenic mice,” *Nat. Methods*, vol. 6, no. 3, pp. 219–224, 2013.

[52] C. Lutz, T. S. Otis, V. DeSars, S. Charpak, D. A. DiGregorio, and V. Emiliani, “Holographic photolysis of caged neurotransmitters,” *Nat. Methods*, vol. 5, no. 9, pp. 821–827, 2008.

[53] Z. V Guo, A. C. Hart, and S. Ramanathan, “Optical interrogation of neural circuits in Caenorhabditis elegans,” *Nat. Methods*, vol. 6, no. 12, pp. 891–U47, 2009.

[54] A. M. Leifer, C. Fang-Yen, M. Gershow, M. J. Alkema, and A. D. T. Samuel, “Optogenetic manipulation of neural activity in freely moving Caenorhabditis elegans,” *Nat. Methods*, vol. 8, no. 2, pp. 147–U71, 2011.

[55] N. Farah, I. Reutsky, and S. Shoham, “Patterned optical activation of retinal ganglion cells,” *2007 Annu. Int. Conf. Ieee Eng. Med. Biol. Soc. Vols 1-16*, pp. 6369–6371 6760, 2007.

[56] T. Instruments, “How DLP Technology Works - DLP&MEMS -Ti.com,” 2013. [Online]. Available: http://www.ti.com/lsds/ti/analog/dlp/how-dlp-works.page.

[57] J. N. Stirman, M. M. Crane, S. J. Husson, S. Wabnig, C. Schultheis, A. Gottschalk, and H. Lu, “Real-time multimodal optical control of neurons and muscles in freely behaving Caenorhabditis elegans,” *Nat Meth*, vol. 8, no. 2, pp. 153–158, 2011.

[58] J. N. Stirman, M. M. Crane, S. J. Husson, A. Gottschalk, and H. Lu, “A multispectral optical illumination system with precise spatiotemporal control for the manipulation of optogenetic reagents,” *Nat. Protoc.*, vol. 7, no. 2, pp. 207–220, Jan. 2012.

[59] E. Papagiakoumou, F. Anselmi, A. Begue, V. de Sars, J. Gluckstad, E. Y. Isacoff, and V. Emiliani, “Scanless two-photon excitation of channelrhodopsin-2,” *Nat. Methods*, vol. 7, no. 10, pp. 848–U117, 2010.

[60] N. Grossman, V. Poher, M. S. Grubb, G. T. Kennedy, K. Nikolic, B. McGovern, R. Berlinguer Palmini, Z. Gong, E. M. Drakakis, M. a a Neil, M. D. Dawson, J. Burrone, and P. Degenaar, "Multi-site optical excitation using ChR2 and micro-LED array.," *J. Neural Eng.*, vol. 7, no. 1, p. 16004, Feb. 2010.

[61] Y. Zhao, S. Inayat, D. A. Dikin, J. H. Singer, R. S. Ruoff, and J. B. Troy, "Patch clamp technique: review of the current state of the art and potential contributions from nanoengineering," *Proc. Inst. Mech. Eng. Part N J. Nanoeng. Nanosyst.*, vol. 222, no. 1, pp. 1–11, Jan. 2008.

[62] C. A. Thomas, P. A. Springer, G. E. Loeb, Y. Berwald-Netter, and L. M. Okun, "A miniature microelectrode array to monitor the bioelectric activity of cultured cells," *Exp. Cell Res.*, vol. 74, no. 1, pp. 61–66, 1972.

[63] F. Hofmann and H. Bading, "Long term recordings with microelectrode arrays: Studies of transcription-dependent neuronal plasticity and axonal regeneration," *J. Physiol.*, vol. 99, no. 2–3, pp. 125–132, 2006.

[64] "Scientifica." Kingfisher Court, Brambleside, Bellbrook, Industrial Estate, Uckfield East Sussex, TN22 1QQ, United Kingdom.

[65] K. Y. Kwon, B. Sirowatka, W. Li, and A. Weber, "Opto- µ ECoG Array : Transparent µ ECoG Electrode Array and Integrated LEDs for Optogenetics."

[66] D. S. Peterka, H. Takahashi, and R. Yuste, "Imaging voltage in neurons.," *Neuron*, vol. 69, no. 1, pp. 9–21, Jan. 2011.

[67] J. Butler, "Optogenetics: shining a light on the brain," *Biosci. Horizons*, vol. 5, no. 0, pp. hzr020–hzr020, Mar. 2012.

[68] W. Akemann, H. Mutoh, A. Perron, J. Rossier, and T. Knöpfel, "Imaging brain electric signals with genetically targeted voltage-sensitive fluorescent proteins.," *Nat. Methods*, vol. 7, no. 8, pp. 643–9, Aug. 2010.

[69] A. Perron, H. Mutoh, W. Akemann, S. G. Gautam, D. Dimitrov, Y. Iwamoto, and T. Knöpfel, "Second and third generation voltage-sensitive fluorescent proteins for monitoring membrane potential.," *Front. Mol. Neurosci.*, vol. 2, no. June, p. 5, Jan. 2009.

[70] C. Grienberger and A. Konnerth, "Imaging calcium in neurons.," *Neuron*, vol. 73, no. 5, pp. 862–85, Mar. 2012.

[71] A. Stroh, F. Schmid, L. Wachsmuth, B. Berninger, V. Riedl, A. Wohlschlaeger, J. Kressel, C. Zimmer, and C. Faber, "Bridging the gap : perspectives of combining optogenetics , calcium imaging and fMRI," p. 4.

[72] S. Su, S. C. Phua, R. DeRose, S. Chiba, K. Narita, P. N. Kalugin, T. Katada, K. Kontani, S. Takeda, and T. Inoue, "Genetically encoded calcium indicator illuminates calcium dynamics in primary cilia," *Nat Meth*, vol. 10, no. 11, pp. 1105–1107, Nov. 2013.

[73] A. Miyawaki, O. Griesbeck, R. Heim, and R. Y. Tsien, "Dynamic and quantitative Ca2+ measurements using improved cameleons," *Proc. Natl. Acad. Sci.* , vol. 96 , no. 5 , pp. 2135–2140, Mar. 1999.

[74] R. Cossart, Y. Ikegaya, and R. Yuste, “Calcium imaging of cortical networks dynamics.,” *Cell Calcium*, vol. 37, no. 5, pp. 451–7, May 2005.

[75] V. Gradinaru, M. Mogri, K. R. Thompson, J. M. Henderson, and K. Deisseroth, “Optical Deconstruction of Parkinsonian Neural Circuitry,” *Science (80-.).*, vol. 324, no. 5925, pp. 354–359, 2009.

[76] P. S. Lagali, D. Balya, G. B. Awatramani, T. A. Munch, D. S. Kim, V. Busskamp, C. L. Cepko, and B. Roska, “Light-activated channels targeted to ON bipolar cells restore visual function in retinal degeneration.,” *Nat. Neurosci.*, vol. 11, no. 6, pp. 667–75, Jun. 2013.

[77] E. F. Schubert, T. Gessmann, and J. K. Kim, *Light Emitting Diodes, Kirk-Othmer Encyclopedia of Chemical Technology*. Hoboken, NJ, USA: John Wiley & Sons, Inc., 2000.

[78] S. Nakamura and S. F. Chichibu, *Introduction to Nitride Semiconductor Blue Lasers and Light Emitting Diodes*. Taylor & Francis, 2000.

[79] Z. Y. Fan, J. Y. Lin, and H. X. Jiang, “III-nitride micro-emitter arrays: development and applications,” *J. Phys. D-Applied Phys.*, vol. 41, no. 9, p. -, 2008.

[80] E. F. Schubert, *Light-Emitting Diodes*. Cambridge University Press, 2006.

[81] F. Scholz, “Compound semiconductors: Physics, technology and device concepts.” [Online]. Available: http://www-opto.e-technik.uni-ulm.de/lehre/cs/.

[82] N. Holonyak and S. F. Bevacqua, “COHERENT (VISIBLE) LIGHT EMISSION FROM Ga(As1−xPx) JUNCTIONS,” *Appl. Phys. Lett.*, vol. 1, no. 4, p. 82, 1962.

[83] S. Nakamura, M. Senoh, and T. Mukai, “P-GaN/N-InGaN/N-GaN Double-Heterostructure Blue-Light-Emitting Diodes,” *Jpn. J. Appl. Phys.naka*, vol. 32, pp. L8–L11, 1993.

[84] H. Amano, M. Kito, K. Hiramatsu, and I. Akasaki, “P-Type Conduction in Mg-Doped GaN Treated with Low-Energy Electron Beam Irradiation (LEEBI),” *Jpn. J. Appl. Phys.*, vol. 28, pp. L2112–L2114, 1989.

[85] S. Strite and H. Morkoc, “GaN, AlN, and InN: A review,” *J. Vac. Sci. Technol. B Microelectron. Nanom. Struct.*, vol. 10, no. 4, pp. 1237–1266, 1992.

[86] T. Mukai, K. Takekawa, and S. Nakamura, “InGaN-Based Blue Light-Emitting Diodes Grown on Epitaxially Laterally Overgrown GaN Substrates,” *Jpn. J. Appl. Phys.*, vol. 37, no. Part 2, No. 7B, pp. L839–L841, Jul. 1998.

[87] S. Nakamura, M. Senoh, N. Iwasa, S. Nagahama, T. Yamada, and T. Mukai, “Superbright Green InGaN Single-Quantum-Well-Structure Light-Emitting Diodes,” *Jpn. J. Appl. Phys.*, vol. 34, pp. L1332–L1335, 1995.

[88] S. D. Lester, F. A. Ponce, M. G. Craford, and D. A. Steigerwald, “High dislocation densities in high efficiency GaN-based light-emitting diodes,” *Appl. Phys. Lett.*, vol. 66, no. 10, p. 1249, 1995.

[89] C. Das Naresh and C. Wayne, “Performance Comparison of Bottom and Top Emitting LWIR (8 ?m) LED Devices,” 2009, p. CTuW6.

[90] Z. Gong and et al., “Efficient flip-chip InGaN micro-pixellated light-emitting diode arrays: promising candidates for micro-displays and colour conversion,” *J. Phys. D. Appl. Phys.*, vol. 41, no. 9, p. 94002, 2008.

[91] H. Xu, J. Zhang, K. M. Davitt, Y. K. Song, and A. V Nurmikko, “Application of blue-green and ultraviolet micro-LEDs to biological imaging and detection,” *J. Phys. D-Applied Phys.*, vol. 41, no. 9, p. -, 2008.

[92] H.-Y. Gao and et al., “Improved Light Extraction of GaN-based LEDs with Nano-roughened p-GaN surfaces,” vol. 25, no. 9, p. 3448, 2008.

[93] A. David, T. Fujii, B. Moran, S. Nakamura, S. P. DenBaars, C. Weisbuch, and H. Benisty, “Photonic crystal laser lift-off GaN light-emitting diodes,” *Appl. Phys. Lett.*, vol. 88, no. 13, p. -, 2006.

[94] S. Tanriseven, P. Maaskant, and B. Corbett, “Broadband quantum dot micro-light-emitting diodes with parabolic sidewalls,” *Appl. Phys. Lett.*, vol. 92, no. 12, p. -, 2008.

[95] C. Griffin, E. Gu, H. W. Choi, and A. Al, “Fluorescence excitation and lifetime measurements using GaN / InGaN micro LED arrays,” vol. 40, pp. 896–897, 2004.

[96] N. McAlinden, D. Massoubre, E. Richardson, E. Gu, S. Sakata, M. D. Dawson, and K. Mathieson, “Thermal and optical characterization of micro-LED probes for in vivo optogenetic neural stimulation.,” *Opt. Lett.*, vol. 38, no. 6, pp. 992–4, Mar. 2013.

[97] Z. Gong, H. X. Zhang, E. Gu, C. Griffin, M. D. Dawson, V. Poher, G. Kennedy, P. French, and M. Neil, “Matrix-addressable micropixellated InGaN light-emitting diodes with uniform emission and increased light output,” *IEEE Trans. Electron Devices*, vol. 54, no. 10, pp. 2650–2658, 2013.

[98] G. Nagel, T. Szellas, W. Huhn, S. Kateriya, N. Adeishvili, P. Berthold, D. Ollig, P. Hegemann, and E. Bamberg, “Channelrhodopsin-2, a directly light-gated cation-selective membrane channel.,” *Proc. Natl. Acad. Sci. U. S. A.*, vol. 100, no. 24, pp. 13940–5, Nov. 2003.

[99] “mLED,” *http://www.mled-ltd.com/applications*. 50 Richmond Street, Glasgow, G1 1XP, Scotland, UK.

[100] R. Smith and E. Judd, “Geometrical Optics and Lens Design,” *MsC Photonics Cours Lab.*, 2011.

[101] P. Nussbaum, R. Volke, H. P. Herzig, M. Eisner, and S. Haselbeck, “Design , fabrication and testing of microlens arrays for sensors and microsystems,” vol. 6, no. 6, pp. 617–636, 1997.

[102] H. Ottevaere, R. Cox, H. P. Herzig, K. Naessens, T. Miyashita, M. Taghizadeh, R. Volkel, H. J. Woo, and H. Thienpont, “Comparing glass and plastic refractive microlenses fabricated with different technologies,” *J. Opt. A Pure Appl. Opt.*, vol. 8, no. 7, pp. S407–S429, Jul. 2006.

[103] S. Chen, X. Yi, and H. Ma, “A novel method of fabrication of microlens arrays,” *Infrared Phys. & Technol.*, vol. 44, no. 2, pp. 133–135, 2003.

[104] C. T. Pan, Y. C. Chen, M. F. Chen, and Y. C. Hsu, “Fabrication and design of various dimensions of multi-step ashperical microlens arrays for OLED package,” *Opt. Commun.*, vol. 284, no. 13, pp. 3323–3330, 2011.

[105] B. D. Gates, Q. B. Xu, M. Stewart, D. Ryan, C. G. Willson, and G. M. Whitesides, “New approaches to nanofabrication: Molding, printing, and other techniques,” *Chem. Rev.*, vol. 105, no. 4, pp. 1171–1196, 2005.

[106] K. H. Liu, M. F. Chen, Y. C. Chen, Y. M. Hwang, C. T. Pan, S. C. Shen, M. Y. Chang, W. Y. Huang, and W. C. Li, “Fabrication of an Aspherical Microlens for OLED with Modified Etching Process,” in *Electrical and Control Engineering (ICECE), 2010 International Conference on*, 2010, pp. 4838–4841.

[107] M. V Kunnavakkam, F. M. Houlihan, M. Schlax, J. a. Liddle, P. Kolodner, O. Nalamasu, and J. a. Rogers, “Low-cost, low-loss microlens arrays fabricated by soft-lithography replication process,” *Appl. Phys. Lett.*, vol. 82, no. 8, p. 1152, 2003.

[108] “Glyndwr Innovations Ltd.” The OpTIC Centre Ffordd William Morgan City of St. Asaph LL17 0JD, North Wales, UK.

[109] “RPC Photonics, Inc.” 330 Clay Road, Rochester, NY 14623, USA.

[110] “Introduction to microlenses.” SUSS MicroOptics, Rouges-Terres 61, CH 2068 Hauterive, Switzerland, Phone: +41 32 566 44 44, 2011.

[111] G. Schlingloff, H. J. Kiel, and A. Schober, “Microlenses as amplification for CCD-based detection devices for screening applications in biology, biochemistry, and chemistry,” *Appl. Opt.*, vol. 37, no. 10, pp. 1930–1934, 1998.

[112] R. Stevens, “Standards for microlenses and microlens arrays.” 2008.

[113] S. D. D. SCHREIBER P. KUDAEV and Z. U., “Homogeneous LED-illumination using microlens arrays,” vol. 5942, 2005.

[114] C. L. Lee, M. D. Dawson, and E. Gu, “Diamond double-sided micro-lenses and reflection gratings,” *Opt. Mater. (Amst).*, vol. 32, no. 9, pp. 1123–1129, 2010.

[115] H. W. Choi, E. Gu, C. Liu, J. M. Girkin, and M. D. Dawson, “Fabrication and evaluation of GaN negative and bifocal microlenses,” *J. Appl. Phys.*, vol. 97, no. 6, p. -, 2005.

[116] J. S. Liu, A. J. Caley, M. R. Taghizadeh, E. Gu, J. M. Girkin, and M. D. Dawson, “Design of diffractive optical elements for beam shaping of micro-pixellated LED light to a tightly focused spot,” *J. Phys. D-Applied Phys.*, vol. 41, no. 9, p. -, 2008.

[117] H. W. Choi, C. Liu, E. Gu, G. McConnell, J. M. Girkin, I. M. Watson, and M. D. Dawson, “GaN micro-light-emitting diode arrays with monolithically integrated sapphire microlenses,” *Appl. Phys. Lett.*, vol. 84, no. 13, pp. 2253–2255, 2004.

[118] C. W. Jeon, E. Gu, C. Liu, J. M. Girkin, and M. D. Dawson, “Polymer microlens arrays applicable to AlInGaN ultraviolet micro-light-emitting diodes,” *Ieee Photonics Technol. Lett.*, vol. 17, no. 9, pp. 1887–1889, 2005.

[119] C. W. Jeon, E. Gu, and M. D. Dawson, “Mask-free photolithographic exposure using a matrix-addressable micropixellated AlInGaN ultraviolet light-emitting diode,” *Appl. Phys. Lett.*, vol. 86, no. 22, 2005.

[120] B. C. Platt and R. Shack, “History and Principles of Shack-Hartmann Wavefront Sensing,” *J. Refract. Surg.*, vol. 17, no. September/October 2001, pp. S573–S577, 2001.

[121] E. Moreno-Barriuso and R. Navarro, “Laser Ray Tracing versus Hartmann–Shack sensor for measuring optical aberrations in the human eye,” *J. Opt. Soc. Am. A*, vol. 17, no. 6, p. 974, 2000.

[122] R. Ng, M. Levoy, M. Brédif, and E. Al., “Light Field Photography with a Hand-Held Plenoptic Camera,” *Stanford Univ. Comput. Sci. Tech Rep. CSTR*, vol. 2005–02.

[123] “SUSS MicroOptics.” SUSS MicroOptics, Rouges-Terres 61, CH 2068 Hauterive, Switzerland, Phone: +41 32 566 44 44, 2012.

[124] Advance Microoptics Systems gmbh, “[aμs] advanced microoptic systems gmbh.” Lebacher Straße 6a D-66113 Saarbrücken, Germany, Tel. +49 - 681 400 00 - 30.

[125] “Flexible Optical B.V.” Polakweg 10-11 2288 GG Rijswijk ZH The Netherlands, Tel: +31-70-2629420, 2013.

[126] “Adaptive Optics Associates Xinetics.” Systems and Services Product Design & Maintenance Business Area 10 Wilson Road Cambridge, MA 02138-1128, USA Phone: +1 617-806-1400 Fax: +1 617-806-1899.

[127] Hamamatsu, “High Resolution Digital B/W CCD Camera Orca ER,” *Data sheet*, 2004. .

[128] W. J.Smith, *Modern Lens Design*, Second. Mc Graw Hill, 2005.

[129] C. M. Griot, “Optical Performance Factors,” *CVI Melles Griot Technical Guide, Fundamental Optics*, Freiburg, 2013.

[130] “Aplanatic Meniscus Glass Lenses Application Note,” *CVI Melles Griot Optical Components, Application Note*, Freiburg, 2013.

[131] “http://www.radiantzemax.com/en/,” 2013. [Online]. Available: http://www.radiantzemax.com/en/.

[132] “http://www.silloptics.de/,” 2013. [Online]. Available: http://www.silloptics.de/.

[133] “Bellingham + Stanley Ltd.” Longfield Road, Tunbridge Wells, Kent TN2 3EY, UK.

[134] “Norland Products.” 2540 Route 130, Suite 100, Cranbury, NJ 08512, US.

[135] eMagin, “WFO5 prism optics and Microviewer Module - eMagin.” .

[136] Ocularinc, “Ocular Imaging Eye Model.” [Online]. Available: http://www.ocularinc.com/products/educational-aides/ocular-imaging-eye-model.html.

[137] T. C. Van Cader, “History of Ophthalmic Photography,” *J. Ophthalmic Photogr.*, pp. cader7–9, 1978.

[138] M. Kaschke, K.-H. Donnerhacke, and M. S. Rill, *Optical Devices in Ophthalmology and Optometry*. Wiley-VCH, 2014.

[139] Zeiss, “Eye Examination with the Slit Lamp.” Carl Zeiss Meditec AG,Goeschwitzer Str. 51-52, 07745 Jena,Germany,Phone: +49 (0) 36 41 / 22 0-3 33.

[140] E. DeHoog and J. Schwiegerling, “Fundus camera systems: a comparative analysis.,” *Appl. Opt.*, vol. 48, no. 2, pp. 221–8, Jan. 2009.

[141] “Volk Optical Inc.” 7893 Enterprise Drive, Mentor, Ohio 44060, USA, 001 4409426161.

[142] Y. Geng, L. A. Schery, R. Sharma, A. Dubra, K. Ahmad, R. T. Libby, and D. R. Williams, “Optical properties of the mouse eye.,” *Biomed. Opt. Express*, vol. 2, no. 4, pp. 717–38, Jan. 2011.

[143] B. Guilhabert, D. Massoubre, E. Richardson, J. J. D. Mckendry, G. Valentine, R. K. Henderson, I. M. Watson, E. Gu, M. D. Dawson, and A. The, “Sub-Micron Lithography Using InGaN of LED Arrays,” *IEEE Photonics Technol. Lett.*, vol. 24, no. 24, pp. 2221–2224, 2012.

Appendices

A.1 Optical set-ups estimation spreadsheet

A.1.1 Mathematical formulas

Collection efficiency

Intensity of the light:

$$I_V(\theta) = \frac{\phi(\theta)}{\Omega(\theta)} => \ \phi(\theta) \ = \ I_V(\theta).\Omega(\theta) \qquad \text{A.1}$$

Where Iv(θ) is in W, ϕ(θ) the flux in W/mm2 and Ω(θ) the solid angle. The flux of light is calculated for light emitted through a cone between 0 and θ. For a Lambertian emission, the intensity of the light emitted is:

$$I_V(\theta) = I_0.\cos(\theta) \qquad \text{A.2}$$

Flux of light between 0 and θ:

$$\phi(\theta) = \int_0^\theta I_V(\theta).d(\Omega(\theta)) \qquad \text{A.3}$$

Where

$$\Omega(\theta) = 2.\pi.(1 - \cos(\theta)) \qquad \text{A.4}$$

And therefore $d\big(\Omega(\theta)\big) = \ 2\pi.sin(\theta).d\theta$

$$\phi(\theta) = \ 2\pi \int_0^\theta I_V(\theta).\sin(\theta).d\theta \ = \ 2\pi.I_0.\int_0^\theta \cos(\theta).\sin(\theta).d\theta \ = \ 2\pi.I_0.\left[\frac{\sin^2(\theta)}{2}\right]_0^\theta$$

$$\phi(\theta) = \pi.I_0.\sin^2(\theta) \qquad \text{A.5}$$

Optical system efficiency (E_{system}) or light collected by a lens is equal to:

$$E_{system} = \frac{\phi_{Collection}(\theta)}{\phi_{Emission}(\theta)} = \frac{\pi.I_0.\sin^2\theta_{Collection}}{\pi.I_0.\sin^2\theta_{Emission}} = \frac{NA^2_{Collection}}{NA^2_{Emission}} \qquad \text{A.6}$$

Micro-lens array

Numerical Aperture:

$$NA_{\mu Lens} = \frac{\emptyset_{\mu Lens}/_2}{f_{\mu Lens}} \quad \text{A.7}$$

Radius of curvature:

$$R_C = (n-1).f_{\mu Lens} \quad \text{A.8}$$

Sag at the lens vertex:

$$h_L = R - \sqrt{R^2 - r^2} \quad \text{A.9}$$

Effective Diameter $\emptyset_{Eff(\mu Lens)}$ of a Micro-lens:

$$\emptyset_{Eff(\mu Lens)} = Min(\emptyset_{\mu Lens}, 2.NA_{Emission}.f_{\mu Lens}) \quad \text{A.10}$$

Where $Min()$ means that the lowest value between the $\emptyset_{\mu Lens}$ and the diameter of the light emitted will be selected as the effective diameter. It means that as long as the NA of the emission is higher or equal to the NA of the collection, the effective diameter of the micro-lens will be equal to the diameter of the micro-lens. It is not shown here because the relay optics tested had a higher or equal NA to the one from the micro-lens array.

Microscope Objective

Effective Magnification *M*:

$$M_{Eff} = \frac{f_{Tube\ lens}}{f_{Olympus}}.M_{Obj} \quad \text{A.11}$$

Effective *NA*:

$$NA_{Eff} = \frac{NA_{Obj}}{M_{Eff}} \quad \text{A.12}$$

Where $f_{Tube\ lens}$ is the tube lens focal length used, $f_{Olympus}$, the focal length lens of the tube lens used originally by Olympus in their microscope and M_{Obj}, the magnification of the microscope objective for the light going through the entrance aperture (see Figure A-1)

Figure A-1: Microscope objective schematic

Sample plane

Image size in µm:

$$\emptyset_{Image}(\mu m) = \frac{1000.\emptyset_{Eff(\mu Lens)}(mm)}{M_{Eff}} \quad \text{A.13}$$

Fill Factor (FF):

$$FF(\%) = \frac{A_{Image}}{A_{Total}} = \frac{\pi.(\emptyset_{Image}/2)^2}{\frac{Pitch_{\mu lens\ array}(mm).1000}{M_{Eff}}} \quad \text{A.14}$$

Where A_{Total} is the total area of the square contact where one emitter is, with a side equal to the pitch between 2 emitters. A_{Image} is the Area of the image of the emitter.

Power Density on the emitter image:

$$D_{Power} = \frac{P_{Image}(mW)}{A_{Image}} = \frac{P_{Image}(mW)}{\left(\left(\frac{\emptyset_{Image}(cm)}{2}\right)^2.\pi\right)} \quad \text{A.15}$$

Defocus Power Density or Power Density on the image of the entire square containing the emitter:

$$D_{Power-Defocus} = \frac{P_{Image}(mW)}{A_{Total}} = \frac{P_{Image}(mW)}{\left(Pitch_{\mu lens\ array}(cm)\right)^2} \quad \text{A.16}$$

A.1.2 Estimation Spreadsheet examples

The estimated results are shown below for a MLA with a Lambertian emission and a planned AoV of 22^{O}, several tube lenses used (f = 180 mm and f = 100 mm) and for the micro-optics used.

MLA without projection Optics

A maximum of 0.2% of light is collected with a Lambertian emitter. For a similar configuration to the one that should be used (a 100 mm focal tube lens and a 40x 0.8NA microscope objective), a collection efficiency of 0.13% is reached with a Lambertian emitter and 0.52% for an emitter with 22^{O} AoV with a FF of 2.18%.

MLA with projection Optics

With Projection Optics, more than 1% of the light is collected easily with a Lambertian emitter and more than 28% with a lower viewing angle LED.

Magnification	Micro-LED array			Microscope Objective and Tube lens					Results on Sample Plan		
	ϕ_{LED} (mm)	α (°)	NA_{LED}	$F_{tube\ lens}$ (mm)	M_{Obj} (x)	NA_{Obj}	M_{Eff}	$NA_{Eff\ tube\ lens}$	E_{image} (%)	ϕ_{Image} (µm)	FF (%)
1	0.025	90	1	180	4	0.16	4	0.04	0.16%	6.25	2.18%
				100	4	0.16	2.222	0.072	0.52%	11.25	
					10	0.3	5.556	0.054	0.29%	4.5	
					20	0.4	0.000	0.036	0.13%	2.25	
					40	0.8	22.222	0.036	0.13%	1.125	
		22	0.375	180	4	0.16	4.000	0.04	1.14%	6.25	
					10	0.3	10.000	0.054	0.64%	2.5	
					20	0.4	0.000	0.036	0.29%	1.25	
					40	0.8	40	0.036	0.29%	0.625	
				100	4	0.16	2.222	0.072	3.69%	11.25	
					10	0.3	5.556	0.054	2.08%	4.5	
					20	0.4	0.000	0.036	0.92%	2.25	
					40	0.8	22.222	0.036	0.92%	1.125	

Table A-1: Spreadsheet summarizing the estimated results without projection optics

Magnification	Micro-LED array			Relay optics		Micro-optics			
	ϕ_{LED} (mm)	α (°)	NA_{LED}	NA_{Relay}	E_{RElay} (%)	$\phi_{\mu Lens}$ (mm)	F_{uLens} (mm)	$NA_{\mu Lens}$	$E_{\mu Lens}$ (%)
1	0.025	90	1	0.14	1.96%	0.146	5.2	0.014	0.02%
1.48		90	1	0.17	2.89%	0.21	0.92	0.114	2.77%
1.67		90	1	0.366	13.40%	0.25	0.57	0.219	13.36%
		90	1	0.21	4.41%	0.25	1	0.125	4.34%
		22	1		31.43%				30.93%
		22	1						

Microscope Objective and Tube lens					Results on Sample Plan		
$F_{tube\ lens}$ (mm)	M_{Obj} (x)	NA_{Obj}	M_{Eff}	$NA_{Eff\ tube\ lens}$	E_{image} (%)	ϕ_{Image} (µm)	FF (%)
160	4	0.16	3.56	0.045	0.020%	41.0625	74.41%
160	20	0.4	17.78	0.0225	0.020%	8.2125	74.41%
100	4	0.16	2.22	0.072	2.77%	18.900	70.28%
100	40	0.8	22.22	0.036	2.77%	9.450	70.28%
100	4	0.16	2.22	0.072	13.36%	112.500	78.51%
100	40	0.8	22.22	0.036	12.91%	11.250	78.51%
100	4	0.16	2.22	0.072	4.34%	112.500	78.51%
100	40	0.8	22.22	0.036	4.34%	45.000	78.51%
100	4	0.8	2.22	0.360	30.93%	22.500	78.51%
100	40	0.8	22.22	0.036	30.93%	11.250	78.51%
180	4	0.16	4.00	0.040	30.93%	62.500	78.51%
180	10	0.3	10.00	0.030	30.93%	25.000	78.51%
180	20	0.4	20.00	0.020	28.49%	12.500	78.51%
180	40	0.8	40.00	0.020	28.49%	6.250	78.51%

Table A-2: Spreadsheet summarizing the estimated results with projection optics

A.2 Micro-lens arrays parameters

Figure A-2 shows the important parameters of a micro-lens and the different ways to pack them.

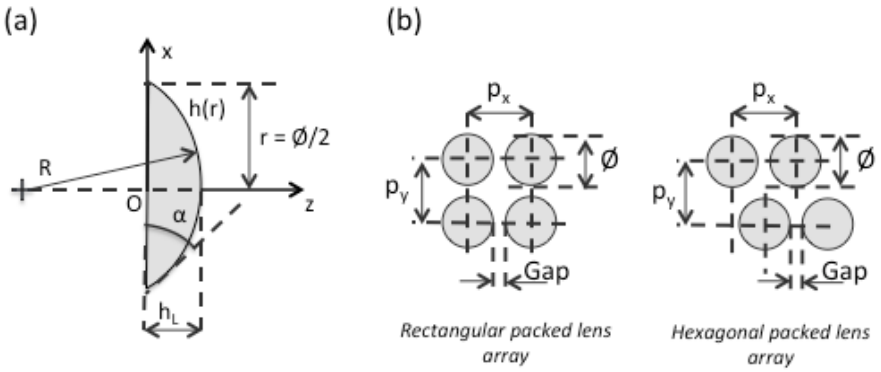

Figure A-2: Micro-lens array schematics
(a) Piano-convex micro-lens with a radius of curvature *R*, a radius *r* equal to the diameter divided by two, the sag at the lens vertex h_L and the contact angle at the lens border. (b) Rectangular and (c) hexagonal array with pitch in -x and -y directions[101]

The numerical aperture *NA* needs to be known to be able to get an idea of the collection efficiency of the system. For a Lambertian source, it is given by:

$$\eta \approx NA^2 \tag{A.17}$$

Effective focal length:

$$f_E = \frac{R}{n_1 - 1} \tag{A.18}$$

Numerical aperture:

$$NA = sin\alpha \approx \frac{r}{f_E} \tag{A.19}$$

Sag at the lens vertex:

$$h_L = R - \sqrt{R^2 - r^2} \tag{A.20}$$

Radius of curvature:

$$R = \frac{r^2}{2h_L} + \frac{(k+1)}{2} h_L \qquad \text{A.21}$$

F-number of a lens of diameter 2r is given by:

$$F = \frac{f}{\emptyset} \approx \frac{1}{2 \cdot NA} \qquad \text{A.22}$$

A.3 Cost of the RO studied and developed

RO Solutions	Suppliers	Off-the-shelf lenses	Custom lenses	NA	Cost (£)
1	CVI-MG	01LAO479, 01LAO524		0.139	248
2	Sill Optics	S5lpj1446, S5lpj1475		0.208	2040
3	CVI-MG and KO	01LAO479, 01LAO524	ML (f = 79.4mm)	0.208	528
4	CVI-MG, KO and Qo	01LAO524, LPX-30.0-31.1-C, G314332322	2 ML and 1 AD (f = 60mm)	0.208	854

***CVI-MG**: CVI-Melles-griot, **KO:** Knight Optical, **Qo:** Qioptiq, **ML:** Meniscus lens, **AD:** Achromatic doublet*

Table A-3: Characteristics of different RO solutions

A.4 Abbe Diagram n_d-v_d

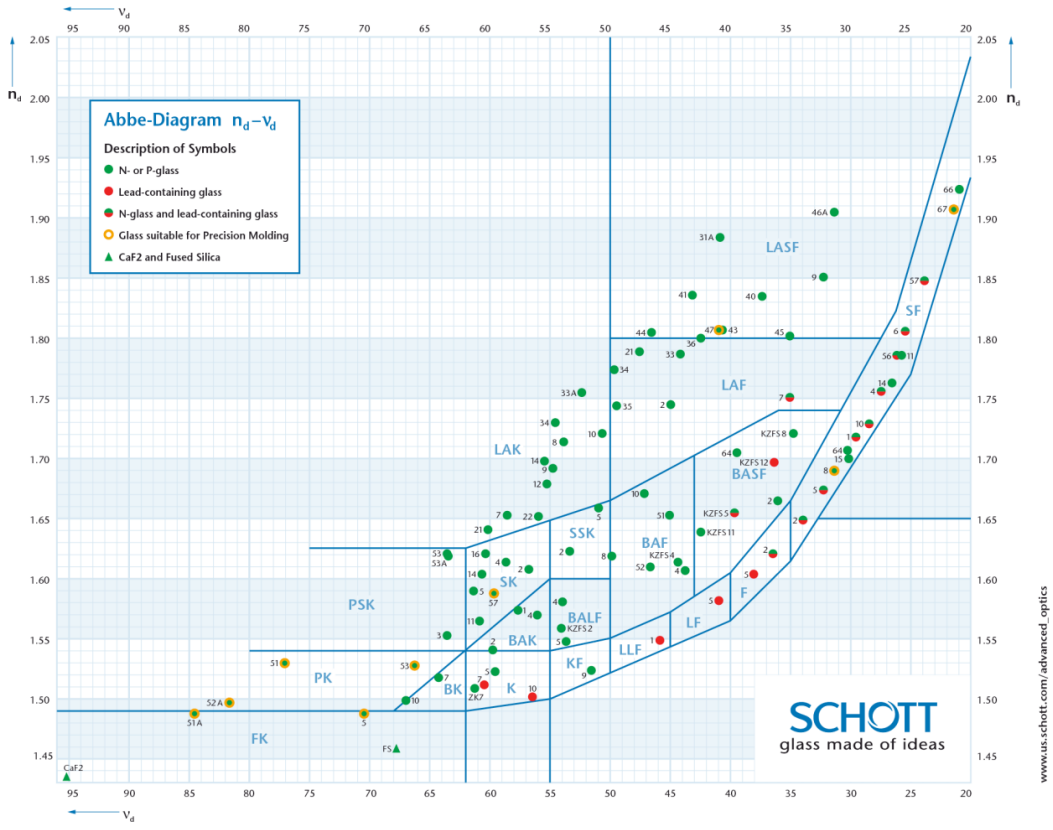

Figure A-3: Abbe Diagram nd – vd for Schott glasses [23]

A.5 Demonstration of the aplanatic condition

A.5.1 For a thin lens

$$\frac{1}{f'} = (n-1).\left(\frac{1}{r_1} - \frac{1}{r_2}\right) = \frac{(r_2 - r_1)}{r_1.r_2}.(n-1) \qquad \text{A.23}$$

From the formula shown in section 4.2.5, we can deduce f' and check the formulas:

$$f' = \frac{s}{n-1} \qquad \text{A.24}$$

A.5.2 For a thick lens

However, in real life, the thick lens formula is closer to the reality and is as well used by companies manufacturing aplanatic meniscus lenses. It is therefore used to determine the radii for a specified focal length and thickness

$$\frac{1}{f'} = (n-1).\left(\frac{1}{r_1} - \frac{1}{r_2} + \frac{(n-1).t_c}{n.r_1.r_2}\right) \qquad \text{A.25}$$

With $M = \frac{1}{n}$ and $s'' = \frac{n}{n_{Lens}}.s = \frac{s}{n_{Lens}}$ when n=1, we deduce r_2 :

$$r_2 = s'' - t_c = \frac{s}{n} - t_c = \frac{r_1.(n+1)}{n} - t_c \qquad \text{A.26}$$

We then replace r_2 into the previous equation (number) and deduce a quadratic equation from where the first radius is calculated:

$$r_1 = \frac{t_c + f'.\frac{n-1}{n} + \sqrt{\left(t_c + f'.\frac{n-1}{n}\right)^2 - 4.\frac{n+1}{n}.f'.\frac{n-1}{n}.t_c}}{2.\frac{n+1}{n}} \qquad \text{A.27}$$

The Back Focal Length *BFL* could as well be calculated:

$$BFL = f'.\left(1 - \frac{(n-1).t_c}{n.r_1}\right) \qquad \text{A.28}$$

A.6 Projection optics PO 2 detailed parameters

Surface	Lens	Rc (mm)	Thickness (mm)	Glass	Semi-Diameter (mm)
0	Object	0.000	6.000		1.700
1	Custom ML	-8.800	9.000	N-LAK7	7.000
2		-12.536	26.016		7.000
3	LPX-30.0-31.1-C	infinity	5.800	N-BK7	15.000
4		-31.123	1.000		15.000
5	Custom AD	75.261	2.500	N-SF5	15.000
6		21.588	10.000	N-SK11	15.000
7		-197.618	20.000		15.000
8		infinity	53.692		15.000
9	01LAO524	64.280	6.200	N-SK11	15.000
10		-44.980	2.500	N-SF5	15.000
11		-180.440	50.292		15.000
12	Custom ML	11.242	8.000	N-LAK7	6.350
13		14.027	2.500		6.350
14	314332000	-26.039	1.500	N-BK7	6.350
15		infinity	1.000		6.350
16	Image	infinity	0.000		2.844

***Rc**: Radius of curvature*

Table A-4: Projection optics PO 2 parameters shown also in Figure 6-1

A.7 LED Material characteristics

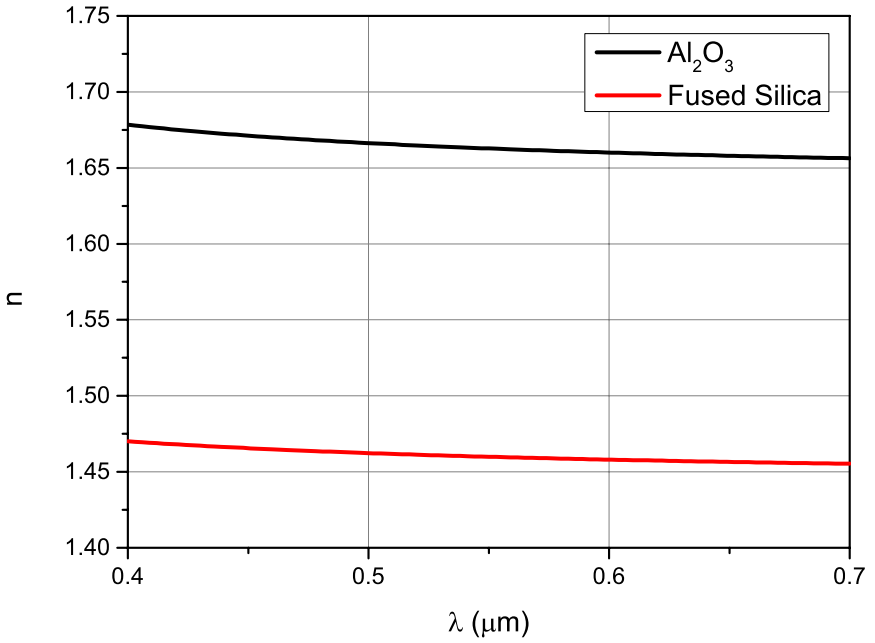

Figure A-4: Refractive index variation in the visible for Fused silica and Al_2O_3

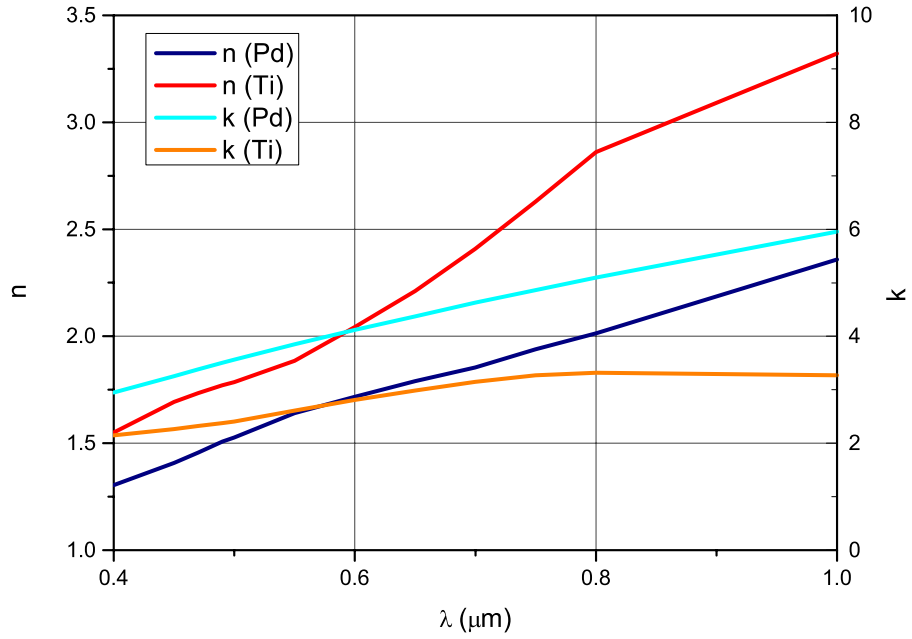

Figure A-5: Refractive index and extinction coefficient in the visible for Palladium (Pd) and Titanium (Ti)

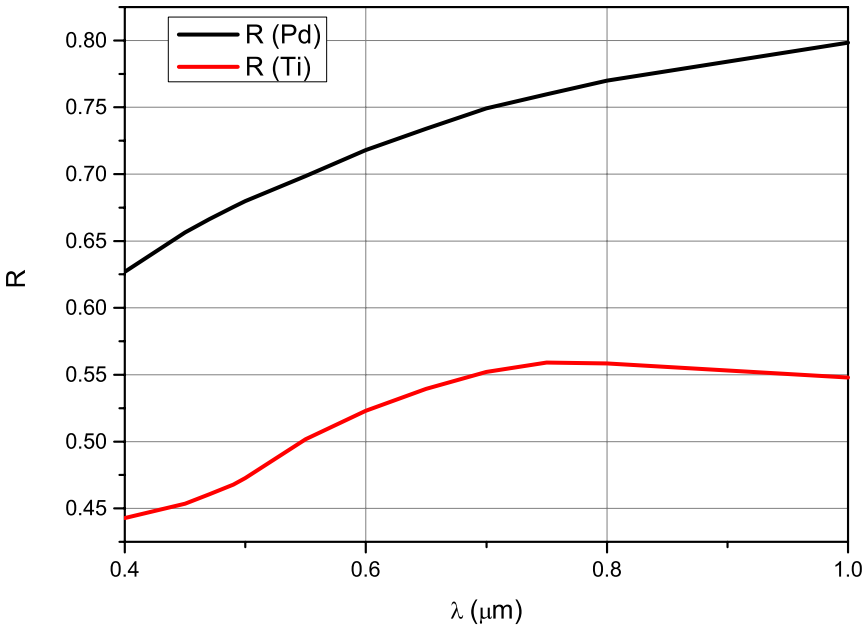

Figure A-6: Reflectivity in the visible for Palladium (Pd) and Titanium (Ti)

A.8 MO characteristics for different magnifications and tube lenses used for microscopes with 150 and 80μm diameter

M (Obj) (x)	NA (Obj 1)	Optimised focal ulens array (μm)	Radius of curvature (μm)	ø(micro-Lens) (μm)	NA micro-Lens Array)(μm)	Sag at the center for a square lens (μm)
4	0.16	305.000	157.929	80	131.148	10.4788
				150	245.902	40.9180
10	0.3	406.667	210.572	80	98.361	7.7406
				150	184.426	28.6639
20	0.5	488.000	252.686	80	81.967	6.4133
				150	153.689	23.3386
40	0.8	610.000	315.858	80	65.574	5.1069
				150	122.951	18.3411
60	0.9	813.333	421.144	80	49.180	3.8165
				150	92.213	13.5753

Table A-5: Optimised micro-lens characteristics for different magnifications and tube lenses used for microscopes with 80 and 150μm diameter MO

A.9 Equation to calculate the optimum thickness for each material for the MLA/MO system

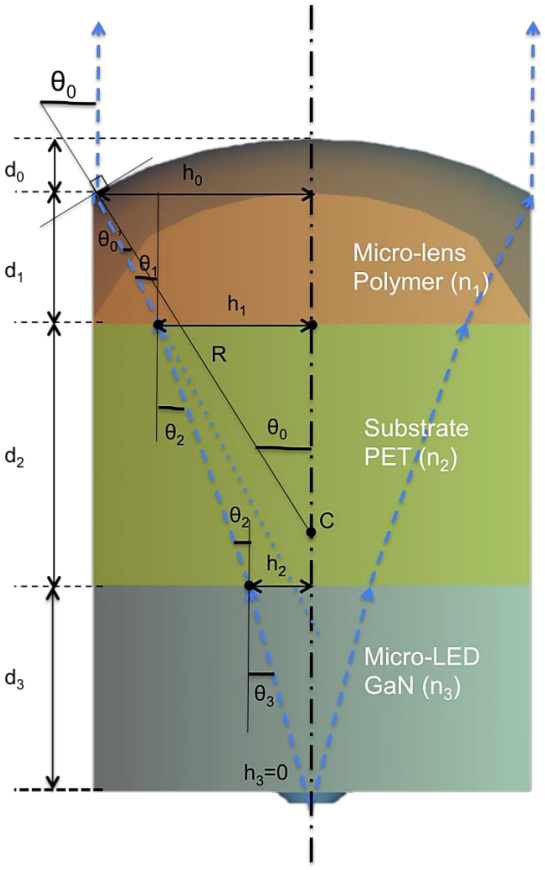

Figure A-7: Schematic of MLA/MO system with marginal rays displayed

Optimal micro-LED thickness calculus using Paraxial rays

Power K of the lens:

$$K = \frac{n_1 - 1}{R} = \frac{1}{f_{\mu L}} \qquad \text{A.29}$$

Where $f_{\mu L}$ is the focal of the micro-lens.

The angle of the principle ray u_1 in the micro-lens polymer is:

$$u_1 = -h_0 . \frac{n_1 - 1}{n_1 . R} \qquad \text{A.30}$$

The distance from the optical axis h_1 at the interface between the micro-lens and the substrate is:

$$h_1 = h_0 + u_1.d_1 = h_0 - h_0.\frac{n_1 - 1}{n_1.R}.d_1 \qquad \text{A.31}$$

The formulas for u_2, $h_2$and h_3 are deduces using the same basic formulas:

$$u_2 = \frac{n_1.u_1}{n_2} = -h_0.\frac{n_1 - 1}{n_2.R}$$

$$h_2 = h_1 + u_2.d_2 = h_1 - h_0.\frac{n_2 - 1}{n_2.R}.d_2$$

$$h_3 = h_2 - h_0.\frac{n_1 - 1}{n_3.R}.d_3 = 0$$

h_3 is equal to 0 because a point source is used in the calculus.

From these equations, the paraxial focus of the micro-lens can be deduced:

$$f_{\mu L} = \frac{d_1}{n_1} + \frac{d_2}{n_2} + \frac{d_3}{n_3} \qquad \text{A.32}$$

$f_{\mu L}$ and d_3 are the two unknown, however one of these two parameters is fixed by the manufacturer leaving only one unknown.

<u>Optimal micro-LED thickness calculus using Marginal ray</u>

Snell-Descartes law and trigonometry are used here.

- Angles: θ_0, θ_1, θ_2 and θ_3

The angle θ_0 corresponds to the angle between the tangent at the micro-lens exit point and the collimated beam exiting it:

$$\sin\theta_0 = \frac{h_0}{R} \qquad \text{A.33}$$

$$\sin\theta_0{}' = \frac{\sin\theta_0}{n_1} = \frac{h_0}{n_1.R} \qquad \text{A.34}$$

The following angles are going through plane surfaces and are therefore in the same repair:

$$n_1.\sin\theta_1 = n_2.\sin\theta_2 = n_3.\sin\theta_3 \qquad \text{A.35}$$

The beam exiting the micro-lens is parallel to the optical axis. Therefore, it can be deduced that $\theta_1 = \theta_0 - \theta_0{}'$. From there, the angles can be calculated.

$$\begin{aligned}\sin\theta_1 = \sin(\theta_0 - \theta_0{}') &= \frac{h}{n_1.R}.\left[\sqrt{{n_1}^2 - \sin{\theta_0}^2} - \cos\theta_0\right] \\ &= \frac{h}{n_1.R}.\left[\sqrt{{n_1}^2 - \left({h_0}/{R}\right)^2} - \frac{R-d_0}{R}\right]\end{aligned} \qquad \text{A.36}$$

And therefore:

$$\sin\theta_3 = \frac{n_2.\sin\theta_2}{n_3} = \frac{n_1.\sin\theta_1}{n_3} = \frac{h}{n_3.R}.\left[\sqrt{{n_1}^2 - \left({h_0}/{R}\right)^2} - \frac{R-d_0}{R}\right] \qquad \text{A.37}$$

- Distances to the optical axis: h_1, h_2 and h_3

$$\begin{cases} h_1 = h_0 - d_1.\tan\theta_1 \\ h_2 = h_1 - d_2.\tan\theta_2 \\ h_3 = h_2 - d_3.\tan\theta_3 = 0 \end{cases} \qquad \text{A.38}$$

h_0 corresponds to the maximum distance from the optical axis. If the system is optimised for a circular micro-lens, $h_0 = \emptyset_{\mu L}/2$. In this project, it is optimised for a square micro-lens. The square must be filed and the largest distance is: $h_0 = \left(\emptyset_{\mu L}/2\right).\sqrt{2}$.

A.10 Dispersion diagrams for PET and D263 (Schott)

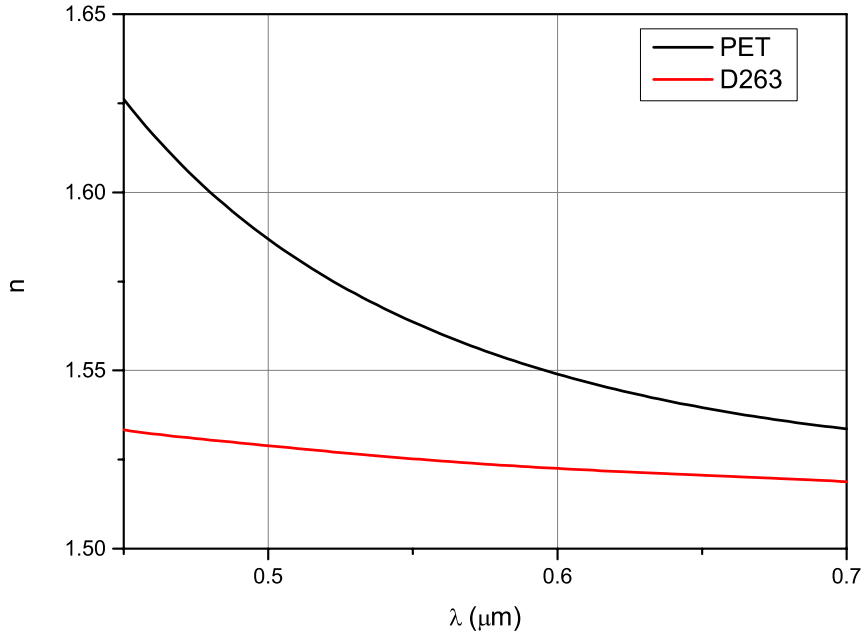

Figure A-8: Dispersion diagrams for PET and Borosilicate (D263 Schott)

A.11 Modelling results for the 80µm pitch GaN MLA and MO

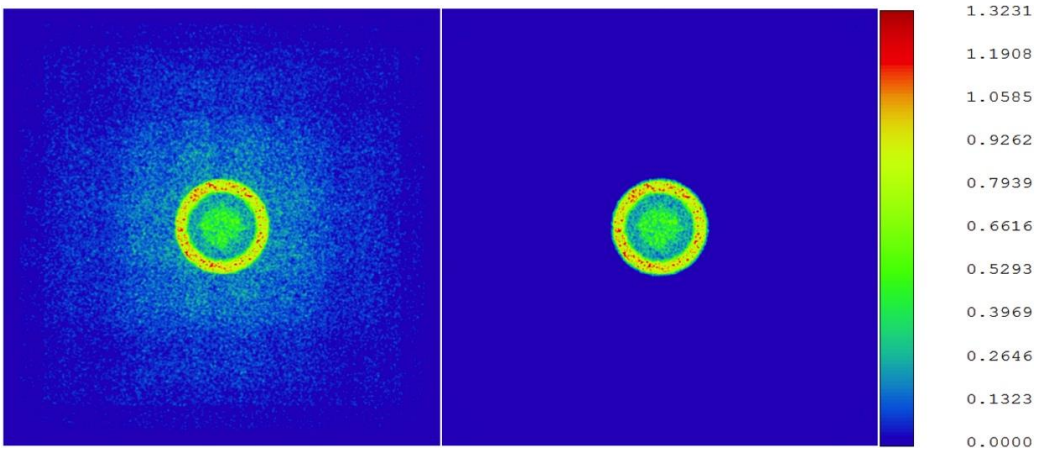

Figure A-9: NSC modelling of the 80µm GaN MLA image before and after the pupil of the microscope objective (left and right)

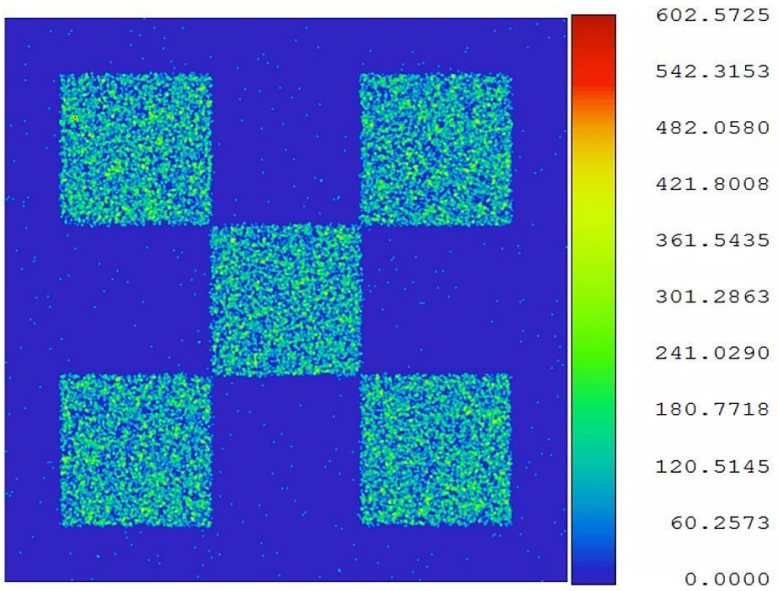

Figure A-10: NSC modelling of the 80µm pitch MO on the sample with the 80µm GaN MLA

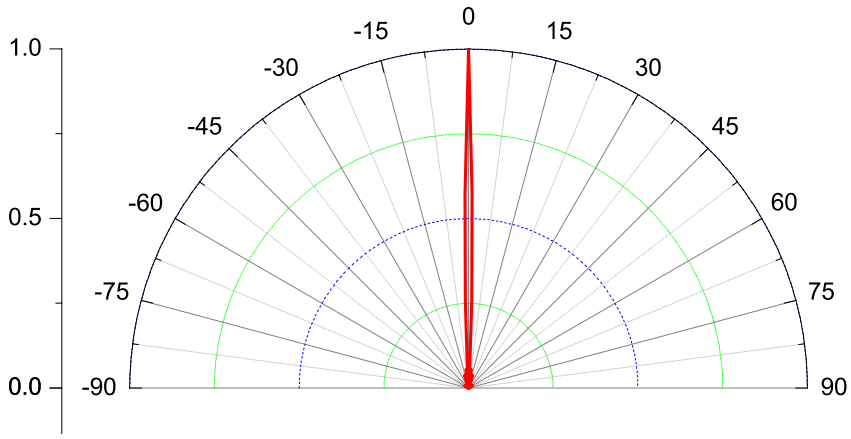

Figure A-11: Modelling of the 80µm pitch GaN MLA and MO light distribution

A.12 Modelling results for the 80µm pitch GaN/Al_2O_3 MLA and MO

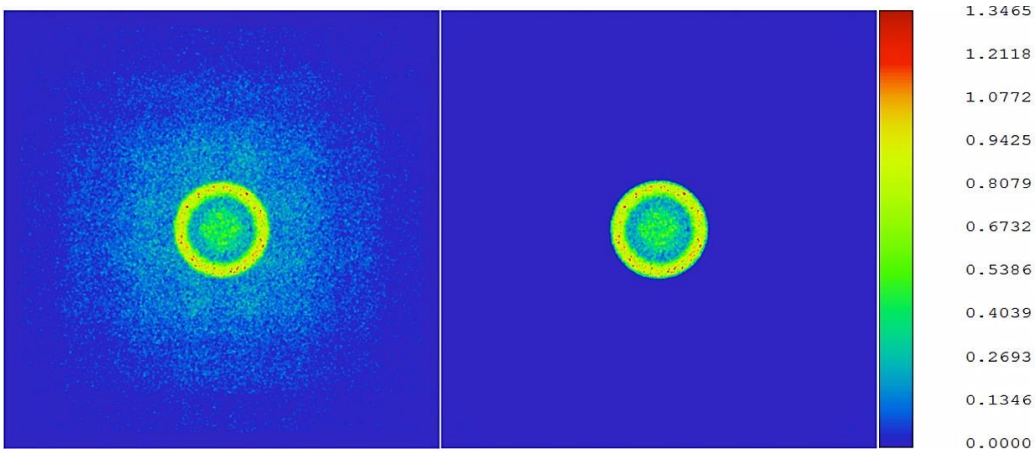

Figure A-12: NSC modelling of the 80µm GaN/Sapphire (Al_2O_3) MLA image before and after the pupil of the microscope objective (left and right)

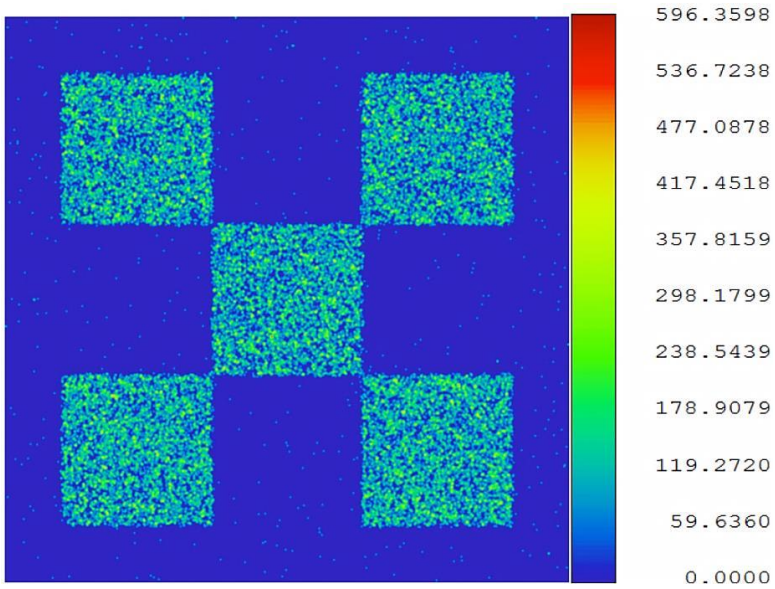

Figure A-13: NSC modelling of the 80µm pitch MO on the sample with the the 80µm GaN/Sapphire (Al_2O_3) MLA

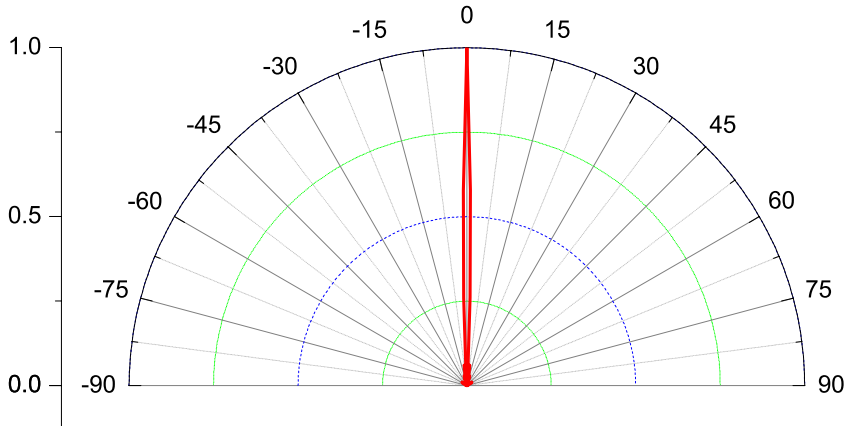

Figure A-14: Modelling of the 80µm pitch GaN/Sapphire (Al2O3) MLA and MO light distribution

A.13 Track length and pupil shift calculation study

Figure A-15: Simplified virtual reality set-up shows a simplified schematic of the different distances in the VR optics set-up.

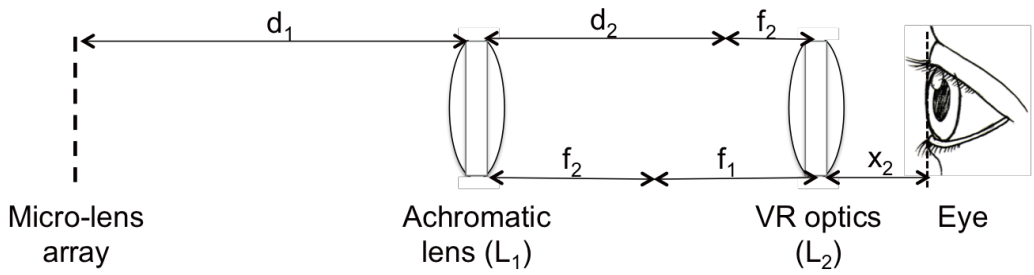

Figure A-15: Simplified virtual reality set-up

The track length $d_{Tot} = d_1 + d_2$ is calculated and its variation displayed in a diagram as a function of the magnification M of the image of the micro-lens array.

$$d_2 = M.d_1$$

$$\frac{1}{d_1} + \frac{1}{d_2} = \frac{1}{f_1} \Longrightarrow f_1 = \frac{M.{d_1}^2}{d_1(M+1)} \Longrightarrow d_1 = \frac{M+1}{M}.f_1$$

$$\Longrightarrow d_1 + d_2 = d_1(M+1) = f_1\left(M + 2 + {}^1/_M\right)$$

The VR optics was originally optimised for an OLED screen (SVGA+OLED-XL) having a viewing area of 12.78 x 9 mm. The micro-lens array imaged at the VR pupil is square and therefore its maximum magnification should be not more than $M = 9/4 = 2.25$. Figure A-16 shows its variation with M between 0 and 3 with the 4 lenses L_1 tested.

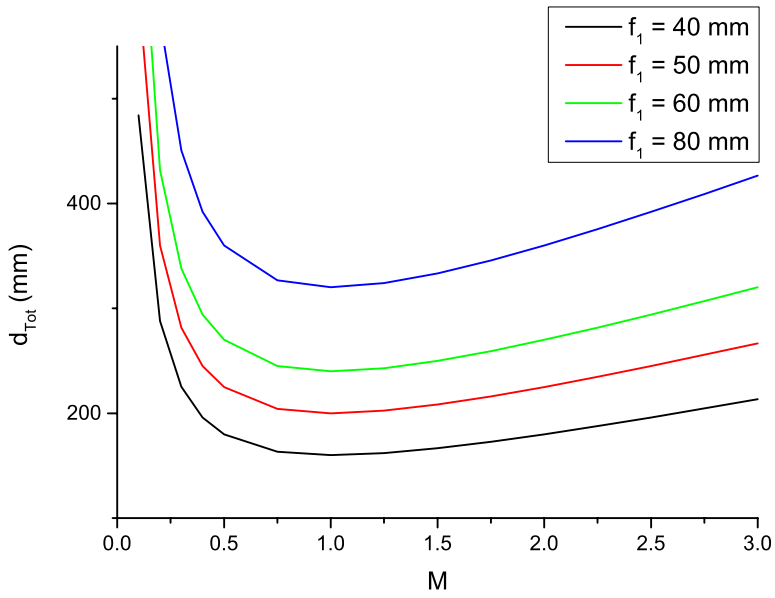

Figure A-16: Track length d_{Tot} variation with the magnification *M* of the micro-lens array image for 4 different lenses L_1

The pupil position is determined by the image plane of the individual microLEDs produced by the combination of the micro-lenses, the achromat and the VR optic. This shift of the pupil position is thus deduced from the variation of the position x_2.

$$x_1 = f_2 + d_2 - f_1 = f_2 + M.f_1$$

$$x_2 = \frac{f_2.x_1}{x_1 - f_2} = f_2 + \frac{{f_2}^2}{M.f_1}$$

Where $\left({f_2}^2/M.f_1\right)$ is the pupil shift from the focal plane of the lens.

Figure A-17 shows its variation with M for the 4 lenses tested.

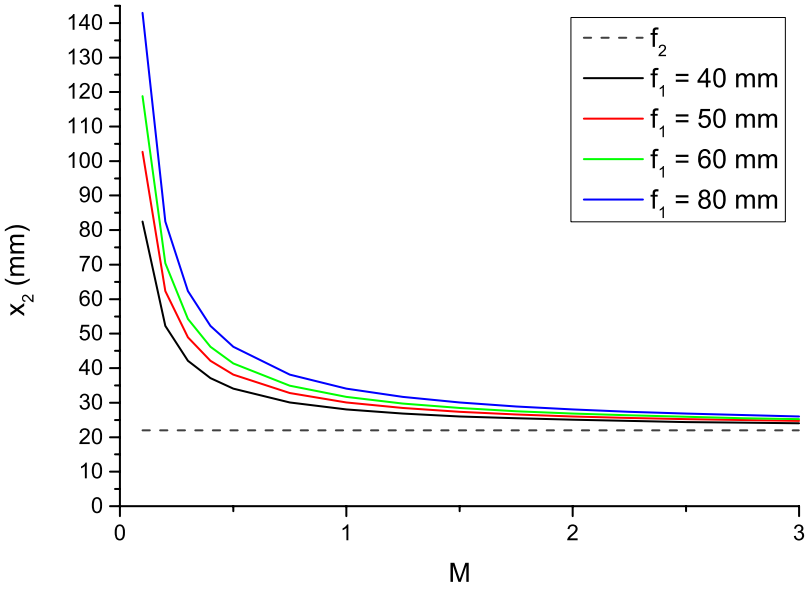

Figure A-17: Shift of the pupil position relative with the magnification *M* of the micro-lens array image for 4 different lenses L_1

A.14 Summary of permission for third party copyright works

Page Number	Type of work: figure, etc.	Source work	Copyright holder & year	Work out of copyright	Permission to re-use	Permission requested	permission refused	Orphan work
24	Figure 2-4	PLoS One, vol. 4, no. 11, p. e7679, Jan 2009	Open-Access License		✓			
31	Figure 2-7	Nat. Methods, vol. 8, no 12, pp1011-1013, 2011	© 2011 Nature Publishing Group		✓			
34	Figure 2-8	Nat. Neurosci., vol. 16, no. 7, pp 805-15, Jul. 2013	©2013 Nature Publishing Group		✓			
46	Figure 3-4	Prof Dr. F. Sholz, Institut fur Optoelektronik, Universitaet Ulm, Germany	© 2014, Prof Dr. F. Sholz,		✓			

53, 53	Figure 3-8, Figure 3-9	J. Neural Eng., vol. 7, no. 1, p. 16004, Feb. 2010	© IOP Publishing Material.		✓			
53	Figure 3-8 (Use work from another paper)	Proc. Natl. Acad. Sci. U. S. A., vol. 100, no. 24, pp. 13940–5, Nov. 2003.	© Natl. Acad. Sci. U. S. A.			✓		
54	Figure 3-10	J. Neural Eng., vol. 6, no. 3, 2009	© IOP Publishing Material.		✓			
66	Figure 3-20	J. Opt., A Pure Appl. Opt, vol. 8, no. 7, pp. S407-429, 2006	© IOP Publishing Material.		✓			
67	Figure 3-21	Opt. Commun., vol. 284, no. 13, pp. 3323-3330, 2011	© Elsevier Limited		✓			
85	Figure 4-13	pp. 42, fig. 2.8, Modern Lens Design (book),	©The McGraw-Hill Companies		✓			

		McGraw-Hill Prof. Engin., SPIE Press, ISBN 00714838300						

A.15 Permissions for third party copyright works

A.15.1 Figure 2.7

NATURE PUBLISHING GROUP LICENSE TERMS AND CONDITIONS

Jun 09, 2014

This is a License Agreement between Lionel Chaudet ("You") and Nature Publishing Group ("Nature Publishing Group") provided by Copyright Clearance Center ("CCC"). The license consists of your order details, the terms and conditions provided by Nature Publishing Group, and the payment terms and conditions.

All payments must be made in full to CCC. For payment instructions, please see information listed at the bottom of this form.

License Number	3404780424396
License date	Jun 09, 2014
Licensed content publisher	Nature Publishing Group
Licensed content publication	Nature Methods
Licensed content title	The Lego-logic of optogenetics
Licensed content author	Thomas G Oertner
Licensed content date	Nov 29, 2011
Volume number	8
Issue number	12
Type of Use	reuse in a dissertation / thesis
Requestor type	academic/educational
Format	print and electronic
Portion	figures/tables/illustrations
Number of figures/tables /illustrations	1
High-res required	no
Figures	Figure 1
Author of this NPG article	no
Your reference number	None
Title of your thesis / dissertation	Micro-optics for optogenetic neuro-stimulation with micro-LED arrays
Expected completion date	Jun 2014
Estimated size (number of pages)	230
Total	0.00 USD
Terms and Conditions	

A.15.2 Figure 2.8

NATURE PUBLISHING GROUP LICENSE
TERMS AND CONDITIONS

Jun 09, 2014

This is a License Agreement between Lionel Chaudet ("You") and Nature Publishing Group ("Nature Publishing Group") provided by Copyright Clearance Center ("CCC"). The license consists of your order details, the terms and conditions provided by Nature Publishing Group, and the payment terms and conditions.

All payments must be made in full to CCC. For payment instructions, please see information listed at the bottom of this form.

License Number	3404780847563
License date	Jun 09, 2014
Licensed content publisher	Nature Publishing Group
Licensed content publication	Nature Neuroscience
Licensed content title	Targeting neurons and photons for optogenetics
Licensed content author	Adam M Packer, Botond Roska, Michael Häusser
Licensed content date	Jun 25, 2013
Volume number	16
Issue number	7
Type of Use	reuse in a dissertation / thesis
Requestor type	academic/educational
Format	print and electronic
Portion	figures/tables/illustrations
Number of figures/tables /illustrations	1
High-res required	no
Figures	figure 4: Patterned illuminations strategies
Author of this NPG article	no
Your reference number	None
Title of your thesis / dissertation	Micro-optics for optogenetic neuro-stimulation with micro-LED arrays
Expected completion date	Jun 2014
Estimated size (number of pages)	230
Total	0.00 USD
Terms and Conditions	

A.15.3 Figure 3.4

Communication by mail with Prof. Dr. Ferdinand Scholz on the 17/03/2014:

"Dear Lionel,

no problem to use the diagram. It would be great if you indicate
accordingly where it comes from.
Please check the attached diagram, which is an improved version where on
the top axis the interatomic distance is plotted. Hence cubic and
hexagonal material can be fairly plotted in one diagram (only the slight
c/a changes for hexagonal material are not taken into account).
Best regards

Ferdinand Scholz"

A.15.4 Figure 3.8, 3.9, 3.10, 3.20

Communication by mail with Lucy Evans from IOP Publishing Material on the 10/06/2014:

"Dear Lionel Chaudet,

Thank you for your request to reproduce IOP Publishing material.
Figure 6 b- 2009 J. Neural Eng. 6 035007
Figures 4 & 6 - J. Neural Eng. 7 016004
Figure 1 - J opt A 8 2006 S407
please note that figure 4 from "Multi-site optical excitation using ChR2 and micro-LED array"contains
copy right material from [25] therefore you may need to seek permission from them also.
We are happy to grant permission for the use you request on the terms set out below.
If you have any questions, please feel free to contact our Permissions team at permissions@iop.org.
I should be grateful if you would acknowledge receipt of this email.
Kind regards,

Lucy Evans

Publishing Assistant
IOP Publishing"

A.15.5 Figure 3.21

ELSEVIER LICENSE
TERMS AND CONDITIONS

Jun 09, 2014

This is a License Agreement between Lionel Chaudet ("You") and Elsevier ("Elsevier") provided by Copyright Clearance Center ("CCC"). The license consists of your order details, the terms and conditions provided by Elsevier, and the payment terms and conditions.

All payments must be made in full to CCC. For payment instructions, please see information listed at the bottom of this form.

Supplier	Elsevier Limited The Boulevard,Langford Lane Kidlington,Oxford,OX5 1GB,UK
Registered Company Number	1982084
Customer name	Lionel Chaudet
Customer address	26 Hilgay Court Guildford, Surrey GU1 2ED
License number	3404810887738
License date	Jun 09, 2014
Licensed content publisher	Elsevier
Licensed content publication	Optics Communications
Licensed content title	Fabrication and design of various dimensions of multi-step ashperical microlens arrays for OLED package
Licensed content author	C.T. Pan,Y.C. Chen,M.F. Chen,Y.C. Hsu
Licensed content date	15 June 2011
Licensed content volume number	284
Licensed content issue number	13
Number of pages	8
Start Page	3323
End Page	3330
Type of Use	reuse in a thesis/dissertation
Portion	figures/tables/illustrations
Number of figures/tables /illustrations	2
Format	both print and electronic
Are you the author of this Elsevier article?	No
Will you be translating?	No

A.15.6 Figure 4.11

PERMISSION LICENSE: COMMERCIAL PRINT & ELECTRONIC USE

Request ID/Invoice Number: LIO48711

Date: July 10, 2014

To: Lionel Chaudet
Imperial College London
Physics Dept., Photonics Group
Blackett Laboratory, Imperial College
London, UK SW7 2BZ
UNITED KINGDOM
"Licensee"

McGraw-Hill Material

Author: W. Smith
Title: Modern Lens Design
Description of material: One Figure 2.8 on pg. 42

Fee: Waived

Licensee Work

Author: Lionel Chaudet
Title: *Micro-optics for Opto-genetic stimulation with Micro-LED Arrays [thesis]*
Publisher: Imperial College London
Publication Date: 2014
Print Run: 5
Format: Print and Imperial College's website
Distribution/territory: UK
Languages: English

Permission for the use described above is granted under the following terms and conditions:

1. McGraw-Hill Education hereby grants Licensee the non-exclusive right to include the McGraw-Hill Education Material in the Licensee Work and to reproduce and distribute the

McGraw-Hill Education Material as part of the Licensee Work. The McGraw-Hill Education material may be used only in the Licensee Work. All use of the McGraw-Hill Education material is subject to the terms and conditions of this Agreement.

2. No changes may be made to the McGraw-Hill Education material without the prior written consent of McGraw-Hill Education.

3. Licensee will provide to McGraw-Hill Education the URL and password for the web site in which the McGraw-Hill Education material appears (if applicable).

4. McGraw-Hill Education makes no representations or warranties as to the accuracy of any information contained in the McGraw-Hill Education material, including any warranties of merchantability or fitness for a particular purpose. In no event shall McGraw-Hill Education have any liability to any party for special, incidental, tort, or consequential damages arising out of or in connection with the McGraw-Hill Education material, even if McGraw-Hill Education has been advised of the possibility of such damages. All persons provided with the McGraw-Hill Education material must be provided with written notice of this disclaimer and limitation liability, either in an end-user license and/or with an on-screen notice that is visible each time the end-user initiates access to the McGraw-Hill Education material.

5. A credit to McGraw-Hill Education shall be visible each time the end-user initiates access to any screen or page containing any of the McGraw-Hill Education material. Such credit shall include the title and author of the work and a copyright notice in the name of McGraw-Hill Education LLC.

6. The permission fee of $0.00 must be received by McGraw-Hill Education LLC, and MUST BE ACCOMPANIED BY A SIGNED COPY OF THIS AGREEMENT.

7. **This permission does not cover the use of any third-party copyrighted material, including but not limited to photographs and other illustrations, which appears in the McGraw-Hill Education material with a credit to other sources. Written permission to use such material must be obtained from the cited source.**

8. McGraw-Hill Education shall have the right to terminate this Agreement immediately upon written notice to Licensee if Licensee is in material breach of this Agreement.

9. Licensee shall indemnify McGraw-Hill Education from any damages, lawsuits, claims, liabilities, costs, charges, and expenses, including attorney's fees, relating to its use of the McGraw-Hill Education material.

10. This Agreement incorporates the parties' entire agreement with respect to its subject matter. This Agreement may be amended only in writing and signed by both parties and shall be governed by the laws of New York. Licensee may not assign this Agreement or any rights granted hereunder to any third party.

Please sign both copies and return one to the McGraw-Hill Education Permissions Department, 2 Penn Plaza, 20th Floor, New York, NY 10121.

For McGraw-Hill Education LLC:

_____

Cynthia Aguilera
Permissions Department
McGraw-Hill Education LLC

For Licensee:

Name Lionel CHAUDET

Title Dr